



ISSN 1605-2730  
E-ISSN 1605-8119

# MATERIALS PHYSICS AND MECHANICS

Vol. 48, No. 2, 2022

# MATERIALS PHYSICS AND MECHANICS

## Principal Editors:

**Dmitrii Indeitsev**  
*Institute of Problems of Mechanical Engineering  
of the Russian Academy of Science (RAS), Russia*

**Andrei Rudskoi**  
*Peter the Great St.Petersburg Polytechnic University, Russia*

## Founder and Honorary Editor: Ilya Ovid'ko (1961-2017)

*Institute of Problems of Mechanical Engineering  
of the Russian Academy of Sciences (RAS), Russia*

## Associate Editors:

**Anna Kolesnikova**  
*Institute of Problems of Mechanical Engineering  
of the Russian Academy of Sciences (RAS), Russia*

**Alexander Nemov**  
*Peter the Great St.Petersburg Polytechnic University, Russia*

## Editorial Board:

**E.C. Aifantis**  
*Aristotle University of Thessaloniki, Greece*

**K.E. Aifantis**  
*University of Florida, USA*

**U. Balachandran**  
*Argonne National Laboratory, USA*

**A. Bellosi**  
*Research Institute for Ceramics Technology, Italy*

**A.K. Belyaev**  
*Institute of Problems of Mechanical Engineering (RAS), Russia*

**S.V. Bobylev**  
*Institute of Problems of Mechanical Engineering (RAS), Russia*

**A.I. Borovkov**  
*Peter the Great St.Petersburg Polytechnic University, Russia*

**G.-M. Chow**  
*National University of Singapore, Singapore*

**Yu. Estrin**  
*Monash University, Australia*

**A.B. Freidin**  
*Institute of Problems of Mechanical Engineering (RAS), Russia*

**Y. Gogotsi**  
*Drexel University, USA*

**I.G. Goryacheva**  
*Institute of Problems of Mechanics (RAS), Russia*

**D. Hui**  
*University of New Orleans, USA*

**G. Kiriakidis**  
*IESL/FORTH, Greece*

**D.M. Klimov**  
*Institute of Problems of Mechanics (RAS), Russia*

**G.E. Kodzhaspirov**  
*Peter the Great St.Petersburg Polytechnic University, Russia*

**S.A. Kukushkin**  
*Institute of Problems of Mechanical Engineering (RAS), Russia*

**T.G. Langdon**  
*University of Southampton, U.K.*

**V.P. Matveenko**  
*Institute of Continuous Media Mechanics (RAS), Russia*

**A.I. Melker**  
*Peter the Great St.Petersburg Polytechnic University, Russia*

**Yu.I. Meshcheryakov**  
*Institute of Problems of Mechanical Engineering (RAS), Russia*

**N.F. Morozov**  
*St.Petersburg State University, Russia*

**R.R. Mulyukov**  
*Institute for Metals Superplasticity Problems (RAS), Russia*

**Yu.V. Petrov**  
*St.Petersburg State University, Russia*

**N.M. Pugno**  
*Politecnico di Torino, Italy*

**B.B. Rath**  
*Naval Research Laboratory, USA*

**A.E. Romanov**  
*Ioffe Physico-Technical Institute (RAS), Russia*

**A.M. Sastry**  
*University of Michigan, Ann Arbor, USA*

**B.A. Schrefler**  
*University of Padua, Italy*

**N.V. Skiba**  
*Institute of Problems of Mechanics (RAS), Russia*

**A.G. Sheinerman**  
*Institute of Problems of Mechanics (RAS), Russia*

**R.Z. Valiev**  
*Ufa State Aviation Technical University, Russia*

**K. Zhou**  
*Nanyang Technological University, Singapore*

## "Materials Physics and Mechanics" Editorial Office:

**Phone:** +7(812)552 77 78, ext. 224 **E-mail:** mpmjournal@spbstu.ru **Web-site:** <http://www.mpm.spbstu.ru>

International scientific journal "Materials Physics and Mechanics" is published by Peter the Great St.Petersburg Polytechnic University in collaboration with Institute of Problems of Mechanical Engineering of the Russian Academy of Sciences in both hard copy and electronic versions.

The journal provides an international medium for the publication of reviews and original research papers written in English and focused on the following topics:

- Mechanics of composite and nanostructured materials.
- Physics of strength and plasticity of composite and nanostructured materials.
- Mechanics of deformation and fracture processes in conventional materials (solids).
- Physics of strength and plasticity of conventional materials (solids).
- Physics and mechanics of defects in composite, nanostructured, and conventional materials.
- Mechanics and physics of materials in coupled fields.

Owner organizations: Peter the Great St. Petersburg Polytechnic University; Institute of Problems of Mechanical Engineering RAS.

*Materials Physics and Mechanics is indexed in Chemical Abstracts, Cambridge Scientific Abstracts, Web of Science Emerging Sources Citation Index (ESCI) and Elsevier Bibliographic Databases (in particular, SCOPUS).*



# **МЕХАНИКА И ФИЗИКА МАТЕРИАЛОВ**

## **Materials Physics and Mechanics**

**Том 48, номер 2, 2022 год**

Учредители:

ФГАОУ ВО «Санкт-Петербургский политехнический университет Петра Великого»  
ФГБУН «Институт проблем машиноведения Российской Академии Наук»

## Редакционная коллегия журнала

### Главные редакторы:

д.ф.-м.н., чл.-корр. РАН **Д.А. Индейцев**  
Институт проблем машиноведения Российской Академии Наук  
(РАН)

д.т.н., академик РАН **А.И. Рудской**  
Санкт-Петербургский политехнический университет  
Петра Великого

**Основатель и почетный редактор:** д.ф.-м.н. **И.А. Овидько (1961-2017)**

Институт проблем машиноведения Российской Академии Наук (РАН)

### Ответственные редакторы

д.ф.-м.н. **А.Л. Колесникова**  
Институт проблем машиноведения Российской Академии Наук  
(РАН)

к.т.н. **А.С. Немов**  
Санкт-Петербургский политехнический университет Петра  
Великого

### Международная редакционная коллегия:

д.ф.-м.н., проф. **А.К. Беляев**  
Институт проблем машиноведения РАН, Россия  
д.ф.-м.н. **С.В. Бобылев**  
Институт проблем машиноведения РАН, Россия  
к.т.н., проф. **А.И. Боровков**  
Санкт-Петербургский политехнический у-т Петра Великого, Россия  
д.ф.-м.н., проф. **Р.З. Валнев**  
Уфимский государственный технический университет, Россия  
д.ф.-м.н., академик РАН **И.Г. Горячева**  
Институт проблем механики РАН, Россия  
д.ф.-м.н., академик РАН **Д.М. Климов**  
Институт проблем механики РАН, Россия  
д.т.н., проф. **Г.Е. Коджаспиров**  
Санкт-Петербургский политехнический у-т Петра Великого, Россия  
д.ф.-м.н., проф. **С.А. Кукушкин**  
Институт проблем машиноведения РАН, Россия  
д.ф.-м.н., академик РАН **В.П. Матвеев**  
Институт механики сплошных сред РАН, Россия  
д.ф.-м.н., проф. **А.И. Мелькер**  
Санкт-Петербургский политехнический у-т Петра Великого, Россия  
д.ф.-м.н., проф. **Ю.И. Мещеряков**  
Институт проблем машиноведения РАН, Россия  
д.ф.-м.н., академик РАН **Н.Ф. Морозов**  
Санкт-Петербургский государственный университет, Россия  
д.ф.-м.н., чл.-корр. РАН **Р.Р. Мулюков**  
Институт проблем сверхпластичности металлов РАН, Россия  
д.ф.-м.н., чл.-корр. РАН **Ю.В. Петров**  
Санкт-Петербургский государственный университет, Россия  
д.ф.-м.н., проф. **А.Е. Романов**  
Физико-технический институт им. А.Ф. Иоффе РАН, Россия  
д.ф.-м.н. **Н.В. Скиба**  
Институт проблем машиноведения РАН, Россия  
д.ф.-м.н., проф. **А.Б. Фрейдин**  
Институт проблем машиноведения РАН, Россия  
д.ф.-м.н. **А.Г. Шейнман**  
Институт проблем машиноведения РАН, Россия

Prof., Dr. **E.C. Aifantis**  
Aristotle University of Thessaloniki, Greece  
Dr. **K.E. Aifantis**  
University of Florida, USA  
Dr. **U. Balachandran**  
Argonne National Laboratory, USA  
Dr. **A. Bellosi**  
Research Institute for Ceramics Technology, Italy  
Prof., Dr. **G.-M. Chow**  
National University of Singapore, Singapore  
Prof., Dr. **Yu. Estrin**  
Monash University, Australia  
Prof., Dr. **Y. Gogotsi**  
Drexel University, USA  
Prof., Dr. **D. Hui**  
University of New Orleans, USA  
Prof., Dr. **G. Kiriakidis**  
IESL/FORTH, Greece  
Prof., Dr. **T.G. Langdon**  
University of Southampton, UK  
Prof., Dr. **N.M. Pugno**  
Politecnico di Torino, Italy  
Dr. **B.B. Rath**  
Naval Research Laboratory, USA  
Prof., Dr. **A.M. Sastry**  
University of Michigan, Ann Arbor, USA  
Prof., Dr. **B.A. Schrefler**  
University of Padua, Italy  
Prof. Dr. **K. Zhou**  
Nanyang Technological University, Singapore

Тел.: +7(812)552 77 78, доб. 224 E-mail: [mpmjournal@spbstu.ru](mailto:mpmjournal@spbstu.ru) Web-site: <http://www.mpm.spbstu.ru>

### Тематика журнала

Международный научный журнал "Materials Physics and Mechanics" издается Санкт-Петербургским политехническим университетом Петра Великого в сотрудничестве с Институтом проблем машиноведения Российской Академии Наук в печатном виде и электронной форме. Журнал публикует обзорные и оригинальные научные статьи на английском языке по следующим тематикам:

- Механика композиционных и наноструктурированных материалов.
- Физика прочности и пластичности композиционных и наноструктурированных материалов.
- Механика процессов деформации и разрушения в традиционных материалах (твердых телах).
- Физика прочности и пластичности традиционных материалов (твердых тел).
- Физика и механика дефектов в композиционных, наноструктурированных и традиционных материалах.
- Механика и физика материалов в связанных полях.

Редколлегия принимает статьи, которые нигде ранее не опубликованы и не направлены для опубликования в другие научные издания. Все представляемые в редакцию журнала "Механика и физика материалов" статьи рецензируются. Статьи могут отправляться авторам на доработку. Не принятые к опубликованию статьи авторам не возвращаются.

Журнал "Механика и физика материалов" ("Materials Physics and Mechanics") включен в систему цитирования Web of Science Emerging Sources Citation Index (ESCI), SCOPUS и ПИНЦ.

© 2022, Санкт-Петербургский политехнический университет Петра Великого

© 2022, Институт проблем машиноведения Российской Академии Наук

## Contents

<b>Effects of different factors on the heat conduction properties of carbon nanotubes .....</b>	<b>147-160</b>
Junjie Chen	
<b>Study of the influence of structural heritage and operating conditions on the durability of safety valve springs from steel 50KHFA.....</b>	<b>161-174</b>
M. Tupitsin, I. Trishkina, S. Sycheva, E. Storozheva, R. Novikov	
<b>Changes in rock permeability near-wellbore due to operational loads.....</b>	<b>175-183</b>
V.V. Poplygin, E.P. Riabokon, M.S. Turbakov, E.V. Kozhevnikov, M.A. Guzev, H. Jing	
<b>Analysis of CuCrZr/316L(N) bimetallic joint with and without nickel interlayer for plasma-facing components .....</b>	<b>184-198</b>
P. Piskarev, A. Gervash, S. Bobrov, V. Ruzanov, A. Ogurski, I. Mazul, R. Giniyatulin, B. Ermakov, O. Sevryukov	
<b>Experimental study of ductile and fragile pipe cracked in High-Density Polyethylene (HDPE).....</b>	<b>199-207</b>
Azzeddine Belaziz, Mohamed Mazari, Mohammed Bouamama, Samir Zahaf, Dahmane Mouloud	
<b>Unstable plastic flow in structural materials: time series for analysis of experimental data .....</b>	<b>208-216</b>
Vladislav K. Kazankov, Anna G. Shmeleva, Ekaterina V. Zaitseva	
<b>Experimental investigation of the mechanical behavior of honeycomb sandwich composite under three-point bending fatigue .....</b>	<b>217-231</b>
Hocine Mzad	
<b>Stability analysis of nanoscale surface patterns in ultrathin film coating.....</b>	<b>232-241</b>
G.M. Shuvalov, S.A. Kostyrko	
<b>Failure analysis of semi-elliptical crack behavior in the cement mantle of a total hip prosthesis .....</b>	<b>242-271</b>
Samir Zahaf, Mouloud Dahmane, Azzeddine Belaziz, Ismail Bouri, Nasreddine Afane	
<b>Glass formation and some physical properties in NaPO<sub>3</sub>– LiF and NaPO<sub>3</sub>– (0.4 AlF<sub>3</sub> – 0.6 CaF<sub>2</sub>) systems.....</b>	<b>272-281</b>
V.A. Klinkov, V.B. Archelkov	
<b>Mechanical properties of marble dust reinforced aluminum matrix structural composites fabricated by stir casting process .....</b>	<b>282-288</b>
Sandeep Kashyap, Hariom Tripathi, Naveen Kumar	
<b>Study of polylactide 3D-printed samples with double-layer weave .....</b>	<b>289-299</b>
A.V. Pogrebnoi	



## EFFECTS OF DIFFERENT FACTORS ON THE HEAT CONDUCTION PROPERTIES OF CARBON NANOTUBES

Junjie Chen✉

Department of Energy and Power Engineering, School of Mechanical and Power Engineering, Henan  
Polytechnic University, 2000 Century Avenue, Jiaozuo, Henan, 454000, P.R. China

✉ [cjjtpj@163.com](mailto:cjjtpj@163.com)

**Abstract.** The effects of structure, purity, and alignment on the thermal conductivity of carbon nanotube-based films and fibers were studied experimentally to understand the heat transport phenomena occurring in the nanostructured materials. The thermal conductivity of the macroscopic films and fibers was determined by employing the parallel thermal conductance technique. The effects of different factors on the heat conduction properties were investigated to evaluate the roles of bulk density and cross-sectional area in the thermal conductivity of the nanostructured materials. The results indicated that macroscopic films and fibers produced from carbon nanotubes can conduct heat very efficiently, depending on a variety of factors. The structure, purity, and alignment play fundamentally important roles in determining the heat conduction properties of carbon nanotube-based films and fibers. Macroscopic films and fibers produced from single-walled carbon nanotubes typically possess high heat conduction properties. The non-carbonaceous impurities negatively affect the heat conduction properties because of the low degree of bundle contact. Carbon nanotube-based films and fibers give rise to a power-law dependence of thermal conductivity with respect to temperature. The specific thermal conductivity decreases with increasing bulk density. Low bulk density can compensate for the adverse effect of poor alignment on specific thermal conductivity. A maximum specific thermal conductivity is achieved at room temperature, but Umklapp scattering occurs. The specific thermal conductivity of carbon nanotube-based fibers is significantly higher than that of carbon nanotube-based films because of the increased degree of bundle alignment.

**Keywords:** Carbon nanotubes; Material properties; Thermal conductivity; Thermal physics; Thermal properties; Phonon scattering

**Acknowledgements.** No external funding was received for this study.

**Citation:** Chen J. Effects of different factors on the heat conduction properties of carbon nanotubes. *Materials Physics and Mechanics*. 2022;48(2): 147-160. DOI: 10.18149/MPM.4822022\_1.

### 1. Introduction

Carbon nanotubes, also called buckytubes, are nanoscale hollow tubes composed of carbon atoms. The cylindrical carbon molecules feature high aspect ratios, typically above  $10^3$ , with lengths up to millimeters and diameters from about one nanometer up to tens of nanometers [1,2]. This unique one-dimensional structure and concomitant properties endow carbon nanotubes with special natures, rendering them with unlimited potential in

© Junjie Chen, 2022. Publisher: Peter the Great St. Petersburg Polytechnic University

This is an open access article under the CC BY-NC 4.0 license (<https://creativecommons.org/licenses/by-nc/4.0/>)

nanotechnology-associated applications [1,2]. Carbon nanotubes are members of the fullerene family. Although the first fullerene molecules were discovered in 1985 [3], it was not until Sumio Iijima reported his findings in 1991 about needlelike carbon tubes in *Nature* that carbon nanotubes came to public awareness [4]. Since then, carbon nanotubes with various structures have been discovered [5,6]. According to the number of graphic shells, they are mainly categorized as single-walled and multi-walled carbon nanotubes. A single-walled carbon nanotube can be described as a long tube formed by wrapping a single graphene sheet into a cylinder with a diameter of about one nanometer, the ends of which are capped by fullerene cages. Multi-walled carbon nanotubes are concentrically aligned single-walled carbon nanotube assemblies with different diameters. The distance between adjacent shells is about 0.34 nanometer. Single-walled carbon nanotubes differ from multi-walled carbon nanotubes not only in their dimensions, but also in their corresponding properties.

Novel mechanical, electrical, and chemical properties absent in other materials have been discovered in carbon nanotubes [7,8]. As for thermal properties, carbon nanotubes outperform diamond as the best thermal conductor [9,10]. Carbon nanotubes can exhibit unique ability to conduct heat [9,10], referred to as heat conduction properties. Specifically, carbon nanotubes are a highly effective thermal conductor in the longitudinal direction. However, a thermal barrier is formed in the radial direction. At room temperature, the thermal conductivity of an individual single-walled carbon nanotube in the radial direction is about 1.52 W/(m·K) at room temperature [11]. In contrast, carbon nanotubes show superior heat conduction properties along the longitude directions, with the highest known elastic modulus and tensile strength among known materials. At room temperature, the thermal conductivity in the longitudinal direction is about 3500 W/(m·K) [12]. When macroscopic, ordered assemblies of single-walled carbon nanotubes are formed, the thermal conductivity of carbon nanotube-based films and fibers could reach up to around 1500 W/(m·K) at room temperature [13]. The heat conduction properties of carbon nanotube networks vary significantly, with a minimum of thermal conductivity less than 0.1 W/(m·K) [14]. The heat conduction properties depend on a variety of factors, for example, misalignment and impurities. Single-walled carbon nanotube are stable up to around 1000 K in air and around 3000 K in vacuum [15]. While various techniques have been developed to produce carbon nanotubes in sizable quantity, high yield, and purity, the study of heat transport phenomena involved in carbon nanotubes is still an active area of interest [16] because of the potential for applications in thermal management.

The thermal conductivity of carbon nanotubes depends heavily upon the crystallographic defects of cylindrical sidewalls. Phonons can scatter because of the crystallographic defects of cylindrical sidewalls. This will lead to the increased relaxation rate, thereby decreasing the thermal conductivity of carbon nanotubes associated with the reduced mean free path of phonons [17,18]. In single-walled carbon nanotubes, the mean free path of phonons varies from 50 nm to 1500 nm [19,20]. The crystallographic defects of cylindrical sidewalls will lead to a significant reduction in mean free path [21], for example, 4 nm or less [22]. The thermal conductivity of carbon nanotubes depends heavily upon the structure of the carbon nanotubes. The thermal conductance of multi-walled carbon nanotubes is significantly higher than the sum of that of each individual shell because of the inter-wall interactions [23]. The thermal conductivity of a multi-walled carbon nanotube is lower than that of a single-walled carbon nanotube with an identical diameter configuration [24] because of an increase in cross-sectional area. Applications of carbon nanotubes are aimed to make use of their unique heat conduction properties to solve problems at the nanoscale.

Bulk carbon nanotubes can be used as composite fibers in polymers, but the bulk structure will reduce the ability to conduct heat, causing a decrease in thermal conductivity. The thermal conductivity of carbon nanotube-based fibers is comparable to that of common

metals [25]. Through chemical modification, however, the ability to conduct heat is comparable to or higher than that of highly conductive metals [26], for example, copper. The thermal conductivity varies significantly depending upon the density and cross-sectional area of the bulk material. The bulk carbon nanotube material contains pores [27,28]. Consequently, the thermal conductivity of the non-compact bulk material is much lower than that of the skeletal material, since the bulk volume is inclusive of the void fraction. The skeletal portion of the bulk material is often referred to as the "matrix" or "frame". However, there is considerable uncertainty in determination of the density of the bulk material. Consequently, the effects of structure, purity, and alignment on the thermal conductivity of carbon nanotube-based films and fibers are still poorly understood. Little research has been conducted to determine which parameters are important for high thermal conductivity.

This study relates to the heat conduction properties of carbon nanotube-based films and fibers. Carbon nanotube-based films and fibers were produced, and the parallel thermal conductance technique was employed to determine the thermal conductivity of carbon nanotubes. The effects of structure, purity, and alignment on the thermal conductivity of carbon nanotube-based films and fibers were investigated to understand the characteristics of thermal transport in the nanostructured materials. The effects of different factors on the heat conduction properties were investigated to evaluate the roles of bulk density and cross-sectional area in the thermal conductivity of the nanostructured materials. The objective is to gain insight into the fundamental characteristics of thermal transport in carbon nanotubes. Particular emphasis is placed on the dependence of thermal conductivity on carbon nanotube structure, purity, and alignment, with an attempt to improve the heat conduction properties for carbon nanotube-based films and fibers.

## 2. Experimental methods

**Preparation of carbon nanotube-based films and fibers.** Carbon nanotube-based films were produced by spinning continuously onto a single rotational winder of a spinning machine. The preparation process of carbon nanotube-based films is depicted schematically in Figure 1. A dense film was laid down with aligned carbon nanotube bundles. The dense film was sprayed with acetone to further condense the carbon nanotube networks. By preparing a dense film in such a manner, the carbon nanotubes were highly aligned [29], although the surface tension effect is significant in the extrusion process [30]. A laser was used to cut the carbon nanotube-based film into small pieces for the measurement of thermal conductivity. Carbon nanotube-based fibers were produced by stretching the dense film with two rotational winders of the spinning machine. The two rotational winders operate with only a small difference in rotation rate.

**Thermal conductivity measurement methods.** To determine the thermal conductivity, the parallel thermal conductance technique was employed [31,32], since the diameter of the needle-like samples was very small. Fourier's Law was used to compute the thermal conductivity. This steady-state method has been carried out to measure the thermal conductivity of boron nitride nanotube sheets [33], and carbon nanotube sheets [34] and yarns [35,36]. The configuration of the parallel thermal conductance technique is depicted schematically in Figure 2. A preliminary measurement of thermal conductance was performed with respect to the sample holder itself so as to determine the background or base-line heat conduction and losses associated with the sample stage. The sample was attached and the thermal conductance of the system was measured. The parallel thermal conductance can be obtained by subtraction. In this method, all conductance factors arising from the thermal contacts, sample, and thermal radiation from the sample accounted for. The radiative heat losses were caused primarily by the thermal radiation from the hot surface of the heater. However, such heat losses were already included in the baseline. Therefore, a correction

factor of 0.5 was introduced into the method [31,32] to account for the radiative heat losses.

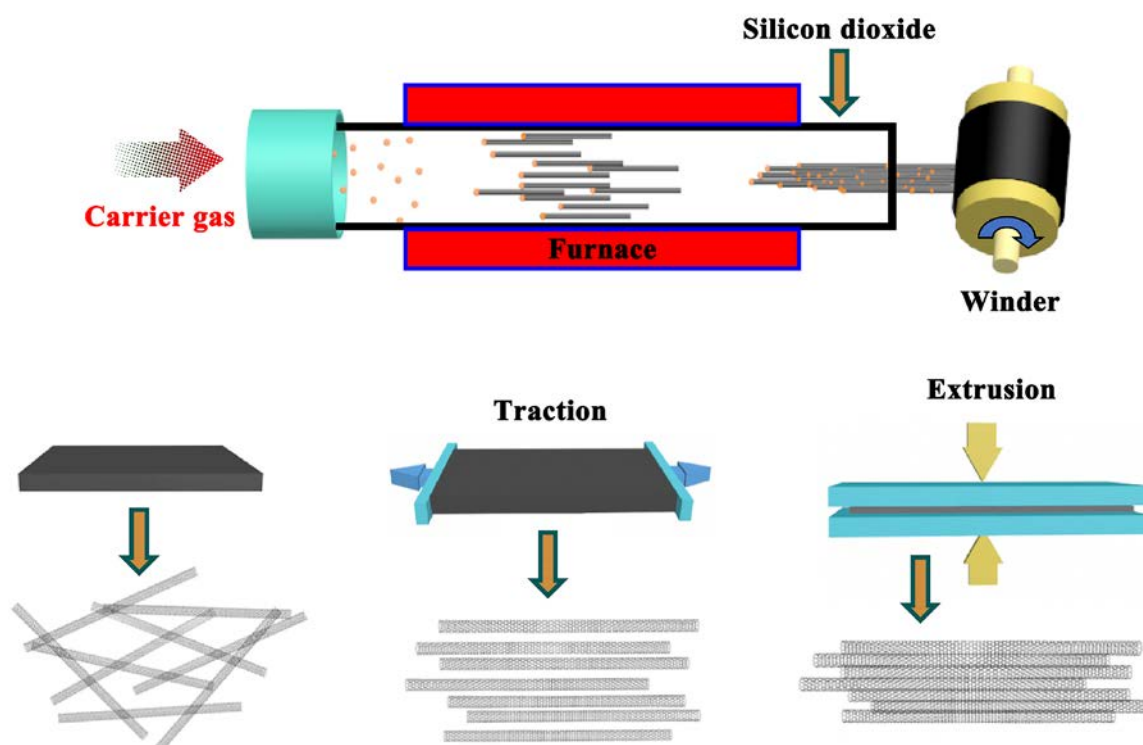


**Fig. 1.** Schematic illustration of the preparation process of carbon nanotube-based films. A dense film was laid down with aligned carbon nanotube bundles

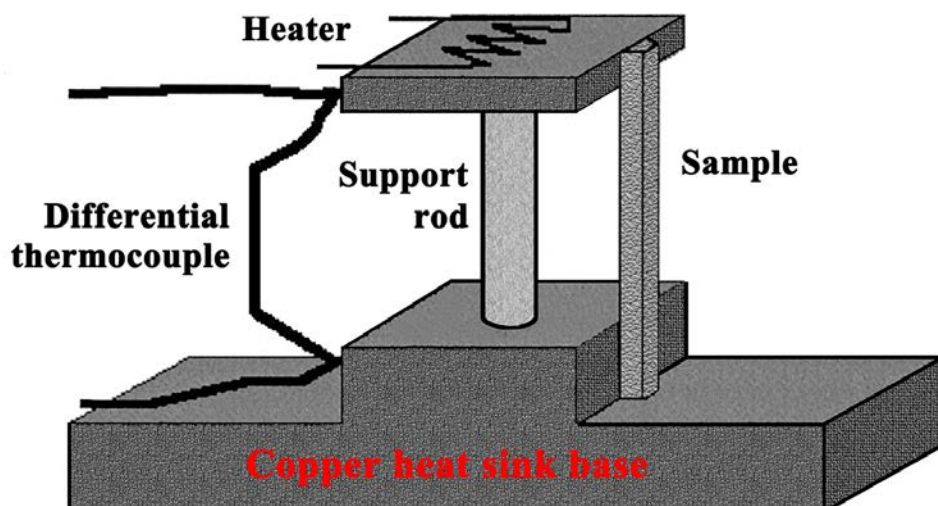


**Fig. 2.** Schematic illustration of the configuration of the parallel thermal conductance technique. The baseline was measured with the sample holder itself and then the sample was attached to perform the measurement of parallel thermal conductance in which the baseline was subtracted

**Linear mass density measurement methods.** The linear mass density of the carbon nanotube-based films was measured by using a gravimetric method [37]. In contrast, the linear mass density of the carbon nanotube-based fibers was measured by using a vibroscope method [37,38]. The carbon nanotube-based fibers were tensioned between two hard points of a mechanical vibroscope. Mechanical vibration was induced, and the fundamental frequency

was measured. The specific thermal conductivity was defined as the thermal conductivity normalized by bulk density. The bulk density was determined in terms of the cross-sectional area and the linear mass density.

### 3. Results and discussion

**Material characterization.** The macroscopic fibers produced from carbon nanotubes are characterized by scanning electron microscopy. The surface morphology is analyzed with scanning electron microscope SU3800, Hitachi High-Tech Corporation. Scanning electron microscopy images are presented in Fig. 3 for the carbon nanotube fibers prepared by the method described above. The carbon nanotubes are highly aligned. However, the carbon nanotube-based fiber material contains a relatively small amount of short, deformed carbon nanotubes. The carbon nanotubes are of the order of several hundred microns.

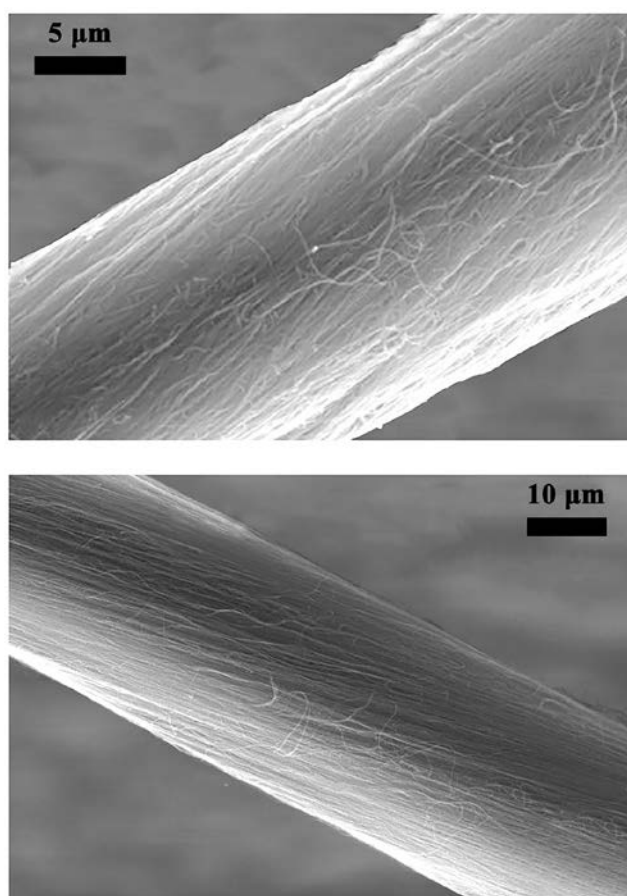


**Fig. 3.** Scanning electron microscopy images of the carbon nanotube fibers prepared by the method described in detail above

Four samples are prepared with different structure, purity, and alignment in order to investigate the effects of various factors on the thermal conductivity. Three structural parameters are selected in terms of alignment, purity, and the number of walls. The structural parameter space for the selection of the carbon nanotube-based materials is illustrated in Fig. 4 in the style of the design of measurement experiments. For type A, the carbon nanotube-based films or fibers are composed mostly of multi-walled carbon nanotubes. In addition, there is a small amount of short deformed carbon nanotubes. For type B, a mixture of carbon nanotubes is produced. More specifically, the carbon nanotube-based films or fibers are composed of single-walled and multi-walled carbon nanotubes. In addition, there is a

small amount of amorphous carbon. For type C, the carbon nanotube-based films or fibers are composed mostly of single-walled carbon nanotubes. In addition, there is a small amount of non-carbonaceous impurities. For type D, the carbon nanotube-based films or fibers are composed of single-walled carbon nanotubes with very high purity. The understanding of which parameters are important for high thermal conductivity is made possible through the comparison of heat conduction properties between the carbon nanotube-based materials.

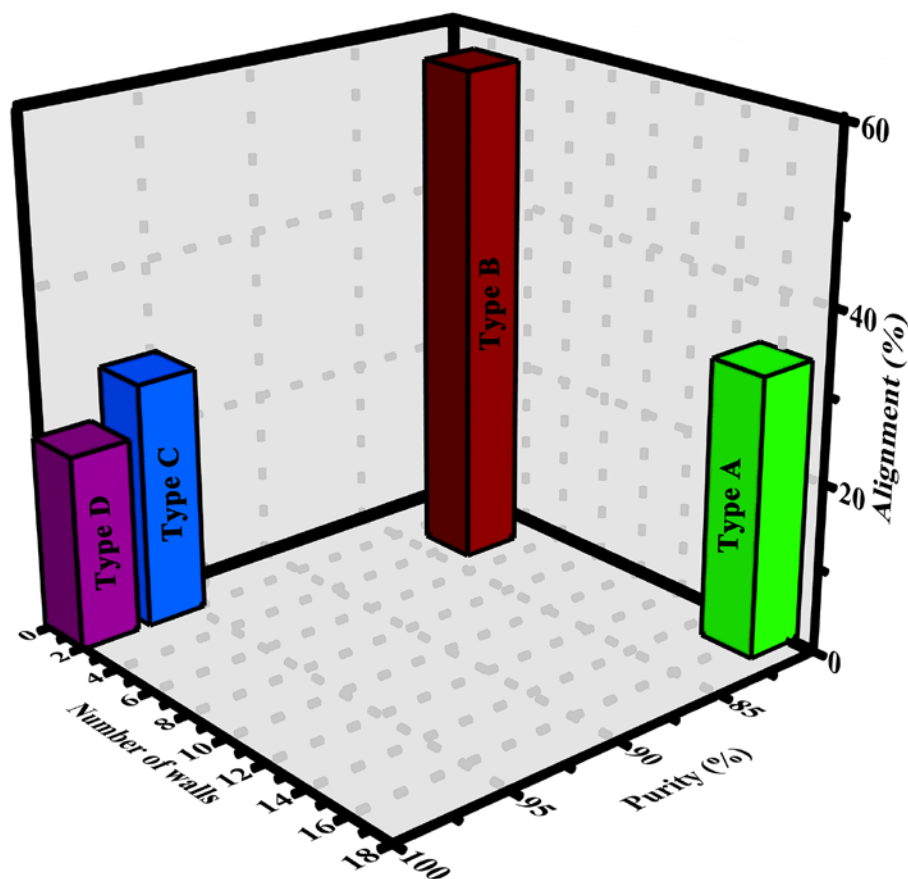


**Fig. 4.** Structural parameter space for the selection of the carbon nanotube-based materials in the style of the design of measurement experiments

**Thermal conductivity of carbon nanotube-based films.** The effects of structure, purity, and alignment on the specific thermal conductivity of carbon nanotube-based films are illustrated in Fig. 5 at different temperatures. The specific thermal conductivity of the A-type film is lower than that of the other-type films. Multi-walled carbon nanotubes generally have low thermal conductivity. The A-type film is composed mostly of multi-walled carbon nanotubes. Therefore, the specific thermal conductivity is lower than that of the film composed of single-walled carbon nanotubes. The specific thermal conductivity of the C-type film is higher than that of the A-type film, since the structure is different from each other. The structural variation will lead to the difference in thermal conductivity. However, the specific thermal conductivity of the C-type film is much lower than that of the D-type film. This is because the presence of non-carbonaceous impurities reduces the degree of bundle contact between single-walled carbon nanotubes, which increases the thermal resistance at the interface junctions and degrades the thermal performance of the C-type film.

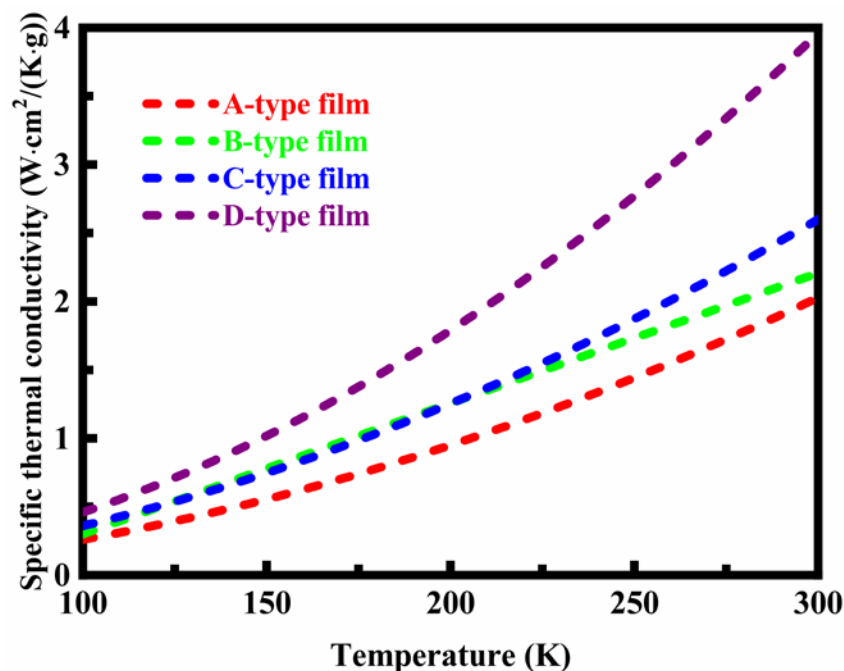


**Fig. 5.** Specific thermal conductivity of the carbon nanotube-based films at different temperatures. There exist significant differences in terms of structure, purity, and alignment between the films

While the specific thermal conductivity increases with temperature, the effect of temperature is different between the B-type film and the other-type films. The specific thermal conductivity of the B-type film has a linear relationship with temperature. For the other-type films, there is an exponential increase in the specific thermal conductivity of the nanostructured material. The effect of temperature on thermal conductivity is illustrated in Figure 6 for the carbon nanotube-based films. The thermal conductivity of all the carbon nanotube-based films presents a power-law dependence with respect to temperature, except that of the B-type film. The power law index is about 1.87, 1.80, and 1.96 for the thermal conductivity of the A, C, and D type films, respectively. In contrast, the temperature index is 0.99 for the thermal conductivity of the B-type film. The temperature index is small, which reduces the dimensionality of the propagation of phonons [39,40] because of an increase in the degree of bundle alignment and contact.

The effect of bulk density on the specific thermal conductivity at room temperature is illustrated in Figure 7 for the carbon nanotube-based films. At room temperature, the highest specific thermal conductivity is achieved for the D-type film. In addition, the power law index is largest, although the degree of bundle alignment is very low, which reduces the mechanical stiffness of the carbon nanotube-based film. At room temperature, the lowest specific thermal conductivity is obtained for the A-type film. A tentative explanation could be made for the distinctive phenomenon. The specific thermal conductivity of the nanostructured material decreases with increasing bulk density. The low bulk density of the D-type film compensates for the adverse effect of poor alignment on the specific thermal conductivity of the nanostructured material. Therefore, the bulk density may be controlled to produce carbon nanotube-based films with high thermal conductivity.

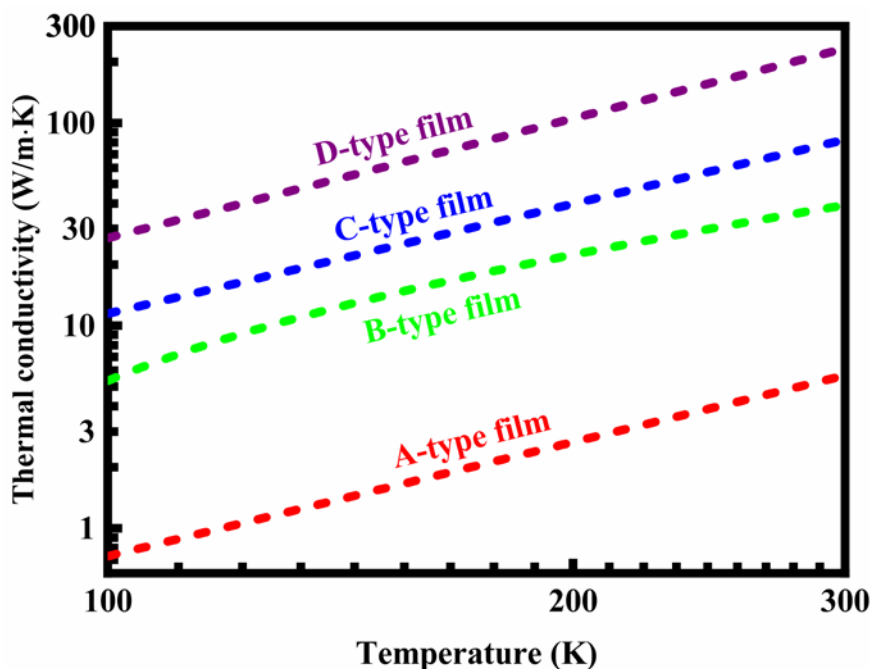


**Fig. 6.** Thermal conductivity of the carbon nanotube-based films at different temperatures. The thermal conductivity is indicated with points plotted on a logarithmic coordinate system

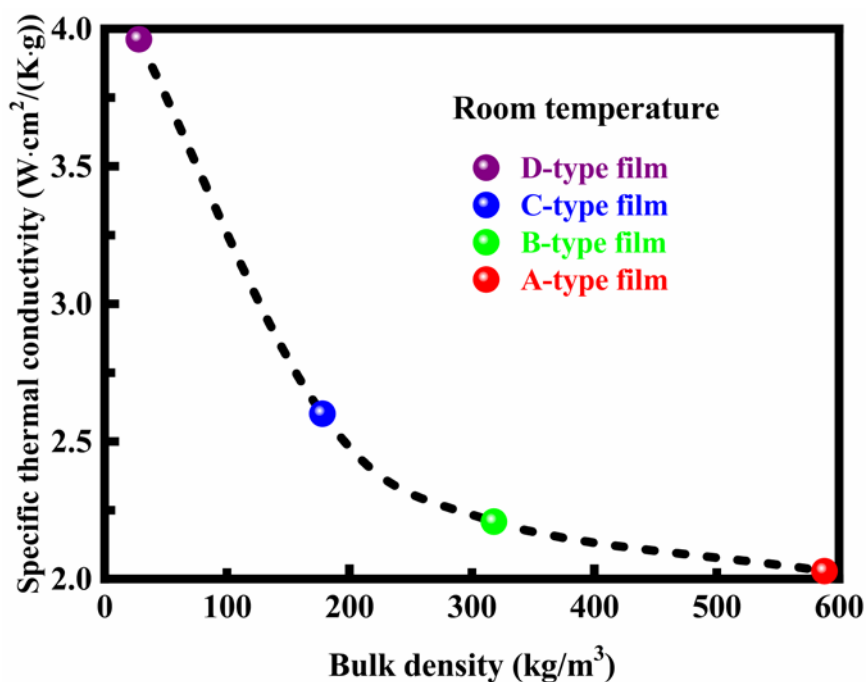


**Fig. 7.** Effect of bulk density on the specific thermal conductivity of the carbon nanotube-based films at room temperature

**Thermal conductivity of carbon nanotube-based fibers.** The effects of structure, purity, and alignment on the specific thermal conductivity of carbon nanotube-based fibers are illustrated in Fig. 8 at different temperatures. The specific thermal conductivity of the carbon nanotube-based fibers is around  $10 \text{ W}\cdot\text{cm}^2/(\text{K}\cdot\text{g})$  at room temperature, which is comparable to or higher than that of pristine and chemically modified carbon nanotube-based fibers [25,26]. A maximum specific thermal conductivity is obtained at room temperature, which appears as a peak in the dependence of temperature in Figure 8, as determined previously [26,40]. The maximum specific thermal conductivity represented by the peaks indicates the occurrence of

Umklapp scattering. The Umklapp scattering is the dominant process for thermal resistivity, which limits the specific thermal conductivity. High thermal conductivity of carbon fibers is often associated with a high modulus of elasticity [41,42]. Therefore, the carbon nanotube-based fibers have sufficient strength to be used as a reinforcement for composite materials. Clearly, the specific thermal conductivity of the carbon nanotube-based fibers is significantly higher than that of the carbon nanotube-based films. This is caused by the improved degree of bundle alignment for the carbon nanotube-based fibers. A high degree of bundle alignment will lead to an increase in thermal conductivity because of the increased interfacial area between the carbon nanotubes.

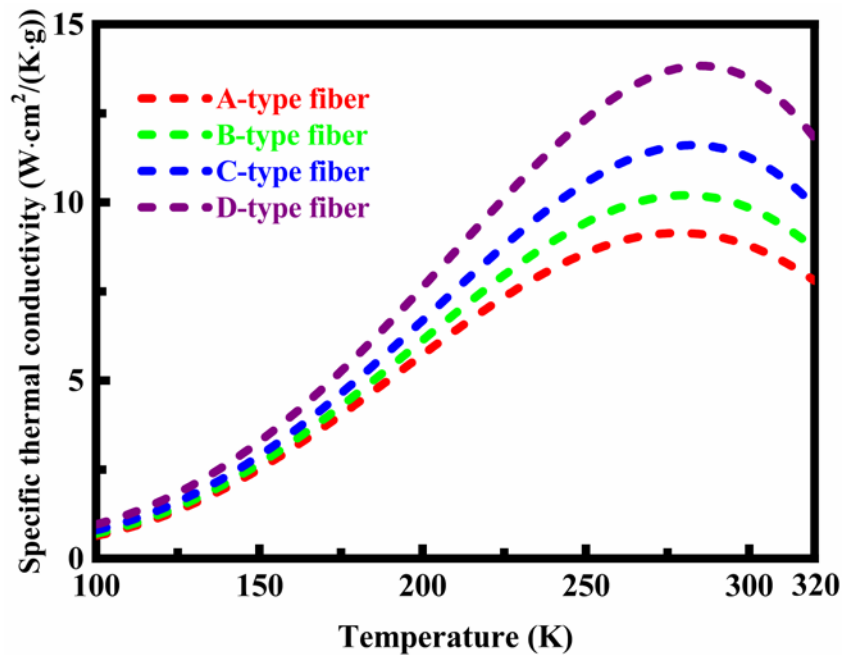


**Fig. 8.** Specific thermal conductivity of the carbon nanotube-based fibers at different temperatures. There exist significant differences in terms of structure, purity, and alignment between the carbon nanotube-based fibers

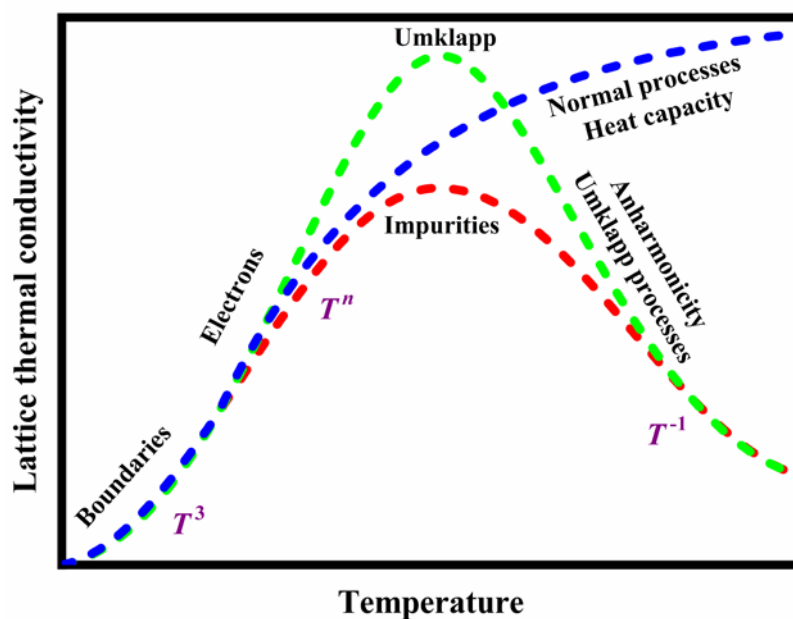


**Fig. 9.** Schematic illustration of the various mechanisms responsible for the temperature dependence of lattice thermal conductivity

It is important to understand the physics behind the observed behavior of the specific thermal conductivity, for example, the maximum specific thermal conductivity caused by the occurrence of Umklapp scattering. The various mechanisms responsible for the temperature dependence of lattice thermal conductivity are illustrated in Fig. 9. Assuming that the Boltzmann transport equation is valid and the relaxation time and phonon group velocity are independent of frequency, the lattice thermal conductivity  $k$  can be written as  $k = \frac{1}{3} C v_g \Lambda = \frac{1}{3} C v_g^2 \tau$ , where  $C$  is the heat capacity,  $v_g$  is the phonon group velocity,  $\Lambda$  is the phonon mean free path, and  $\tau$  is the relaxation time. Note that this assumption breaks down when the scale of the physical system is comparable to or smaller than the wavelength of the phonons responsible for thermal transport. Although the above model is fairly crude, the expression for the lattice thermal conductivity is actually a surprisingly good approximation. Very often, the above equation is used to estimate the phonon mean free path on the basis of experimental results for the other parameters in the equation. If the lattice vibrations are entirely the normal modes, the temperature dependence of lattice thermal conductivity is determined by the specific heat is therefore proportional to the cube of temperature [43,44], as illustrated in Fig. 9. A heat flow will transport without decaying or scattering, which implies that the lattice thermal conductivity be infinite as harmonic oscillations. In fact, anharmonicity persists along with the normal processes. The major mechanism of anharmonicity is called the Umklapp processes, as indicated in Fig. 9. While the normal processes conserve the total phonon momentum, the Umklapp processes change the phonon momentum, causing the scattering of phonons [43,44]. The Umklapp processes increase with increasing temperature. From the above equation, since the velocity of sound is independent of temperature, the lattice thermal conductivity depends upon the phonon mean free path and the heat capacity. At low temperatures, the Umklapp processes are reduced, and the phonon mean free path may reach several micrometers, being comparable with the scale of the physical system. The phonon mean free path thus becomes constant at the grain boundaries. Therefore, the lattice thermal conductivity depends upon the heat capacity that varies as the cube of temperature, as illustrated in Fig. 9. At high temperatures, the heat capacity is almost constant, and the phonon mean free path is inversely proportional to temperature. In this case, the Umklapp processes predominate the lattice thermal conductivity so that the lattice thermal conductivity is inversely proportional to temperature, as illustrated in Fig. 9. This dependency originates from the temperature dependency of the probability for the Umklapp processes to occur.

The effect of cross-sectional area on the specific thermal conductivity at room temperature is illustrated in Figure 10 for the carbon nanotube-based films and fibers. Some previous data are also included for comparison. These previous data are available in the literature [26,35,36,45-48]. The carbon nanotube-based fibers have higher specific thermal conductivity than the carbon nanotube-based films. Under the same cross-sectional area conditions, the specific thermal conductivity of the carbon nanotube-based films and fibers is higher than that previously reported in the literature. The carbon nanotubes are of the order of several hundred microns, which is significantly greater than the phonon mean free path. As the length of carbon nanotubes increases, the effect of temperature on thermal conductivity becomes more pronounced [12,48]. The length of the carbon nanotubes contained in the carbon nanotube-based films and fibers is much greater than that of the carbon nanotubes used in the literature. Consequently, the carbon nanotube-based films and fibers are very efficient at conducting heat and typically have higher specific thermal conductivity in comparison to the previous data.

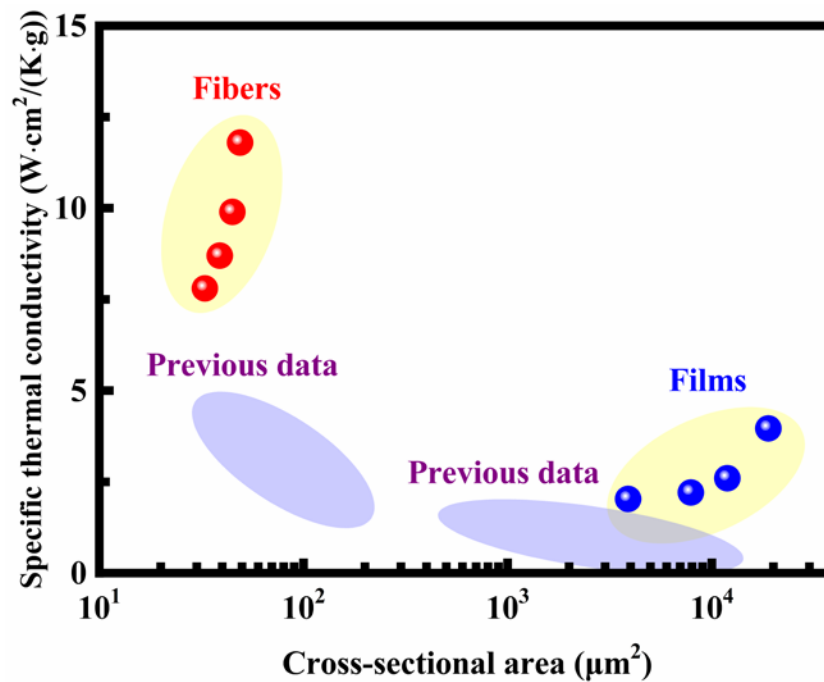


**Fig. 10.** Effect of cross-sectional area on the specific thermal conductivity of the carbon nanotube-based films and fibers at room temperature. Some previous data are also included for comparison

#### 4. Conclusions

Carbon nanotube-based films and fibers were produced, and the parallel thermal conductance technique was employed to determine the thermal conductivity of carbon nanotubes. The effects of structure, purity, and alignment on the heat conduction properties of carbon nanotube-based films and fibers were investigated to understand the characteristics of thermal transport in the nanostructured materials. The major conclusions are summarized as follows:

- Macroscopic films and fibers produced from multi-walled carbon nanotubes generally have low thermal conductivity.
- The presence of non-carbonaceous impurities reduces the degree of bundle contact between carbon nanotubes, thereby increasing the thermal resistance at the interface junctions and degrading the thermal performance.
- The thermal conductivity presents a power-law dependence with respect to temperature or has a linear relationship with temperature.
- The specific thermal conductivity decreases with increasing bulk density. Low bulk density can compensate for the adverse effect of poor alignment on specific thermal conductivity.
- A maximum specific thermal conductivity is obtained at room temperature because of the occurrence of Umklapp scattering.
- The specific thermal conductivity of carbon nanotube-based fibers is significantly higher than that of carbon nanotube-based films. The improved thermal properties are caused by the increased degree of bundle alignment.
- The prepared carbon nanotube films and fibers can conduct heat very efficiently because of the increased length of the carbon nanotubes.

#### References

- [1] Popov VN. Carbon nanotubes: properties and application. *Materials Science and Engineering: R: Reports*. 2004;43(3): 61-102.

- [2] Dresselhaus MS, Dresselhaus G, Saito R. Physics of carbon nanotubes. *Carbon*. 1995;33(7): 883-891.
- [3] Kroto HW, Heath JR, O'Brien SC, Curl RF, Smalley RE. C<sub>60</sub>: Buckminsterfullerene. *Nature*. 1985;318(14): 162-163.
- [4] Iijima S. Helical microtubules of graphitic carbon. *Nature*. 1991;354(6348): 56-58.
- [5] Iijima S, Ichihashi T. Single-shell carbon nanotubes of 1-nm diameter. *Nature*. 1993;363(6430): 603-605.
- [6] Bethune DS, Kiang CH, Vries MSD, Gorman G, Savoy R, Vazquez J, Beyers R. Cobalt-catalysed growth of carbon nanotubes with single-atomic-layer walls. *Nature*. 1993;363(6430): 605-607.
- [7] Baughman RH, Zakhidov AA, Heer WAD. Carbon nanotubes-the route toward applications. *Science*. 2002;297(5582): 787-792.
- [8] Thostenson ET, Ren Z, Chou TW. Advances in the science and technology of carbon nanotubes and their composites: A review. *Composites Science and Technology*. 2001;61(13): 1899-1912.
- [9] Ebbesen TW. Carbon nanotubes. *Physics Today*. 1996;49(6): 26-32.
- [10] Ando Y, Zhao X, Sugai T, Kumar M. Growing carbon nanotubes. *Materials Today*. 2004;7(10): 22-29.
- [11] Ibrahim KS. Carbon nanotubes-properties and applications: A review. *Carbon Letters*. 2013;14(3): 131-144.
- [12] Pop E, Mann D, Wang Q, Goodson K, Dai H. Thermal conductance of an individual single-wall carbon nanotube above room temperature. *Nano Letters*. 2006;6(1): 96-100.
- [13] Koziol KK, Janas D, Brown E, Hao L. Thermal properties of continuously spun carbon nanotube fibres. *Physica E: Low-dimensional Systems and Nanostructures*. 2017;88: 104-108.
- [14] Kumanek B, Janas D. Thermal conductivity of carbon nanotube networks: A review. *Journal of Materials Science*. 2019;54(10): 7397-7427.
- [15] Thostenson ET, Li C, Chou TW. Nanocomposites in context. *Composites Science and Technology*. 2005;65(3-4): 491-516.
- [16] Rathinavel S, Priyadarshini K, Panda D. A review on carbon nanotube: An overview of synthesis, properties, functionalization, characterization, and the application. *Materials Science and Engineering: B*. 2021;268: 115095.
- [17] Mingo N, Stewart DA, Broido DA, Srivastava D. Phonon transmission through defects in carbon nanotubes from first principles. *Physical Review B*. 2008;77(3): 033418.
- [18] Sevik C, Sevinçli H, Cuniberti G, Çağın T. Phonon engineering in carbon nanotubes by controlling defect concentration. *Nano Letters*. 2011;11(11): 4971-4977.
- [19] Kim P, Shi L, Majumdar A, McEuen PL. Thermal transport measurements of individual multiwalled nanotubes. *Physical Review Letters*. 2001;87(21): 215502.
- [20] Chang C, Okawa D, Garcia H, Majumdar A, Zettl A. Breakdown of Fourier's Law in nanotube thermal conductors. *Physical Review Letters*. 2008;101(7): 075903.
- [21] Sääskilähti K, Oksanen J, Volz S, Tulkki J. Frequency-dependent phonon mean free path in carbon nanotubes from nonequilibrium molecular dynamics. *Physical Review B*. 2015;91(11): 115426.
- [22] Gspann TS, Juckes SM, Niven JF, Johnson MB, Elliott JA, White MA, Windle AH. High thermal conductivities of carbon nanotube films and micro-fibres and their dependence on morphology. *Carbon*. 2017;114: 160-168.
- [23] Zhang X, Zhou WX, Chen XK, Liu YY, Chen KQ. Significant decrease in thermal conductivity of multi-walled carbon nanotube induced by inter-wall van der Waals interactions. *Physics Letters A*. 2016;380(21): 1861-1864.
- [24] Goh B, Kim KJ, Park CL, Kim ES, Kim SH, Choi J. In-plane thermal conductivity of multi-walled carbon nanotube yarns under mechanical loading. *Carbon*. 2021;184: 452-462.

- [25] Mayhew E, Prakash V. Thermal conductivity of high performance carbon nanotube yarn-like fibers. *Journal of Applied Physics*. 2014;115(17): 174306.
- [26] Behabtu N, Young CC, Tsentelovich DE, Kleinerman O, Wang X, Ma AWK, Bengio EA, Waarbeek RFT, Jong JJD, Hoogerwerf RE, Fairchild SB, Ferguson JB, Maruyama B, Kono J, Talmon Y, Cohen Y, Otto MJ, Pasquali M. Strong, light, multifunctional fibers of carbon nanotubes with ultrahigh conductivity. *Science*. 2013;339(6116): 182-186.
- [27] Misak HE, Mall S. Investigation into microstructure of carbon nanotube multi-yarn. *Carbon*. 2014;72: 321-327.
- [28] Wu AS, Chou TW. Carbon nanotube fibers for advanced composites. *Materials Today*. 2012;15(7-8): 302-310.
- [29] Zhan H, Chen YW, Shi QQ, Zhang Y, Mo RW, Wang JN. Highly aligned and densified carbon nanotube films with superior thermal conductivity and mechanical strength. *Carbon*. 2022;186: 205-214.
- [30] Li S, Zhang X, Zhao J, Meng F, Xu G, Yong Z, Jia J, Zhang Z, Li Q. Enhancement of carbon nanotube fibres using different solvents and polymers. *Composites Science and Technology*. 2012;72(12): 1402-1407.
- [31] Zawilski BM, Littleton RT, Tritt TM. Description of the parallel thermal conductance technique for the measurement of the thermal conductivity of small diameter samples. *Review of Scientific Instruments*. 2001;72(3): 1770-1774.
- [32] Zawilski BM, Tritt TM. Dynamic measurement access, a new technique for fast thermal conductivity measurement. *Review of Scientific Instruments*. 2001;72(10): 3937-3939.
- [33] Jakubinek M, Niven JF, Johnson MB, Ashrafi B, Kim KS, Simard B, White MA. Thermal conductivity of bulk boron nitride nanotube sheets and their epoxy-impregnated composites. *Physica Status Solidi (A)*. 2016;213(8): 2237-2242.
- [34] Pöhls JH, Johnson MB, White MA, Malik R, Ruff B, Jayasinghe C, Schulz MJ, Shanov V. Physical properties of carbon nanotube sheets drawn from nanotube arrays. *Carbon*. 2012;50(11): 4175-4183.
- [35] Niven JF, Johnson MB, Juckes SM, White MA, Alvarez NT, Shanov V. Influence of annealing on thermal and electrical properties of carbon nanotube yarns. *Carbon*. 2016;99: 485-490.
- [36] Jakubinek MB, Johnson MB, White MA, Jayasinghe C, Li G, Cho W, Schulz MJ, Shanov V. Thermal and electrical conductivity of array-spun multi-walled carbon nanotube yarns. *Carbon*. 2012;50(1): 244-248.
- [37] Lord PR. *Handbook of Yarn Production: Technology, Science and Economics*. Cambridge: Woodhead Publishing Limited; 2003.
- [38] Gandhi KL. *Woven Textiles: Principles, Developments and Applications*. Cambridge: Woodhead Publishing Limited; 2012.
- [39] Gonnet P, Liang Z, Choi ES, Kadambala RS, Zhang C, Brooks JS, Wang B, Kramer L. Thermal conductivity of magnetically aligned carbon nanotube buckypapers and nanocomposites. *Current Applied Physics*. 2006;6(1): 119-122.
- [40] Hone J, Llaguno MC, Nemes NM, Johnson AT. Electrical and thermal transport properties of magnetically aligned single wall carbon nanotube films. *Applied Physics Letters*. 2000;77(5): 666-668.
- [41] Emmerich FG. Young's modulus, thermal conductivity, electrical resistivity and coefficient of thermal expansion of mesophase pitch-based carbon fibers. *Carbon*. 2014;79: 274-293.
- [42] Jang D, Lee S. Correlating thermal conductivity of carbon fibers with mechanical and structural properties. *Journal of Industrial and Engineering Chemistry*. 2020;89: 115-118.
- [43] Ashcroft NW, Mermin ND. *Solid State Physics*. New York: Holt, Rinehart and Winston Publisher; 1976.

- [44] Ziman JM. *Electrons and Phonons: The theory of transport phenomena in solids*. Oxford: Clarendon Press; 1960.
- [45] Ericson LM, Fan H, Peng H, Davis VA, Zhou W, Sulpizio J, Wang Y, Booker R, Vavro J, Guthy C, Parra-Vasquez ANG, Kim MJ, Ramesh S, Saini RK, Kittrell C, Lavin G, Schmidt H, Adams WW, Billups WE, Pasquali M, Hwang WF, Hauge RH, Fischer JE, Smalley RE. Macroscopic, neat, single-walled carbon nanotube fibers. *Science*. 2004;305(5689): 1447-1450.
- [46] Liu P, Fan Z, Mikhalchan A, Tran TQ, Jewell D, Duong HM, Marconnet AM. Continuous carbon nanotube-based fibers and films for applications requiring enhanced heat dissipation. *ACS Applied Materials & Interfaces*. 2016;8(27): 17461-17471.
- [47] Qiu J, Terrones J, Vilatela JJ, Vickers ME, Elliott JA, Windle AH. Liquid infiltration into carbon nanotube fibers: Effect on structure and electrical properties. *ACS Nano*. 2013;7(10): 8412-8422.
- [48] Aliev AE, Guthy C, Zhang M, Fang S, Zakhidov AA, Fischer JE, Baughman RH. Thermal transport in MWCNT sheets and yarns. *Carbon*. 2007;45(15): 2880-2888.

## THE AUTHOR

**Chen J.**

e-mail: [cjtpj@163.com](mailto:cjtpj@163.com)

ORCID: 0000-0002-4222-1798

# STUDY OF THE INFLUENCE OF STRUCTURAL HERITAGE AND OPERATING CONDITIONS ON THE DURABILITY OF SAFETY VALVE SPRINGS FROM STEEL 50KHFA

M. Tupitsin<sup>✉</sup>, I. Trishkina, S. Sycheva, E. Storozheva, R. Novikov

Joint stock company "Research, Design and Technological Institute of Oil Refining and Petrochemical  
Equipment", Volgograd, Russia

✉ matupicin@vnikti.rosneft.ru

**Abstract.** The reasons for the premature failure of a spring made of steel 50KhFA, which operated in the safety valve of the column's head part of the flare facility, were investigated using analytical chemistry, energy dispersive analysis, macro- and microstructural analysis, electron microscopy, macro- and electron fractography, phase chemical and X-ray structural analysis, hardness and microhardness tests and reductive heat treatment according to the regime recommended for safety valve springs in the standard process documentation and reference literature. The influence of non-metallic inclusions, such as carbides, their chemical composition, shape, and distribution on the operational properties of springs from steel 50KhFA has been investigated. Information on the characteristic external signs, typical micro damages, and the mechanism of destruction during low-temperature hydrogen sulfide corrosion of steel 50KhFA with the most dangerous accompanying process – hydrogenation was obtained. The analysis of the research results showed that the premature failure of the spring is due to both technological heredity and contact with the working environment not envisaged by the project.

**Keywords:** steel 50KhFA, spring, safety valve, failure, fracture, low-temperature hydrogen sulfide corrosion, cracking, failure mechanism

**Acknowledgements.** No external funding was received for this study.

**Citation:** Tupitsin M, Trishkina I, Sycheva S, Storozheva E, Novikov R. Study of the influence of structural heritage and operating conditions on the durability of safety valve springs from steel 50KHFA. *Materials Physics and Mechanics*. 2022;48(2): 161-174. DOI: 10.18149/MPM.4822022\_2.

## 1. Introduction

The continuity of equipment operation in the oil refining industry depends on the reliability of safety valves, of which springs are the most important part.

The durability and reliability of springs are laid down at the design stage and must be ensured by the manufacturing technology, quality control, and operating conditions [1,2]. During operation the condition of the safety valve and springs is diagnosed in the manner and volumes provided for by the current regulatory documents, for example, IPKM-05 "Procedure for the operation, revision, and repair of safety valve springs and membrane safety devices of oil refining and petrochemical enterprises of the Ministry of Industry and Energy of Russia".

© M. Tupitsin, I. Trishkina, S. Sycheva, E. Storozheva, R. Novikov, 2022.

Publisher: Peter the Great St. Petersburg Polytechnic University

This is an open access article under the CC BY-NC 4.0 license (<https://creativecommons.org/licenses/by-nc/4.0/>)

However, there have been cases of premature failure of safety valve springs during the operations of refineries. The issues of investigating the damageability of safety valve springs during the operation of oil refineries are covered in the literature to a lesser extent in comparison with the issues of damageability of equipment and pipelines. Moreover, literary sources mainly provide descriptions of the results of fractographic studies of springs [3-10]. Meanwhile, there is mostly no information on the use of other no less informative methods of laboratory research of broken springs. Therefore, the development of a laboratory testing methodology for safety valve springs for establishing the causes of premature failure, the results of the study of the physical and mechanical properties of the metal obtained during its implementation, and the development of recommendations for safe operation in the oil refining industry are of certain scientific interest and have practical significance.

## 2. Subjects and methods of research

The investigated safety valve springs were made of steel 50HFA, intended for helical cylindrical springs for valve compression. The material of the safety valve springs must have high operational properties, such as elastic limit, endurance limit, and relaxation resistance. The subject of the study is the springs of the SPPK 4r 200-16 (17S7nzh) safety valve installed at the outlet of the column into the flare system of one of the primary oil refining units, which collapsed after 6 years of operation and 6 operating cycles with a design life of at least 30 years and an average operating time failure 360 cycles. The operating temperature of the valve was 51°C, and the pipeline operating environment was C1-C2 hydrocarbon gas with a mass fraction of hydrogen sulfide 0.02%.

To determine the causes of springs failure classical research methods and modern equipment were used, as well as modeling of the initial structural and mechanical condition of the spring material before operation by means of reductive heat treatment. During the study, the following were carried out: visual and measurement control, chemical analysis of the steel composition, energy-dispersive X-ray spectroscopy (EDS) of metal in local areas and corrosion deposits on the surface of the spring, macro- and microstructural analysis, macro- and electron fractography, phase chemical and X-ray structural analysis, hardness and microhardness tests and reductive heat treatment according to the regime recommended for safety valve springs in the standard process documentation and reference literature [11,12]: quenching at 860±10°C and medium tempering at 420±10°C.

Metallographic studies were carried out using a complex of software and hardware for microstructure analysis of the surface of solids based on an optical microscope, as well as a scanning electron microscope for identification of structural components and study of their morphology, mutual orientation, determination of the presence of modified structures in surface layers and defects. The chemical composition of steel and carbide analysis of the metal were determined by analytical methods using a spectrophotometer, an automatic titrator, and an express analyzer for carbon. X-ray structural analysis was carried out on an X-ray apparatus. Microhardness was measured using a microhardness tester with a load of 100 g, and the hardness was measured using the Rockwell method. In addition to the study of the physical and mechanical properties of the metal, a study of corrosion deposits from the surface of the spring was carried out.

## 3. Results and discussion

The investigated fragment of the spring is shown in Fig. 1a. Visual inspection showed that the number of spring turns, the outer diameter, the diameter of the rod, and other dimensions corresponded to the original parameters of the spring according to the manufacturer's specification. The protective coating on the surface of the spring was damaged in the form of swelling, flaking, side wear, and corrosion (Fig. 1b, 5).



**Fig. 1.** Fragment of spring after failure: a – fracture surface; b – defects in the protective coating

The chemical composition of the spring's metal, given in Table 1, corresponds to steel 50HFA according to GOST 14959-2016 [13].

Table 1. Results of the analysis of the chemical composition of the spring's metal

Material	Mass fraction of elements, %						
	C	Si	Mn	Cr	V	S	P
Spring	0.517	0.32	0.55	0.97	0.103	0.0053	0.019
Steel 50KhFA GOST 14959-2016	0.46- 0.54	0.17- 0.37	0.50- 0.80	0.80- 1.10	0.10- 0.20	≤0.025	≤0.025

The hardness of the test samples (Table 2) is lower than the recommended by the regulatory documentation and reference literature. After the heat treatment carried out by the quenching and medium tempering regime, according to the recommendations of ST TsKBA 030-2006 [11] and reference literature [12], the hardness became within permissible limits, which indicates a non-optimal heat treatment regime used during the production of the spring. Low hardness may indicate a decrease in elastic limit, relaxation resistance, and endurance limit. However, during the audit shortly before the failure during the test for threefold compression of the spring, no deformations were found, which indicates the preservation of its elastic properties. The endurance limits for bending  $\sigma_{-1}$  and torsion  $\tau_{-1}$  can be roughly estimated by the characteristics of static strength, for example, Brinell hardness, using relations (1) and (2) given in the reference literature [14,15]:

$$\sigma_{-1} = 0.18 \text{ HB}, \tag{1}$$

$$\tau_{-1} = (0.50 \dots 0.65) \sigma_{-1} . \tag{2}$$

An approximate estimation according to formulas (1) and (2) shows that the endurance limits of the metal after operation were approximately 1.2 times lower than the endurance limits after reductive heat treatment, while the calculated value of  $\tau_{-1}$  after the operation (410-500 MPa) turned out to be lower than the value given in the reference literature [15] for the recommended heat treatment regime (519 MPa).

Despite the spring's low hardness, it is still exceeded the limiting values of 20-22 HRC, at which steel does not expose to hydrogen sulfide stress cracking [16], which is important due to the presence of hydrogen sulfide in the working environment.

The microstructure of metal with the different fineness of special carbides (Table 3), which manifests itself in areas with different etching on the microsection (Fig. 2 a, b) and visible on SEM images at  $\times 25000$  (Fig. 3 a), as well as the orientation along martensite

indicated quenching and medium tempering. The presence of bright polyhedral grains with carbide precipitates and low hardness (Table 2) indicated an insufficient heating temperature or a low cooling rate during quenching with the formation of regions of non-martensitic structures. After reductive heat treatment, the structure became more homogeneous (Fig. 2 c, d).

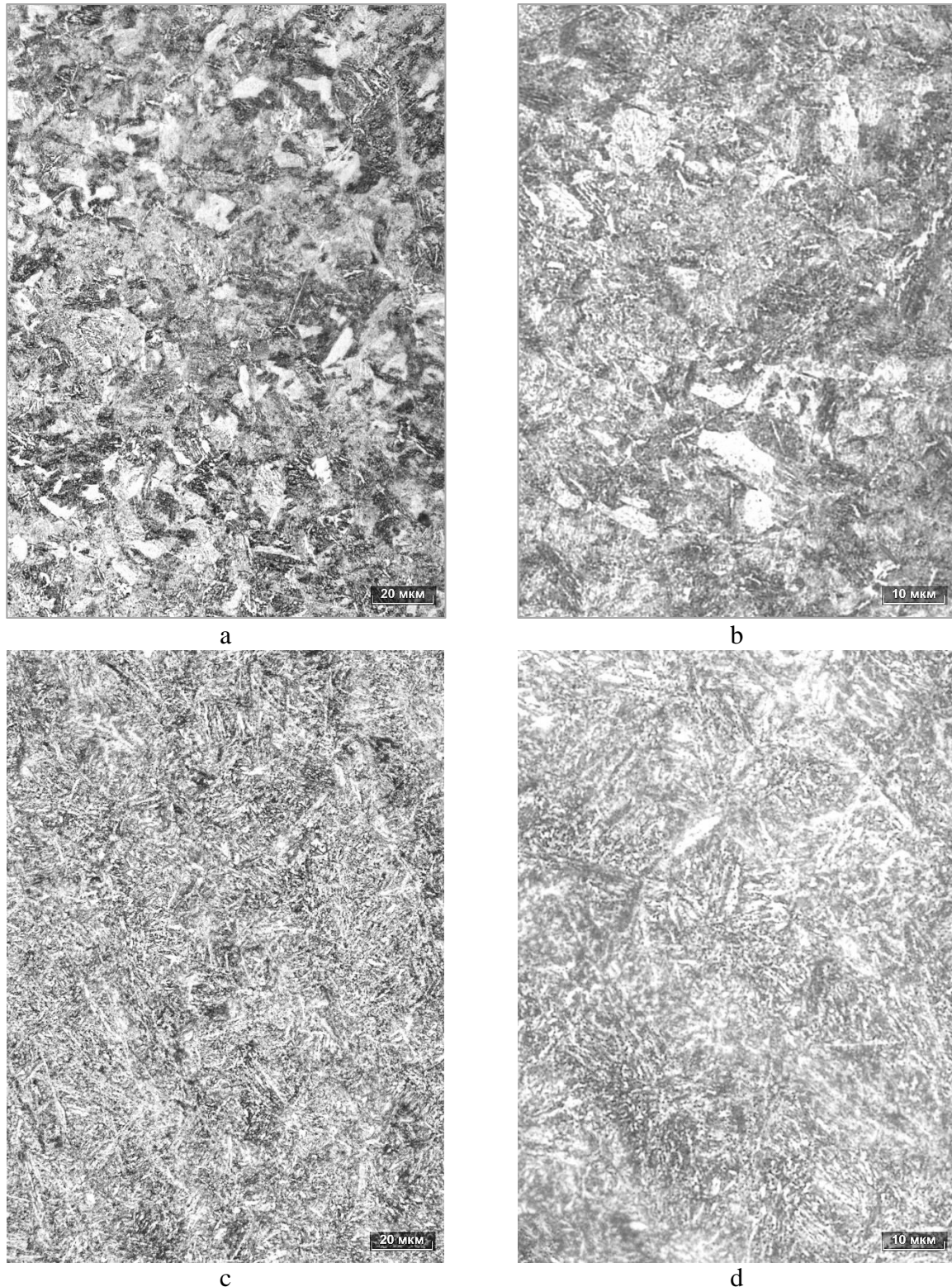
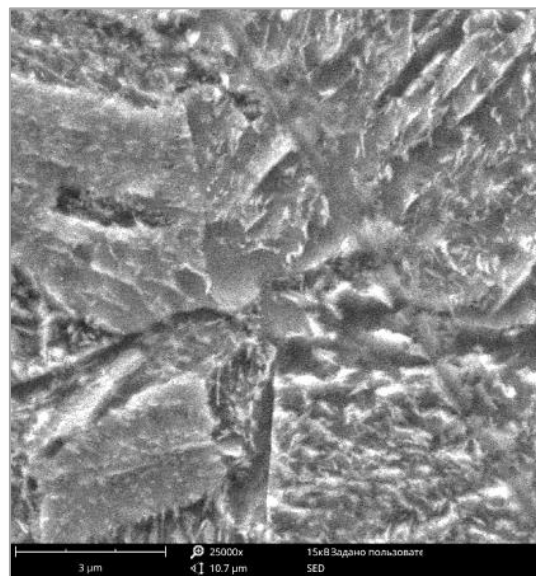


**Fig. 2.** The microstructure of the spring's metal after the operation (a, b) and after heat treatment (c, d): a, c –  $\times 500$ ; b, d –  $\times 1000$

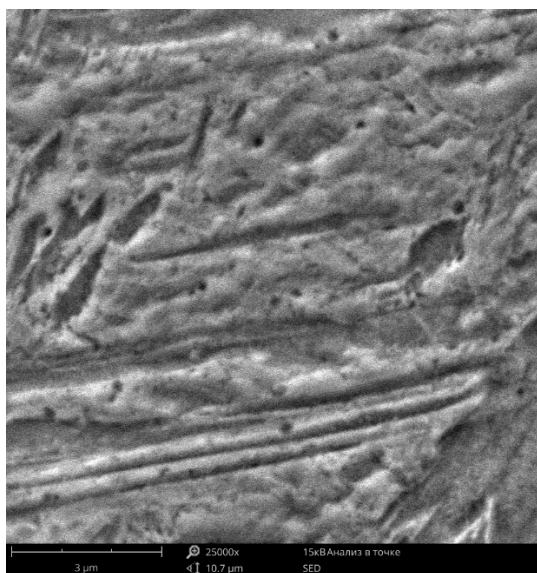
Table 2. Results of the springs hardness testing

Material	Hardness HRC	
	After operation	After reductive heat treatment
Investigated spring, 50KhFA	38-45 (40.8) *	46-51 (48)
Steel 50KhFA GOST 13764-86 [17]	44.0-51.5	
Steel 50KhFA ST TsKBA 030-2006 [11]		
Steel 50KhFA [14]	42-49	
Steel 50KhFA [12]	44-49	

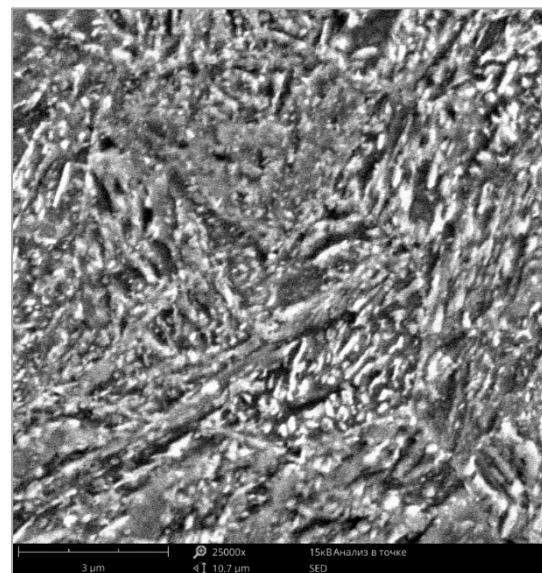
Note: \* - mean values in brackets



a



b



c

**Fig. 3.** Morphology of the carbide phase in the spring's metal, x25000, SEM image: a – after operation; b – after operation + quenching; c – after operation + quenching + tempering

A comparison of the morphology of the carbide phase before (Fig. 3 a) and after (Fig. 3 c) reductive heat treatment showed that the initial material had a lower distribution density of carbides with a predominance of lamellar precipitates. After the reduction heat treatment, the structure was dominated by round-shaped carbides with a size of 0.1  $\mu\text{m}$ . It should be noted that the presence of carbides in the form of plates is not a defect and it's typical for spring steel after quenching and medium tempering, in contrast to coagulated carbides after high tempering, which reduces the elastic properties of springs.

The results of the phase X-ray diffraction analysis of the spring's metal (Table 3) indicated that the main type of carbide was a carbide  $\text{Me}_7\text{C}_3$ , in particular  $(\text{Cr}, \text{Fe})_7\text{C}_3$ , typical for steel 50KhFA in the condition after medium tempering and operation at 51°C [18]. Vanadium carbides were absent in the carbide deposit because their precipitation usually occurs at a higher tempering temperature (above 500°C) [19]. Therefore, the embrittlement of the spring's metal due to the possible precipitation of fine vanadium carbides during tempering did not occur.

Table 3. Results of carbide analysis

Material	Mass fraction of elements, %			The relative content of the Cr in carbides, %	Carbide type	
	Carbide precipitate		Solid solution			
	Fe	Cr	$\Sigma$			
50KhFA	2.198	0.071	2.269	0.899	7	$\text{Me}_7\text{C}_3$

Phase chemical analysis showed that only 7% of chromium turns into carbides, and the rest remained in a solid solution, which, along with carbide and dislocation hardening mechanisms, provides a solid solution mechanism for steel hardening. However, the total chromium content in steel of 0.98% cannot provide corrosion resistance in the working environment of the safety valve in question, which entails the need to protect against the working environment falling on its surface via a high-quality seal of the detachable valve connections and a protective coating that turned out to be damaged.

In the study of the macro- and microstructure of the samples, a decarbonized layer with a depth of 0.056-0.1 mm was revealed, which was formed, probably, during technological operations of spring production. The minimum values of the metal microhardness, measured by the cross-section of the rod, corresponded to the zone of the decarbonized layer (Table 4). Since most of the elastic elements work in torsional conditions, when the maximum stresses fall on the surface layer, the presence of a soft decarbonized layer contributed to the damage to the surface under the protective coating and the formation of crack origin.

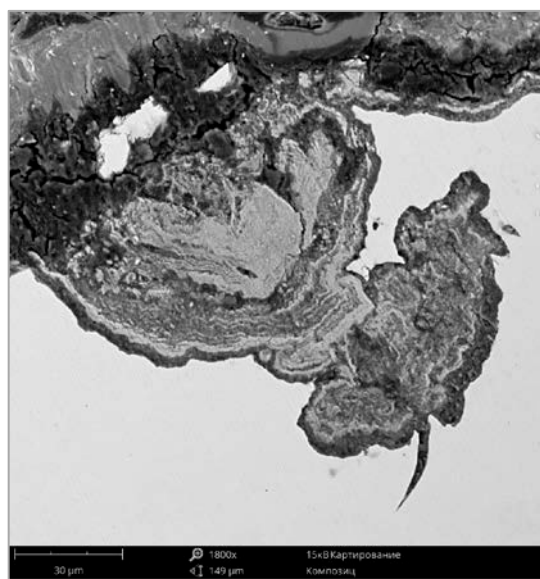
Table 4. Microhardness of metal measured on microsection

Microhardness $\text{HV}_{0.1}$		
Microsection edges	The central part of the microsection	Decarburized layer
30.5-42.6 (38.2) *	30.0-37.8 (35.3)	18.2-21.4 (20.2)

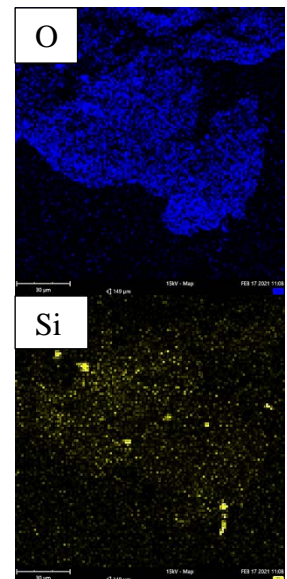
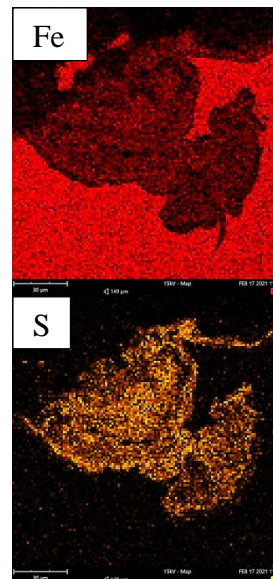
Note: \* - mean values in brackets

The study of the microstructure in the places of damage to the protective coating, revealed during visual and measurement control, showed the presence of multiple surface microdefects of the metal in the form of ulcerative damage and penetrating of corrosion products into the deep layers of metal (up to 1/3 of the rod section), as well as the destruction of metal near non-metallic inclusions and cracking mainly along the boundaries of primary austenite grains (Fig. 4). Analysis of the distribution of chemical elements in cavities and

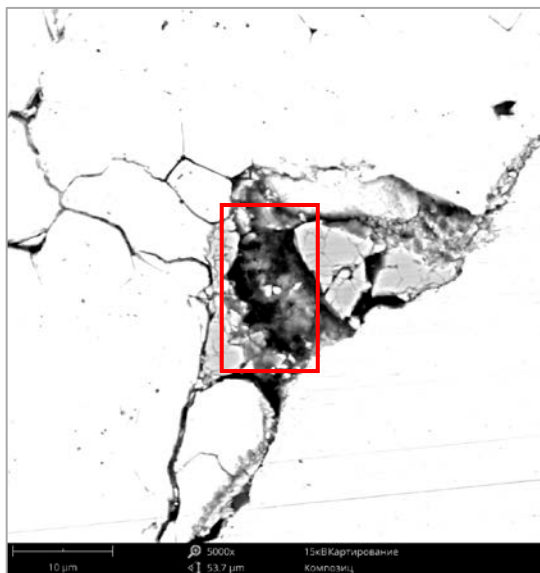
cracks (Fig. 4 a-d) indicated a significant content of sulfur and oxygen, which indicated the occurrence of low-temperature hydrogen sulfide corrosion. The propagation of damage along with the structural elements and the morphology of cracks on microsections after etching with a 4% of HNO<sub>3</sub> solution are shown in Fig. 5, from which it can be seen that cracks propagate not only along the boundaries of primary austenite grains, where the largest precipitates of carbides are located but also along the interphase boundaries of oriented plates of carbides, pores in the matrix of the solid solution are also visible (Fig. 5 a, b). The smallest micropores up to 0.5 μm in martensite, which were not eliminated by quenching during the reduction heat treatment (Fig. 3 b), were also found on microsections cut away from the surface of the spring, which may be due to the presence of hydrogen in the steel formed during low-temperature hydrogen sulfide corrosion.



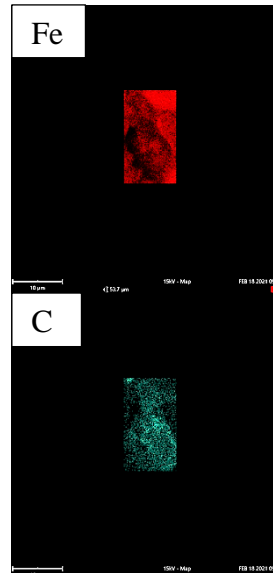
a



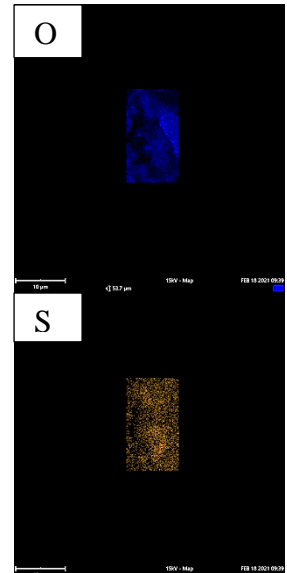
b



c



d



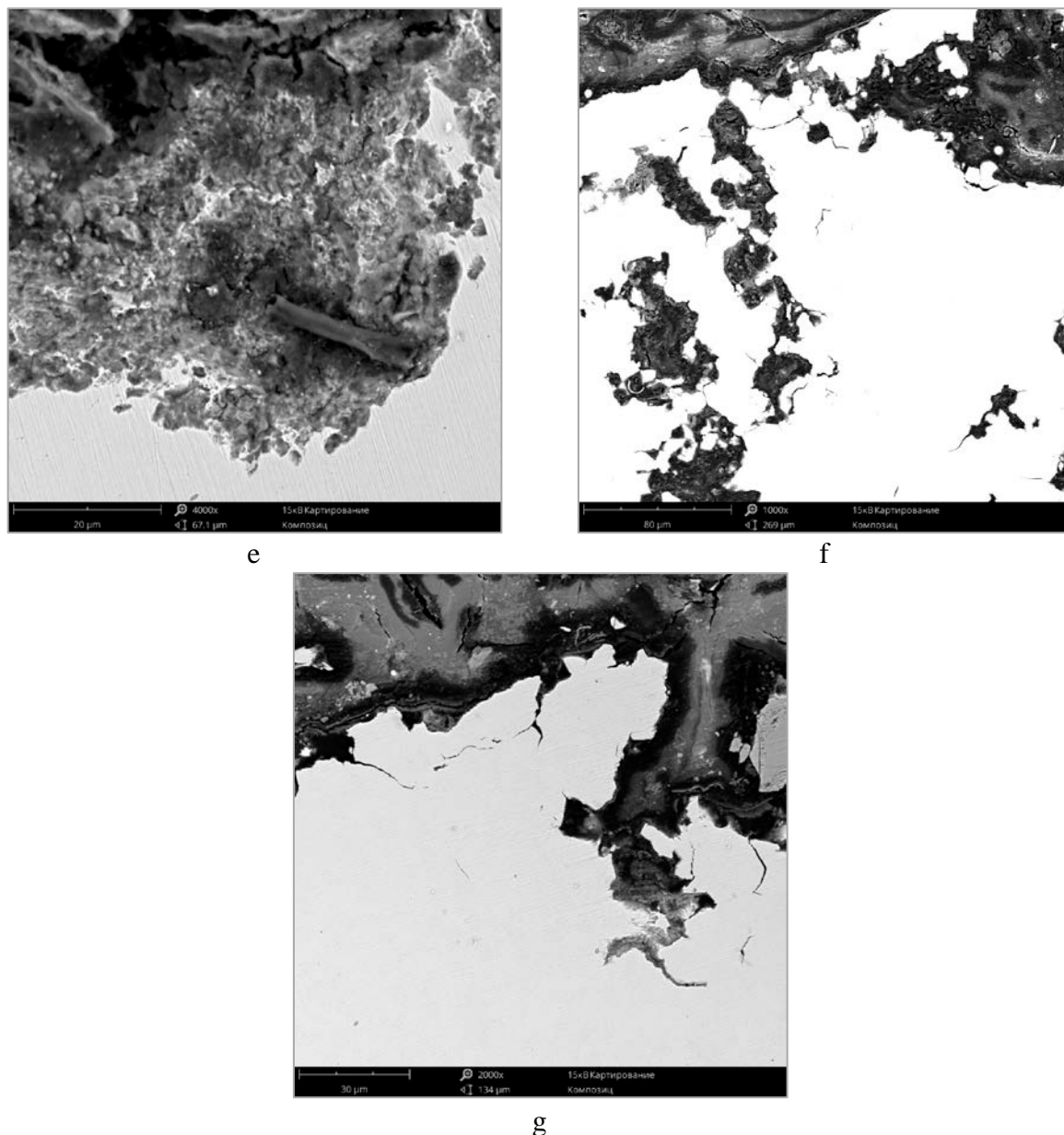


**Fig. 4.** Defects in the spring's metal at the crack origin, not etched:  
 a, c – analyzed surface; b, d – element distribution map; e – destruction of metal at sulfide;  
 f, g – cracks and penetration of corrosion products into the deep layers of the metal

Figure 5 b shows that when the cracks form an almost closed loop, the metal is deformed under hydrogen pressure with the subsequent formation of cavities that reduce the resistance to operational loads and lead to failure.

Fractographic research has established that the fracture is matte, dark gray in color. The fracture surface was oriented at an angle of  $45^\circ$  to the axis of the rod and perpendicular to the direction of action of the maximum tensile stresses during torsion, in the central part there was a concavity characteristic of quasi-brittle materials [20]. The macrogeometry of the fracture indicates the formation of fracture during the workloads. According to the macrostructure, the spring's fracture was characterized by the following successive zones: first – zone of crack origin with smooth relief, second – zone of failure crack propagation with ratchet marks, and third – fast fracture zone with less rough areas (Fig. 6). At the crack origin, determined by the convergence of ratchet marks, and located on the outer surface of

the spring between the small and large turn radius, there was a loss of protective coating, as well as ulcerative damage on the surface (Fig. 6).

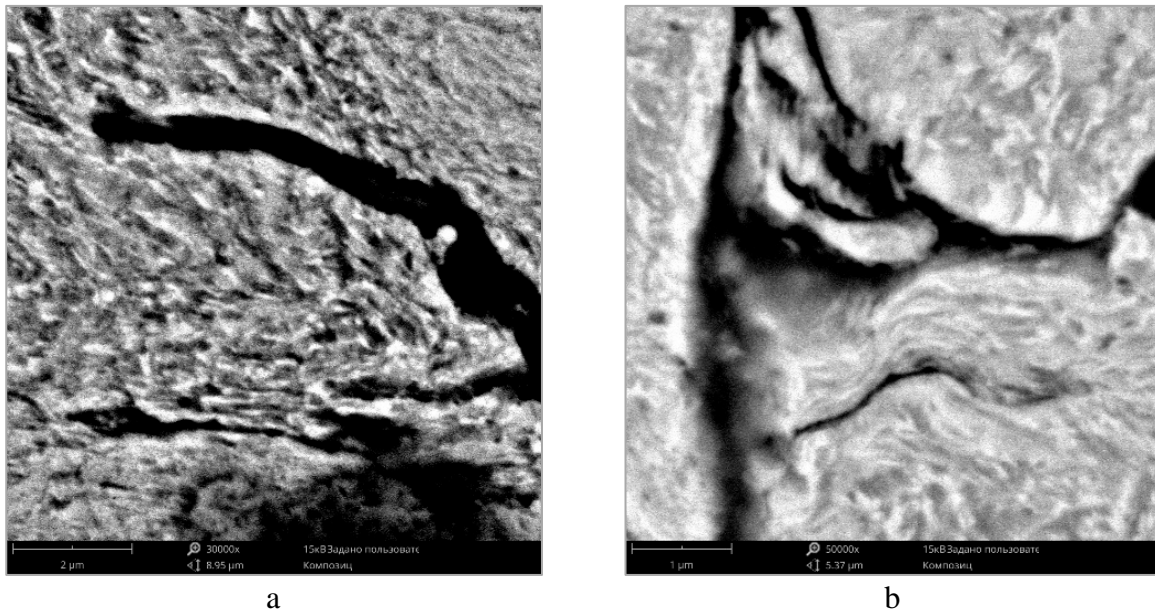


**Fig. 5.** View of cracks after etching: a –  $\times 30000$ , b –  $\times 50000$

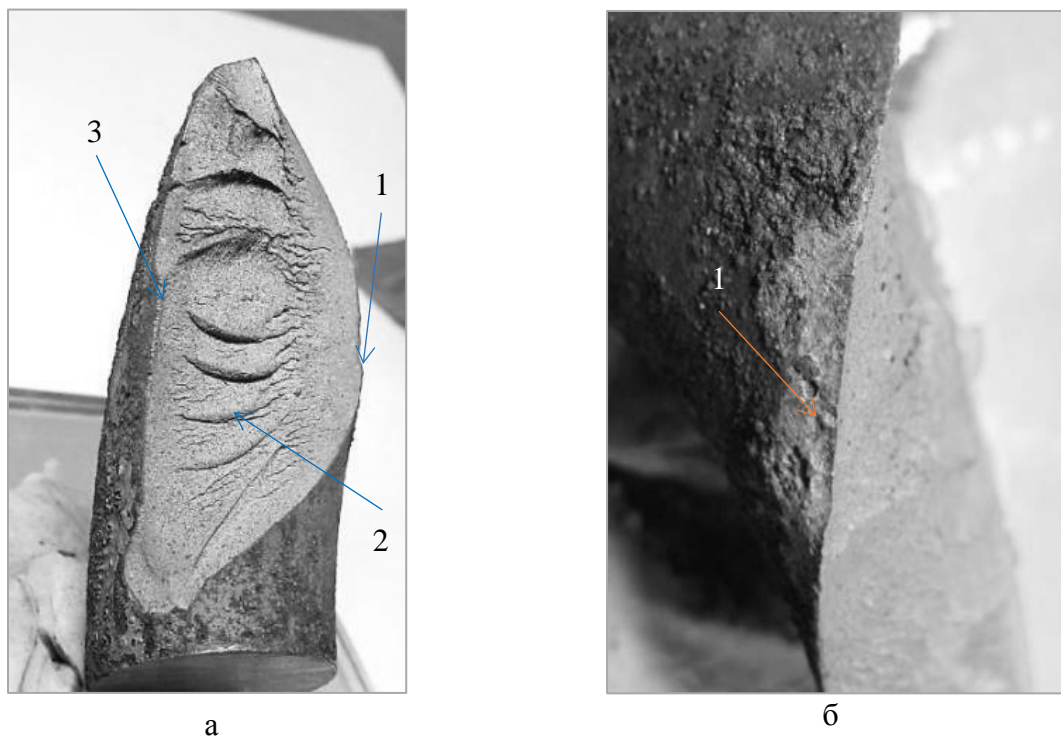
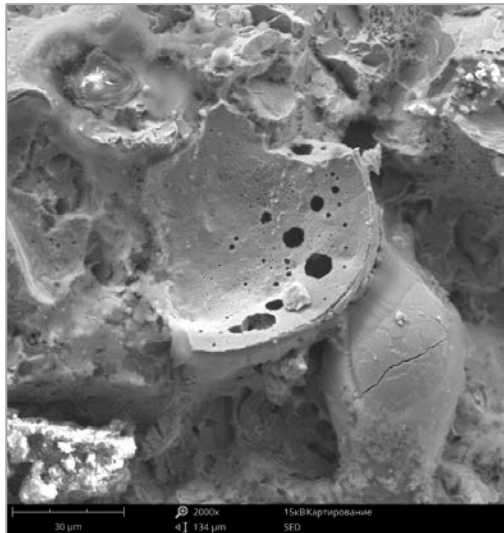
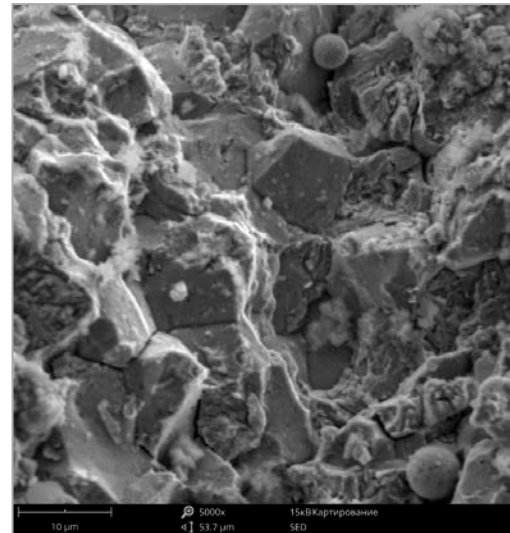


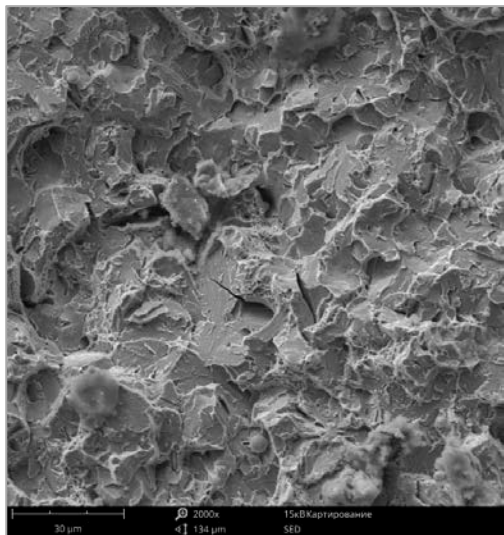
**Fig. 6.** General view of the fracture of the spring:  
1 – crack origin; 2 – failure crack propagation zone; 3 – fast fracture zone



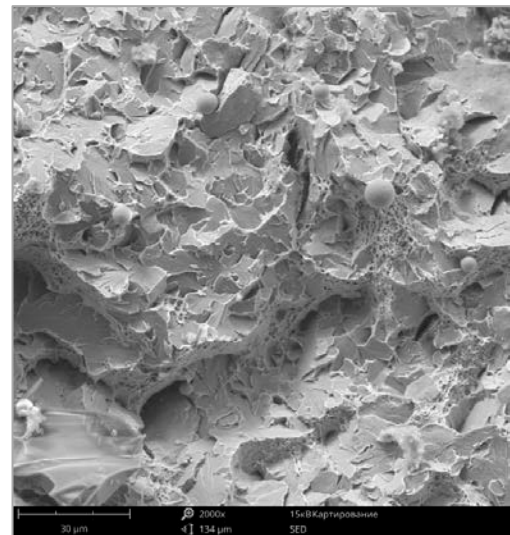
a



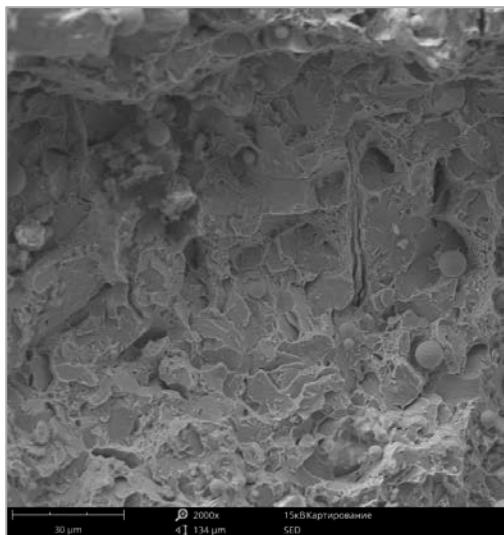
b



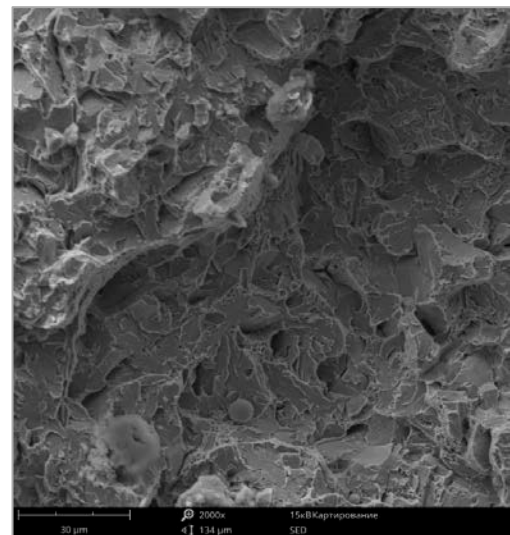
c



d



e



f

**Fig. 7.** Electron fractography of the spring's failure surface:  
 a, b – crack origin; c, d – failure crack propagation zone, zone of ratchet marks,  
 e, f – fast fracture zone

According to electron-fractographic studies, corrosion products were present in the crack origin coinciding with the place of damage to the coating, in the decarbonized surface layer there were open cavity-bubbles, bubbles with cracks (Fig. 7 a), non-metallic inclusions, intergrain facets, and cracks characteristic of corrosion damage were observed (Fig. 7 b). In the zone of failure crack propagation (Fig. 7 c, d) there were facets of cleavage and quasi cleavage, splitting by non-metallic inclusions, as well as pores typical for slow cracking under the influence of hydrogen [4,20-22]. The fracture surface in the ratchet marks zone was formed by facets of intercrystalline fracture with alternating quasi-cleavage and some areas of the dimple fracture. The fast fracture zone was characterized by facets of intergranular, transcrystalline fracture with areas of dimple fracture (Fig. 7 e, f). Thus, the propagation of the crack along the body of the spring proceeded by the mixed brittle-ductile mechanism.

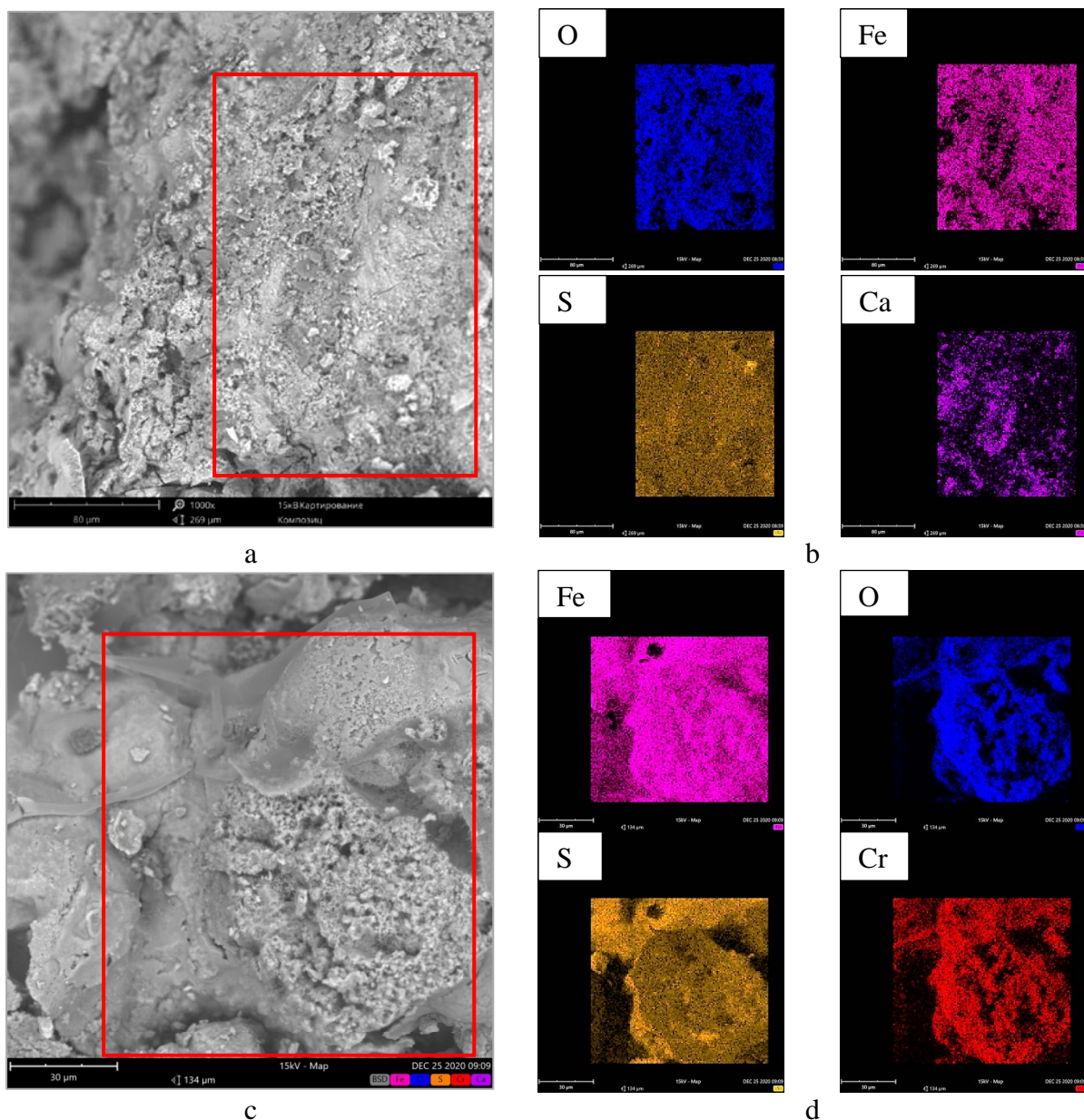


**Fig. 8.** Results of EDS of corrosion deposits from the metal surface:  
a, c – analyzed surface; b, d – element distribution map

Using EDS corrosion deposits collected from the surface of the spring were investigated (Fig. 8), on the basis of the results of which it can be argued that the environment is highly

aggressive, the deposits mainly consist of iron sulphides FeS, oxide compounds of iron and sulfur, as well as particles containing a large number of chemical elements represented by pigments and fillers included in the composition of the protective coating.

Thus, the summation of the results of the study allowed us to conclude that the cause of the spring failure was low-temperature hydrogen sulfide corrosion. The most dangerous concomitant process of low-temperature hydrogen sulfide corrosion is the hydrogenation of steel, which is confirmed by the presence of blistering under the deposits. Such blistering is the result of the presence in the cavities of either hydrogen sulfide itself or hydrogen released during the reaction of hydrogen sulfide with iron. Hydrogen, diffusing deep into the steel, accumulates in places within crystal lattice defects and non-metallic inclusions, eventually forming internal pores and causing the development of microcracks, which ultimately lead to the creation of significant internal stresses and embrittlement of the metal. The presence of moisture in the working environment significantly accelerated low-temperature hydrogen sulfide corrosion and hydrogen saturation of steel, thereby accelerating its embrittlement.

#### 4. Conclusions

1. A comprehensive method has been developed for determining the causes of the safety valve spring's failure using standard and special research methods, including reductive heat treatment.

2. Analysis of the results of metal research showed that premature failure of the safety valve spring is due to technological heredity (alloying system that does not provide corrosion resistance in the hydrogen sulfide environment, non-optimal heat treatment regime with the formation of a structure corresponding to insufficient hardness, strength, reduced fatigue resistance, low corrosion resistance of the surface of the rod with the presence of a decarburized layer, insufficient protection of the spring against corrosion by the protective coating) upon contact with the working environment not provided for by the project.

3. Based on the results of the analysis of corrosion deposits, it was revealed that the environment is highly aggressive, the deposits mainly consist of iron sulfides FeS, oxide compounds of iron and sulfur, as well as particles containing a large number of chemical elements represented by pigments and fillers included in the protective coating, and the cause of the spring failure was low-temperature hydrogen sulfide corrosion.

4. It has been established that at low-temperature hydrogen sulfide corrosion of steel 50KhFA, blistering and ulcerative damage are formed on the surface of the spring with the penetration of corrosion products into the spring's metal. The destruction of the metal occurs at non-metallic inclusions, along the boundaries of the primary austenitic grains, where the largest carbides are located, as well as along the interphase boundaries of the oriented carbide plates. When cracks form an almost closed loop, the metal is deformed under the pressure of hydrogen, followed by the formation of cavities that reduce resistance to operating loads and lead to failure. The solid solution contains multiple micropores up to 0.5  $\mu\text{m}$  in size, which cannot be closed by reductive heat treatment. The information obtained on the characteristic external signs, typical microdamages, and the mechanism of failure during low-temperature hydrogen sulfide corrosion of steel 50KhFA with the most dangerous concomitant process – hydrogenation can be used by researchers in the diagnosis of spring failure.

5. On the basis of the studies carried out, a set of measures was recommended to improve the reliability and prevent the failure of safety valve springs operating in similar conditions: hardness measurement during receipt inspection, periodic visual measurement control, capillary, and magnetic particle inspection; monitoring the condition of the sealing surfaces; ensuring the quality of valve assembly after repair and alignment of the parts installation; the use of protective covers – bellows made of 08Cr18Ni10Ti steel or more

corrosion-resistant for similar springs, which do not allow penetration of aggressive environment to the surface of the spring.

## References

- [1] Makaryants GM. Fatigue failure mechanisms of a pressure relief valve. *Journal of Loss Prevention in the Process Industries*. 2017;48: 1-13.
- [2] Kumar TSM, Adaveesh B. Application of "8D methodology" for the root cause analysis and reduction of valve spring rejection in a valve spring manufacturing company: A case study. *Indian Journal of Science. Technology*. 2017;10(11): 1-11.
- [3] Goritsky VM, Deren GS, Khromov DP. Analysis of the safety valve springs failure causes. *Chemical and petroleum engineering*. 1994;4: 27-29.
- [4] Goritsky VM. *Diagnostics of metals*. Moscow: Metallurgist; 2004. (In-Russian)
- [5] Engel L, Klingele G. *Scanning Electron Microscopy. Fracture (Handbook)*. 1986.
- [6] Grigorenko VB, Morozova LV. The usage of fractographic analysis to diagnostic the causes of destruction of products from medium-carbon steel. *Proceedings of VIAM*. 2018;8: 98-111.
- [7] Liu BC, Yang ZG. Failure Analysis of shock Absorption spring is motorcycle. *Journal of Failure Analysis and Prevention*. 2016;16: 337-345.
- [8] Das S, Taukdar S, Solanki V, Kumar A, Mukhopadhyay G. Breakege of spring steel during manufacturing: A Metallurgical investigation. *Journal of Failure Analysis and Prevention*. 2020;20: 2462-2469.
- [9] Xing XQ. Effect of environment-assisted cracking on the premature fatigue failure of high-strength valve springs. *Engineering Failure Analysis*. 2021;126: 105466.
- [10] Pal U, Mukhopadhyay G, Bhattacharya S. Failure analysis of spring of hydraulic operated valve. *Engineering Failure Analysis*. 2019;95: 191-198.
- [11] Screw-type cylindrical springs. *General technical specifications. ST CKBA 030-2006 Pipeline fittings*. 2009. (In-Russian)
- [12] Sorokin BG, Volosnikova AV, Vyatkin SA. *Grade guide of steels and alloys*. Moscow: Mechanical engineering; 1989. 105466
- [13] GOST 14959-2016. *Spring nonalloy and alloy steel products. Specifications*. 2016.
- [14] Tylkin MA. *Repair service thermist handbook*. Moscow: Metallurgy; 1981. (In-Russian)
- [15] Anuryev VI. *Handbook of mechanical engineer: In 3 volumes, Volume 1*. 8th ed. Moscow: Mechanical engineering; 2001. (In-Russian)
- [16] Bernshtein ML, Rakhstadt AG. *Metallurgy and heat treatment of steel. Volume 2. Fundamentals of thermal treatment. Reference book. In 3 volumes*. 3rd ed. Moscow: Metallurgy; 1983. (In-Russian)
- [17] GOST 13764-86. *Cylindrical helical compression (tension) springs made of round steel. Classification*.
- [18] Goldshtein MI, Grachev SV, Veksler YuG. *Special steels*. 2nd ed. Moscow: MISIS; 1999. (In-Russian)
- [19] Goodremont EA. *Special steel*. 2nd ed. Metallurgy; 1966. (In-Russian)
- [20] Fellows J. *Fractography and Atlas of Fractograms. Handbook*. Moscow: Metallurgy; 1982. (In-Russian)
- [21] Ren CX, Wang DQQ, Wang Q, Guo YS, Zhang ZJ, Shao CW, Yang HJ, Zhang ZF. Enhanced bending fatigue resistance of a 50CrMnMoVNb spring steel with decarburized layer by surface spinning strengthening. *International Journal of Fatigue*. 2019;124: 277-287.
- [22] Grigorenko VB, Morozova LV. Application of fractographic analysis to determine the causes of destruction of products made of medium-carbon steels. *Proceedings of VIAM*. 2018;8: (68).

**THE AUTHORS****Tupitsin M.**

e-mail: matupicin@vnikti.rosneft.ru

ORCID: 0000-0002-6060-7205

**Trishkina I.**

e-mail: irina\_trishkina@bk.ru

ORCID: 0000-0002-1596-3796

**Sycheva S.**

e-mail: SSSycheva@vnikti.rosneft.ru

ORCID: 0000-0002-6870-2258

**Storozheva E.**

e-mail: eistorozheva@vnikti.rosneft.ru

ORCID: 0000-0002-8396-8003

**Novikov R.**

e-mail: RENovikov@vnikti.rosneft.ru

ORCID: 0000-0003-1247-1291

## CHANGES IN ROCK PERMEABILITY NEAR-WELLBORE DUE TO OPERATIONAL LOADS

V.V. Poplygin<sup>1</sup>, E.P. Riabokon<sup>1✉</sup>, M.S. Turbakov<sup>1</sup>, E.V. Kozhevnikov<sup>1</sup>, M.A. Guzev<sup>2</sup>,  
H. Jing<sup>3</sup>

<sup>1</sup>Perm National Research Polytechnic University, 29 Komsomolsky Ave., Perm, Russia, 614990

<sup>2</sup>Institute for Applied Mathematics of the Far Eastern Branch of the Russian Academy of Sciences, st. Radio, 7,  
Vladivostok 690041, Russia

<sup>3</sup>State Key Laboratory for Geomechanics and Deep Underground Engineering, China University of Mining and  
Technology, 1 Daxue Rd., Xuzhou, Jiangsu 221116, China

✉ riabokon.evgenii@gmail.com

**Abstract.** The paper presents the results of studies of changes in the permeability of rocks in the bottom hole zone of wells in the process of oil production. Using the exponential equation for predicting the permeability of the rock with a change in reservoir pressure based on the data of well test data, an improved model is proposed. The developed model takes into account operational conditions that lead to a change in the structure of the rock matrix and oil degassing as a result of a reservoir pressure decrease. The proposed model includes empirical parameters. The model describes the hysteresis of the rock permeability for oil during the subsequent decrease and increase in reservoir pressure. For the model under consideration, the average change (decrease) in the permeability at the wellbore with an increase and subsequent decrease in the load is 30% of the initial value. Using the proposed model, numerical hydrodynamic calculations of the change in the time of oil production with a change in pressure were carried out. The lower the reservoir pressure, the longer the period of oil production. A significant decrease in reservoir pressure at the initial stages of oil production and its subsequent production leads to an increase in the terms of the development of recoverable oil reserves.

**Keywords:** stress-sensitive reservoir, rock, matrix, permeability, oil production

**Acknowledgements.** The research was supported by the grant from the Russian Science Foundation (project no.19-79-10034).

**Citation:** Poplygin VV, Riabokon EP, Turbakov MS, Kozhevnikov EV, Guzev MA, Jing H. Changes in rock permeability near-wellbore due to operational loads. *Materials Physics and Mechanics*. 2022;48(2): 175-183. DOI: 10.18149/MPM.4822022\_3.

### 1. Introduction

The permeability of rocks is sensitive to changes in their stress state caused by changes in reservoir pressure. The change in reservoir pressure in rock pores leads to a change in effective pressure which represents a difference between lithostatic pressure and reservoir pressure [1]. With an increase in effective rock pressure associated with a decrease in reservoir pressure during oil recovery, the matrix is compressed, compacted, resulting in a

decrease in the permeability of the rock and, in the long term, a decrease in the well flow rate and oil production in the field as a whole.

Exponential [2-4], power [5-7], logarithmic and power [8], as well as other combined [9,10] empirical equations are used to model the changes in the permeability of rocks under the action of effective rock pressures. Information on the relations used can also be found in [11].

There are no doubt that modeling in laboratory conditions on core samples is necessary to understand what equations should be used to predict changes in rock permeability with a change in effective pressure. However, a feature of the mentioned equations is that they do not take into account the influence on the rock permeability of the processes that are often observed in field conditions during oil production. These include, in particular, a change in the rock structure and oil degassing.

A change in the structure of the rock is observed when the effective pressure exceeds the ultimate strength of the rock. In this case, the change in the structure is determined by the process of destruction of the porous rock matrix, the fragments of which block the channels connecting the pores. As a result, during pumping the liquid through the rock at a constant flow rate, an additional pressure drop occurs  $\Delta P$ , which leads to a decrease in rock permeability  $k$ , since  $k \sim 1/\Delta P$ . As a result of such a change in the rock structure the permeability of the matrix also irreversibly decreases [12]. This means that with a decrease in effective pressure (an increase in reservoir pressure in the pores of the rock), the permeability will not be restored to its original value. A similar case is often observed in the near-wellbore zone of the reservoir, where there is an intensive decrease in reservoir pressure  $P_{res.}$  to bottom hole pressure  $P_{BH}$  as the flow of oil approaches the well.

Degassing of oil, associated with the release of gas from oil with a decrease in reservoir pressure below the saturation pressure of oil with gas, leads to the appearance of two phases in the rock. In this case, with an increase in the amount of released gas, the relative phase permeability of the rock for gas will increase, and the permeability for oil will decrease [13]. Moreover, the process is irreversible. If the effective pressure is increased, then not all of the gas released into the free phase will dissolve back into oil, and the phase permeability of the rock for oil will not reach the initial value. This phenomenon is observed in laboratory conditions but is not taken into account when predicting changes in the permeability of the near-wellbore formation zone.

In connection with the mentioned above, in order to predict the technological parameters of oil field development, such as well flow rate and pressure distribution in the reservoir, it is necessary to take into account the permeability hysteresis caused by changes in the rock structure and oil degassing. To overcome such an issue, this article proposes to modify the existing relationships in such a way that they take into account these phenomena.

The basis for the construction of model relationships is given by the studies carried out by many authors both on the study of permeability depending on changes in the structure of rocks, and on the study of permeability depending on the presence of two-phase flow in the rock under conditions of oil degassing.

Based on experimental data from the results of well testing in Section 2 an improved model of changes in rock permeability under conditions of a changed structure of the matrix material and degassing is constructed. Using the model obtained numerical modeling of changes in rock permeability was performed in Section 3 taking into account its deformation under degassing conditions. Section 4 concludes with the results obtained.

## 2. Formulation of the rock permeability change model

When extracting oil from a reservoir, two factors should be pointed out, the action of which leads to a decrease in reservoir pressure  $P_{res.}$ . The first factor takes into account the decrease

in reservoir pressure from the initial pressure value  $P_{res.0}$  down to a certain current  $P_{res.}$ . In models [2-11], the value  $P_{res.}$  is assumed to be the same over the entire area of the reservoir and equal to the value in its remote area from the well. The second factor is related to the existence of a non-uniform distribution of reservoir pressure in the rock, i.e. relation of  $P_{res.}$  on the distance to a well: reservoir pressure decreases from  $P_{res.}$  to  $P_{BH}$  as oil approaches the production well from a remote part of the formation, the so-called depression funnel or pressure drawdown on the reservoir  $\Delta P = P_{res.} - P_{BH}$  is observed (Fig. 1a).

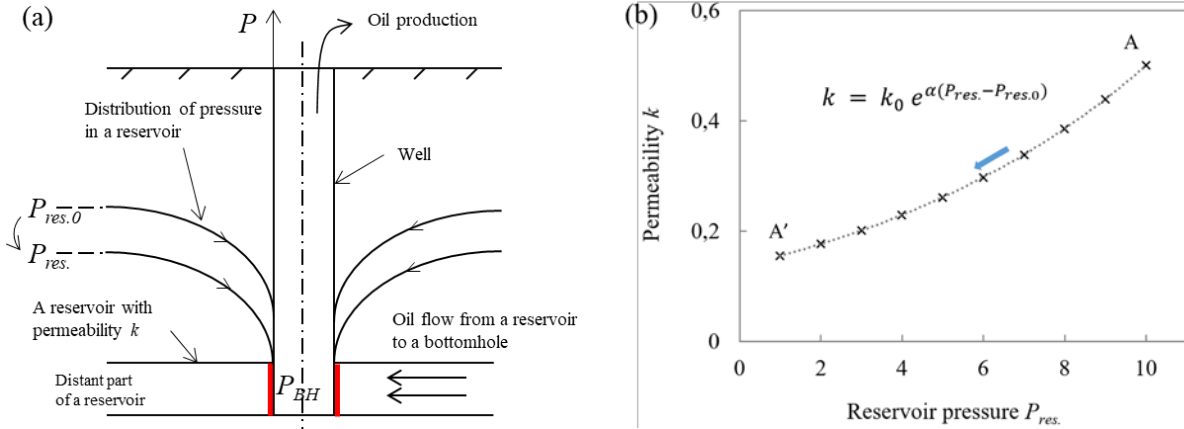


**Fig. 1.** Distribution of rock characteristics during oil production: (a) change in reservoir pressure with distance from the well; (b) dependence of the rock matrix permeability on reservoir pressure without taking into account operational conditions (on the example of the model in [4])

The factors described above lead to a decrease in rock permeability. Modeling the change in permeability in a remote part of the reservoir (in the area where the well operation does not affect the pressure in the reservoir) depending on pressure can be performed in laboratory conditions on core samples using equations such as in [2-11] (see Fig. 1b). At the same time, the effect of pressure reduction around the well on rock permeability is not taken into account in [2-11].

We will show below how to formulate a model that takes into account both factors described above. As an example, we will proceed from the model of V.N. Nikolaevsky and A.T. Gorbunov [4]. To predict changes in rock permeability  $k$  with a decrease in pressure changes, they proposed an exponential equation:

$$k = k_0 e^{\alpha(P_{res.} - P_{res.0})}, \quad (1)$$

where initial reservoir permeability  $k_0$ , initial  $P_{res.0}$ , and certain current  $P_{res.}$  reservoir pressures and rock matrix deformation coefficient  $\alpha$ ,  $\text{MPa}^{-1}$  are considered as independent parameters.

In order to take into account the change in rock matrix permeability in the well area, caused by pressure drawdown on the formation, it is necessary to enter the bottom hole pressure  $P_{BH}$ . Keeping the functional (exponential) relationship between permeability and pressure, we change the argument  $P_{res.}$  for a convex combination  $\alpha P_{res.} + \beta P_{BH}$ , where  $\alpha + \beta = 1$ . In the limiting case when the well is closed and the pressure in the reservoir  $P_{res.} = P_{BH}$ , we have the model (1). Since the task is to build another model, it is necessary to specify  $\alpha$  and  $\beta$ . The easiest way to choose is to take into account the influence of reservoir and bottom hole pressures in a symmetrical way, i.e.  $\alpha = \beta = 1/2$ . Then equation (1) is reduced to the form

$$k = k_0 e^{\alpha_d \left( \frac{P_{res.} + P_{BH}}{2} - P_{res.0} \right)}. \quad (2)$$

Relation (2) describes the change in rock permeability  $k$  using known values of field parameters. Equation (2) is substituted with the permeability value obtained experimentally from the results of well tests [14]. The values  $P_{res.}$  and  $P_{BH}$  correspond to the current values of reservoir pressure and well bottom hole pressure during well test,  $k_0$  and  $P_{res.0}$  correspond to the initial permeability and reservoir pressure. The only selectable parameter is the empirical deformation factor  $\alpha_d$ , the selection of which is given in [15].

Equation (2), on the one hand, when the well is shut off ( $P_{res.} = P_{BH}$ ) allows determining the change in rock permeability with a decrease in pressure in the reservoir from  $P_{res.0}$  down to  $P_{res.}$  during oil production. On the other hand, when the well is shut-in, the bottom hole pressure is lower than the reservoir pressure  $P_{BH} < P_{res.}$ , therefore substituting the value of the current bottom hole pressure  $P_{BH}$  in the equation (2) will allow determining how much rock permeability is changed, taking into account the pressure drawdown during well operation. Thus, in addition to the main change in permeability due to a decrease in pressure in the reservoir, an additional contribution of a change in permeability in the well zone is taken into account.

Equation (2) describes the change in permeability when the reservoir pressure is above the saturation pressure level  $P_{sat.} < P_{res.}$ , which corresponds to a zone  $AB$  in Fig. 2. Existence of saturation pressure  $P_{sat.}$  leads to hysteresis in permeability behavior. The effect of hysteresis is shown in Fig. 2 and is represented as a discrepancy between the curves of changes in rock permeability for oil between its values with a decrease and a subsequent increase in reservoir pressure.

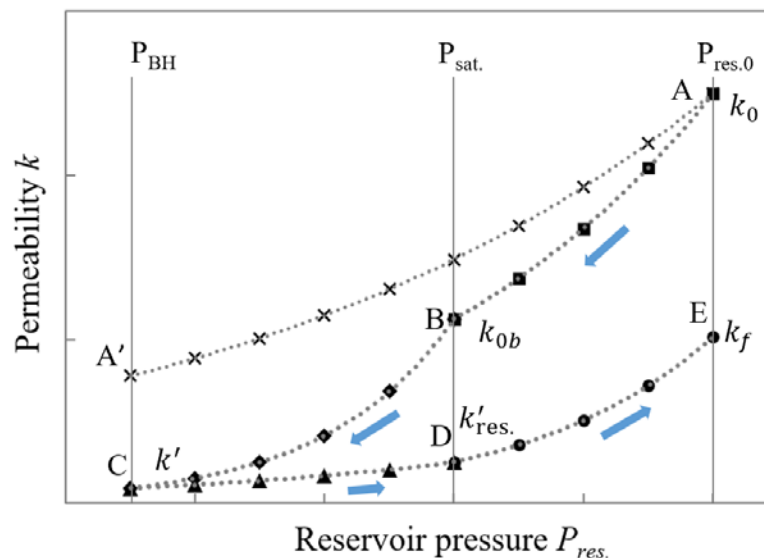


**Fig. 2.** Hysteresis of rock permeability for oil with a decrease in reservoir pressure taking into account additional changes in the matrix due to pressure drawdown during well operation and taking into account oil degassing due to a decrease in reservoir pressure below the saturation pressure of oil with gas (curve ABCDE). The curve AA' corresponds to a change in permeability with a change in reservoir pressure according to the model [4], which does not take into account operational factors

Let us explain from the point of view of physics the hysteresis of rock permeability with respect to oil. If reservoir pressure becomes equal to saturation pressure. If reservoir pressure becomes equal to saturation pressure  $P_{res.} = P_{sat.}$  two-phase flow begins in the reservoir near the well and the initial permeability is equal to the value  $k = k_{0b}$ . With a further decrease in pressure below the saturation pressure in the region  $BC$  bottom hole pressure becomes the

dominant parameter that affects the permeability of the rock. Therefore, in the area  $BC$  by formation pressure we mean bottom hole pressure. The lower the bottom hole pressure in the reservoir than saturation pressure, the more intense the degassing of oil and, as a result, the decrease in the phase permeability for oil. With an increase in bottom hole pressure in the area  $CD$ , initial permeability in which  $k = k'$ , the gas released from the oil at the previous stage begins to dissolve back into the oil. However, the permeability of the matrix is not completely restored, since part of the usable space in pores is already irreversibly occupied by free gas, and the changed structure of the matrix does not allow the rock to return to its original state. Thus, we obtain the hysteresis of the permeability behavior (curve ABCDE).

Due to the conservativeness of the modeling ideology, we will keep the functional relationship (1) between the permeability and pressure for the  $BC$  area by changing the argument in the equation:

$$k = k_{0b} e^{\alpha_1(P_{BH}-P_{sat.})}. \quad (3)$$

The parameter  $\alpha_1$  is chosen empirically for the region  $BC$ . To describe the change in permeability with increasing pressure in the area from bottom hole pressure  $P_{BH}$  up to saturation pressure  $P_{sat.}$  we denote the pressure in the reservoir in this area as  $P_{res.}$ , then for the region  $CD$  we get:

$$k = k' e^{\alpha_2(P_{res}-P_{BH})}, \quad (4)$$

where the parameter  $\alpha_2$  is chosen empirically.

With a further increase in reservoir pressure in the  $DE$  region, the free gas is already partly dissolved back into the oil. The other part of the undissolved gas remaining in the free state reduces the phase permeability of the rock for oil. In addition, the changes acquired by the rock matrix do not allow the permeability to take its original value, at a similar pressure in the reservoir. Therefore, the initial for the region  $DE$  the permeability of the rock is equal to the value  $k = k'_{res.}$ , the value of which is higher than the value of the initial permeability of the rock at the previous stage  $CD$ , but below the initial permeability in the areas  $AB$  and  $BC$   $k' < k'_{res.} < k_{0b} < k_0$ .

In the region  $DE$  the rock permeability equation has a similar to (2) form:

$$k = k'_{res.} e^{\alpha_d\left(\frac{P_{res.}+P_{BH}}{2}-P_{res.}\right)}. \quad (5)$$

At the boundary of the  $DE$  region, with increasing pressure in the reservoir, the final permeability is  $k_f$ , which is lower than the original  $k_f < k_0$ . As a result of the decrease and subsequent restoration of the reservoir and, accordingly, effective pressure, the rock and the fluid contained in the pores undergo irreversible changes, which lead to permeability hysteresis.

Estimation of the change of empirical parameters  $\alpha_1$  and  $\alpha_2$  for different values of rock permeability can be performed based on the analysis of well test results. It was found that in the range of empirical parameters  $\alpha_1$  in (3) and  $\alpha_2$  (4) the following approximations can be specified (Fig. 3):

$$\alpha_1 = 0.3247 - 0.03 \times \ln(k/k_{av.}), \quad (k = 0.01 \dots 1.27 \times 10^{-3} \mu\text{m}^2),$$

$$\alpha_2 = 0.25 + 0.015 \times \ln(k/k_{av.}),$$

where  $k_{av.}$  and  $k/k_{av.}$  denote to average and relative permeability of sandstone. Empirical parameter values  $\alpha_d$  are also selected based on well test results.

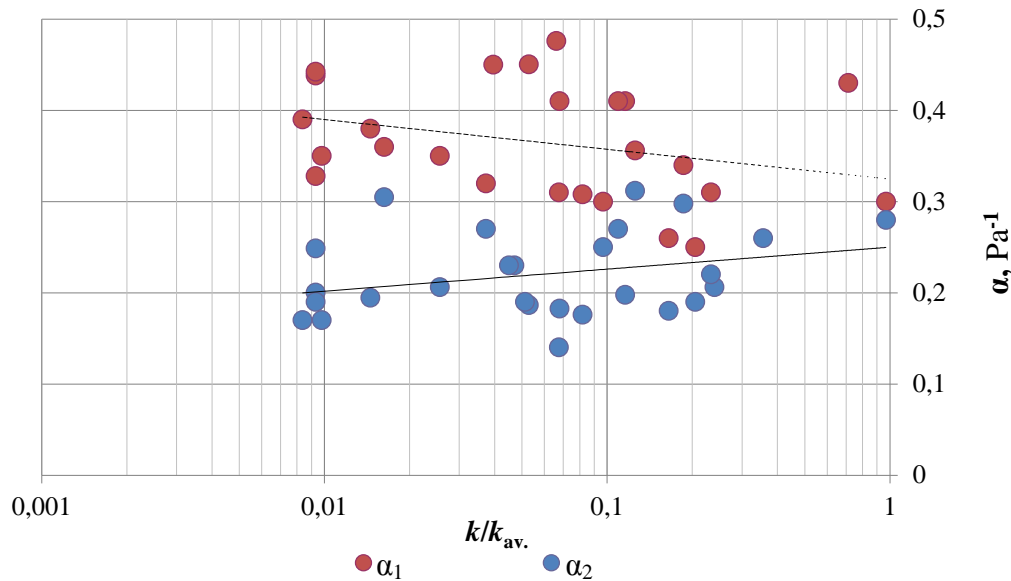


**Fig. 3.** Dependence of empirical parameters  $\alpha_1$  and  $\alpha_2$  on the rock's relative permeability

It is seen from Fig. 3 that with an increase in reservoir permeability, and the values of the parameter  $\alpha_1$  decrease, the values of parameter  $\alpha_2$  increase. From the point of view of the model (2)-(5), a decrease in the empirical parameter  $\alpha_1$  with a decrease in relative permeability corresponds to a decrease in reservoir pressure, a change in the rock matrix, and oil degassing, which manifests itself in an increase in the slope of the curve  $BC$  (see Fig. 2). An increase in parameter  $\alpha_2$  with a decrease in relative permeability corresponds to an increase in reservoir pressure, dissolution of released free gas in oil, and an increase in rock permeability at the interval  $CD$ .

Equations (2)-(5) were obtained for clastic (sandstone) reservoirs of the Perm region of porous type as a result of experimental studies of a number of production wells (well test). Under similar conditions, relations (2)-(5) allow predicting of the change in permeability in other producing wells without conducting well tests. In addition, relations (2)-(5) are of great importance for modeling the development of oil fields and predicting optimal scenarios for oil production from the fields with similar characteristics of the rock and the oil that saturates it.

Considering that during the development of an oil field, a decrease in rock permeability in the near-wellbore zone leads to an increase in the terms of oil extraction from the reservoir, it is relevant to predict the change in the permeability of the rock using the obtained model (2)-(5). In section 3 a numerical simulation of the change in permeability in a hydrodynamic simulator is performed.

### 3. Numerical simulation using the refined model

Numerical modeling allows predicting the dynamics of technological indicators of oil deposit development, taking into account changes in rock permeability during reservoir deformation. Hydrodynamic modeling was performed in a hydrodynamic simulator Tempest (ROXAR). In the simulator, the flow of oil (o), water (w), and gas (g) in a porous medium obeys the Darcy law, the equations of continuity of the flow of a weakly compressible multiphase fluid, and the Newtonian flow.

Continuity equations for water, oil, and gas include formation permeability  $k$ . Permeability changes its value with changes in reservoir pressure.

The following calculation algorithm is proposed:

1) determining the pressure in the reservoir and saturation of the reservoir with oil, water, and gas by solving the material balance equation;

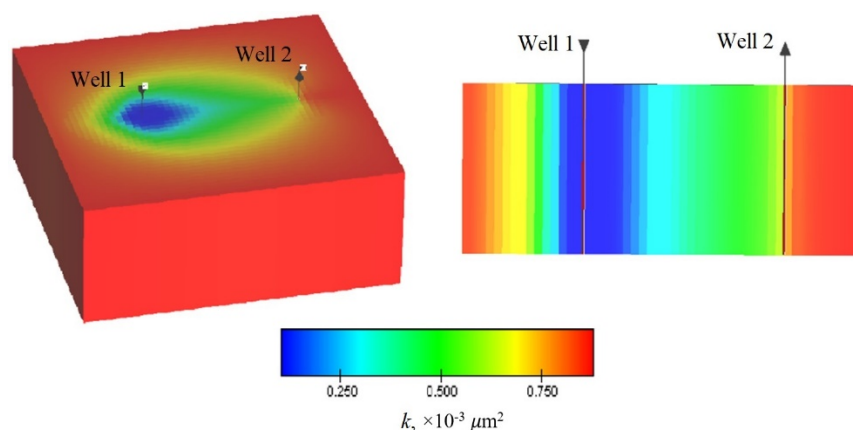
- 2) calculation of effective pressure;
- 3) calculation of reservoir permeability;
- 4) determination of fluid flow between cells.

To study the effect of pressure changes on deformation, permeability, and productivity, a model of a field area with two wells was created using the example of a typical oil reservoir in Perm region. Modelling on a field section with two wells allows for evaluation of the dynamics of oil production under various scenarios for changing reservoir pressures and creates the basic foundations for regulating production at oil fields.

The main parameters of the reservoir are given below:

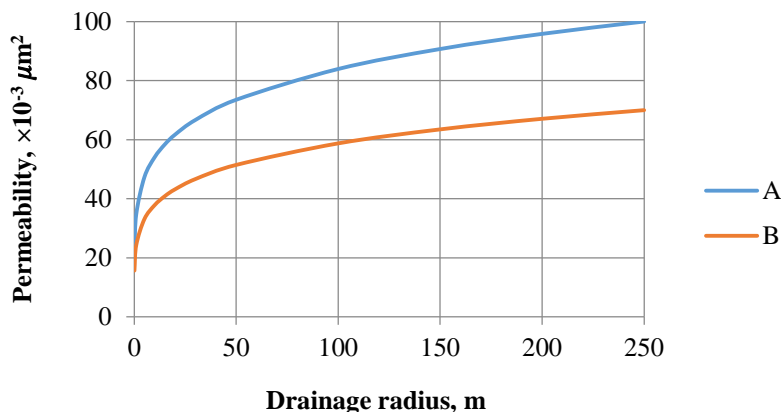
Permeability, $\times 10^{-3} \mu\text{m}^2$	100
Reservoir thickness, m	10
Porosity, %	20
Depth, m	1400
Gas saturation pressure, MPa	8.6
Pore pressure, MPa	16
Bottom hole pressure, MPa	10
Injection pressure, MPa	22

Figure 4 shows a 3D model of the reservoir area at the end of development with water injection.



**Fig. 4.** A 3D model of the reservoir area at the end of development with water injection (one of the options): Well 1 represents an injection well; Well 2 represents a production well

It was obtained during modeling, that the permeability near the production well decreases more intensively than the permeability at the periphery (which confirms the experimental well test data). In addition, the average reservoir permeability in the absence of water injection into the reservoir (that is, without compensation/restoration of reservoir (pore) pressure) at the end of development becomes 30% lower than the initial permeability (Fig. 5). It can be seen from the fluid pressure contours that the pressure gradients change dramatically in the area of change in the structure of the rock matrix (blue color). The pressure profiles were strongly influenced by permeability and porosity. This means that an increase in the experimental parameters for porosity and permeability presented in this paper leads to a strong change in the rock matrix, with a decrease in pressure, as can be seen in the vertical section (Fig. 4 on the right), which can be interpreted as a decrease in permeability caused by a change in the structure of the rock with constant productivity of the production well.



**Fig. 5.** Dependence of the permeability on the drainage radius without water injection at the beginning of modeling (A) and after a year of production (B)

#### 4. Conclusion

Using experimental data from the well testing on oil fields in the north of the Perm region an improved model of changes in rock permeability during oil production was obtained. The model is based on the exponential dependence of rock permeability. In addition to the parameters generally accepted in models, the refined model additionally contains saturation pressure (to take into account oil degassing) and pressure at the bottom of the well (to take into account changes in the structure of the rock). The resulting model describes the hysteresis of the rock matrix permeability caused by the technological conditions during well operation. According to the results of numerical modeling using the refined model in the simulator, it was obtained that the average reservoir permeability in the absence of water injection into the reservoir (without compensation/restoration of reservoir pressure) at the end of development becomes 30% lower than the initial permeability. Taking into account the additional influence of the degassing effect, the permeability of the rock around the well is not overestimated and approaches the real one. Taking into account the change in the structure of the rock and the corresponding decrease in permeability as a result of oil degassing, the period for the development of the oil field increases, which has to be taken into account in reservoir engineering.

#### References

- [1] Wang H-X, Wang G, Chen Z-XJ, Wong RCK. Deformational characteristics of rock in low permeable reservoir and their effect on permeability. *Journal of Petroleum Science and Engineering*. 2010;75: 240-243.
- [2] Main IG, Kwon O, Ngwenya BT, Elphick SC. Fault sealing during deformation-band growth in porous sandstone. *Geology*. 2000;28: 1131-1134.
- [3] David C, Wong T-F, Zhu W, Zhang J. Laboratory measurement of compaction-induced permeability change in porous rocks: Implications for the generation and maintenance of pore pressure excess in the crust. *Pure and Applied Geophysics*. 1994;143: 425-456.
- [4] Nikolaevskii VN, Basniev KS, Gorbunov AT, Zotov GA. *The Mechanics of Saturated Porous Media*. Moscow: Nedra; 1970. (In Russian)
- [5] Ghabezloo S, Sulem J, Guédon S, Martineau F. Effective stress law for the permeability of a limestone. *International Journal of Rock Mechanics and Mining Sciences*. 2009;46(2): 297-306.
- [6] Nelson RA, Handin J. Experimental study of fracture permeability in porous rock. *AAPG Bulletin*. 1977;61(2): 227-236.

- [7] Kilmer NH, Morrow NR, Pitman JK. Pressure sensitivity of low permeability sandstones. *Journal of Petroleum Science and Engineering*. 1987;1: 65-81.
- [8] Metwally YM, Sondergeld CH. Measuring low permeabilities of gas-sands and shales using a pressure transmission technique. *International Journal of Rock Mechanics and Mining Sciences*. 2011;48(7): 1135-1144.
- [9] Jones SC. Two-point determinations of permeability and pv vs. net confining stress. *SPE Formation Evaluation*. 1990;3: 235-241.
- [10] Li M, Bernabé Y, Xiao W-I, Chen Z-Y, Liu Z-Q. Effective pressure law for permeability of e-bei sandstones. *Journal of Geophysical Research: Solid Earth*. 2009;114: B07205.
- [11] Kozhevnikov EV, Turbakov MS, Riabokon EP, Poplygin VV. Effect of effective pressure on the permeability of rocks based on well testing results. *Energies*. 2021;14(8): 2306.
- [12] DeJong JT, Christoph GG. Influence of particle properties and initial specimen state on one-dimensional compression and hydraulic conductivity. *Journal of Geotechnical and Geoenvironmental Engineering*. 2009;135(3): 449-454.
- [13] Jia W, McPherson B, Pan F, Dai Z, Moodie N, Xiao T. Impact of Three-Phase Relative Permeability and Hysteresis Models on Forecasts of Storage Associated With CO<sub>2</sub>-EOR. *Water Resources Research*. 2018;54(2): 1109-1126.
- [14] Escobar FN. *Novel, Integrated and Revolutionary Well Test Interpretation and Analysis*. London: IntechOpen; 2018.
- [15] Shi L, Zeng Z, Fang Z, Li X. Investigation of the Effect of Confining Pressure on the Mechanics-Permeability Behavior of Mudstone under Triaxial Compression. *Geofluids*. 2019;2019: 1796380.

## THE AUTHORS

### **Poplygin V.V.**

e-mail: poplygin@bk.ru

ORCID: 0000-0003-2142-5246

### **Riabokon E.P.**

e-mail: riabokon.evgenii@gmail.com

ORCID: 0000-0003-0555-3977

### **Turbakov M.S.**

e-mail: msturbakov@gmail.com

ORCID: 0000-0002-9336-5847

### **Kozhevnikov E.V.**

e-mail: kozhevnikov\_evg@mail.ru

ORCID: 0000-0002-6084-0795

### **Guzev M.A.**

e-mail: guzev@iam.dvo.ru

ORCID: 0000-0001-9344-154X

### **Jing H.**

e-mail: hwjing@cumt.edu.cn

ORCID: -

## ANALYSIS OF CuCrZr/316L(N) BIMETALLIC JOINT WITH AND WITHOUT NICKEL INTERLAYER FOR PLASMA-FACING COMPONENTS

P. Piskarev<sup>1,2✉</sup>, A. Gervash<sup>1</sup>, S. Bobrov<sup>1</sup>, V. Ruzanov<sup>1</sup>, A. Ogurski<sup>1</sup>, I. Mazul<sup>1</sup>,  
R. Giniyatulin<sup>1</sup>, B. Ermakov<sup>2</sup>, O. Sevryukov<sup>3</sup>

<sup>1</sup>JSC "NIIEFA", St Petersburg, 196641 Russia

<sup>2</sup>Peter the Great St. Petersburg Polytechnic University, St. Petersburg, 195251, Russia

<sup>3</sup>National Research Nuclear University MEPhI, Moscow, 115409, Russia

✉ piskarev@sintez.niiefa.spb.su

**Abstract.** The work considers the CuCrZr/316L(N) bimetallic joint, which is obtained by diffusion bonding using hot isostatic pressing (HIP) and is a design element of the plasma-facing components (PFC) of a thermonuclear reactor. A comparative analysis of the specified bimetallic joint with a nickel interlayer obtained by different methods and without it has been carried out. A study of the structure and elemental composition of the bimetallic joint was made, where the brittle zirconium phases were identified in the interface zone for all the considered variants. The results of microhardness testing are obtained, demonstrating the presence of a sharp transition of hardness values by more than two times at the interface of two metals. A series of rupture tests of the bimetallic samples was carried out and almost identical values of the rupture stress were obtained for all the considered bimetallic joint variants. The fracture of the samples during the testing at temperatures up to 150°C occurred on the base metal and at higher temperatures – on the bimetallic joint.

**Keywords:** Bimetallic joint, CuCrZr/316L(N), diffusion bonding, Nickel interlayer, brittle layer, plasma-facing components, microhardness, rupture test, embrittlement

**Acknowledgements.** *The research is partially funded by the Ministry of Science and Higher Education of the Russian Federation as part of World-class Research Center program: Advanced Digital Technologies (contract No. 075-15-2020-934 dated from 17.11.2020).*

**Citation:** Piskarev P, Gervash A, Bobrov S, Ruzanov V, Ogurski A et al. Analysis of CuCrZr/316L(N) bimetallic joint with and without Nickel inter-layer for plasma-facing components. *Materials Physics and Mechanics*. 2022;48(2): 184-198. DOI: 10.18149/MPM.4822022\_4.

### 1. Introduction

The low-alloy copper dispersion-hardening alloys, such as CuCrZr, have a number of advantageous characteristics: tensile strength up to 500 MPa at room temperature; maximum operating temperature up to 300°C; values of the thermal and electrical conductivity coefficients at the level of 75-90% of pure copper; corrosion resistance. These characteristics have determined the scope of application of such alloys: products and components operating

under the high thermal/electrical and mechanical loads and having active cooling, which allows for maintaining a relatively low operating temperature. One of such applications is the PFC of the thermonuclear reactor [1], which are multilayer structures made of dissimilar metals, including CuCrZr. The density of the heat flux from the plasma on the surface of the PFC reaches  $20 \text{ MW/m}^2$ . At the same time, the distributed mechanical loads on the PFC from electromagnetic forces are the consequence of the magnetic trap holding the plasma, reaching about  $180 \text{ kN/m}$ . The CuCrZr alloy in the composition of the PFC acts as a heat-sink layer, which is cooled by water and bonded using brazing with a shielding layer (beryllium/tungsten) on the one hand [2] and by diffusion bonding or explosion bonding with a structural layer (AISI 316L(N)) on the other hand [3,4,5]. For a certain PFC design, the CuCrZr/316L(N) bimetallic joint is located at the water/vacuum boundary (Fig. 1), which leads to strict requirements for the leak tightness of the joint: no more than  $1 \times 10^{-11} \text{ Pa} \times \text{m}^3/\text{s}$  at room temperature.

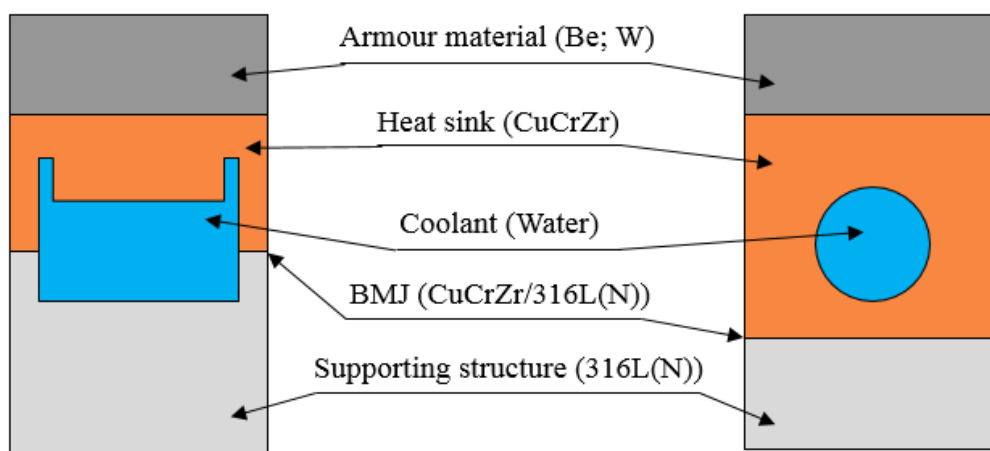


**Fig. 1.** The cross-section of the various variants of the plasma-facing components with the CuCrZr/316L(N) bimetallic joint

Loss of the bimetallic joint leak tightness under the influence of the operational loads will lead to a loss of the vacuum of the reactor plant and the need for challenging maintenance. The information about such cases is unknown since the PFC of this design has never been used in thermonuclear reactor installations before. However, now there are known cases of destruction considered by the bimetallic joint under the influence of the thermal stresses during the manufacture of the PFC [6,7]. The destruction of the bimetallic joint with a loss of leak-tightness occurred due to the propagation of a crack in the CuCrZr layer along the interface zone.

The well-known feature of the CuCrZr/316L(N) bimetallic joint is a layer with the zirconium phases, which appear in a copper alloy along an interface zone [6-8]. At the same time, the crack noted earlier spreads during the destruction of the bimetallic joint precisely along with the specified layer with zirconium phases [6,7]. The literature notes a method for optimizing the CuCrZr/316L(N) bimetallic joint by introducing an intermediate layer of nickel into the joint [10-12]. The purpose of this work is to study the effect of the nickel interlayer on the chemical composition and characteristics of the CuCrZr/316L(N) bimetallic joint.

## 2. Materials and Methods

In this work, the study of the CuCrZr/316L(N) bimetallic joint samples with and without a nickel interlayer, made by the diffusion bonding using HIP, was carried out. Four variants of

the nickel interlayer were used, differing in the thickness and in the method of the production. Thus, the following types of the CuCrZr/316L(N) bimetallic joint were studied:

1. Without an intermediate layer.
2. With an intermediate layer of nickel foil with a thickness of 25  $\mu\text{m}$ .
3. With an intermediate layer of nickel foil with a thickness of 50  $\mu\text{m}$ .
4. With an intermediate layer in the form of the nickel coating with a thickness of 15  $\mu\text{m}$  on a billet made of CuCrZr.
5. With an intermediate layer in the form of the nickel cover with a thickness of 15  $\mu\text{m}$  on both CuCrZr and 316L(N) blanks.

The chemical composition and the type of the used materials are presented in Table 1.

In order to obtain the bimetallic blanks, the initial blanks of materials after the chemical etching were placed in a capsule, where a vacuum of no worse than  $10^{-3}$  kPa was created. The capsules are processed in a Quintus QIH gas-static press 0.31 $\times$ 0.890-1500-1250 M in the following modes: 150 MPa, 980°C, exposure time 2 hours. Next, the finished bimetallic blanks were "extracted" from the capsule, and the quality of the bimetallic joint was tested by ultrasound control.

The metallographic studies were carried out on the grinds etched in solution (13%  $\text{K}_2\text{Cr}_2\text{O}_7$ +17%  $\text{H}_2\text{SO}_4$ ) using the Olympus GX-51 optical microscope with a SIAMS 800 image analysis system and a JEOL JSM-6510LV scanning electron microscope with an E2v X-ray spectral analysis prefix. Microhardness measurements were carried out on the EMCO-TEST DuraScan 50 microhardness meter.

Bimetallic samples were made for the rupture test, which allows conducting the testing according to a special loading scheme. Previously, the bimetallic fabricated parts were heat-treated (HT) in order to obtain optimal CuCrZr mechanical properties [13]: solution annealing (SA) at 980°C for 30 minutes, followed by water quenching, and then aging (A) at 480°C for 2 hours, followed by air cooling. The rupture tests of the bimetallic samples were performed on a universal testing machine Instron 8802 with an Instron SFL 3119-408 climate chamber. The samples assembled with the equipment were heated in the atmosphere. The maximum temperature on the existing equipment is 600°C. The heating time to the maximum temperature was about 2 hours.

### 3. Research results

Figure 2 shows the micrographs of the sections of the several bimetallic joint variants at magnifications of 100 and 1000 times. The other variants of the bimetallic joint with a nickel interlayer differ visually only in the thickness of the intermediate layer. The average grain size of CuCrZr in all analyzed bimetallic samples is 20-30  $\mu\text{m}$ , and the maximum grain size does not exceed 170  $\mu\text{m}$ .

The CuCrZr/316L(N) bimetallic joint (without an interlayer (Fig. 2, a-b) contains a typical line of phases with a size of 1-2  $\mu\text{m}$  located on the CuCrZr side along with the interface. The CuCrZr/316L (N) bimetallic samples with a nickel interlayer in the form of a foil (Fig. 2, c-d) have a more evident visual interface between the base metals and the intermediate layer, in comparison with the bimetallic joint, which is having a layer in the form of an electrochemical coating (Fig. 2, e-f). This is due to the fact that the electrochemical coating initially has a metallurgical contact with one of the base metals, and the diffusion processes move faster in this case. All the variants of the CuCrZr/316L(N) bimetallic joint with a nickel interlayer do not contain an evident continuous phase line, as in the case of the bimetallic joint without an interlayer but contain separate phases and larger phase lines. These phases are located at the interface of the nickel interlayer and CuCrZr.

An additional study of the CuCrZr/316L(N) bimetallic samples with and without a nickel interlayer after the performed HT (SA + A) showed that there are no changes in the

size and density of the phases located in the bimetallic joint zone, and there is no increase in the size of CuCrZr grains.

Table 1. The chemical composition and the type of the used materials

Material	The base elements of the alloy and impurities (wt.%)																			
CuCrZr	Hot-rolled sheets	Cu		Cr		Zr		O		Other elements		Other elements in all								
		gen.		0.6 – 0.9		0.07-0.15		Max. Min.		Co <0.05		<0.1								
316L(N)	Cold-rolled sheets	Fe	C	Mn	Si	P	S	Cr	Ni	Mo	N	Cu	B	Co	Nb	Ta	Ti			
		Gen.	0.030	1.60-2.00	0.50	0.025	0.010	17.00 – 18.00	12.00– 12.50	2.30 – 2.70	0.060 – 0.080	0.30	0.0020	0.05	0.01	0.01	0.10			
Ni interlayer	Cold-rolled foil with a thickness of 25 μm	Ni	Fe	C	Si	Mn	S	P	Cu	As	Pb	Mg	Zn	Sb	Bi	Sn	Cd	Impurities in all		
		min 99.5	till 0.1	till 0.1	till 0.15	till 0.05	till 0.005	till 0.002	till 0.1	till 0.002	till 0.002	till 0.1	till 0.007	till 0.002	<0.5					
	Cold-rolled foil with a thickness of 30 μm	Ni	Fe	C	Si	Mn	S	P	Co	Al	Cu	As	Pb	Mg	Zn	O	Sb	Bi	Sn	Cd
		min 99.9	till 0.03	till 0.03	till 0.01	till 0.002	till 0.001	till 0.001	till 0.1	till 0.01	till 0.015	till 0.001	till 0.001	till 0.01	till 0.002	till 0.003	till 0.001	till 0.001	till 0.001	till 0.001
Galvanic cover with a thickness of 15/215 μm	Ni		Impurities																	
	100 (Teor.)		The control is not regulated																	

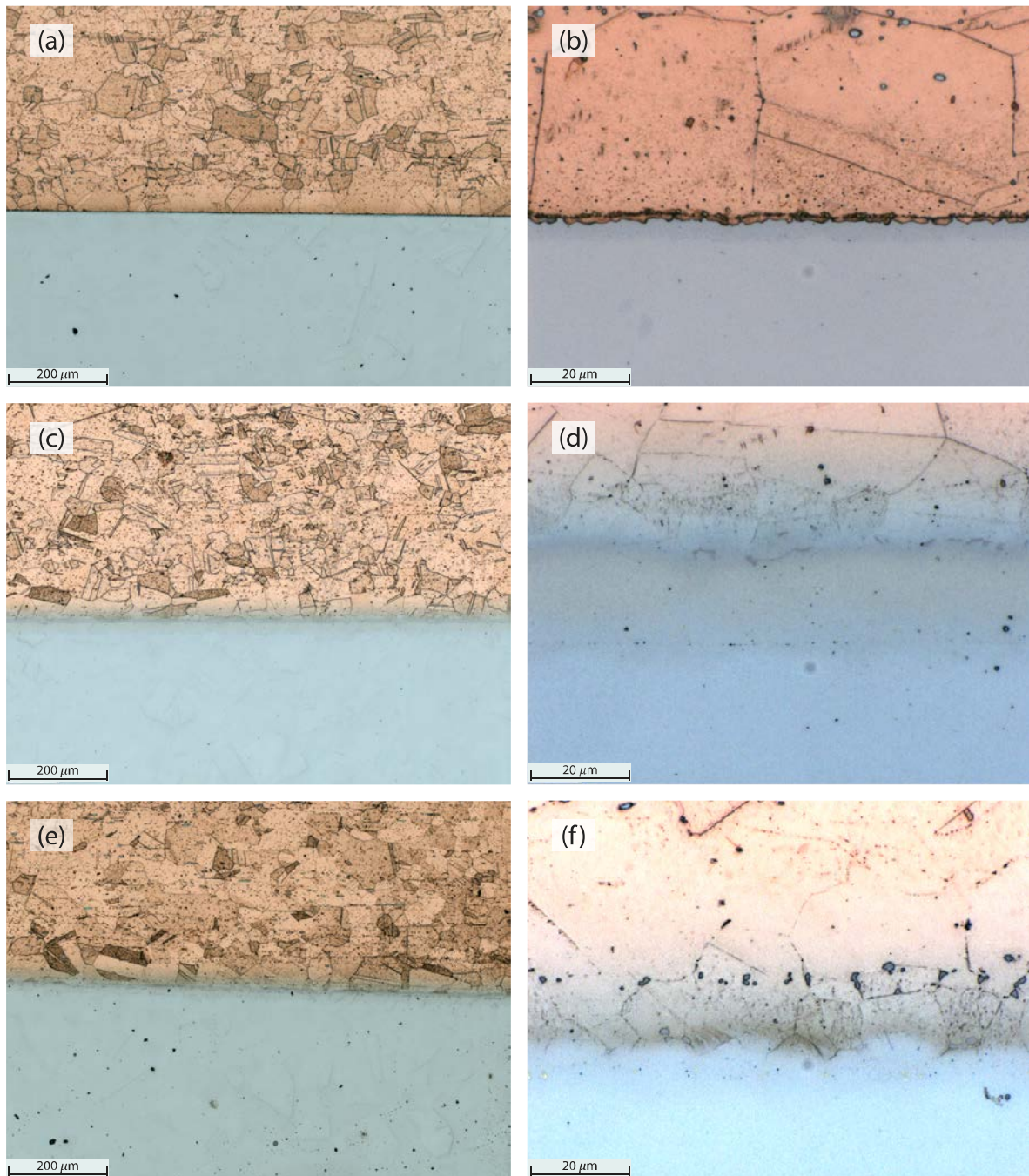


**Fig. 2.** The micrographs of the CuCrZr/316L(N) bimetallic joint:

(a) Without an intermediate layer (magnification 100 times); (b) Without an intermediate layer (magnification 1000 times); (c) With an intermediate layer in the form of a nickel foil, 25  $\mu\text{m}$  (magnification 100 times); (d) With an intermediate layer in the form of a nickel foil, 25  $\mu\text{m}$  (magnification 1000 times); (e) With an intermediate layer in the form of a nickel coating on both materials, 15  $\mu\text{m}$  (magnification 100 times); (f) With an intermediate layer in the form of a nickel coating on both materials, 15  $\mu\text{m}$  (magnification of 1000 times)

Figure 3 shows the results of the microhardness testing of the CuCrZr/316L(N) bimetallic joint for the several analyzed variants. The results for both variants of the bimetallic joint with a nickel layer in the form of a coating turned out to be almost equivalent, so they are summarized further. The measurements were carried out in sections with a step between shots of about 50  $\mu\text{m}$ .

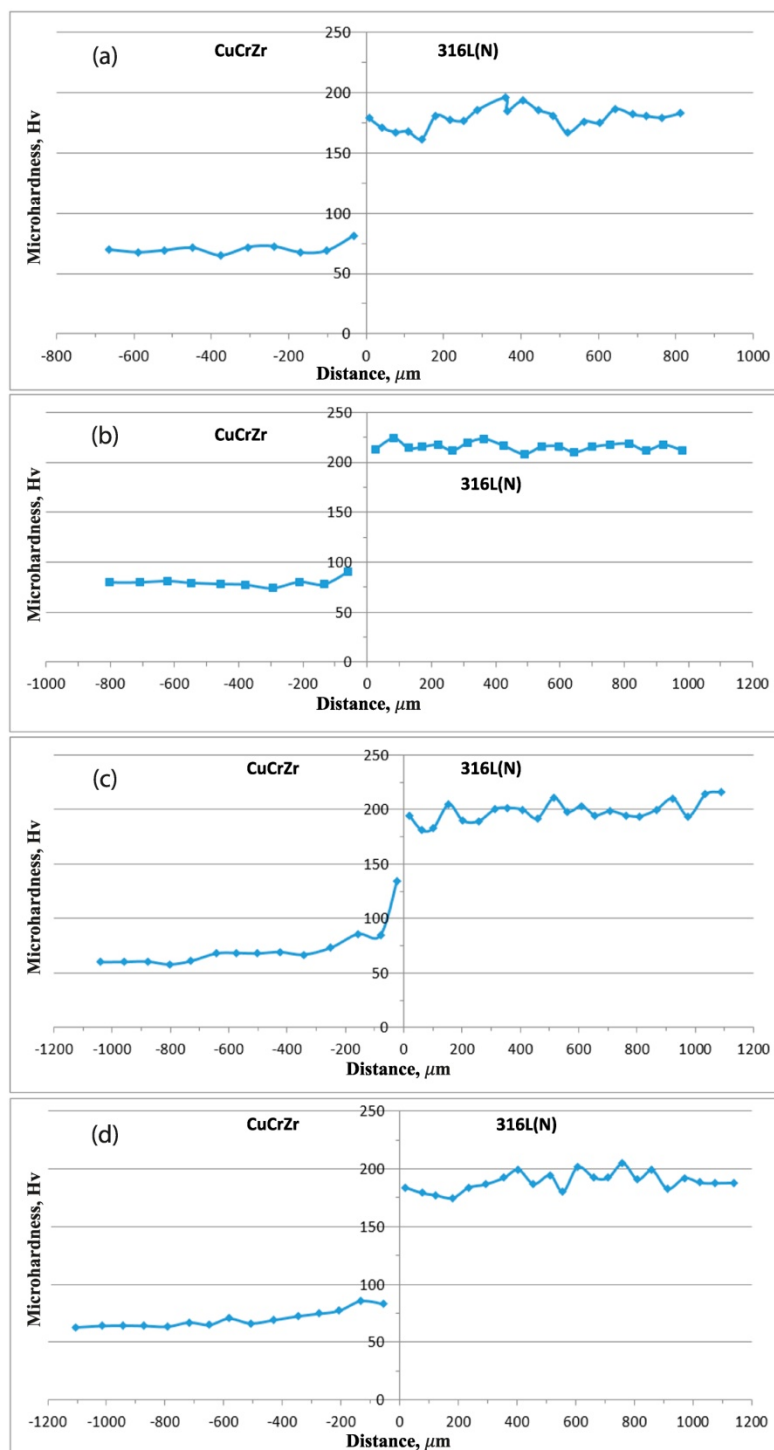


**Fig. 3.** The results of the microhardness testing of the CuCrZr/316L(N) bimetallic joint: (a) Without an intermediate layer; (b) With an intermediate layer in the form of a nickel foil, 25 μm; (c) With an intermediate layer in the form of a nickel foil, 50 μm; (d) With an intermediate layer in the form of a nickel coating of 15-30 μm.

The hardness of the CuCrZr and 316L(N) differs by more than two times and changes almost abruptly at the interface: on the average, 70 HV for CuCrZr; on average, 180...200 HV for 316L(N). The hardness of CuCrZr after HT (SA + A) is on average 105 HV, the hardness of 316L(N) after is slightly reduced to 160-180 HV. At the same time, the hardness of 316L(N) in the bimetallic joint with a nickel interlayer is on average greater than the hardness

of 316L(N) in the bimetallic joint without an interlayer. This fact is probably related to the diffusion of nickel into steel, but this issue requires a separate study. In the current work, the properties of 316L(N) are not analyzed detailed and more attention is paid to CuCrZr, as a weaker metal in the CuCrZr/316L(N) bimetallic joint. The hardness of the nickel interlayer, which was measured for the bimetallic joint with a nickel foil of 50 microns (Fig. 3, c) is about 135 HV. Figure 4 shows a photo of the bimetallic sample with a nickel foil of 50  $\mu\text{m}$  after microhardness testing.

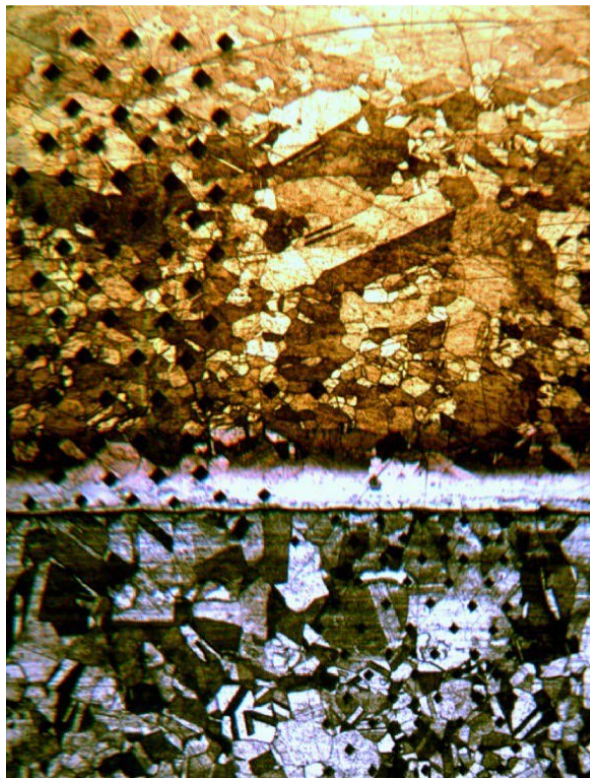


**Fig. 4.** The photo of the CuCrZr/316L(N) bimetallic sample with an intermediate layer in the form of a nickel foil of 50  $\mu\text{m}$  after microhardness testing

In the structure of the base metal of the analyzed samples, no local increase in hardness was detected since the presence of the large hardening phases or a structure deformed due to mechanical hardening was not detected. In turn, it is impossible to carry out the measurements in the zone of the location of the zirconium phase line using a microhardness tester, due to the small size of the phases and their location near the interface of two metals with different hardness.

Figure 5 shows the results of the X-ray spectral analysis (XRSA) of the CuCrZr/316L(N) bimetallic joint along the line across the interface.

For the CuCrZr/316L(N) bimetallic joint without a nickel interlayer (Fig. 5, a), a peak of zirconium concentration is observed on the CuCrZr side near the interface. On the side of 316L(N), there is a slight increase in the concentration of chromium with a decrease in the concentration of nickel. In the work [7], the structural and phase composition of the boundary layer of 316L(N) in the CuCrZr/316L(N) bimetallic joint was analyzed and the presence of  $\delta$ -ferrite and  $\sigma$ -phase was revealed. In the current work, the boundary layer of 316L(N) was not analyzed and more attention is paid to the CuCrZr layer, as the weakest material in the bimetallic joint. For all the variants of the CuCrZr/316L(N) bimetallic joint with a nickel interlayer, a similar peak of the zirconium concentration on the CuCrZr side is observed.

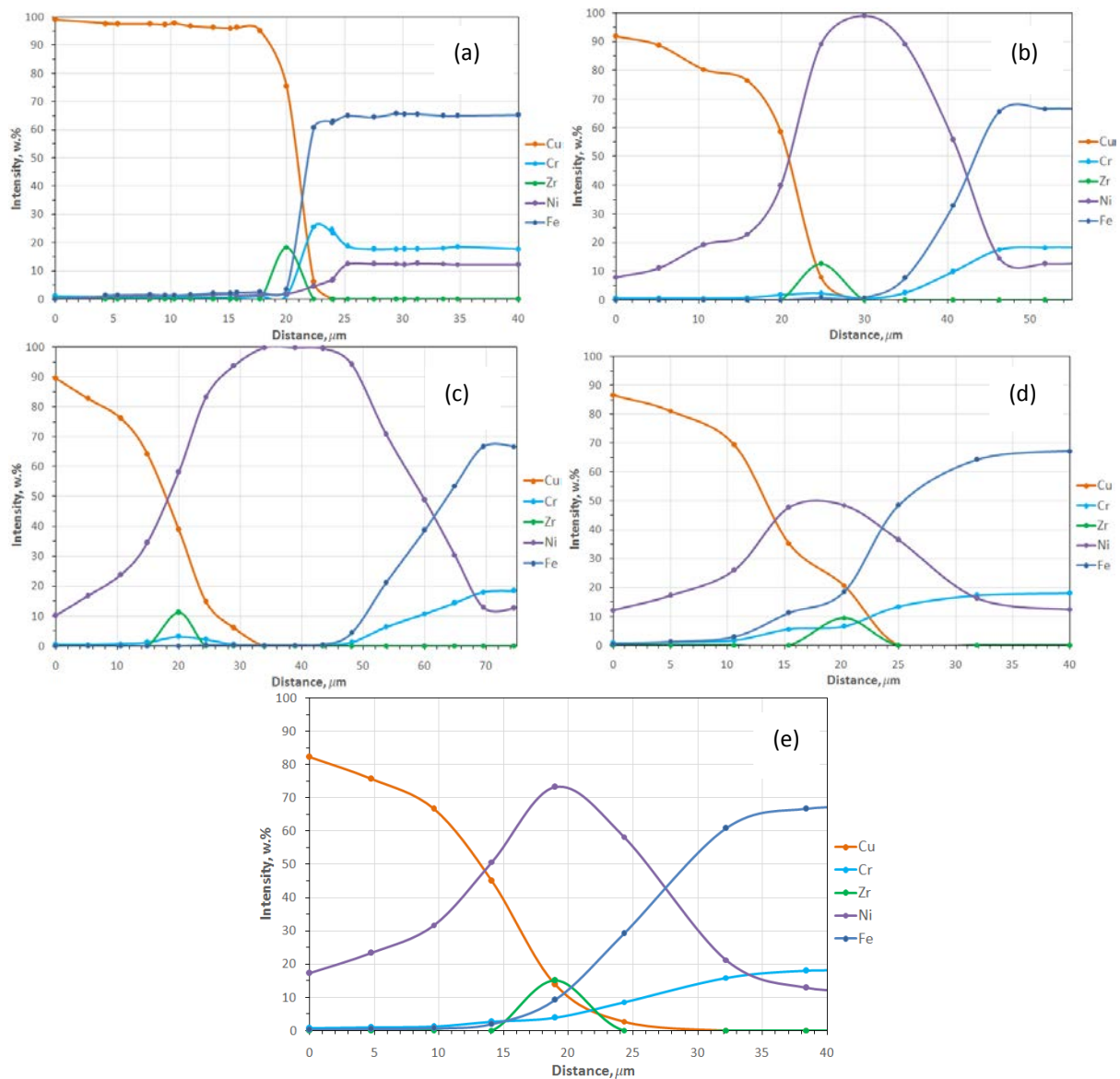


**Fig. 5.** The results of the XRSA of the CuCrZr/316L(N) bimetallic joint: (a) Without an intermediate layer; (b) With an intermediate layer of nickel foil of 25  $\mu\text{m}$ ; (c) With an intermediate layer of nickel foil of 50  $\mu\text{m}$ ; (d) With an intermediate layer in the form of a nickel coating on CuCrZr of 15  $\mu\text{m}$ ; (e) With an intermediate layer in the form of a nickel coating on CuCrZr and 316L(N),  $2 \times 15 \mu\text{m}$

Special attention is paid to the analysis of the chemical composition of the zirconium phases in the bimetallic joint without an interlayer because in the literature there are different hypotheses about their chemical composition: intermetallides, carbides, or nitrides of zirconium [7-9]. The results of the XRSA of the CuCrZr layer with zirconium phases are shown in Fig. 6. There are intersecting peaks of the concentration of zirconium and nitrogen, which gives an opportunity to suggest the chemical composition of the phases as zirconium nitride.

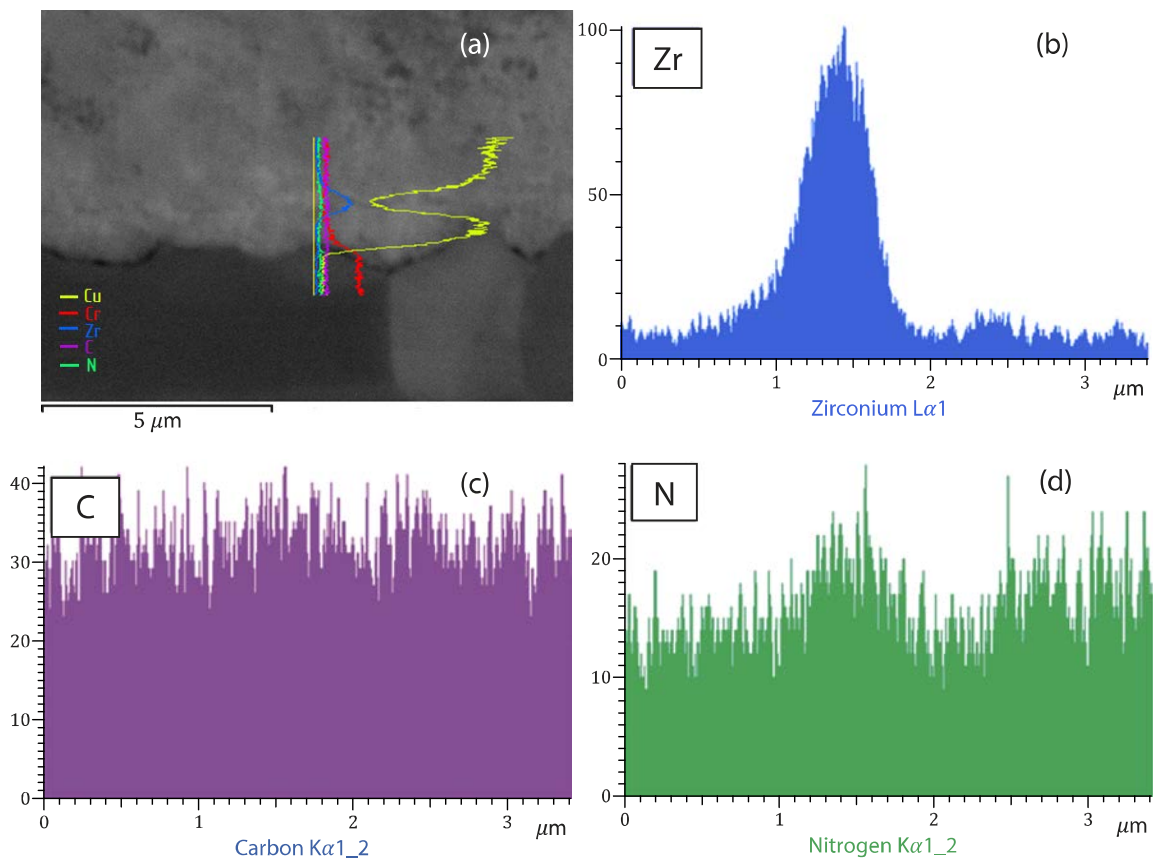


**Fig. 6.** The results of the XRSA of the zirconium phase layer in the CuCrZr/316L(N) bimetallic joint without an interlayer: (a) the concentrations of the main elements; (b) the concentration of Zr; (c) the concentration of C; (d) the concentration of N

Table 2. The results of the analysis of the zirconium phases

CuCrZr/316L (N)		Spectrum №	The elemental composition of the spectrum						The chemical composition of the phase
Without interlayer (Fig. 7, a)	1	Zr, weight. %	N, weight. %	result, weight. %	Zr, at. %	N, at. %	result, at. %	ZrN	
		89,55	10,45	100,00	56,82	43,18	100,00		
With a nickel interlayer in the form of	foil (Fig. 7, b)	-	Zr, weight. %	Ni, weight. %	result, weight. %	Zr, at. %	Ni, at. %	result, at. %	-
		1	27.73	72.27	100.00	19.81	80.19	100.00	Ni <sub>5</sub> Zr
		2	27.68	72.32	100.00	19.76	80.24	100.00	
	3	26.44	73.56	100.00	18.79	81.21	100.00		
	cover (Fig. 7, c)	1	31.18	68.82	100.00	22.58	77.42	100.00	Ni <sub>7</sub> Zr <sub>2</sub>
2		31.67	68.33	100.00	22.98	77.02	100.00		

The micro-XRSA of the individual zirconium phases allowed us to clarify the assumptions about their chemical composition for all analyzed variants of the bimetallic joint. Figure 7 shows the electronic images of the studied phases, and Table 2 shows their elemental composition. The results for both variants with a nickel foil, as well as both variants with a nickel coating, were identical, so they are summarized further. According to Ni-Zr diagram, the chemical composition of the phases of the zirconium nickelides is identified. Table 2 presents the results of the micro-XRSA for all bimetallic joint variants.

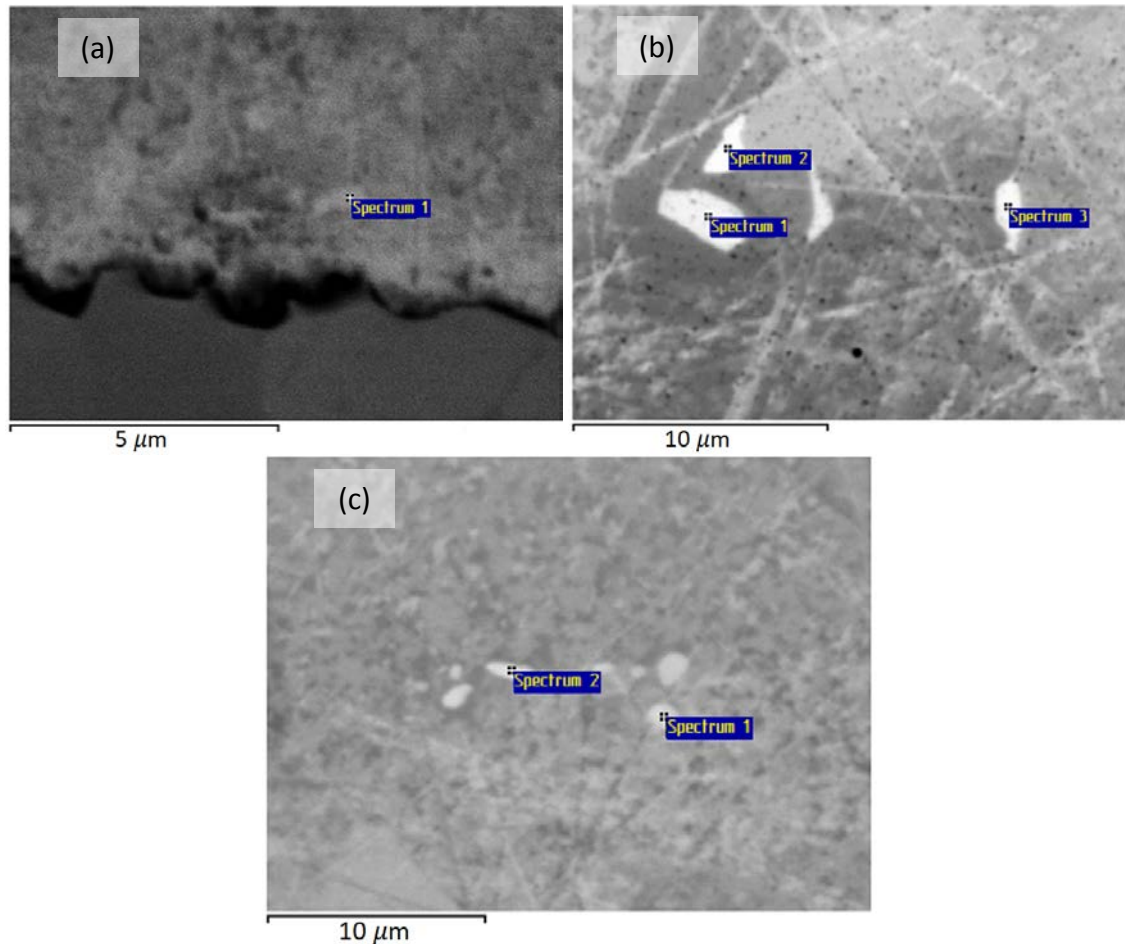


**Fig. 7.** The analysis of the chemical composition of the zirconium phases: (a) the bimetallic joint without an interlayer; (b) the bimetallic joint with a foil interlayer; (c) the bimetallic joint with an interlayer in the form of a coating

In the case, where the nickel foil is used as an interlayer, Ni<sub>5</sub>Zr intermetallic phases are formed in the bimetallic joint zone. In the case of a nickel coating, Ni<sub>7</sub>Zr<sub>2</sub> phases are formed and the location density of phases in the bimetallic zone is higher, which indicates a greater amount of zirconium involved in the formation of this layer. Nickel is initially applied to the surface of CuCrZr in the form of a coating, which leads to a faster interaction with zirconium during the HIP.

The rupture tests of the bimetallic samples were performed at three temperature levels. The test results are presented in Table 3.

Table 3. Test results of bimetallic samples

The type of the bimetallic joint CuCrZr/316L(N)		The test results at a given temperature (averaged)					
		RT		150°C		600°C	
		Rupture stress, MPa	Fracture zone	Rupture stress, MPa	Fracture zone	Rupture stress, MPa	Fracture zone
Without interlayer		431	CuCrZr	367	CuCrZr	115	The bimetallic joint
With the nickel interlayer	Foil with a thickness of 25 $\mu\text{m}$	426	CuCrZr	368	CuCrZr	128	The bimetallic joint
	Foil with a thickness of 50 $\mu\text{m}$	425	CuCrZr	373	CuCrZr	133	The bimetallic joint
	Foil with a thickness of 15 $\mu\text{m}$ on CuCrZr	426	CuCrZr	369	CuCrZr	112	The bimetallic joint
	Foil with a thickness of 15 $\mu\text{m}$ on CuCrZr and 316L(N)	422	CuCrZr	371	CuCrZr	118	The bimetallic joint

The value of the rupture stress for all the variants of the bimetallic joint at room temperature and 150°C differ by no more than 2%, and at 600°C – up to 20%. At the same time, higher values of the rupture stress at elevated temperatures are observed for the variants with an intermediate layer of nickel foil. However, the increased spread of the values at the maximum temperature is probably a consequence of lower test statistics (2-3 samples of each type). The fracture types of the samples for all the bimetallic joint variants are the same: the fracture of the base metal at the temperature of up to 150°C and the fracture of the joint zone at the maximum temperature. For example, the bimetallic samples without the intermediate layer after testing are shown in Fig. 8. Samples with a nickel interlayer have a similar view.



**Fig. 8.** The photos of the bimetallic samples after the rupture tests

The results of the XRSA of the fracture surface on the tested samples at the maximum temperature indicate fracture along with the layer with the inclusions of the zirconium phases: a similar spectrum is observed with an evident zirconium peak on both parts of the tested sample. For example, Fig. 9 shows the analyzed spectrum of the fracture surface of the bimetallic samples with and without nickel interlayer.

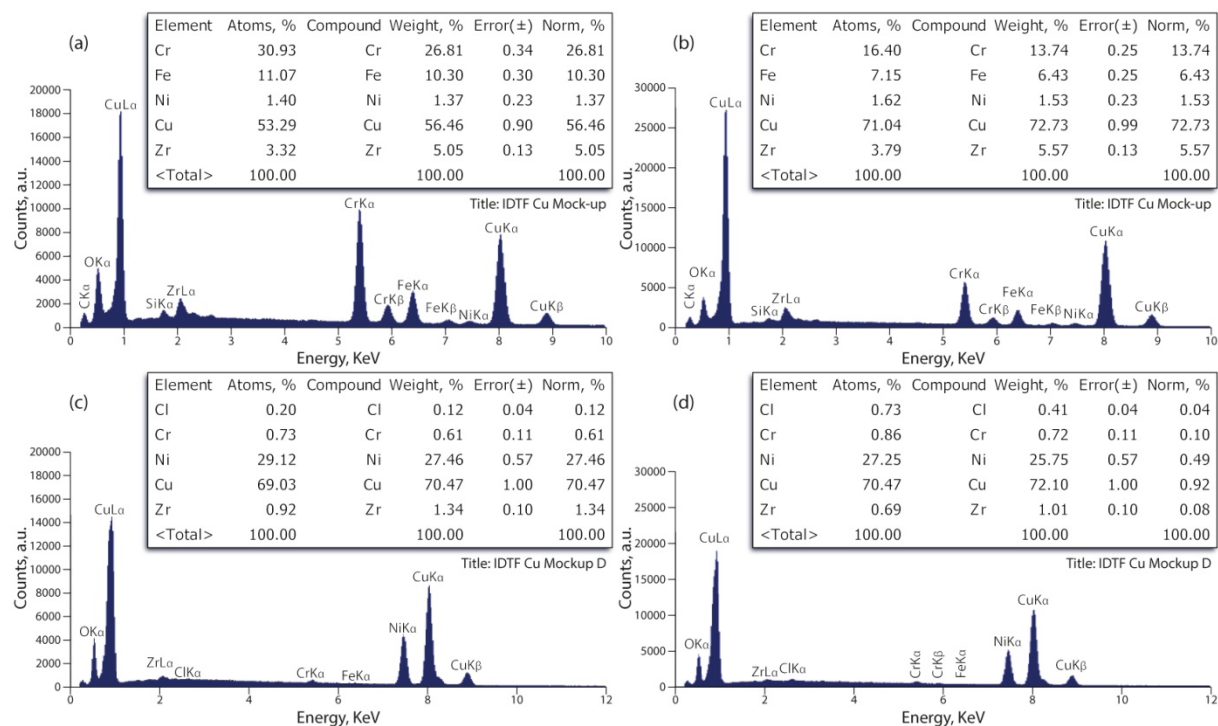


**Fig. 9.** The XRSA of the fracture surface of the bimetallic samples with and without nickel interlayer: (a) the surface of the CuCrZr part of the sample without nickel interlayer; (b) the surface of the 316L(N) part of the sample without nickel interlayer; (c) the surface of the CuCrZr part of the sample with nickel interlayer; (d) the surface of the 316L(N) part of the sample with nickel interlayer

Probably, the fracture of the bimetallic samples and the cases of the destruction of the bimetallic joint in the PFC (as indicated in the introduction) are the results of the same feature. However, unlike the PFC, where all the HT operations are performed in a vacuum, the heating of the bimetallic samples before testing is performed in the atmosphere. Therefore, it is necessary to exclude the influence of the oxidation of the surface of the samples on the feature of the fracture during the rupture tests. For this purpose, two series of additional rupture tests were performed. In the first case, a corrosion-resistant nickel coating was applied to the surface of the bimetallic samples. The thickness of the coating of 30  $\mu\text{m}$  was selected experimentally for specific heating conditions. These samples were tested at a maximum temperature of 600°C. In the second case, the samples were heated before testing in the atmospheric furnace to a target temperature of 600°C and cooled after 0.5 hours of exposure. Further, the samples were tested at room temperature. Both types of samples after the testing are shown in Fig. 10.

Regardless of the presence of surface oxidation during heating, the fracture of the samples during the rupture tests occurred as before: on the bimetallic joint at maximum temperature; on the base metal at room temperature.

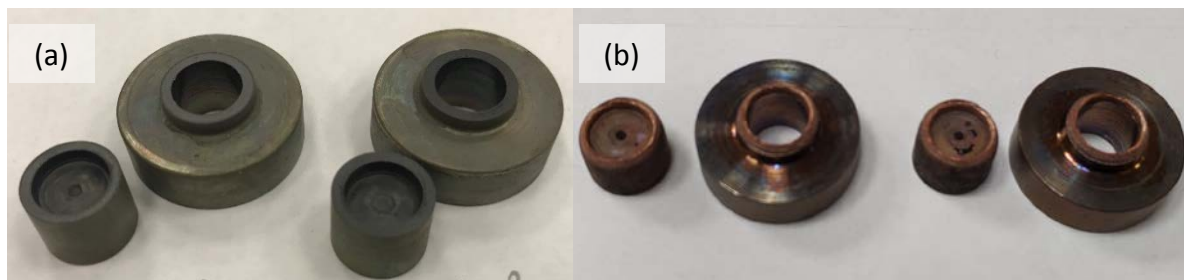


**Fig. 10.** The photos of the bimetallic samples after the additional tests:

(a) sample with corrosion-resistant nickel coating tested at 600°C; (b) sample pre-heated at 600°C and tested at room temperature

#### 4. Discussion of results

The comparative analysis performed by the metallographic methods demonstrates a clear difference between the considered variants of the CuCrZr/316L(N) bimetallic joint with a nickel interlayer and the variant without an interlayer. Instead of an evident layer of zirconium nitrides in the bimetallic joint without an interlayer, invariants with a nickel interlayer, there are separate phases and short lines of zirconium intermetallides. However, these changes in the structure do not significantly affect the analyzed characteristics of the CuCrZr/316L(N) bimetallic joint.

For all the considered variants of the bimetallic joint, the hardness values change more than twice at the interface between CuCrZr and 316L(N) by a "jump" (sharply). Such an interface between two metals with these differences in properties can itself be a stress concentrator that weakens the bimetallic joint, which may be one of the reasons for the destruction of the joint in samples/components. The layer of the zirconium phases also weakens the bimetallic joint. Moreover, the results of the rupture tests of the bimetallic samples demonstrate a clear dependence of the type of fracture of samples on the temperature conditions of the test. With an increase in the temperature, the type of fracture changes from the viscous fracture in the base metal to fracture in the bimetallic joint. Probably, in this case, the influence of the "ductility failure", which is peculiar to most copper alloys, is observed [14]. In a certain range of elevated temperature, the ductility properties of CuCrZr decrease, which, together with the previously mentioned structural features of the CuCrZr/316L(N) bimetallic joint (an interface with a sharp transition of hardness; a layer with zirconium phases), leads to an increase in the stress level in the bimetallic joint of the components/sample and subsequent destruction along the joint. Taking into account all the above, it is impossible to single out and evaluate separately the level of influence of each structural feature of the CuCrZr/316L(N) bimetallic joint on its characteristics without additional research.

Based on the results of the conducted work, we can suggest, that the intermediate layer of nickel, obtained by each of the considered methods does not lead to the significant changes in these features of the bimetallic joint. Although, the value of the microhardness of the nickel layer, which was tested for 50 μm interlayer of foil, was the intermediate value between CuCrZr and 316L(N). Therefore, the nickel interlayer provides a smoother transition of the hardness values in the CuCrZr/316L(N) bimetallic joint. In other works, a positive influence of the nickel interlayer on such characteristics of bimetallic joint as impact strength is noted [12]. Probably, under the dynamic loads, the nickel interlayer of the bimetallic joint performs the role of a "damping" layer. With reference to the current work, it is planned to conduct additional mechanical tests of the CuCrZr/316L(N) bimetallic samples with and without a nickel interlayer, as well as to perform a more detailed study of the previously listed features of this bimetallic joint.

#### 5 Conclusions

The method of optimizing the CuCrZr/316L(N) bimetallic joint by introducing an intermediate layer of nickel does not lead to a significant change in the characteristics of the bimetallic joint, defined as design criteria for the PFC. The nickel interlayer affects the chemical composition of the bimetallic joint, however, it does not completely exclude the formation of brittle phases of zirconium along with the interface. The conducted tests of the bimetallic samples with and without a nickel interlayer demonstrated almost identical results for the compared variants. At the same time, all the bimetallic samples during the tests at the elevated temperature up to  $\sim 600^\circ$  fracture in the bimetallic joint. Probably, the known cases of the destruction of the bimetallic joint in the PFC and the specified cases of the fracture of the bimetallic samples are associated with the same features of the considered bimetallic joint. Therefore, the urgent task is to conduct further studies of the features of the CuCrZr/316L(N) bimetallic joint and find out the decision for its optimization.

## References

- [1] Raffray AR, Nygren R, Whyte DG, Abdel-Khalik S, Doerner R, Escourbiac F, Evans T, Goldston RJ, Hoelzer DT, Konishi S, Lorenzetto P, Merola M, Neu R, Norajitra P, Pitts RA, Rieth M, Roedig M, Roglien T, Suzuki S, Tillack MS, Wong C. High heat flux components—Readiness to proceed from near term fusion systems to power plants. *Fusion Engineering and Design*. 2010;85(1): 93-108.
- [2] Gervash AA, Giniyatulin RN, Guryeva TM, Glazunov DA, Kuznetsov VE, Mazul IV, Ogursky AY, Piskarev PY, Safronov VM, Eaton R, Raffray R, Sevryukov ON. The development of technology of Be/CuCrZr joining using induction brazing. *Fusion Engineering and Design*. 2019;146: 2292-2296.
- [3] Gervash AA, Glazunov DA, Lyanzberg DV, Mazul IV, Ogursky AY, Piskarev PY, Ruzanov VV. Refinement of the technology of hot isostatic pressing of vacuum-tight bimetallic joint of ITER in-Vessel components. In: *Innovative Designs and Technologies of Nuclear Power: Collection of papers of V International Scientific and Technical Conference*. Moscow: Publishing House of JSC "NIKIET"; 2018. p.2428-2434.
- [4] Xu JF, Yang M, Ma HH, et al. Fabrication and performance studies on explosively welded CuCrZr/316L bimetallic plate applied in extreme environments. *Journal of Materials Research and Technology*. 2020;9(4): 8971-8984.
- [5] Gonzalez JM, Chiumenti M, Cervera M, Agelet de Saracibar C, Samaniego F, Cobo I. Numerical analysis of the manufacturing processes of a mock-up of the ITER NHF First Wall Panel. *Fusion Engineering and Design*. 2018;135: 65-73.
- [6] Piskarev PY, Gervash AA, Ogursky AY, Mazul IV, Ruzanov VV, Bobrov SV, Khokholov MV, Lyanzberg DV. Formation of brittle layers during hot isostatic pressing of bimetal joints of ITER components. In: *46th International Conference on Plasma Physics and CF*. Zvenigorod; 2019. p.259.
- [7] Piskarev PY, Gervash AA, Vologzhanina SA, Ermakov BS. Analysis of the Destruction of a diffusion bimetallic compound CuCrZr-IG / 316L(N)-IG obtained under hot isostatic pressing. In: *International symposium 'Nanophysics and Nanomaterials*. St. Petersburg: Saint-Petersburg Mining University; 2020. p.258-264.
- [8] Goods SH, Puskar JD. Solid state bonding of CuCrZr to 316L stainless steel for ITER applications. *Fusion Engineering and Design*. 2011;86: 1634-1638.
- [9] Ordas N, Samaniego F, Iturriza I, Gomez A, Escudero C, Fernandez-Calvo AI, Cobo I, Banetta S, Heikkinen S, Cicero T. Mechanical and microstructural characterization of HIP joints of a simplified prototype of the ITER NHF First Wall Panel. *Fusion Engineering and Design*. 2017;124: 999-1003.
- [10] Marois GLe, Dellis Ch, Gentzittel JM, Moret F. HIP'ing of copper alloys to stainless steel. *Journal of Nuclear Materials*. 1996;233-237: 927-931.

- [11] Singh KP, Alpesh Patel, Kedar Bhope, Khirwadkar SS, Mayur Mehta. Optimization of the diffusion bonding parameters for SS316L/CuCrZr with and without Nickel interlayer. *Fusion Engineering and Design*. 2016;112: 274-282.
- [12] Wei R, Zhao SX, Dong H, Che HY, Li Q, Wang WJ, Wang JC, Wang XL, Sun ZX, Luo GN. Enhancing the CuCrZr/316L HIP-joint by Ni electroplating. *Fusion Engineering and Design*. 2017;117: 58-62.
- [13] Mayo Diaz MA, Gustavo ME. Effect of Solution Treatment in CuCrZr Alloy Structure. *AASCIT Journal of Materials*. 2017;3(3): 14-18.
- [14] Laporte V, Mortensen A. Intermediate temperature embrittlement of copper alloys. *International Materials Reviews*. 2009;54(2): 94-116.

## THE AUTHORS

### **Piskarev P.Y.**

e-mail: piskarev@sintez.niiefa.spb.su

ORCID: 0000-0002-8551-9594

### **Gervash A.**

e-mail: gervash@sintez.niiefa.spb.su

ORCID: 0000-0002-5376-3787

### **Bobrov S.**

e-mail: bobrov@sintez.niiefa.spb.su

ORCID:

### **Ruzanov V.**

e-mail: ruzanov@sintez.niiefa.spb.su

ORCID: 0000-0002-3343-1769

### **Ogurski A.**

e-mail: ogursky@sintez.niiefa.spb.su

ORCID: 0000-0001-8274-4852

### **Mazul I.**

e-mail: mazul@niiefa.spb.su

ORCID: 0000-0001-9381-1600

### **Giniyatulin R.**

e-mail: radmir.giniyatulin@iter.org

ORCID: 0000-0002-4067-5374

### **Ermakov B.**

e-mail: ermakov\_bs@spbstu.ru

ORCID:

### **Sevryukov O.**

e-mail: sevr54@mail.ru

ORCID: 0000-0002-8711-8962

## EXPERIMENTAL STUDY OF DUCTILE AND FRAGILE PIPE CRACKED IN HIGH-DENSITY POLYETHYLENE (HDPE)

Azzeddine Belaziz<sup>1✉</sup>, Mohamed Mazari<sup>2</sup>, Mohammed Bouamama<sup>1</sup>, Samir Zahaf<sup>3</sup>,  
Dahmane Mouloud<sup>4</sup>

<sup>1</sup>Mechanics Research Center (CRM), BP N73B, Ain El Bey, 25021 Constantine, Algeria

<sup>2</sup>Laboratory of Materials and Reactive Systems (LMSR), Mechanical Engineering Department, Faculty of  
Technology, University of Sidi Bel Abbas, 22000, Sidi Bel Abbe, Algeria

<sup>3</sup>Department of Technology, University of Djilali Bounaama-Khamis Meliana, Road Théniet El had, 44225,  
Algeria

<sup>4</sup>LMA, Mechanical Engineering Department, USTO-MB, BP 1055 El Menaour, 31000, Oran, Algeria

✉ belaziz2013@gmail.com

**Abstract.** In this paper the experimental study of the fragility, ductility fracture and the mechanical behavior of high-density polyethylene pipe cracked is subject with know the damage law taken account of the deformation velocity which related to the cracking speed. The ductile fracture of HDPE pipes is characterized by a short crack that propagates rapidly perpendicular to the direction of stretching. The tests were carried out on different specimens cracked and uncracked taken from high density polyethylene (HDPE). The main aim of this study is studied the damage and material HDPE with two cases cracked and uncracked specimens of HDPE and knowing the physical quantities and the understanding of the effect of the deformation velocity on the mechanical behavior.

**Keywords:** density polyethylene (HDPE) pipes, ductile fracture, characteristics, damage, fragility, tensile test, crack, propagation

**Acknowledgements.** *No external funding was received for this study.*

**Citation:** Belaziz A, Mazari M, Bouamama M, Zahaf S, Mouloud D. Experimental study of ductile and fragile pipe cracked in High-Density Polyethylene (HDPE). *Materials Physics and Mechanics*. 2022;48(2): 199-207. DOI: 10.18149/MPM.4822022\_5.

### 1. Introduction

Drinking water distribution has taken a great evolution. It is carried out using pipes made of thermoplastic material, such as high density polyethylene (HDPE) [1-3]. The drinking water distribution over a long distance by HDPE tubes requires the knowledge of the distributed water flow and the conditions on the ground to ensure good distribution and avoid leakage faults (Fig. 1). Generally, these leaks are the cause of poor removal of drinking water from the pipes. In this context, scientific research becomes necessary to identify the mechanical behavior of the material (HDPE).

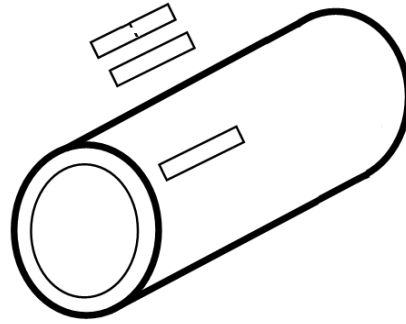


**Fig. 1.** Rotation sampling of the test tube

Many studies can be found in the literature on the subject of the brittle ductile in HDPE pipes [4,5]. Moreover, other researchers [6,7] investigated the crack and fracture properties of HDPE.

Mizera et al. [8] analysed the influence of process parameters change on mechanical properties of the surface layer of HDPE product, characterised by its hardness. Andreas Frank et al. [9] demonstrates the potential of the cyclic CRB test not only for a standardized quick material ranking by SCG resistance, but also for fracture mechanics based lifetime prediction of modern polyethylene (PE) pipe grades. [10] The Craze branching in thermoplastic material such as HDPE with an inhomogeneous microstructure may therefore increase the toughness. The interpenetration of molten chains leads to entanglement phenomenon, for any chain longer than a molar mass critical [11].

The dislocations which have been observed on monocrystals are mainly located in the crystallographic planes containing the chains [12,13].

The plastic zone is given by "stress whitening" which is caused by density fluctuations, probably due to crazing and voiding processes [14].

In thermoplastic material, Lee et al. [15] have shown experimentally that the increase in fracture toughness of many engineering polymers derives from the formation of multiple crazes at crack tips.

The study aim concerns the identification and the study of the behavior (fragile and ductile) of thermoplastic and high density polyethylene tubes cracked under internal pressure to obtain the true mechanical behavior in real working conditions and to solve the rupture problem which usually occurs at the wall outer surface.

Butler et al., Aboulfaraj et al. [16-19] have examined the microscopic structure and the plastic deformation processes of HDPE thin films.

## **2. Experimental work**

In this study, in order to determine the behavior law of the two cracked and non-cracked structures, an experimental study based on mechanical tests under static loading is conducted. Series of tests are studied to characterize the material, followed by tests of mechanical analysis of the resistance of the different deformation rates.

## **3. Study material**

The study material is a thermoplastic material with a complex viscoelastic-viscoplastic behavior and good corrosion resistance, called high density polyethylene (HDPE).

The used material was manufactured over time in the form of granules imported by the company STPM CHIALI located in Sidi Bel Abbes (ALGERIA) [20]. It was then extruded to make tubes of different diameters. The extrusion conditions are determined in order to guarantee the most homogeneous cooling possible. This material is designed to work at a

pressure of 4 bars. The technical, physical and chemical specifications of the material are grouped in Table 1.

Table 1. Parameters and characteristics of HDPE

Density	930 kg/m <sup>3</sup>
Molecular weight ( $M_w$ )	310,000 (g/mol)
Crystallinity rate ( $X_c$ )	74%
Fusion temperature ( $T_f$ )	203°C
Fluidity index	0.2–1; 4 g/10 (min)
Black carbon	2–2.5%

In this study, the tensile test pieces made of HDPE (Figure1) were taken from a tube with a diameter of 315 mm, 28.2 mm thick and 300 mm long. Two tests were carried for each case and for the same drawing speeds ( $V_e = 10$  and 50 mm / min). The temperature of all tests was equal to ambient one ( $T_a \approx 23$  °C).

**Tensile Test.** In this study, the experimental tensile tests are tests which enable the damaged tubes identification and classify the degradation of the used HDPE. In the literature, several works have confirmed the efficiency and the adequacy of the cracking technique for studying the ductility and brittleness of the tubes and have demonstrated that the use of tensile tests makes it possible to reproduce stresses close to reality.

To characterize the material mechanical behaviour and to study the damaged tube degradation, tensile tests are used on flat-shaped test pieces (Fig. 2).

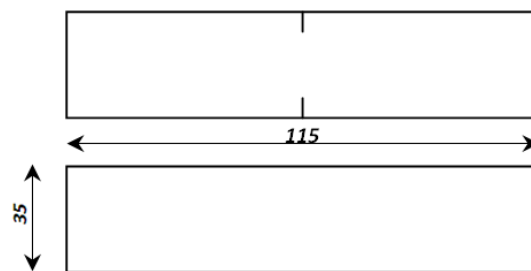


Fig. 2. Geometry of flat specimens (mm)

The tensile tests on this type of test piece were carried out using a servo-hydraulic fatigue machine of the INSTRON 8516 type with a capacity of 100 KN [21]. This machine makes it possible to impose uniaxial forces to measure the displacement of the machine jaws and the load applied at a maximum frequency of 50 Hz.

Cracking tests on flat test specimens were carried out at the Reactive Materials and Systems Laboratory (LMSR) of Sidi Bel Abbes University. To carry out the experimental tests, a longitudinal crack on the flat specimens was created and in this case, a double crack whose ratio  $a/t = 0.08$  and  $a/t = 0.16$  was chosen.

**Hardness Test.** The hardness measurement procedure on thermoplastic material is much simpler than other materials. The shore D hardness measurement gives us a first evaluation of the mechanical properties of the material. By this technique, we drew a straight line along the test surface. The hardness shore D tests specimens are prepared by cutting several slabs from the pipe in the longitudinal direction. The hardness shore D procedure is far simpler than the others.

The hardness shore D tests were carried out according to ASTM standard D2240-00 [22] by a shore D durometer set on a milling machine. The indenter is moved into the test

material under a preliminary distance from 2.5 mm; this distance is set according to the ASTM standard D2240-00 (Fig. 3).

In this part, the hardness measurement at the top of a crack with  $a/t = 0.08$  and  $a/t = 0.16$  is generally defined as the resistance of a material. The hardness measurement gives us a first assessment of the mechanical properties. It is used to take the existence of the anelastic zone (ZB) which surrounds the plastic zone (ZA) at the end of the crack (Fig. 4).

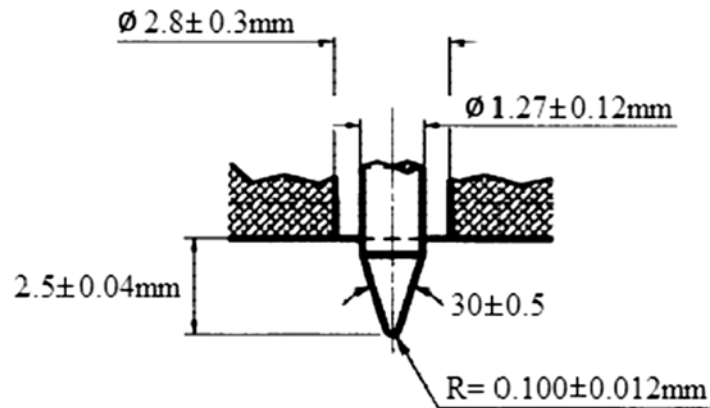


**Fig. 3.** Hardness shore D indentation and measurement

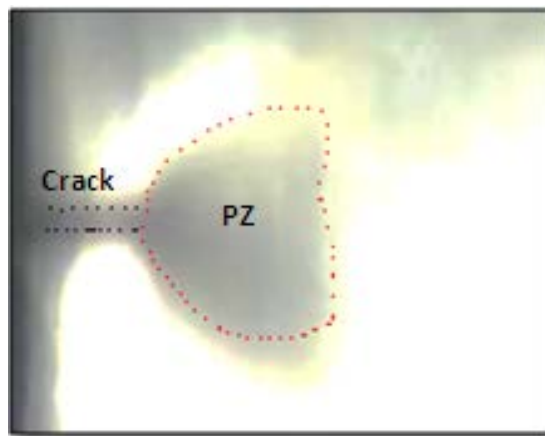


**Fig. 4.** Plastic zone (ZP) illustration at the crack end

#### 4. Results and Discussion

**Tensile test results.** The obtained results from tensile tests for different strain rates are shown graphically in Fig. 5. It can be seen that the general shape of the stress-strain curves is characterized by four main areas: an elastic behaviour at low deformations following a plastic deformation then, a structural hardening due to the reorganization of the chains in the stress direction and finally a significant hardening before the final break.

It is also observed that there is a very significant drop in the elongation value at the break for a deformation speed of 50 mm / min. It is noted that there is a good correlation of the elastic part and that there is a material hardening of at the speed of 10 mm / min.

Also, the material is ductile at high stress for the movement speed of 10 mm / min and with a strain at break equal to 120 mm. For the movement speed of 50 mm / min, the material has a brittle character for which the lifetime is much less sensitive to stress since the deformation at break is of de 40 mm.

According to the stress strain curves (Fig. 6) for the cracked specimens, it can be seen that the study HDPE presents a significant increase in the flow stress with the strain rate, depending on the Young's modulus. HDPE exhibits fragile behaviour at high deformation rates.

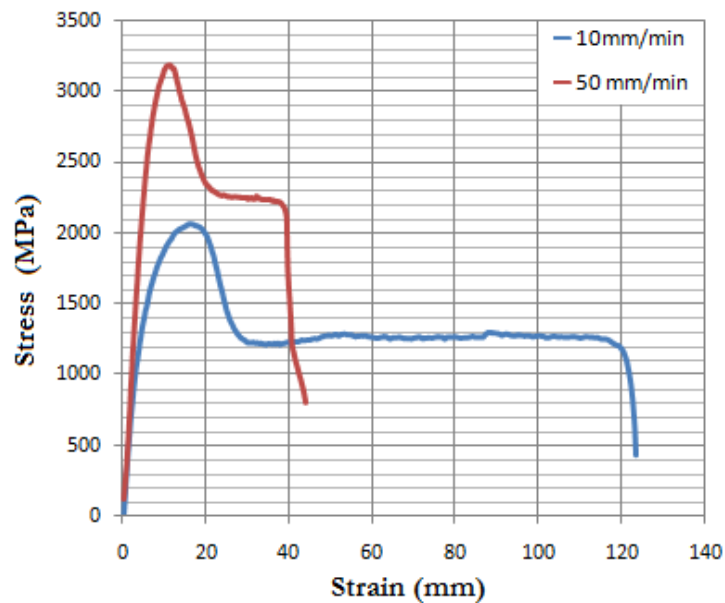


**Fig. 5.** Stress-Strain curve of test pieces without cracking

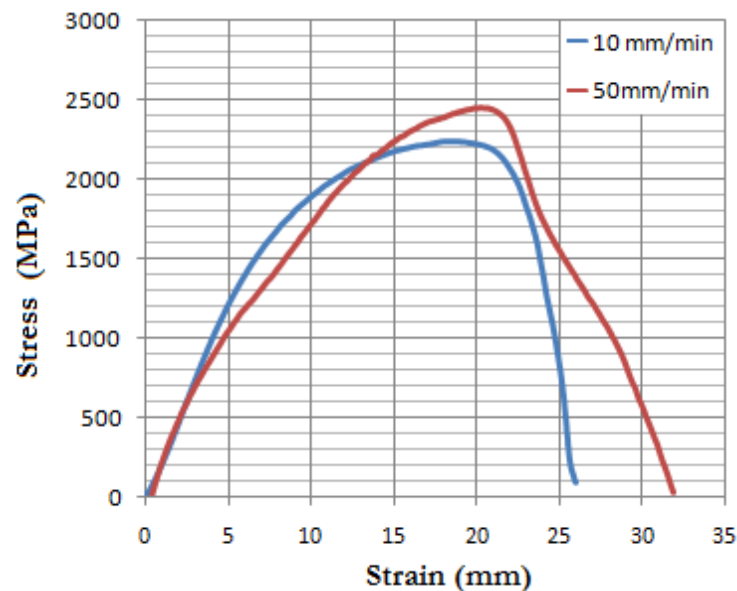


**Fig. 6.** Stress-Strain curve of test pieces with crack. ( $a/t = 0.16$ ).

The fragility revealed by a low elongation value at the break corresponds to the undulation of the internal wall of the tube between the zones.

In multiphase polymers, the value of Young's Modulus is generally lower than the matrix polymer if the second-phase particles are rubbery, but higher if rigid and well-bonded [23].

Figure 7 illustrates the deformation stages of the HDPE tensile test specimen, for no-crack, double-crack and post-break. A HDPE specimen is tested in a mechanical test bench. Figure 8 shows the deformation of the specimen during the test. A neck forms and then propagates through the parallel section of the sample. Then it moves to the supports and a second neck is in the parallel section is created. Eventually, the specimen breaks. Large deformation tensile test with HDPE specimen.

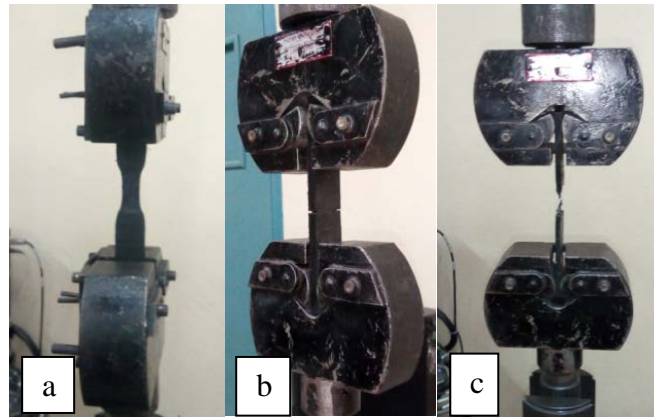


**Fig. 7.** Tensile specimens. a) Without crack; b) Double crack; c) After rupture

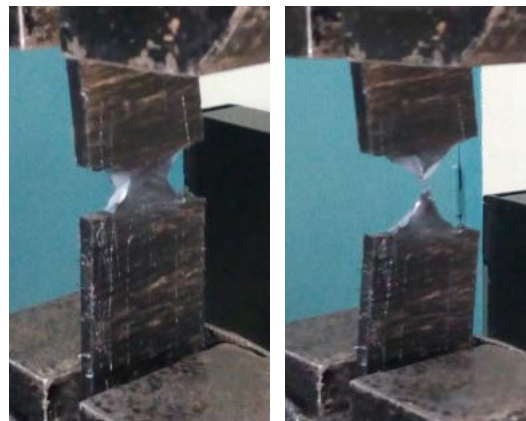


**Fig. 8.** Rotation Test pieces during the test

**Hardness Test Results.** The plastic zone (ZP) microstructure plays an important role in determining the mechanical properties. The mechanical properties of the polyethylene used depend on the crystallinity, density and morphology of the molecules. Figure 9 shows the illustration of the plastic zone (ZP) at the crack end. To see the influence of the hardness on the plastic zone (ZP), one measures the hardness for a value of radius ( $r = 0$ ) of the crack end, with constant measurement steps ( $P$ ) of 0.5 mm (Fig. 9).

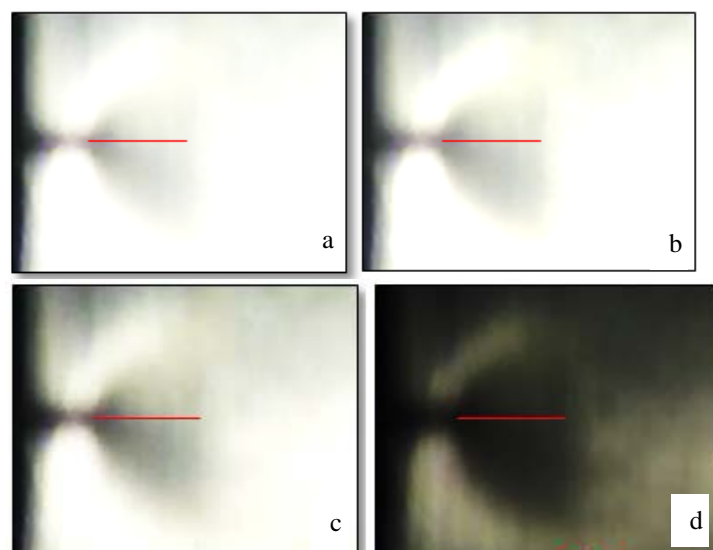


**Fig. 9.** Illustration of the plastic zone (ZP) at the end of the crack. (a and b with  $a/t = 0.08$ ), (c and d with  $a/t = 0.16$ )

Table 2. Results of the hardness of the plastic zone (ZP). ( $a/t=0.16$ )

Step (mm)	0.50	1.00	1.50	2.00
Hardness (Sh D)	56.00	54.50	54.00	53.00

The hardness evolution for the different step values (P) is illustrated in Fig. 10. For a short crack  $a/t = 0.08$ , the hardness presence in the plastic zone leads to a small increase in the stress intensity factor compared to a short crack  $a/t = 0.16$ . This increase is the result of the stress concentration in the notch where the crack begins.

In addition, the stress intensity factor also decreases with the crack advancement according to the test piece thickness.

It can be seen that the stress concentration in the plastic zone has a significant impact. The change in material properties in the plastic zone is mainly caused by changes in crystallinity.

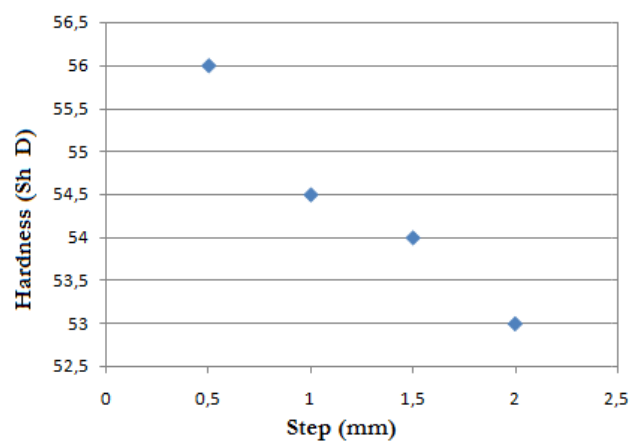


Fig. 10. Illustration of the hardness evolution for the different step values (P)

## 5. Conclusion

The work carried out in this study aims to first know the mechanical behaviour of the damaged pipe. This kind of pipes is widely used in an industrial sector in Algeria for different working conditions and to perform numerical simulation. Thus, complete mechanical, thermal and structural analyses were carried out with regard to thermal phenomena occurring during and after the process.

Thus, complete mechanical analyses were carried out with regard to cracking phenomena and to understand the mechanisms which intervene during cracking and the relationships which exist between the microstructure (hardness) and the mechanical properties in the plastic zone, a set of mechanical tests were carried out on HDPE tubes.

The results presented experimentally allow concluding that the deformation and cracking mechanisms are mainly governed by the different deformation rates.

1. The study material presents a good behaviour for a low strain rate. This made it possible to obtain consolidated materials having good mechanical properties due to the stress intensity factor.

2. The hardness in the plastic zone (ZP) increases as a function of the enlargement of the plasticity zone.

The ductile and fragile behaviour of a material reflects the degree of plastic deformation it is capable of suffering before its final fracture.

## References

- [1] Wunderlich B. *Macromolecular Physics, crystal melting*. NY: Academic Press; 1980.
- [2] Schultz JM. Microstructural aspects of failure in semicrystalline polymers. *Polymer Engineering and Science*. 1984;24(10): 770-785.
- [3] Tabish W, Syed AQP, Sanskar P, Balaji HV. A Review on the use of High Density Polyethylene (HDPE) in Concrete Mixture. *IJERT*. 2020;09(05): IJERTV9IS050569.
- [4] Savini G, Oréface RL. Super ductility in HDPE/EVA blends triggered by synthetic amorphous nanotalc. *Journal of Polymer Research*. 2021;28(1): 1-17.
- [5] Wang D, Li F, Xu X, Zhong L, Guan C, Gao Y, Liang H. Brittle ductile transition of POE toughened HDPE and its lowest rigidity loss: effect of HDPE molecular weight. *Journal of Polymer Research*. 2022;29(2): 1-8.
- [6] Liamani S, Abderahmane S. Modeling the Repair of a Crack in an HDPE Pipe. *Periodica Polytechnica Mechanical Engineering*. 2021;65(2): 134-140.
- [7] Arora G, Pathak H. Experimental and numerical approach to study mechanical and fracture properties of high-density polyethylene carbon nanotubes composite. *Materials Today Communications*. 2020;22: 100829.
- [8] Mizera A, Fiala T, Manas M, Stoklásek P, Ovsik M. Influence of Injection Moulding Process Parameters on High-Density Polyethylene Surface Hardness. *Materials Science Forum*. 2020;994: 189-196.
- [9] Frank A, Berger IJ, Arbeiter F, Hutař P, Pinter G. Lifetime Prediction Of Pe100 And Pe100-Rc Pipes Based On Slow Crack Growth Resistance. In: *Proceedings of the 18th Plastic Pipes Conference PPXVIII, September 2016, Berlin, Germany*. 2016. p.12-14.
- [10] Houari T, Benguediab M, Belaziz A, Belhamiani M, Aid A. Fracture toughness characterization of high-density polyethylene using essential work of Fracture Concept. *Journal of Failure Analysis and Prevention*. 2020;20(1): 315-322.
- [11] Verdu J. *Physique des polymères à l'état fondu*. 2005.
- [12] Holland VF. Dislocations in polyethylene single crystals. *J. Appl. Phys.* 1964;35: 3235-3241.
- [13] Holland VF, Lindenmeyer PH. Direct observation networks in folded-chain crystals of polyethylene. *J. Appl. Phys.* 1965;36: 3049-3056.
- [14] Hernandez M, Santana OO, Ichazo MN, Gonzalez J, Albano C. Fracture behavior at low strain rate of dynamically and statically vulcanized polypropylene/styrene-butadiene-styrene block copolymer blends. *Polymer Testing*. 2008;27: 881-885.
- [15] Lee LH, Mandell JF, McGarry FJ. Fracture toughness and crack instability in tough polymers under plane strain conditions. *Polym. Engng. Sci.* 1987;27: 1128-1136.
- [16] Butler MF, Donald AM. Deformation of spherulitic polyethylene thin film. *J. Mater. Sci.* 1997;32: 3675-3685.
- [17] Butler MF, Donald AM, Ryan AJ. Time resolved simultaneous small and wideangle X-ray scattering during polyethylene deformation-II. Cold drawing of linear polyethylene. *Polymer*. 1998;39: 39-52.
- [18] Aboulfaraj M, G'sell C, Ulrich B, Dahoun A. In situ observation of plastic deformation of polypropylene spherulites under uniaxial tension and simple shear in the scanning electron microscope. *Polymer*. 1995;36: 731-742.
- [19] Belaziz A, Mazari M, Brahami R. Thermo-Mechanical Behavior Of The Bead Weld Of High-Density Polyethylene (Hdpe) Pipes. *Materials Physics and Mechanics*. 2021;47(4): 621-632.
- [20] Azzeddine B, Mazari M. Experimental Study of the Weld Bead Zones of a High-Density Polyethylene Pipe (HDPE). *Journal of Failure Analysis and Prevention*. 2018;18(2): 1-12.

[21] *Laboratoire de Matériaux et systèmes réactifs (LMSR)*. Available from : <https://lmsr-univ-sbadz.fr.gd> [Accessed 11th April 2022].

[22] ASTM D2240. *Standard Test Method for Rubber Property—Durometer Hardness*. 2015.

[23] Kinloch AJ, Young RJ. *Fracture Behaviour of Polymers*. Applied Science Publishers Ltd; 1983.

## THE AUTHORS

### **Azzeddine Belaziz**

e-mail: belaziz2013@gmail.com

ORCID: 0000-0002-4737-753X

### **Mohamed Mazari**

e-mail: mazarim57@gmail.com

ORCID: 0000-0001-9807-8559

### **Mohammed Bouamama**

e-mail: bouamamamohameddoc@gmail.com

ORCID: 0000-0003-1804-9091

### **Samir Zahaf**

e-mail: zahafsamir1983@gmail.com

ORCID: 0000-0003-3210-3445

### **Dahmane Mouloud**

e-mail: dahmanemoul@gmail.com

ORCID: 0000-0002-8510-353X

## UNSTABLE PLASTIC FLOW IN STRUCTURAL MATERIALS: TIME SERIES FOR ANALYSIS OF EXPERIMENTAL DATA

Vladislav K. Kazankov<sup>1</sup>, Anna G. Shmeleva<sup>2</sup>, Ekaterina V. Zaitseva<sup>1</sup>✉

<sup>1</sup>ITMO University – Kronverksky Prospekt 49, bldg. A, Saint Petersburg, 197101, Russia

<sup>2</sup>MIREA – Russian Technological University, 78 Vernadsky Avenue, Moscow 119454, Russia

✉ [zaytskaterina@gmail.com](mailto:zaytskaterina@gmail.com)

**Abstract.** The present study provides the mathematical description of changing metals characteristics during exploitation, as well as identifies behaviors and features during plastic deformation. Modern experimental facilities allow conducting a full-scale experiment, recording the effects observed, determining the patterns of materials behavior of and their alloys to predict the occurrence of unstable plastic flow. The arrays of experimental data obtained in the format of discrete values were processed with the wave-record method for the data interpolation and normalization. The results' comparison enabled to determine the class of materials with similar patterns of deformational plastic behavior. That allowed us to describe the patterns of irreversible deformations and their nature to formulate the postulates for the theory of plasticity, materials science, and prediction of complex systems' behavior. The paper presents the results of experimental studies of plastic deformation of aluminum alloy samples to determine the characteristics of unstable plastic flow in the material. The analysis of the obtained data for the samples confirmed the presence of the Portevin-Le Chatelier effect. Based on the experimental results, deformation diagrams and time series were developed, and the data correlation for the samples was also confirmed. The wave process that occurs in the material during stretching correlates hydrodynamic with the occurrence of rogue waves. It is important to note that when analyzing the time series of experimental data for aluminum alloys, a pattern of correspondence with time series in the analysis of rogue waves was noted.

**Keywords:** Portevin-Le Chatelier effect, aluminum alloys, deformation diagrams, plasticity, time series, rogue waves

**Acknowledgements.** *No external funding has been received for this study.*

**Citation:** Kazankov VK, Shmeleva AG, Zaitseva EV. Unstable plastic flow in structural materials: time series for analysis of experimental data. *Materials Physics and Mechanics*. 2022;48(2): 208-216. DOI: 10.18149/MPM.4822022\_6.

### 1. Introduction

Aluminum and its alloys are used in industry due to their lightness, corrosion resistance, and malleability to stamping. However, aluminum alloys exhibit plastic flow instability, known as the Portevin-Le Chatelier effect. For practical purposes, this effect causes the localization of dislocations and appearance of deformation bands such as Chernov-Luders bands [1]. This effect results in material structure violation and surface roughness appearance. As metals and alloys are widely used in the food, pharmaceutical, and automotive industries, where any

irregularities on the surface are unacceptable, the issue of determining the boundaries separating the areas of stable and unstable plastic flow is acute.

The Portevin-Le Chatelier effect influences most properties of materials. It increases the yield stress, the tensile strength, and the hardening rate of materials. Therefore, the ductility of metals reduces with a corresponding elongation, which decreases the effective cross-sectional area. Alloys under load become susceptible to service failures because of a decrease in viscosity [2,3]. The combination of negative qualities caused by the Portevin-Le Chatelier effect with environmental factors weakening the material leads to early wear of the material. Further embrittlement of the material may be caused by the presence of hydrogen in gaseous and aqueous media, which accelerate corrosion processes, or by physical contact of the bearing materials with other materials, which leads to localized corrosion. Thus, for structural materials, the detection of susceptibility to the Portevin-Le Chatelier effect is one of the key tasks.

The Portevin-Le Chatelier effect is worth both experimental study and theoretical analysis, as well as establishing the stability loss criterion for plastic deformation and determining the instability area [4]. However, the Portevin-Le Chatelier effect has not been sufficiently studied experimentally, despite its broad theoretical basis and widespread use of alloys in industry. As part of this work, we studied the behavior of metals and alloys characteristics by conducting an experiment on the rupture of parts and considering the results obtained. The purpose of this work is to demonstrate a method for analyzing the dynamics of material rupture through the interpretation of experimental data in the time series format. The authors propose to investigate time series in a similar way to the methods of studying hydrodynamic processes of rogue waves.

Rogue waves occur in various physical processes. In addition to the direct appearance of waves in the ocean [5] and in laboratory experiments, they occur in optical systems [6], as well as in plasma physics, condensed matter physics and Bose-Einstein condensate [7,8]. Such a frequent occurrence of rogue waves in various physical systems suggests that the set of processes containing them may be wider. For example, researchers observe the occurrence of similar processes in materials science, in metamaterials [9,10]. In this paper, it is proposed to begin studying the properties of materials using the methodology of the study of rogue waves.

## 2. Methodology

To study the effect of Portevin-Le Chatelier, metal parts were subjected to rupture on the installation. In the experiment, flat samples of a carbonized aluminum alloy with impurity content of no more than 0.5 percent were used. Sample parameters: length 0.12 m, width 0.015 m, thickness 0.003 m. The maximum size deviation is  $\pm 0.0006$  m. The appearance of the parts is shown in Figure 1. To study the effect of Portevin-Le Chatelier, metal parts were subjected to rupture on the installation. In the experiment, flat samples of a carbonized aluminum alloy with impurity content of no more than 0.5 percent were used. The appearance of the parts is shown in Fig. 1.

Each of the aluminum samples was subjected to rupture at the installation with the highest limit load of 5 kN and a measurement range of 0.3-5 kN. During the experiment, the internal stress of the sample and its stretching were recorded. Stretching was carried out at a constant speed (0.000018 m/s), so the time of the experiment turned out to be linearly dependent on stretching. This approach allows us to consider the relationship between the stretching of the sample and the internal stress through time series.

Figure 2 provides the visualization of the experimental results for one of the aluminum alloy samples. The dataset with experimental data is shown in [10].



**Fig. 1.** Samples

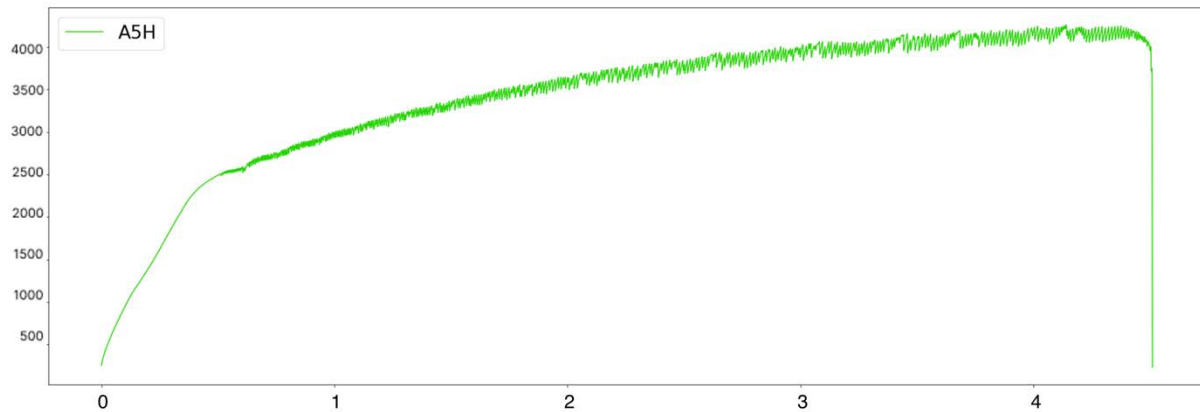


**Fig. 2.** The dependence of the stress on the stretching of the samples. The y-axis is the tension in kN, the x-axis is the time in seconds

Preprocessing of experimental data for all aluminum samples consists of three stages: interpolation, linear normalization, intervals allocation of the Portevin-Le Chatelier effect occurrence.

A program written in Python was developed to study the properties of alloys. The program structure consists of three stages.

At the first stage, experimental data is selected with a minimum number of rows. The minimum number of rows is the interpolation parameter for the remaining samples and corresponds to the total size of all datasets of the same material after interpolation.

Then, the experimental data is linearly normalized, and a correlation matrix is calculated for them; it allows confirming that all samples behave the same way. The result is shown in Fig. 3.

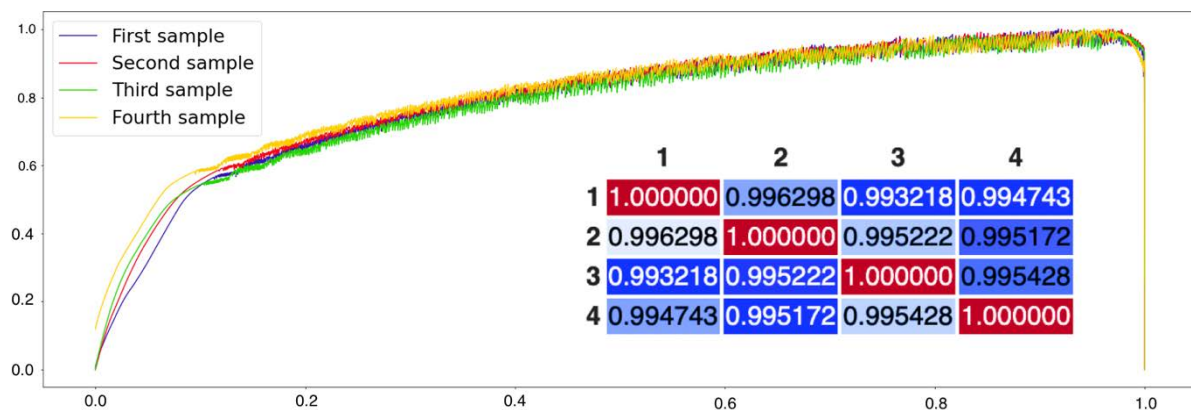


**Fig. 3.** Experimental data on the tension-time dependence of aluminum alloy samples. The y-axis is the tension in kN, the x-axis is the time in seconds

At the last stage of preprocessing for each data set, the moment of the Portevin-Le Chatelier effect occurrence is located, and then all transformations in the study are carried out exclusively from this point in time until the sample breaks. By the moment fluctuations occur, we mean the moment of reaching the first local maximum from the beginning of the experiment.

Methods of time series analysis that allow to identify patterns, build forecasts, and develop models describing the characteristics of the behavior of the object of study in various fields of science [12,13]. The paper [12] describes research directions in the field of analysis and modeling of dynamics of time series of processes in complex systems. At work [6] methods of comparison of algorithms for processing time series are presented, the effectiveness of their application for building practical models and conducting scientific experiments is confirmed. It is noted that the processes considered in practice-oriented studies are extremely rarely stationary, therefore, methods of transition to stationary mathematical models are being developed, for example, the selection and removal of trend, noise, and periodic components from the time series.

The resulting preprocessed datasets can be interpreted as a time series. Wave height  $h_i$  of time series  $X_t$  is calculated using the following formula

$$h_i = x_{max} - (x_{minL} + x_{minR})/2,$$

where  $x_{max}$  is the local maximum, and  $x_{minL}, x_{minR}$  are the nearest local minima surrounding  $x_{max}$ . To construct the wave height distribution, it is necessary to introduce the concept of the wave equivalence class  $[h]$ . We assume that  $h_i$  is equivalent to if the following relation holds

$$\text{round}\left(\frac{h_i}{\delta}\right) = \text{round}\left(\frac{h_j}{\delta}\right),$$

where  $\delta$  is the width parameter of the equivalence class. Figures 4-7 show the wave height distributions for one of the aluminum samples at different  $\delta$ .

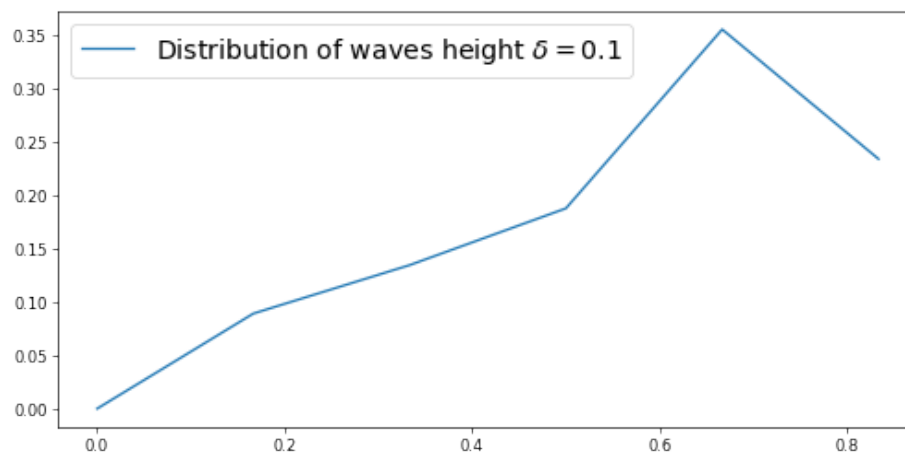


**Fig. 4.** Graph of the dependence of the wave height distribution on the stretching for a sample with  $\delta = 0.1$  (on the y-axis, the normalized number of waves in the equivalence class, on the x-axis, the normalized wave heights)

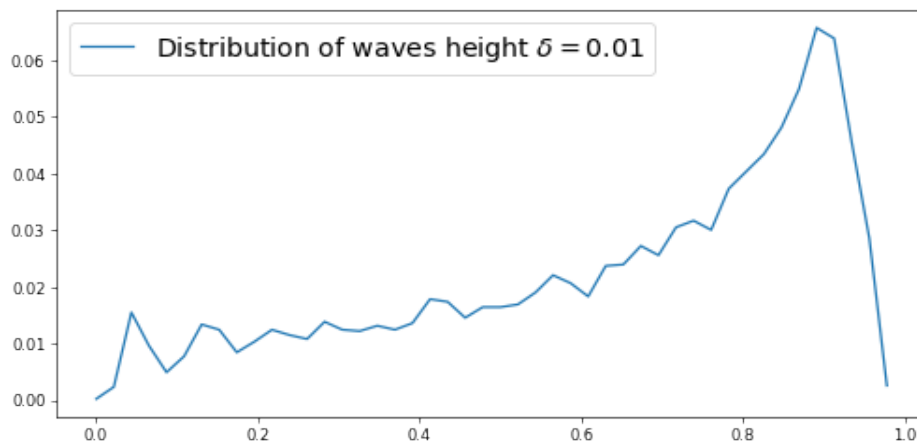


**Fig. 5.** Graph of the dependence of the wave height distribution on the stretching for a sample with  $\delta = 0.01$  (on the y-axis, the normalized number of waves in the equivalence class, on the x-axis, the normalized wave heights)

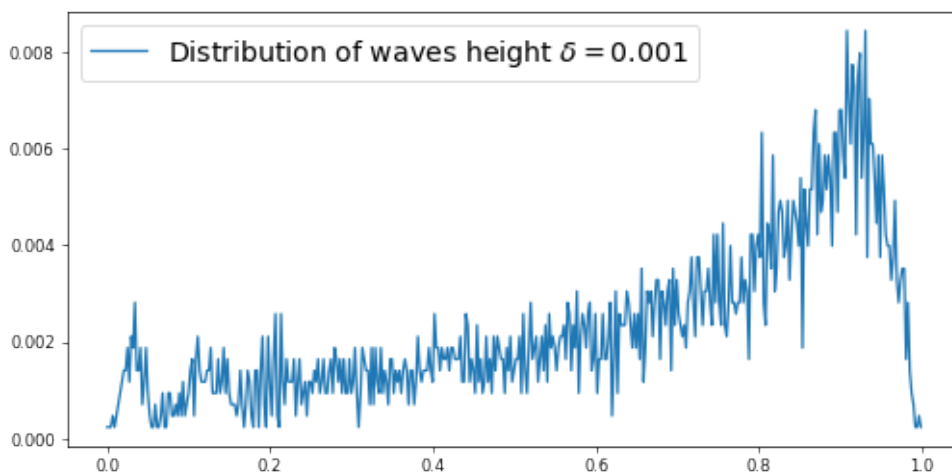


**Fig. 6.** Graph of the dependence of the wave height distribution on the stretching for a sample with  $\delta = 0.001$  (on the y-axis, the normalized number of waves in the equivalence class, on the x-axis, the normalized wave heights)

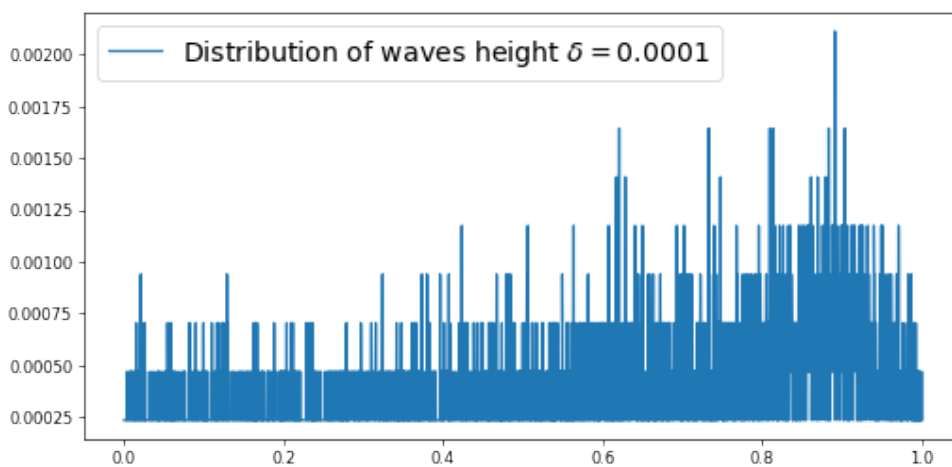


**Fig. 7.** Graph of the dependence of the wave height distribution on the stretching for a sample with  $\delta = 0.0001$  (on the y-axis, the normalized number of waves in the equivalence class, on the x-axis, the normalized wave heights)

When constructing the distributions, the number of unique wave height equivalence classes was found, then the number of class representatives was calculated. The equivalence classes linearly normalized from 0 to 1 are located along the horizontal axis. On the vertical axis, the number of classes encountered was normalized so that the number of all values of each class encountered equals one. Due to this approach, the resulting figures correspond to the density of the wave height distribution, if we consider the result of the experiment as a random process. The distribution profile resembles a beta distribution with parameters  $a = 18, b = 4$ , or the sum of an exponent with a damped harmonic closer to the maximum value of the distribution.

With a decrease in the value of parameter  $\delta$ , the number of equivalence classes  $[h]$  increases, with  $\delta \ll 1e - 6$ , the distribution is almost uniformly distributed over the segment  $[0,1]$ . The most informative picture is obtained at  $\delta = 0.01$ . This value is used later.

In [13], a study of dynamical systems was carried out, using the example of a hydrodynamic process, in the modeling of which random variables were generated based on functions with an exponential profile. It was noticed that the obtained simulation results correspond to the results of computational experiments [14,15]. The revealed pattern in the experimental data allows considering the hypothesis of the rogue waves existence in systems with the Portevin-Le Chatelier effect [16,17]. By a rogue wave, we mean a wave with amplitude criterion  $H \geq 2.1$  calculated by the following formula

$$H = \frac{h_i}{h_{sm}},$$

where  $h_i$  is the height of the wave with number  $i$ , and  $h_{sm}$  is the average height of one-third of the highest waves.

To reduce the values of the noise contribution to the data, we consider the standard deviation among  $n$  waves, denote this value by  $\mu_n$ . Then, for the first  $n - 1$  waves,  $\mu_n = 0$ . Then, in one conventional unit of time, there is a shift by one wave. Thus, for  $n \in [4,100]$ , a set of trajectories  $\mu_n(t)$  is obtained. Among the whole set, we select trajectories based on the following criteria:

1. Rogue waves should occur among the estimates  $\mu_n(t)$ ;
2. The number of rogue waves should not be less than twenty and exceed one hundred pieces;
3. Rogue waves should occur with some frequency.

The second criterion is consistent with the data obtained because of computational experiments [8,9], in which the number of rogue waves reached 25 pieces. The third criterion can be interpreted through the estimates  $\mu_n(t)$ , minimizing the average value of the estimates at each time.

Figure 8 shows the dependence of the change in estimate  $\mu_n(t)$  on time, while among other estimates it was minimal, according to the second criterion. The red dots in the figure indicate the registered rogue waves. It can be noticed that after the last recorded rogue wave, the average value begins to decrease up to the rupture of the sample.

A similar dynamic was observed when modeling the hydrodynamic process [13] and when applying a similar technique for processing the results of a computational experiment [8,9].

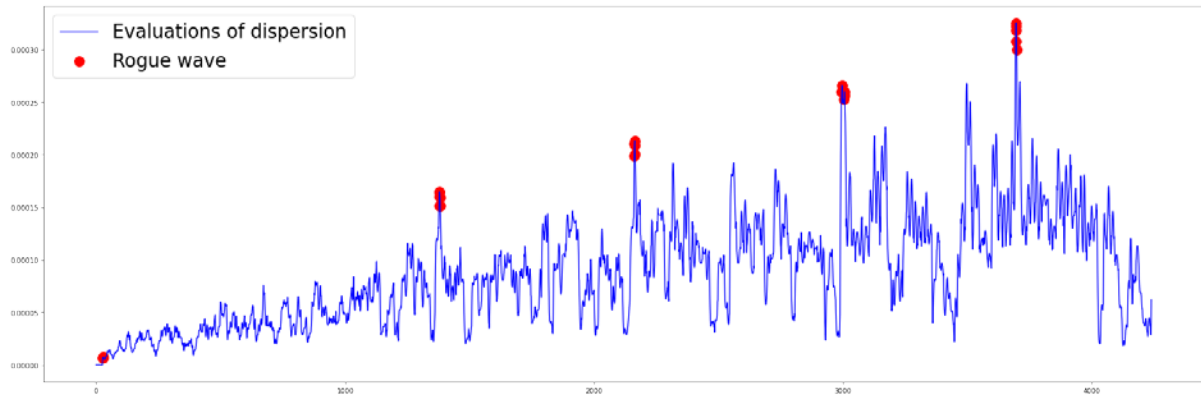


**Fig. 8.** Evaluation of an aluminum sample at  $n = 26$  (on the y-axis, the value of the standard deviation  $\mu_n$ ; on the x-axis, standard units of time)

### 3. Results

Stretching experiments have been carried out for an aluminum alloy. The Portevin-Le Chatelier effect is registered on each sample. The technique for analyzing the Portevin-Le Chatelier effect has been developed based on the interpretation of experimental results as a time series. Wave height distributions are plotted for each sample. It is noted that when the global maximum for  $\mu_n(t)$  is reached, a further decrease is observed in the average value of the estimate for the dispersion of wave heights.

### 4. Discussion

This paper considers the approach to studying the characteristics of the aluminum alloy during deformation and rupture. The authors apply time series analysis methods to study the Portevin-Le Chatelier effect. During the processing of experimental data, it was found that the obtained graphs reflect the process of the emergence of rogue waves.

The similarity of the distribution graphs for rogue waves and the processes of metal rupture can be explained using concentrations. If we consider the hypothesis that rogue waves arise due to a local concentration of energy, then a similar mechanism for alloys is the concentration of dislocations in materials.

### 5. Conclusion

The comparison of numerical processing of experimental data for alloys and liquids promises the use of waveforms for research in metallurgy. Considering the processes in alloys and liquids from the point of view of time series theory allows us to obtain identical distribution graphs. This fact makes further investigation of the Portevin-Le Chatelier effect crucial from the perspective of the theory of random processes. Moreover, it is necessary to study the reverse mechanism to reveal if there is an analog of the Portevin-Le Chatelier effect for liquids when a rogue wave appears. A positive answer to this question will allow identifying the zones of stable and unstable behavior of waves. This will help create methods for predicting the appearance of a rogue wave.

### References

- [1] Zuev LB. Chernov–Luders deformations and Portevin–Le Chatelier in active deformable medium of various nature. *Journal of Applied Mechanics and Technical Physics*. 2017;2: 164-171.
- [2] Brindley BJ, Worthington PJ. Yield-point phenomena in substitutional alloys. *Metallurgical Reviews*. 1970; 45(2): 101-114.

- [3] Robinson JM, Shaw MP. Microstructural and mechanical influences on dynamic strain aging phenomena. *International Materials Reviews*. 1994;39(3): 113-122.
- [4] Franklin S, Mertens F, Marder M. Portevin–Le Chatelier effect. *Physical review. E, Statistical physics, plasmas, fluids, and related interdisciplinary topics*. 2001;62: 206.
- [5] Xiaoyu W, Tian B, Liu L, Sun Y. Rogue waves for a variable-coefficient Kadomtsev–Petviashvili equation in fluid mechanics. *Computers & Mathematics with Applications*. 2018;76(2): 215-223.
- [6] Gao L, Wu Q, Cao Y, Wabnitz S, Zhu T. Optical polarization rogue waves and their identifications. *Journal of Physics: Photonics*. 2020;2(3): 032004.
- [7] Chowdury A, Chang W. Rogue wave fission. *Physics Review Research*. 2021;3(3): 32-60.
- [8] Li S, Li P, Gino B, Gino B. Solitons and rogue waves in spinor Bose-Einstein condensates. *Physical Review*. 2018;97: 220-221.
- [9] Yasuhiro M, Hiromi Y, Jinkyu Y. Feasibility study on the formation of rogue waves in origami-based mechanical metamaterials. In: *Health Monitoring of Structural and Biological Systems XIV*. 2020. p.33.
- [10] Zaitseva E. *The results of the experiment on the stretching of aluminum alloy samples*. Available from: <https://github.com/zaytskaterina/experiment-with-stretching> (accessed 27 March 2022).
- [11] Alaei E, Marks B, Einav I. A hydrodynamic-plastic formulation for modelling sand using a minimal set of parameters. *Journal of the Mechanics and Physics of Solids*. 2021;151: 104388.
- [12] Andrianova EG, Golovin SA, Zykov SV, Lesko SA, Chukalina ER. Review of modern models and methods of analysis of time series of dynamics of processes in social, economic, and socio-technical systems. *Russian Technological Journal*. 2020;8(4): 7-45.
- [13] Kalugin TR, Kim AK, Petrusovich DA. Analysis of the high order ADL(p, q) models used to describe connections between time series. *Russian Technological Journal*. 2020;8(2): 7-22.
- [14] Shkunkov A, Zaitseva E, Kazankov V. Modeling, and information theory. In: *The fifth scientific and technical conference of students and postgraduates of MIREA - Russian Technological University: Proceedings*. 2020. p.446-450.
- [15] Shami R, Yudin A. Simulation of spatiotemporal spread of rogue waves. *Doklady Earth Sciences*. 2013;448(20): 240-242.
- [16] Shamin RV, Gorlenko AV, Smirnova A. On the stability of rogue waves. *Computational Technologies*. 2012;18(1): 96-105.
- [17] Kurkin AA, Pelinovsky EN. *Rogue waves: facts, theory, and modeling*. 1st ed. Berlin; 2016.

## THE AUTHORS

### **Zaitseva E.V.**

e-mail: [zaytskaterina@gmail.com](mailto:zaytskaterina@gmail.com)

ORCID: 0000-0003-3982-3592

### **Shmeleva A.G.**

e-mail: [ann\\_shmeleva@mail.ru](mailto:ann_shmeleva@mail.ru)

ORCID: 0000-0003-2300-3522

**Kazankov V.K.**

e-mail: v.kazankov98@gmail.com

ORCID: 0000-0002-7766-7730

# EXPERIMENTAL INVESTIGATION OF THE MECHANICAL BEHAVIOR OF HONEYCOMB SANDWICH COMPOSITE UNDER THREE-POINT BENDING FATIGUE

Hocine Mzad✉

Department of Mechanical Engineering, Badji Mokhtar University of Annaba, P.O. Box 12, DZ-23000, Algeria

✉ [h\\_mzad@yahoo.fr](mailto:h_mzad@yahoo.fr)

**Abstract.** The present experimental work deals with the mechanical fatigue behavior under 3-point bending stress of composite aluminum panels with an aramid honeycomb core. The testing conditions (applied load and frequency), under cyclic loading, the analysis of rigidity loss, and the damage modes are the tools for this experimental investigation. The specimens consist of aluminum sheets, one millimeter thick each for the skins, and a honeycomb aramid structure, eight millimeters high for the core. As a first approach, the static 3-point bending tests made it possible to determine the deflection variation as a function of the force applied, which will be exploited to carry out fatigue tests on an EPSIFLEX machine type. They are made for three loading levels of imposed deformation with a load ratio of 0.2 and a frequency of 5 Hz. The results obtained allowed the determination of the stiffness loss curves and the Wöhler curves in order to optimize the loading conditions and the service life of the sandwich composite material. The tests were carried out for 3 cyclic loading; they show that the optimal load ensuring better service resistance of the experimented sandwich panels is 0.7 of the material elastic limit (720 N). Static and cyclic flexion fractography showed the different modes of skin damage (indentation) and honeycomb core (delaminating and shearing) leading to the specimens' ruin.

**Keywords:** 3-point bending, composite material, stress amplitude, fatigue threshold, damage

**Acknowledgements.** *No external funding was received for this study.*

**Citation:** Mzad H. Experimental investigation of the mechanical behavior of honeycomb sandwich composite under three-point bending fatigue. *Materials Physics and Mechanics*. 2022;48(2): 217-231. DOI: 10.18149/MPM.4822022\_7.

## 1. Introduction

Composite materials are materials with specific mechanical properties, namely low density, high strength, high rigidity, and excellent durability. There are two main categories of composite materials used in the industry: laminate composites and sandwich composites. In a simple way, sandwich structures are composed of two thin skins and a light-thick core between them. Their lightness and good bending properties have increased their use, particularly in the aeronautical industry and civil infrastructure.

Kiyak et al. [1] have experimented, under three-point bending and compression tests, with various cell structures of sandwich composites having a carbon fiber core. The results show that cell shape and cell density change are parameters that affect bending and

compression peak loads in the same proportion. A numerical validation of the results was performed using the commercial code ANSYS.

Many structural parameters affect the mechanical behavior of these complex systems: the nature of material constituents, the stacking sequences, and the relative thicknesses of the different layers [2, 3].

Du et al. [4] have fabricated, in the laboratory, light-weight sandwich panels containing biofiber-based paper-reinforced polymer (PRP) composites as the skin materials. Their investigation focused on the fabrication process, testing, effects of the honeycomb core cell size and core height on flexural properties, and load-deflection behavior of the sandwich panels.

The tailor-folding method was proposed in order to fabricate a composite sandwich panel with a carbon fiber reinforced polymer (CFRP) hexagon honeycomb core [5]. This method has the potential to automatically fabricate the composite sandwich panel, with the advantage that the continuous fibers reduce the stress concentration and reinforce the constraints between the adjacent cell walls.

Belingardi et al. [6] performed experiments on both undamaged and partially debonded face specimens of sandwich honeycomb beams. The study allows monitoring the specimen's bending stiffness variation during fatigue cycling and determining residual properties after fatigue cycling. In the study presented by Al-Fasih et al. [7], the impact damage under four-point loading of cracked honeycomb composite beams was investigated. The elaborated model helps to prevent any anticipated failure of composite structures containing skin defects.

The effects of environmental factors, as well as loading frequency and block loading, on the fatigue life of honeycomb core composite sandwich structures were considered in several analytical models and experimental works [8-10]. Three-point failure modes in aramid-aluminium composite sandwich beams under dynamic fatigue loading were assessed within a defined range of excitation frequencies and loading levels.

Jen et al. [11] studied the impact of the face sheet thickness on the fatigue strength of aluminum composite panel specimens under four-point bending fatigue tests. A number of local parameters are utilized; they have been shown to correlate adequately with the fatigue life data of the studied specimens with various honeycomb core densities.

The experimental labor proposed by Shi et al. [12] deals with the conception of stronger sandwich structures using carbon-fiber face-sheets and an aluminum-honeycomb core. The approach used combines the concepts of resin-fillet reinforcement and short-Kevlar-fiber interfacial toughening.

Mamchits et al. [13] proposed an alternative composite version of a hatch cover design using an innovative method of manufacturing. Numerical methods were used to select the most rational materials and design parameters. The study was concluded by the assessment of the economic expediency of the production of composite hatch covers.

Han et al. [14] evaluate experimentally the effects of out-of-plane compression and transverse shear of honeycomb-corrugated hybrid sheets under three-point bending. By ensuring good interfacial bonding in the hybrid-cored sandwich, the strength and energy absorption are both greatly improved, which allows the use of these structures for ultralight load-bearing and energy-absorbing applications.

Many studies have been conducted to investigate the effects of potential flaws in composite structures, such as fiber laying direction defect and fiber straightness defect, on the effective mechanical properties [15, 16]. The findings revealed that accounting for imperfections in the composite microstructure, such as fiber laying direction deviation and fiber curvature, was of limited importance. However, the configurations L and W of honeycomb cells affect the sandwich lifetime.

Sankaranarayanan et al. [17] explored the impact of zirconium carbide (ZrC) and magnesium on the mechanical and tribological properties of aluminium matrix composites. Their study revealed that the hybrid aluminium composite can be considered a unique material with high strength, low weight, and wear resistance. Moreover, within the framework of the molecular dynamics method, Rozhkov et al. [18] conducted a simulation on the mechanical behavior of a graphene nano-inclusion in a matrix of zirconium dioxide stabilized by yttrium oxide. According to the constructed model, defect-free graphene manifests itself as an excellent reinforcing element of the composite.

Hussain et al. [19] performed a computational method on the fatigue behavior of honeycomb sandwiches using the commercial package ANSYS. The model based on actual experiments allows the prediction of flexural strength and fatigue life of aluminum honeycomb sandwich structures under three-point bending conditions.

A three-point static bending study was carried out on two types of laminated composite materials to assess the influence of the test speed and the effect of the stacking sequence on their mechanical behavior [20]. The laminates, reinforced with E fibers and an epoxy resin matrix, were manufactured by a successive lamination process of sixteen identical reinforced layers and then subjected to vacuum polymerization. The experiments revealed that the ply orientation has an influence on the flexural modulus and the fatigue resistance, which decreases when the plies at  $0^\circ$  and  $90^\circ$  are alternated.

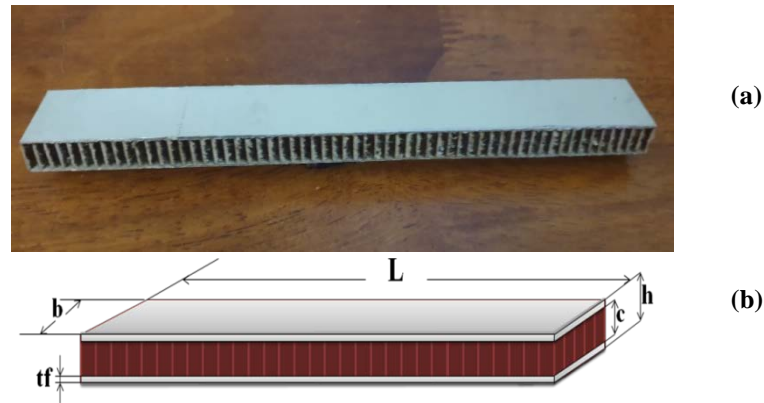
The aim of this work is to determine the mechanical fatigue behavior of sandwich composite (aluminum/aramid) panels with a honeycomb core, in 3-point bending, under varied loads. In particular, the rigidity loss evolution in function of load in order to identify the optimal conditions for using this type of sandwich panel, allowing a better lifetime. Static and cyclic tests were performed on four specimens for the loading levels of 90%, 80%, and 70%. The experimental results obtained on the structure's behavior and damage will be presented and analyzed.

## 2. Test conditions

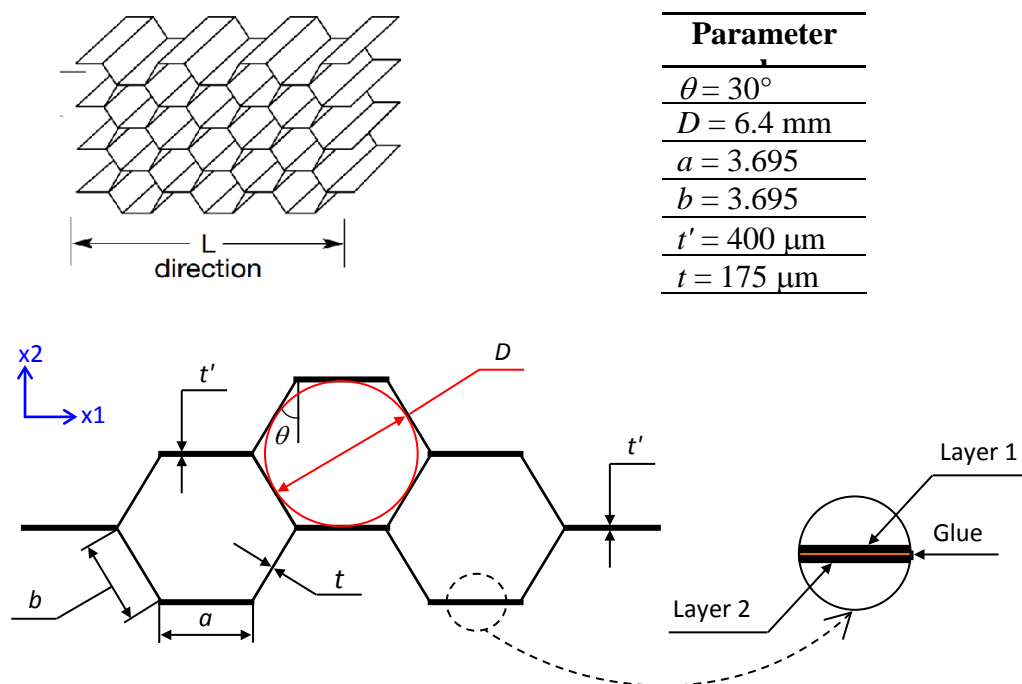
**Geometrical specifications.** Sandwich composites have been designed with the intention of providing greater flexural rigidity while maintaining minimal mass. The materials used are selected according to the rigidity and the desired tensile or compressive strength: metal, composite laminate made of glass or carbon fibers. For applications requiring higher stiffness, honeycomb-structured cores are used.

The considered specimens (Fig. 1a) are cut according to the L-direction of sandwich panel cells (Fig. 2), with aluminum skins and a honeycomb-shaped aramid core. Their dimensions (Fig. 1b) have been defined according to the specifications of ANSI A208-2. The width ( $b$ ) of the specimen is set at 25 mm to meet the standard requirements. The skin ( $t_f$ ) is 1 mm thick, while the core and the structure are, respectively,  $c = 8$  mm and  $h = 10$  mm. The total length ( $L$ ) of the test piece is 210 mm.

**Material properties.** Sole design influences the mechanical properties of sandwich composites. Honeycomb cores have a hexagonal structure that curves moderately, but the cells deform depending on the orientation, and the mechanical properties are modified. The core and skin properties of the studied sandwich panel are given in Table 1. The core is made up of aramid cells with a  $148 \text{ kg/m}^3$  density in the shape of regular hexagons with an inscribed circle of 6.4 mm in diameter (Fig. 2).



**Fig. 1. (a) Sandwich specimen (b) Dimensions according to ANSI A208-2**



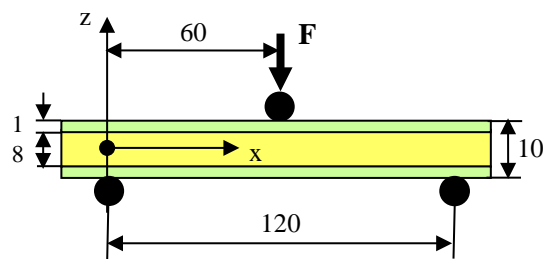
**Fig. 2. Honeycomb cell description**

Table 1. Composite mechanical properties [31]

	Material property	Value
<b>Aramid core</b>	Cell size	3.2 mm
	Density	148 kg/m <sup>3</sup>
	Shear resistance (L direction)	3.5 MPa
	Shear Modulus (L direction)	130 MPa
	Compressive strength (L direction)	15.5 MPa
<b>Aluminium Skins</b>	Young's modulus	70000
	Fracture resistance	270 MPa
	Tensile strength	370 MPa
	Elongation to break	13%
	Poisson coefficient	0.33

**Testing scheme.** The tested sample is mounted in the support fixture. The edges of the panels were mounted between two rounded purlins. In order to avoid horizontal test tubes moving, a pretension  $F_{min}$  is applied to each level, which generates an arrow  $f_{min}$ . Figure 3 shows the load application points, the method of fastening and the point at which the displacements are measured.

$F_0$  is the force applied to the specimen at the beginning of the fatigue test. Its value represents a percentage of the maximum force determined during the static test ( $F_{ei}$ ). This percentage defines the selected three loading levels (90%, 80%, and 70%) under a loading frequency of 5 Hz.



**Fig. 3.** Assembly of the specimen

### 3. Static tests

**Procedure.** Static bending tests were performed on a WDW-5 computer-controlled universal testing machine (Fig. 4), with a load cell of 50 kN. This machine was manufactured in China by Jinan (Shandong).

On the basis of three test tubes, the static bending experiments were carried out. Graphical results obtained show the loading force as a function of displacement (Fig. 5.1). A curve magnification in the elastic zone makes it possible to better discern the experimental results (Fig. 5.2).



#### Test conditions

Number of tests: 4  
Speed: 5 mm/mn  
Standard ANSI A208-2: L = 120 mm  
Temperature: 27°C

**Fig. 4.** Static bending test machine: Universal Machine WDW-5

**Analysis of static results.** As illustrated by static bending tests (Fig. 5.1), the structural response of the sandwich panels investigated can be considered linear until the first failure occurs during in-plane compression loading. The equation below for Young's modulus,  $E_e$ , describes the effective structural response:

$$E_e = \frac{1}{2tf + c} (2tf E_f + c E_c).$$

Material and geometrical properties are expressed in the above equation by skin and core thicknesses  $t_f$  and  $c$ , and, respectively,  $E_f$  and  $E_c$  the moduli in the load direction of the skins and core.

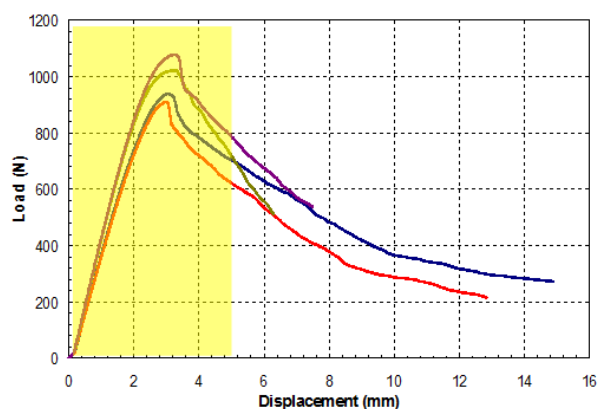


Fig. 5.1. Static bending tests

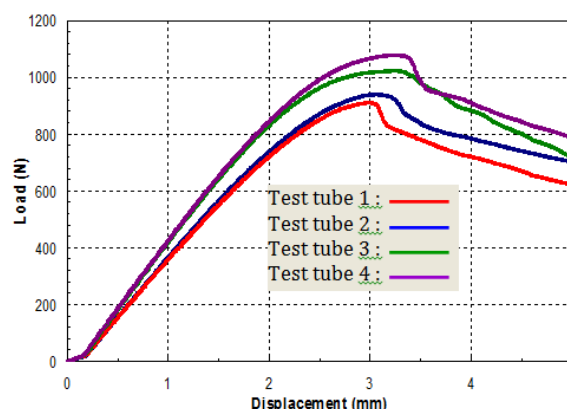


Fig. 5.2. Zoom in elastic zone (in yellow)

When compressed in the in-plane direction, the load is mainly carried by the face-sheets of the sandwich, whereas the core stabilizes the structure and prohibits premature buckling of the face-sheets.

The start of loading causes compression of the core, in particular the adhesive, due to its viscoelastic property. In our opinion, the appearance of a small slope at the beginning of curves is due to imperfect test conditions; there is elimination of gaps, backlashes, etc. If the compression of the structure is continued after the initial failure, the damage will start to propagate through inelastic deformation until the core damage.

In Figure 5, one can make a distinction between two deformation zones:

- A linear zone corresponding to elastic deformation up to the limit value,  $F_{el} = 720$  N.
- A non-linear zone representing plastic deformation up to the maximum value,  $F_{max} = 960$  N.

It is necessary to maintain the stresses to which the material will be subjected in the elastic range. So that the maximum value of the applied force  $F_0$  tends to the elastic limit force  $F_{el}$ .

#### 4. Fatigue tests

**Procedure.** The bending fatigue experiments were carried out on the testing machine INSTRON 4400 (Fig. 6) with a load cell of 250 daN of imposed arrow. A force sensor, mounted on the cell, transmits the measurements to a connected computer-assisted navigation (CAN), equipped with processing software. This machine was manufactured in China by Beijing Jinshengxin Testing Machine Co., Ltd.

Three-point bending fatigue tests were performed for 3 loading levels of the elastic limit force  $F_{el}$  ( $F_0 = 648$  N,  $F_0 = 576$  N, and  $F_0 = 504$  N). As this fatigue machine is of constant deformation, it is necessary to determine the maximum deflection corresponding to  $F_0$  for each level.

Three tests were carried out with loading levels of 90%, 80%, and 70% of the maximum elastic stress amplitude ( $F_{el}$ ). The frequency ( $f_r$ ) was set at 5 Hz and the load ratio ( $R$ ) at 0.2. Sample tests were conducted by determining the displacements and measuring the forces required for them. The displacement, expressed below, corresponds to an arrow difference ( $\Delta f$ ) caused by the initial load force ( $F_0$ ) and a pretension force ( $F_{min}$ ).

$$\Delta f = f_{max} - f_{min}.$$



**Fig. 6.** Bending fatigue machine: INSTRON 4400

Preliminary setting data are as follows:

- At a load level of 90%, the pretension force is set as:  $F_{min} = 130$  N and the fixed displacement is:

$$\Delta f = 1.8 - 0.36 = 1.44 \text{ mm.}$$

- At a load level of 80%, the pretension force is set as:  $F_{min} = 115$  N and the fixed displacement is:

$$\Delta f = 1.57 - 0.32 = 1.25 \text{ mm.}$$

- At a load level of 70%, the pretension force is set as:  $F_{min} = 100$  N and the fixed displacement is:

$$\Delta f = 1.375 - 0.275 = 1.1 \text{ mm.}$$

Table 2. Experimental data with a test end criterion of 90%,  $R = 0.2$ , and  $f_r = 5$  Hz

		Sample 1	Sample 2	Sample 3
<b>90% Load</b>	$N$	11750	18250	96050
	$F/F_0$	0.9		
	Max arrow amplitude (mm)	1.8		
	Deformation amplitude déformation	0.015		
	Stress amplitude (MPa)	1050		
<b>80% Load</b>	$N$	102050	154550	321050
	$F/F_0$	0.8		
	Max arrow amplitude (mm)	1.57		
	Deformation amplitude déformation	0.013		
	Stress amplitude (MPa)	918		
<b>70% Load</b>	$N$	1143050	1435550	2007050
	$F/F_0$	0.7		
	Max arrow amplitude (mm)	1.375		
	Deformation amplitude déformation	0.013		
	Stress amplitude (MPa)	918		

Table 3. Experimental data with a test end criterion of 75%,  $R = 0.2$ , and  $fr = 5$  Hz

		Sample 1	Sample 2	Sample 3
90% Load	$N$	16650	22550	114050
	$F/F_0$	0.9		
	Max arrow amplitude (mm)	1.8		
	Deformation amplitude déformation	0.015		
	Stress amplitude (MPa)	1050		
80% Load	$N$	120050	175550	394550
	$F/F_0$	0.8		
	Max arrow amplitude (mm)	1.57		
	Deformation amplitude déformation	0.013		
	Stress amplitude (MPa)	918		
70% Load	$N$	1435550	2047550	2416550
	$F/F_0$	0.7		
	Max arrow amplitude (mm)	1.375		
	Deformation amplitude déformation	0.013		
	Stress amplitude (MPa)	918		

Composite design in the case of fatigue loading is usually characterized by an S-N curve, from which one may obtain the Wöhler curve. Thereafter, this can be represented as a curve giving the value of the cyclic stress amplitude. Unfortunately, the software used by the available testing machine uses only forces in the ordinate axis instead of stresses. Nevertheless, we believe that the shape of the obtained curve is very significant and similar to the S-N curves usually presented. To achieve Wöhler curves, the experimental tests were carried out at constant deformation amplitude (CDA) with two test end criteria of 90% and 75%. The loading ratio  $R$  and the excitation frequency  $fr$  were maintained constant.

The illustrative tables, Table 2 and Table 3, summarize the results obtained for the four sample groups. It can be seen that the load level and the test end criterion have an influence on the necessary number of cycles to obtain a resistance loss of 10% and 25%, respectively.

Ten years ago, Manca et al. [21] examined the fatigue crack growth in foam-cored and E-glass/polyester face sheet sandwich composites using the mixed mode bending (MMB) test method. Fatigue tests were performed at 80% of the static critical load, at load ratios of  $R = 0.1$  and  $0.2$ . Fatigue crack growth results revealed that the main crack propagated in the core or in the face laminate at the debond crack tip.

**Analysis of fatigue tests.** A series of fatigue tests were conducted on a number of specimens of the material at different stress levels. The stress endured is then plotted against the number of cycles sustained (Fig. 7). The fatigue process is thought to begin at an internal or surface flaw where the stress is concentrated. By choosing lower and lower loading levels, a stress value or load ratio ( $F/F_0$ ) may be found which will not produce failure, regardless of the number of applied cycles  $N$ . This stress value corresponds to the maximum stress amplitude. The applied force varies in amplitude depending on the cycle number resulting from the material resistance loss. The plotted stress-cycle diagrams show no clear fatigue threshold.

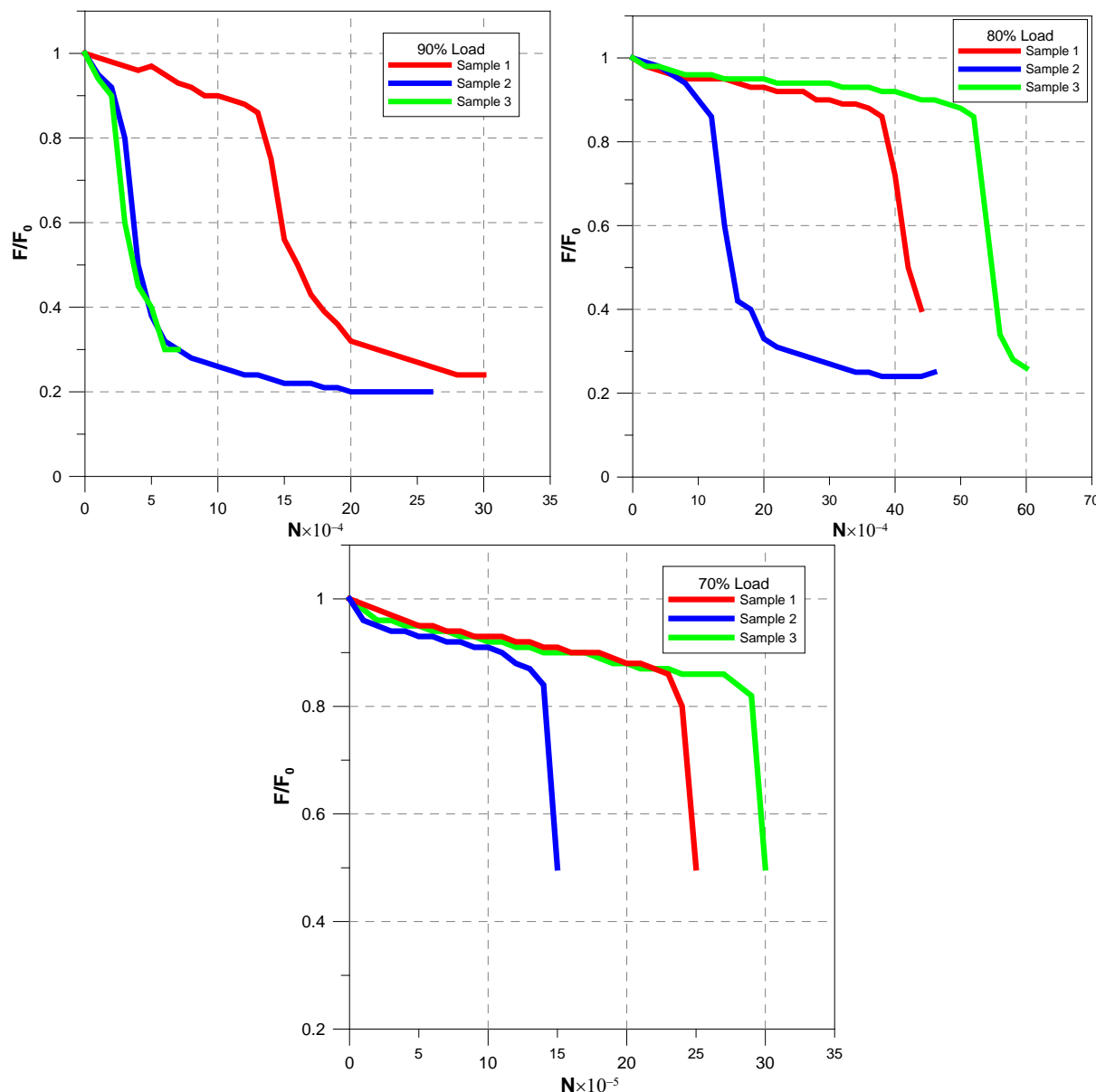


**Fig. 7.** Resistance loss curves for different loading levels

The discrepancies in the fatigue test results obtained for identical samples are due to the unevenness of the adhesive film of the interface between the skins and the core, as well as to the different positions of the section plane of the specimens relative to the core cells. The debonding of the adhesive between the face sheet and the core was identified as the major failure mode when analyzing the four-point bending fatigue strengths of aluminum honeycomb sandwich beams with cores of various relative densities [22].

The possibility of predicting the durability of an adhesive bitumen mix with mineral components of asphalt concrete has been proved [23]. It was established that due to thermostating, the quality of the adhesive bonding of bitumen can be significantly improved, which can provide increased strength, durability, and wear resistance.

The resistance loss presents distortions due to the different positions of the specimen's cutting plane relative to the extreme cell contours that modify the sole section and, consequently, its quadratic moment on the one hand, and the irregularity of the adhesive film between skins and core on the other hand (Fig. 7). In fact, previous experimental results revealed that the main failure mode of sandwich panels made of Nomex and carbon fiber reinforced polymer (CFRP) was the fracture in the honeycomb wall. Sandwich structures in

the form of L-joints have been tested under bending load to investigate the mechanical performance during structural deformation and damage evolution [24]. Moreover, the hexagonal honeycomb cells were characterized in an FE model with an elasto-plastic constitutive model and damage criterion in detail during impact [25].

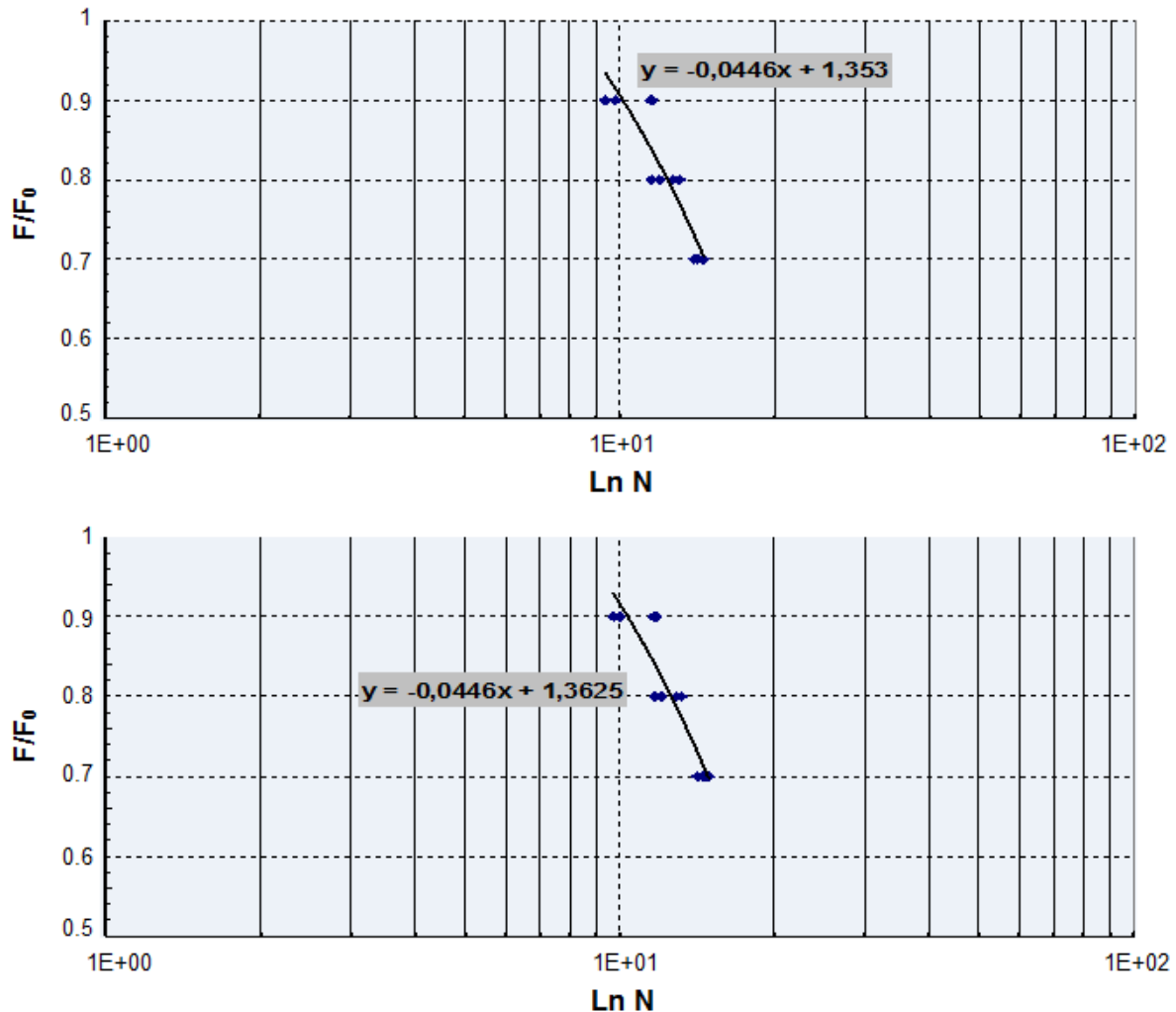


**Fig. 8.** Fatigue testing results

It can be seen that the curve shape (Fig. 8) tends to a constant slope. In fact, the last points show that it will be asymptotic at the value of  $F/F_0 = 0.7$ , representing the fatigue threshold. According to Wöhler curves (Fig. 9), the maximum stress amplitude of this material was reached for the following cycle numbers:

- $2 \times 10^6$  for the test end criterion of 90%.
- $3 \times 10^6$  for the test end criterion of 75%.

In this context, numerical simulations have been carried out to predict the fatigue life of honeycomb sandwich structures. Experimental characterizations were developed to describe the static and fatigue behaviors of the Nomex honeycomb sandwich under out-of-plane pressure load and bending load. From the strength and stiffness calculated results, critical parameters of fatigue behavior experiments could be set, including the maximum load, stress ratio, and loading frequency [26].

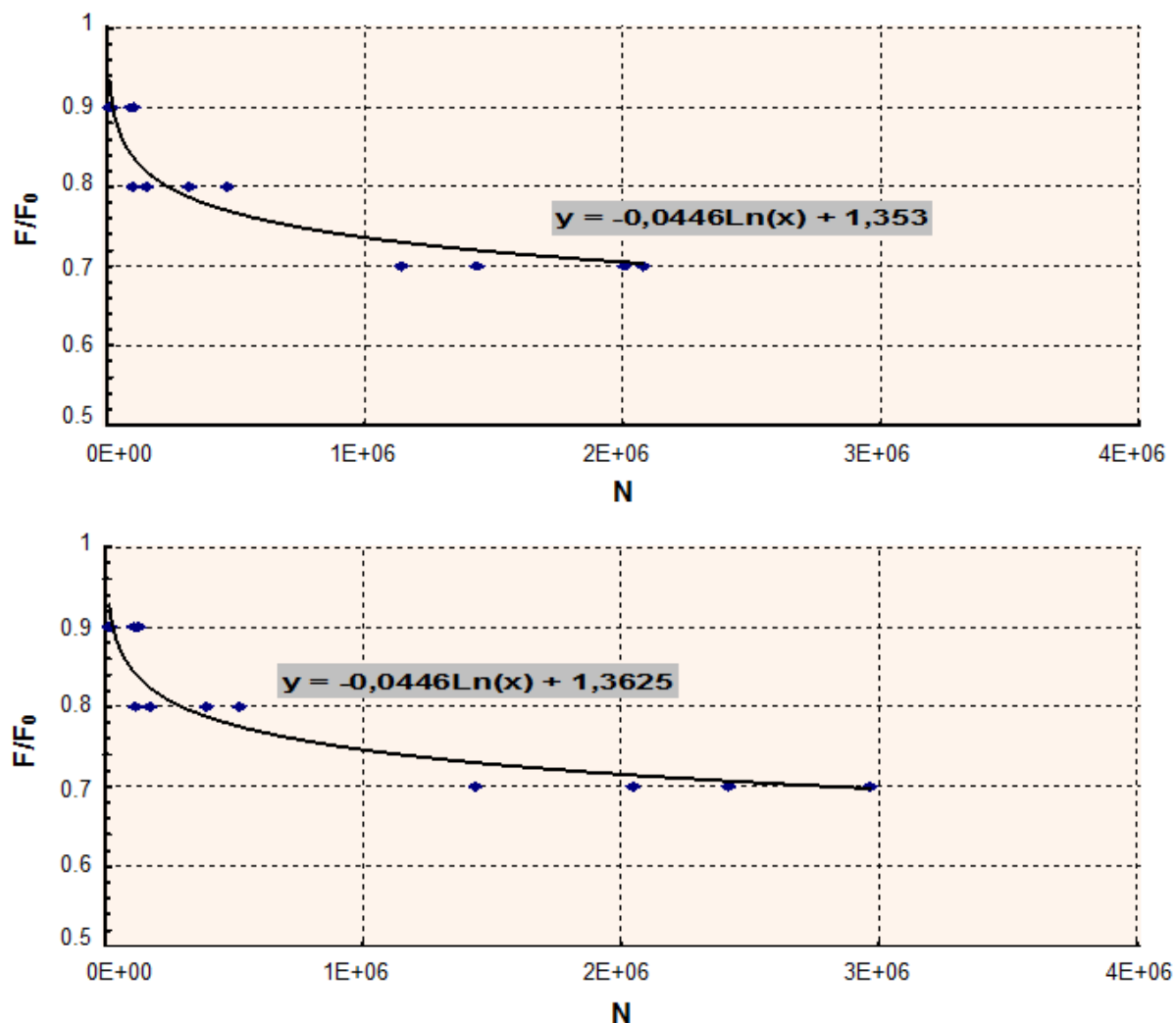


**Fig. 9.** Wöhler curves

The fatigue response of commercial aluminum honeycomb sandwich panels subjected to three-point bending loading conditions was tested experimentally. Two different collapse mechanisms were detected: for larger supports span, a fracture of the tensioned skin was observed, whereas lower supports span produced core shear [27].

### 5. Material damage

For the fracture mechanics analyses in fatigue and bending testing (Figs. 10 and 11), an optical microscope together with image analysis is utilized. The equipment consists of three parts: an optical microscope, a macro-observation system, and a PC with software for image analysis.

Observation of the rupture facies in static and cyclic flexion showed the different modes of damage to the skins (indentation) and the honeycomb core (detachment and shear) causing the deterioration of the samples (Figs. 10 and 11). In terms of damage, we can perceive during static bending and fatigue cyclic stress:

- Shearing occurs when the skins are indented and the sole cells burst, as shown by the red circle in Fig. 10.
- The disbond of the core is indicated by the red arrows in Fig. 11.



**Fig. 10.** Shearing of the core walls

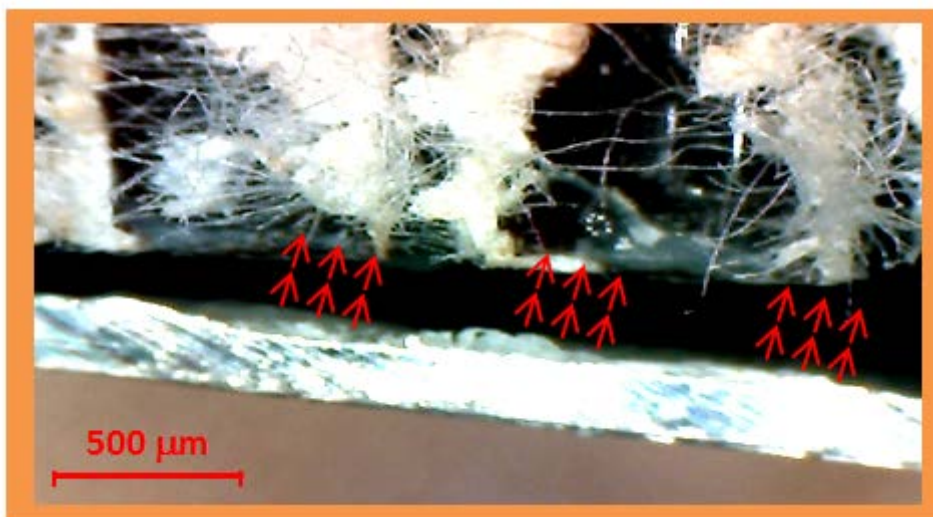


**Fig. 11.** Disbond of the core

The damage propagation due to core disbond in honeycomb sandwich structures was investigated numerically and experimentally, and a two-dimensional finite element model was presented [28]. The effects of geometry parameters, material properties of the face sheet, and material properties of the honeycomb core on the energy release rate have been considered.

A non-destructive evaluation (NDE) method was proposed to determine the debonding location and size of the damaged honeycomb sandwich beam under predetermined parameters [29]. The method proposed utilizes the frequency response function (FRF) measured at one point. It was demonstrated experimentally that the method can inverse damage parameters with acceptable precision.

## 6. Conclusion and perspective

In many of the honeycomb panel's applications, in-service conditions produce fatigue loading; as a result, safer use of aluminum honeycomb sandwich structures requires a deep knowledge of their fatigue response in order to provide a quantitative tool for aluminum honeycomb sandwich structure design.

The undertaken experimental study considers the design investigation of a composite material under physical properties solicitations. It is necessary to select the optimum

honeycomb sandwich structure for each application on the basis of flexural rigidity per unit weight, fatigue life, and failure behavior.

The results that emerge from this study show that sandwich panels with a honeycomb core have mechanical characteristics comparable to homogeneous materials. The loss of resistance becomes significant for a large number of cycles. Indeed, for moderate cyclic loading at average frequencies (from 1 to 10 Hz), the loss of resistance presents a late manifestation. Therefore, they can replace the usual materials by benefiting from their lightness and low cost.

Two damage types are detected:

- The ruin of the sole, which is manifested by the cell walls' shearing and/or the separation of the sole.

- The indentation of the skin is soft during fatigue and hard during static bending.

One notes that the ruin of the sole occurs prematurely in accordance to the skin's ruin, which omits the abrupt and fatal nature of the damage.

The phenomena involved in the static bending response of aluminum honeycomb sandwich structures are mainly dependent on the cell walls buckling. Failure occurred suddenly, and this should be taken into consideration in industrial applications. To overcome this issue, an analytical model was applied to predict fatigue collapse modes and limit loads based on a detailed parametric study to design and achieve the most efficient uniaxial graded auxetic damper (UGAD) [30]. The achieved graded auxetic system has led to a wide plateau region and a variant strength range (1-10 MPa), which justify the superior performance of the UGAD under different blast levels.

The development of modern technologies requires the use of materials with high mechanical properties specific to their use, but with low densities. In fact, it is necessary not only to study the long-term behavior of their fatigue but also to define reliable non-destructive mechanical testing procedures and standardize production methods.

## References

- [1] Kiyak B, Kaman MO. Mechanical properties of new-manufactured sandwich composite having carbon fiber core. *Journal of Composite Materials*. 2019;53(22): 3093-3109.
- [2] Kachanov LM. Rupture time under creep conditions. *International Journal of Fracture*. 1999;97: 11-18.
- [3] Chaboche JL. Continuum Damage Mechanics: Present state and future trends. *Nuclear Engineering and Design*. 1987;105(1): 19-33.
- [4] Du Y, Yan N, Kortschot MT. Light-weight honeycomb core sandwich panels containing biofiber-reinforced thermoset polymer composite skins: Fabrication and evaluation. *Composites Part B: Engineering*. 2012;43(7): 2875-2882.
- [5] Wei X, Li D, Xiong J. Fabrication and mechanical behaviors of an all-composite sandwich structure with a hexagon honeycomb core based on the tailor-folding approach. *Composites Science and Technology*. 2019;184: 107878.
- [6] Belingardi G, Martella P, Peroni L. Fatigue analysis of honeycomb-composite sandwich beams. *Composites Part A: Applied Science and Manufacturing*. 2007;38(4): 1183-1191.
- [7] El-Fasih MY, Kueh ABH, Ibrahim MHW. Failure behavior of sandwich honeycomb composite beam containing crack at the skin. *PLoS ONE*. 2020;15(2): e0227895.
- [8] Sharma N, Gibson RF, Ayorinde EO. Fatigue of foam and honeycomb core composite sandwich structures: A tutorial. *Journal of Sandwich Structures and Materials*. 2006;8(4): 263-319.
- [9] Ait Said A, Bey K, Mzad H. Mechanical fatigue test of aluminium composite panel (ACP) with aramid nida-core under cyclic bending. *Journal of Mechanical Engineering*. 2020;70(2): 1-10.

- [10] Ait Said A, Bey K, Mzad H. Coupled effect of load ratio and frequency on mechanical fatigue behaviour of precast aluminium/aramid fibre composite. *Composites Theory and Practice*. 2021;21(1-2): 46-53.
- [11] Jen YM, Chang LY. Effect of thickness of face sheet on the bending fatigue strength of aluminum honeycomb sandwich beams. *Engineering Failure Analysis*. 2009;16(4): 1282-1293.
- [12] Shi SS, Sun Z, Hu XZ, Chen HR. Carbon-fiber and aluminum-honeycomb sandwich composites with and without Kevlar-fiber interfacial toughening. *Composites Part A: Applied Science and Manufacturing*. 2014;67: 102-110.
- [13] Mamchits D, Nemov A, Karandashev A, Buchler D, Vasilyev R, Ignatiev M. Development of a composite hatch cover. *Materials Physics and Mechanics*. 2020;45(1): 20-30.
- [14] Han B, Wang W, Zhang Z, Zhang Q, Jin F, Lu T. Performance enhancement of sandwich panels with honeycomb-corrugation hybrid core. *Theoretical and Applied Mechanics Letters*. 2016;6(1): 54-59.
- [15] Abbadi A, Tixier C, Gilbert J, Azari Z. Experimental study on the fatigue behavior of honeycomb sandwich panels with artificial defects. *Composite Structures*. 2015;120: 394-405.
- [16] Panina OA, Nemov AS, Zobacheva AY, Kobaykhno IA, Tolochko OV, Yadykin VK. Numerical analysis of mechanical behavior of unidirectional thermoplastic-based carbon fiber composite for 3-D printing. *Materials Today: Proceedings*. 2020;30(3): 559-563.
- [17] Sankaranarayanan G, Balaji AN, Velmanirajan K, Gangatharan K. Mechanical and wear behaviour of the Al-Mg-nano ZrC composite obtained by means of the powder metallurgy method. *Bulletin of the Polish Academy of Sciences: Technical Sciences*. 2018;66(5): 729-735.
- [18] Rozhkov MA, Smirnov AM, Kolesnikova AL, Gutkin MY. Molecular dynamics modeling of the mechanical behavior of YSZ-ceramics/graphene nanocomposite. *Materials Physics and Mechanics*. 2021;47(6): 856-863.
- [19] Hussain M, Khan R, Abbas N. Experimental and computational studies on honeycomb sandwich structures under static and fatigue bending load. *Journal of King Saud University – Science*. 2019;31(2): 222-229.
- [20] Khelifa N, Bey K, Mzad H. Study of mechanical behaviour in three-point bending of fatigue-stressed composite laminates. *Composites Theory and Practice*. 2021;21(3): 107-113.
- [21] Manca M, Quispitupa A, Berggreen C, Carlsson LA. Face/core debond fatigue crack growth characterization using the sandwich mixed mode bending specimen. *Composites Part A: Applied Science and Manufacturing*. 2012;43(11): 2120-2127.
- [22] Jen YM, Chang LY. Evaluating bending fatigue strength of aluminum honeycomb sandwich beams using local parameters. *International Journal of Fatigue*, 2008;30(6): 1103-1114.
- [23] Rudskoy AI, Bashkarev AY, Slavutin LV. Durability of bitumen adhesive bonding in mineral composites. *Advances in Mechanical Engineering*. 2022; 185-193.
- [24] Hou W, Li J, Sang L, Ying L, Han X. On the mechanical performance of honeycomb-core sandwich L-joint under bending load: an experimental-numerical study. *Journal of Adhesion Science and Technology*. 2021. Available from: doi:10.1080/01694243.2021.1959773.
- [25] Zhang X, Xu F, Zang Y, Feng W. Experimental and numerical investigation on damage behavior of honeycomb sandwich panel subjected to low-velocity impact. *Composite Structures*. 2020;236: 111882.
- [26] Wu X, Yu H, Guo L, Zhang L, Sun X, Chai Z. Experimental and numerical investigation of static and fatigue behaviors of composites honeycomb sandwich structure. *Composite Structures*. 2019;213: 165-172.

- [27] Palomba G, Crupi V, Epasto G. Collapse modes of aluminium honeycomb sandwich structures under fatigue bending loading. *Thin-Walled Structures*. 2019;145: 106363.
- [28] Farshidi A, Berggreen C, Schauble R. Numerical fracture analysis and model validation for debonded honeycomb core sandwich composites. *Composite Structures*. 2019;210: 231-238.
- [29] Zhu K, Chen M, Lu Q, Wang B, Fang D. Debonding detection of honeycomb sandwich structures using frequency response functions. *Journal of Sound and Vibration*. 2014;333(21): 5299-5311.
- [30] Al-Rifaie H, Sumelka W. The development of a new shock absorbing uniaxial graded auxetic damper (UGAD). *Materials*. 2019;12(16): 2573.
- [31] Balasingh C, Kanakalatha P, Sridhar MK, Singh AK. Residual stresses in aluminium alloy sheet/aramid fiber laminated composites. *Indian Journal of Physics*. 1989;63A: 262-266.

## THE AUTHORS

### **Mzad H.**

e-mail: h\_mzad@yahoo.fr

ORCID: 0000-0001-9900-6960

# STABILITY ANALYSIS OF NANOSCALE SURFACE PATTERNS IN ULTRATHIN FILM COATING

G.M. Shuvalov✉, S.A. Kostyrko

St. Petersburg State University, 7/9 Universitetskaya nab., St. Petersburg, 199034, Russia

✉ [g.shuvalov@spbu.ru](mailto:g.shuvalov@spbu.ru)

**Abstract.** This paper presents a theoretical approach to the analysis of ultrathin film morphological stability under surface diffusion. Based on the simplified Gurtin–Murdoch model the surface elasticity has been taken into account. Due to the lattices mismatch, the film structure is subjected to misfit stress. It is assumed that the free surface can change its shape via mass transfer in order to minimize the total energy. Surface diffusion is considered the main mechanism leading to the morphological instability of the film surface. It is supposed that the atomic flow along the surface is proportional to the gradient of the chemical potential. The change in surface profile amplitude is described by the linearized evolution equation, which is derived by taking into account the solution of the corresponding plane elasticity problem. Based on the proposed approach, the effect of the physical and geometric parameters on the morphological stability of the ultrathin film surface has been analyzed.

**Keywords:** ultrathin film coating, surface elasticity, morphological instability, surface diffusion

*Acknowledgements.* The reported study was funded by RFBR, project number 19-31-90024.

**Citation:** Shuvalov GM, Kostyrko SA. Stability analysis of nanoscale surface patterns in ultrathin film coating. *Materials Physics and Mechanics*. 2022;48(2): 232-241. DOI: 10.18149/MPM.4822022\_8.

## 1. Introduction

Experimental studies have shown that roughness can be formed on free surfaces and interphases of film coatings at the stage of fabrication [1,2]. During exploitation, these defects evolve resulting in a deterioration in the quality of devices created on their basis. Also, surface roughness is able to provoke crack propagation at the film surface and interface [3]. Therefore, investigation of the processes leading to the growth of surface and interfacial defects in film coatings is an important technological problem. It should be noted that in most of the theoretical works, which have been aimed to understand the surface pattern formation in solids, the surface elasticity effect was neglected since it was believed to be relatively small in comparison with the bulk elastic behavior [4-6]. However, numerous experimental and theoretical results demonstrate that the impact of surface stress becomes important in the mechanics and thermodynamics of nanostructured materials [7-15].

In the present study, we propose a theoretical approach to the analysis of the surface morphological stability of the film coating with a thickness of less than 100 nm. The impact of the surface/interface elastic properties is taken into account based on the Gurtin–Murdoch surface/interface elasticity model [16,17]. It should be noted that there are different mechanisms leading to the surface rearrangement, e.g. surface and volume diffusion [5,18],

evaporation/condensation [19], contact fatigue, and corrosion [20]. However, the main interest of the present paper is to analyze the effect of surface elasticity on the surface evolution of the film coating due to surface diffusion driven by a nonuniform distribution of the chemical potential along the undulated surface. It is expected that the nonuniform distribution of the chemical potential along the surface is caused by changes in the stress field, surface energy, and surface curvature. We consider the evolution of the surface relief as a change in the amplitude of the periodic undulation. To derive the evolution equation, it is necessary to find the stress-strain state of the system under consideration. For this purpose, we formulate the plane elasticity problem for the thin film coating with undulated surface profile considering the relief evolution as a quasi-static process. The solution to the corresponding boundary value problem is derived using the approach proposed in [21]. After that, the governing equation is obtained that gives the amplitude change of surface undulation with time. Its analysis allows us to explore the effect of the physical and geometric parameters on the morphological stability of film surfaces.

## 2. Problem formulation

The model of an ultrathin film coating with thickness  $h_f$  in range 1 – 100 nm deposited on a substrate with thickness  $h_s \gg h_f$  under plain strain conditions is represented as an inhomogeneous elastic half-plane  $B = B_1 \cup B_2$  of the complex variable  $z = x_1 + ix_2$  ( $i^2 = -1$ ) with a curvilinear surface  $S_1$  and a rectilinear interface  $S_2$ :

$$\begin{aligned} S_1 &= \{z: z \equiv \zeta_1 = x_1 + i[h_f + \varepsilon(\tau)f(x_1)]\}, & S_2 &= \{z: z \equiv \zeta_2 = x_1\}, \\ B_1 &= \{z: 0 < x_2 < h_f + \varepsilon(\tau)f(x_1)\}, & B_2 &= \{z: x_2 < 0\}, \end{aligned} \quad (1)$$

$$f(x_1) = a \cos(bx_1), \quad b = 2\pi/a, \quad \varepsilon(\tau) = A(\tau)/a \ll 1 \quad \forall \tau, \quad A(0) = A_0.$$

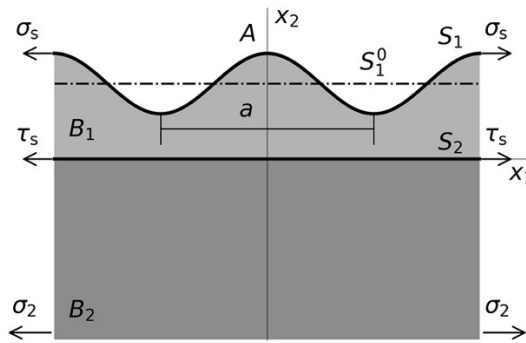


**Fig. 1.** The model of an ultrathin film coating with a slightly undulated surface

In accordance with the Gurtin–Murdoch surface/interface elasticity model, the surface and interphase domains are represented as negligibly thin layers adhering to the bulk without slipping [16, 17]. The constitutive equations of the surface/interface elasticity model are used in the assumption that the surface energy depends only on surface strains and does not depend on displacement gradients:

$$\sigma_{tt}^s(\zeta_j) = \gamma_j^0 + (\lambda_j^s + 2\mu_j^s)\varepsilon_{tt}^s(\zeta_j), \quad \sigma_{33}^s(\zeta_j) = \gamma_j^0 + (\lambda_j^s + \gamma_j^0)\varepsilon_{tt}^s(\zeta_j), \quad \zeta_j \in S_j, \quad (2)$$

where  $\sigma_{tt}^s$  is tangential surface/interfacial stress,  $\varepsilon_{tt}^s$  is tangential surface/interfacial strain,  $\gamma_j^0$  is residual surface/interfacial stress,  $\lambda_j^s$  and  $\mu_j^s$  are the Lamé parameters for the surface/interface domain.

The elastic behavior in the bulk phases of  $B_1$  and  $B_2$  is related by Hooke's law which takes the following form in the case of plane strain

$$\begin{aligned} \sigma_{nn}(z) &= (\lambda_j + 2\mu_j)\varepsilon_{nn}(z) + \lambda_j\varepsilon_{tt}(z), & \sigma_{nt}(z) &= 2\mu_j\varepsilon_{nt}(z), \\ \sigma_{tt}(z) &= (\lambda_j + 2\mu_j)\varepsilon_{tt}(z) + \lambda_j\varepsilon_{nn}(z), \end{aligned} \quad (3)$$

$$\sigma_{33}(z) = \lambda_j / (\lambda_j + \mu_j) [\sigma_{tt}(z) + \sigma_{nn}(z)], \quad z \in B_j.$$

In Eq. (3),  $\sigma_{\alpha\beta}$  and  $\varepsilon_{\alpha\beta}$  are the components of bulk stress and strain tensors, respectively, defined in the Cartesian coordinates  $(n, t)$  ( $\mathbf{n}$  is a normal to  $S_j$ ), and  $\lambda_j$  and  $\mu_j$  are the Lamé constants of the bulk phase  $B_j$ .

The conditions of mechanical equilibrium are formulated in the terms of the generalized Young–Laplace equation and in the case of simplified constitutive equations of Gurtin–Murdoch model can be written as

$$\sigma(\zeta_1) = \kappa(x_1)\sigma_s(x_1) - i \frac{1}{h} \frac{d\sigma_s(x_1)}{dx_1}, \quad \zeta_1 \in S_1, \quad (4)$$

$$\Delta\sigma(\zeta_2) = \sigma^+(\zeta_2) - \sigma^-(\zeta_2) = i \frac{d\tau_s(x_1)}{dx_1}, \quad \zeta_2 \in S_2, \quad (5)$$

where  $\sigma_s(x_1) = \sigma_{tt}^s(\zeta_1)$  is the surface stress,  $\tau_s(x_1) = \sigma_{tt}^s(\zeta_2)$  is the interfacial stress,  $\sigma = \sigma_{nn} + i\sigma_{nt}$  is the complex stress vector,  $\sigma^\pm = \lim_{z \rightarrow \zeta_{2\pm} i0} \sigma(z)$ ,  $h$  and  $\kappa$  are the metric coefficient and local curvature of  $S_1$ , respectively.

At infinity,  $\sigma_{\alpha\beta}$  ( $\alpha, \beta = \{1, 2\}$ ) in Cartesian coordinates  $(x_1, x_2)$  and the rotation angle of the material particle  $\omega$  are specified as

$$\lim_{x_2 \rightarrow -\infty} \sigma_{11} = \sigma_2, \quad \lim_{x_2 \rightarrow -\infty} \sigma_{22} = \lim_{x_2 \rightarrow -\infty} \sigma_{12} = \lim_{x_2 \rightarrow -\infty} \omega = 0. \quad (6)$$

It should be noted that the longitudinal stress can be a result of the lattice mismatch between the film and substrate materials [22]. Although it may also be caused by other factors, such as mechanical loading.

Since the surface/interface and bulk phases are assumed to be coherent, the boundary conditions are as follows

$$\varepsilon_{tt}^s(\zeta_1) = \varepsilon_{tt}(\zeta_1), \quad \zeta_1 \in S_1, \quad \Delta u(\zeta_2) = u^+(\zeta_2) - u^-(\zeta_2) = 0, \quad \zeta_2 \in S_2, \quad (7)$$

where  $u = u_1 + iu_2$  is complex displacement vector,  $u_1$  and  $u_2$  are displacements along axes  $(x_1, x_2)$  and  $u^\pm = \lim_{z \rightarrow \zeta_{2\pm} i0} u(z)$ .

During stress relaxation, the relief of the film surface may change. It is necessary to define the dependence of the relief amplitude  $A$  on the time  $\tau$  taking into account the surface diffusion and elastic deformation of film coating.

### 3. Linear stability analysis

It is assumed that the morphological evolution of the stressed film surface occurs due to the surface diffusion caused by the non-uniform distribution of the chemical potential along the surface. According to [23], the atomic flux along the film surface  $S_1$  is proportional to the gradient of the chemical potential  $\chi$

$$J(\zeta, \tau) = - \frac{D_s C_s}{k_b T} \frac{\partial \chi(\zeta, \tau)}{\partial s}, \quad (8)$$

where  $D_s$  is the self-diffusivity coefficient;  $C_s$  is the number of diffusing atoms per unit area;  $k_b$  is the Boltzmann constant,  $T$  is the absolute temperature and  $s$  is arc length along  $S_1$ .

Following [24], the local chemical potential of the surface can be defined as

$$\chi(\zeta, \tau) = [U(\zeta, \tau) - \kappa(\zeta, \tau)U_s(\zeta, \tau)]\Omega, \quad (9)$$

where  $\Omega$  is the atomic volume,  $U$  is the strain elastic energy density and  $U_s$  is the surface energy.

Considering atomic flow along the surface and taking into account mass conservation law we obtain the following evolution equation which gives the change of surface profile  $g(x_1, \tau) = \varepsilon(\tau)f(x_1)$  with time

$$\frac{\partial g(x_1, \tau)}{\partial \tau} = K_s h(x_1, \tau) \frac{\partial^2}{\partial s^2} [U(\zeta, \tau) - \kappa(\zeta, \tau)U_s(\zeta, \tau)], \quad K_s = D_s C_s \Omega^2 / (k_b T). \quad (10)$$

To integrate the partial differential equation (10) and derive the stability conditions, the elastic strain energy  $U$  and surface energy  $U_s$  along the film surface should be determined.

The elastic strain energy  $U$  can be written as [25]

$$U = \frac{1}{2} \sigma_{\alpha\beta} \varepsilon_{\alpha\beta}, \quad (11)$$

where the summation is implied over repeated indices.

It should be noted that in previous works aimed at studying the evolution of the surface microrelief, the effect of surface strains was assumed to be insignificant and the surface energy  $U_s$  was considered quantitatively equal to the residual surface stress  $\gamma_1^0$ . However, at the nanoscale, the effect of surface elasticity can be significant [6, 15]. So, in the case of a simplified Gurtin–Murdoch surface/interface elasticity model, the surface energy takes the form [26]

$$U_s = \gamma_1^0 (1 + \varepsilon_{tt}^s) + \frac{1}{2} (\lambda_1^s + 2\mu_1^s - \gamma_1^0) \varepsilon_{tt}^s \varepsilon_{tt}^s. \quad (12)$$

Thus, to solve evolution equation (10) it is necessary to know the stress-strain state of the film/substrate system. To this end, we use the solution of the plane strain problem for the nanosized film/substrate system with undulated surface profile, which was proposed in [21]. In accordance with the mentioned above paper, the original boundary value problem (1) – (7) is reduced to the system of integral equations using the boundary perturbation technique, Goursat–Kolosov complex potentials, Muskhelishvili representations for stress components, and the superposition principle. Since we study a weak change of the surface relief, the components of the stress and the strain tensors of the bulk and surface phases are defined using the first-order approximation of the boundary perturbation method [21,27,28]

$$\begin{aligned} \sigma_{ij} &= \sigma_{ij(0)} + \varepsilon \sigma_{ij(1)}, \quad \varepsilon_{ij} = \varepsilon_{ij(0)} + \varepsilon \varepsilon_{ij(1)}, \\ \sigma_{tt}^s &= \sigma_{tt(0)}^s + \varepsilon \sigma_{tt(1)}^s, \quad \varepsilon_{tt}^s = \varepsilon_{tt(0)}^s + \varepsilon \varepsilon_{tt(1)}^s. \end{aligned} \quad (13)$$

Unfortunately, the expressions for the components  $\sigma_{ij(0)}$ ,  $\sigma_{ij(1)}$ ,  $\varepsilon_{ij(0)}$ ,  $\varepsilon_{ij(1)}$ ,  $\sigma_{tt(0)}^s$ ,  $\sigma_{tt(1)}^s$ ,  $\varepsilon_{tt(0)}^s$ ,  $\varepsilon_{tt(1)}^s$  are not given in the paper due to their enormous size, although the detailed algorithm for their construction can be found in [21].

The linearization in the space of the parameter  $\varepsilon$  for the metric coefficient  $h$  and the curvature  $\kappa$  can be written as

$$\kappa(x_1, \tau) = \varepsilon(\tau) f''(x_1), \quad h(x_1, \tau) = 1. \quad (14)$$

Substituting (11) – (14) into (10), we obtain an ordinary differential equation the solution of which gives the amplitude as a function of time, physical and geometrical parameters

$$\ln(A(\tau)/A_0) = R(a, h_f, \lambda_1, \mu_1, \lambda_2, \mu_2, \lambda_1^s, \mu_1^s, \gamma_1^0, \lambda_2^s, \mu_2^s, \gamma_2^0, \sigma_2) \tau.$$

#### 4. Numerical results

As an example, consider a metal-on-metal system. We assume that the Poisson coefficients of the film and substrate materials are equal, i.e.  $\nu_1 = \nu_2$ . This simplification allows us to analyze the effect of the substrate through only one parameter, coating-to-substrate stiffness ratio  $r = \mu_1/\mu_2$ . The bulk Lamé parameters of the film coating correspond to aluminum and are equal to  $\lambda_2 = 58.17$  GPa and  $\mu_2 = 26.13$  GPa. To analyze the effect of surface/interface elasticity, we consider the surface/interface stiffness  $M_j = \lambda_j^s + 2\mu_j^s$ . The surface Lamé parameters for aluminum with the crystal lattice orientation (111) are obtained by molecular modelling in [29] and correspond to the longitudinal surface stiffness  $M_1 = 6.099$  N/m. However, the surface elastic constants depend on the crystallographic orientation and other factors [30], therefore, different values of surface/interface stiffness are considered below.

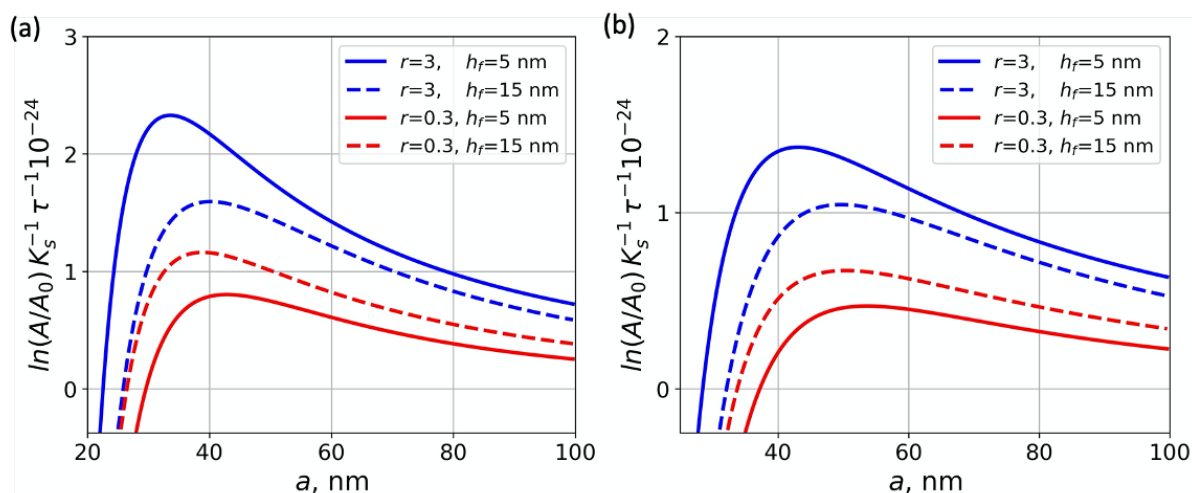


**Fig. 2.** The dependence of normalized amplitude change  $A(\tau)/A_0$  on the perturbation wavelength  $a$

Figure 2 shows the dependence of the normalized amplitude change  $A(\tau)/A_0$  of the film surface relief on the perturbation wavelength  $a$  for different stiffness ratio  $r = \{0.3; 3\}$  (red and blue lines, respectively), film thickness  $h_f = \{5; 15\}$  nm (solid and dashed lines, respectively) and surface stiffness  $M_1 = 6.099$  N/m (a) and  $M_1 = 60$  N/m (b). We take an underestimated value of the residual surface stress to conduct a qualitative analysis of the influence of the surface elastic parameters. Thus, the residual surface stress is assumed to be equal to  $\gamma_1^0 = 0.1$  N/m. The interface stiffness and residual stress are equal to  $M_2 = 6.099$  N/m and  $\gamma_2^0 = 1$  N/m, respectively. The critical wavelength  $a_{cr}$  corresponding to the thermodynamic equilibrium is found from the intersection of the lines with the abscissa. When the initial wavelength is less than the critical wavelength (i.e.  $a < a_{cr}$ ), the perturbation amplitude decreases with time and the relief is smoothed out. If the initial wavelength is greater than the critical wavelength (i.e.  $a > a_{cr}$ ), the undulation amplitude increases with time. The maximum amplitude change corresponds to a wavelength  $a_{max}$  which defines the unstable with the fastest growth rate. The wavelengths  $a_{cr}$  and  $a_{max}$  are presented in Table 1 and Table 2.

Table 1. The critical wavelength  $a_{cr}$  of film coating for various parameters

$M_1$ , N/m	6.099	6.099	60	60
$r$	0.3	3	0.3	3
$h_f$ , nm	$a_{cr}$ , nm			
5	29.6	22.6	37.1	28.6
15	29.6	26.1	33.6	32.1

Table 2. The wavelength  $a_{max}$  of film coating for various parameters

$M_1$ , N/m	6.099	6.099	60	60
$r$	0.3	3	0.3	3
$h_f$ , nm	$a_{max}$ , nm			
5	42.6	33.6	53.6	43.1
15	39.1	40.1	50.6	49.6

The critical wavelength is greater when the substrate is stiffer than the film (i.e., at  $r < 1$ ). As can be seen from the results, the effect of the stiffness ratio increases when the thickness of the film coating decreases. When  $M_1 = 6.099$  N/m and  $h_f = 15$  nm, the influence of stiffness on the critical perturbation wavelength is insignificant. The wavelengths  $a_{max}$  increase with increasing surface stiffness  $M_1$ .

The effect of the interface stiffness  $M_2$  and residual interface stress  $\gamma_2^0$  on the morphological stability of the film surface has been also investigated. It was obtained that the critical wavelength of the film surface undulation marginally depends on interface parameters. In this regard, the interface stiffness and residual stress are assumed to be zero, i.e.  $\gamma_2^0 = 0$  and  $M_2 = 0$ , in further analysis.

The dependence of the critical surface perturbation wavelength  $a_{cr}$  on surface stiffness  $M_1$  and coating-to-substrate stiffness ratio  $r$  is shown in Fig. 3a and Fig. 3b, respectively. The critical wavelength  $a_{cr}$  increases with increasing surface stiffness  $M_1$ . The impact of the stiffness ratio is greater for films with smaller thickness and surface stiffness. The critical wavelength does not depend on the film thickness when the stiffness of the film and substrate materials are equal to each other (i.e.,  $r = 1$ ). In this case, the critical perturbation wavelengths correspond to an uncoated solid surface.

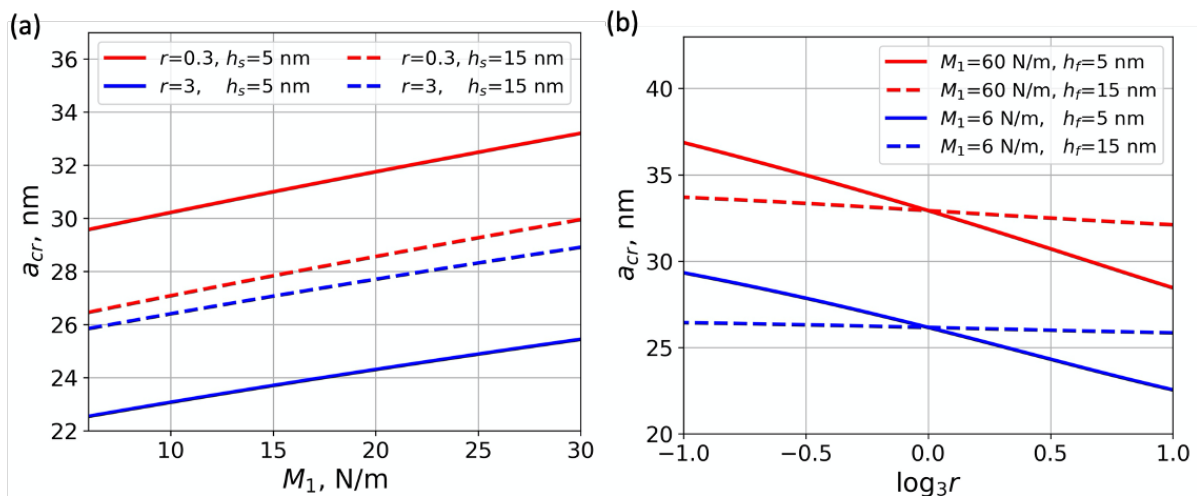


**Fig. 3.** The dependence of critical undulation wavelength  $a_{cr}$  on surface stiffness  $M_1$  and stiffness ratio  $r$

The dependence of critical undulation wavelength  $a_{cr}$  on residual surface stress  $\gamma_1^0$  for  $r = 0.3$  (a) and  $r = 3$  (b) is plotted in Fig. 4. The critical wavelength  $a_{cr}$  increases with increasing of  $\gamma_1^0$ . In addition, the effect of residual surface stress on the morphological stability of the film surface is greater when the film is stiffer than the substrate (i.e., when  $r = 0.3$ ). Also, the impact of the residual surface stress increases with decreasing film thickness in this case. If the substrate stiffness is less than the film stiffness (i.e.  $r > 1$ ), the influence of the residual surface stress on critical wavelength is marginally dependent on film thickness and the surface stiffness.

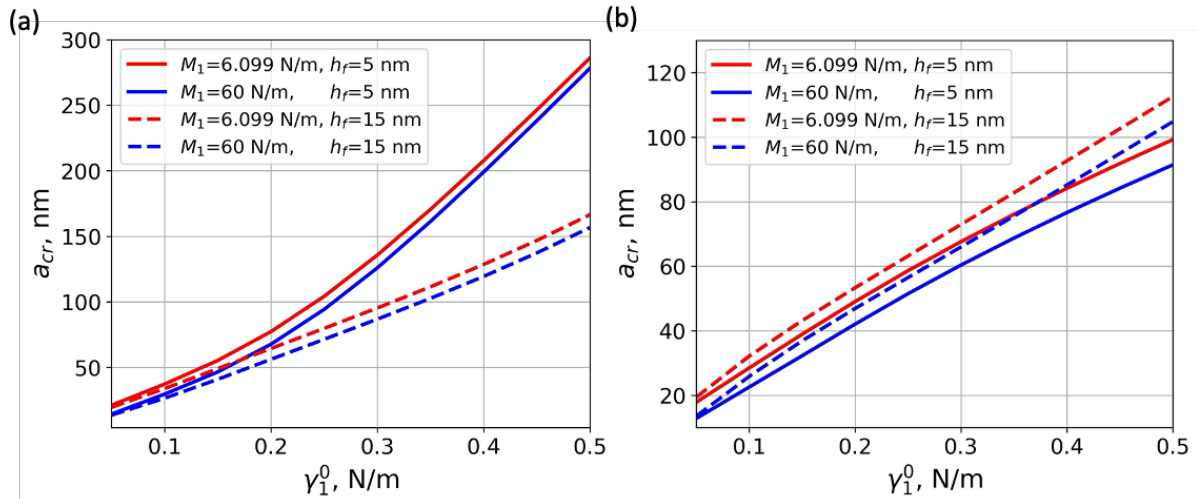


**Fig. 4.** The dependence of critical undulation wavelength  $a_{cr}$  on residual surface stress  $\gamma_1^0$

Figure 5 demonstrates the dependence of critical undulation wavelength  $a_{cr}$  on its thickness  $h_f$  for different stiffness ratio  $r = \{0.3, 3\}$  (blue and red lines, respectively),  $M_1 = 6.099$  N/m (a) and  $M_1 = 60$  N/m (b). The results show that the critical wavelength increase/decrease and tend to the critical wavelength corresponding to an uncoated solid surface with an increasing thickness of the film coating, which stiffness is greater/less than the substrate stiffness. The influence of the film thickness increases with an increasing surface stiffness  $M_1$ . The threshold thickness, exceeding which we can ignore the impact of a substrate, increases with increasing surface stiffness.

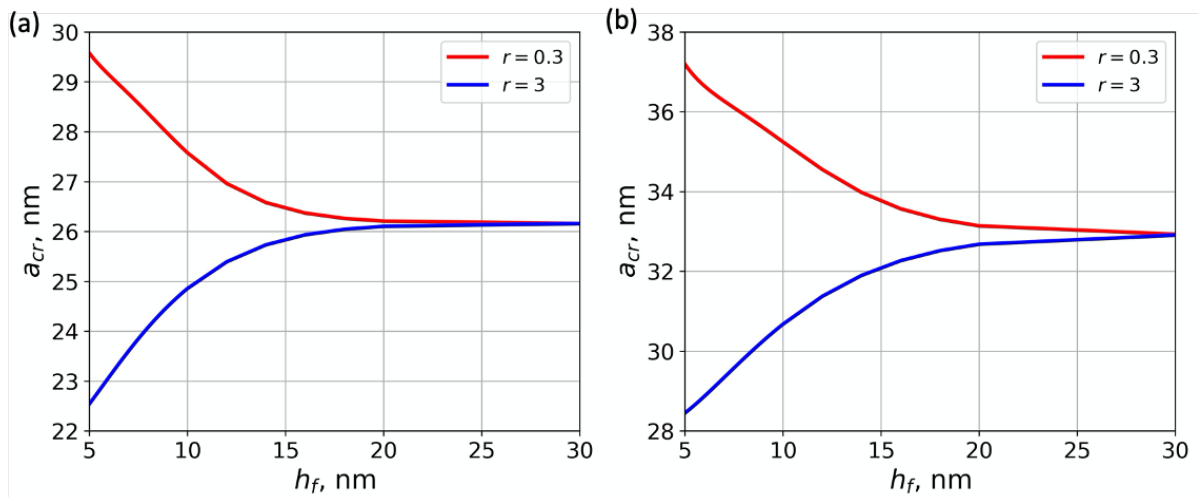


**Fig. 5.** The dependence of normalized deviation amplitude change  $A(\tau)/A_0$  on the initial hole radius  $a$

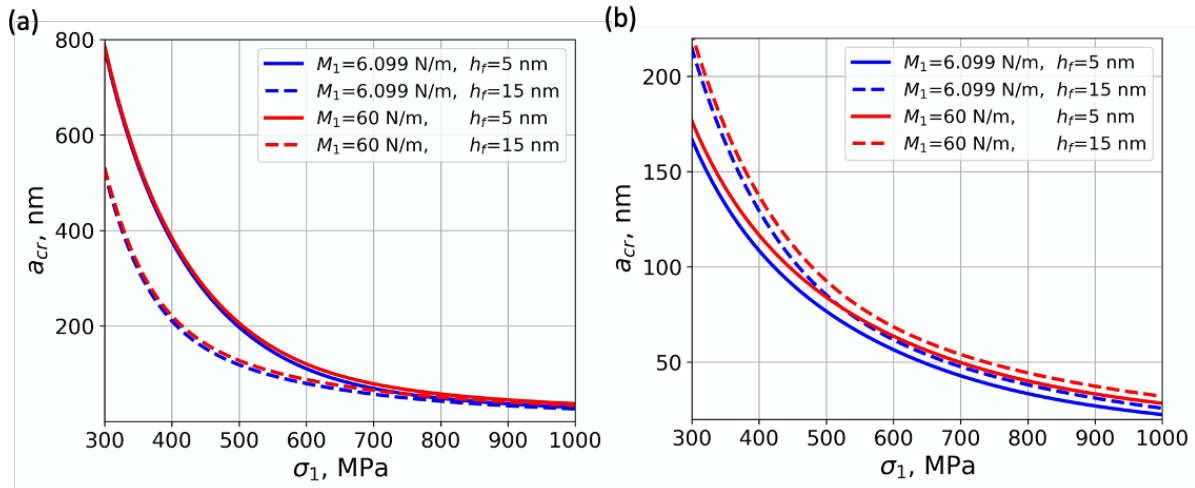


**Fig. 6.** The dependence of critical undulation wavelength  $a_{cr}$  on longitudinal stress  $\sigma_1$

The dependence of critical undulation wavelength  $a_{cr}$  on longitudinal stress  $\sigma_1$  for different surface stiffness  $M_1 = \{6.099; 60\}$  N/m (blue and red lines, respectively), film thickness  $h_f = \{5; 15\}$  nm (solid and dashed lines, respectively), and stiffness ratios  $r = 0.3$  (a) and  $r = 3$  (b) is shown in Fig. 6. One can see that the critical wavelengths decrease with increasing  $\sigma_1$ . The impact of surface stiffness increases with increasing longitudinal stress.

## 5. Conclusion

In this paper, a theoretical approach to the analysis of the surface morphological stability of the ultrathin film coating is developed. The impact of the surface/interface elastic properties is taken into account based on the Gurtin–Murdoch surface/interface elasticity model. It was assumed that the surface evolution of the film coating occurs due to surface diffusion driven by a nonuniform distribution of the chemical potential along the undulated surface. It was also postulated that the nonuniform distribution of the chemical potential along the surface is caused by changes in the stress field, surface energy, and surface curvature. The evolution of the surface relief was considered as a change in the amplitude of the periodic undulation.

The effect of coating-to-substrate stiffness ratio, elastic parameters of surface and interface, film thickness, residual surface/interface stress, and longitudinal stress were investigated. The following results were obtained:

- the interface stiffness and residual interface stress do not affect the morphological stability of the film coating surface;
- the critical perturbation wavelength increases with increasing surface stiffness, residual surface stress as well as with decreasing longitudinal stress and coating-to-substrate stiffness ratio;
- the effect of surface stiffness decreases with an increase in residual surface stress and a decrease in longitudinal stress;
- the critical perturbation wavelength increases/decreases with increasing film thickness when the film is stiffer/softer than the substrate;
- the impact of the substrate decreases with increasing film thickness;
- the threshold coating thickness, exceeding which it is possible to ignore the substrate, increases with an increase in surface stiffness and surface residual stress.

## References

- [1] Shang L, Xu B, Ma S, Liu Q, Ouyang H, Shan H, Hao X, Han B. The Surface Morphology Evolution of GaN Nucleation Layer during Annealing and Its Influence on the Crystal Quality of GaN Films. *Coatings*. 2021;11(2): 188.
- [2] Wei L, Chunlei S, Miao C, Xiaosong Z, Xinggui L. The surface morphology evolution of ZrSi<sub>2</sub> films under different substrate temperature. *Materials Research Express*. 2019;6(11): 116458.
- [3] Pronina Y, Maksimov A, Kachanov M. Crack approaching a domain having the same elastic properties but different fracture toughness: Crack deflection vs penetration. *International Journal of Engineering Science*. 2020;156: 103374.
- [4] Colin J, Grilhe J, Junqua N. Morphological instabilities of a stressed pore channel. *Acta Materialia*. 1997;45: 3835-3841.
- [5] Freund LB. Evolution of waviness on the surface of a strained elastic solid due to stress-driven diffusion. *International Journal of Solids and Structures*. 1995;28: 911-923.
- [6] Duan HL, Weissmuller J, Wang Y. Instabilities of core-shell heterostructured cylinders due to diffusions and epitaxy: spheroidization and blossom of nanowires. *Journal of the Mechanics and Physics of Solids*. 2008;56: 1831-1851.
- [7] Cammarata RC. Surface and interface stress effects in thin films. *Progress in Surface Science*. 1994;46(1): 1-38.
- [8] Fischer FD, Waitz T, Vollath D, Simha NK. On the role of surface energy and surface stress in phase-transforming nanoparticles. *Progress in Materials Science*. 2008;53: 481-527.
- [9] Grekov MA, Kostyrko SA. Surface effects in an elastic solid with nanosized surface asperities. *International Journal of Solids and Structures*. 2016;96: 153-161.
- [10] Shuvalov GM, Kostyrko SA. Surface self-organization in multilayer film coatings. *AIP Conference Proceedings*. 2017;1909: 020196.
- [11] Chan SW, Wang W. Surface stress of nano-crystals. *Materials Chemistry and Physic*. 2021;273: 125091.
- [12] Dai M, Schiavone P. Deformation-Induced Change in the Geometry of a General Material Surface and Its Relation to the Gurtin–Murdoch Model. *Journal of Applied Mechanics*. 2020;87(6): 061005
- [13] Javili A, Bakiler AD. A displacement-based approach to geometric instabilities of a film on a substrate. *Mathematics and Mechanics of Solids*. 2019;24(9): 2999-3023.
- [14] Mikhasev GI, Botogova MG, Eremeyev VA. On the influence of a surface roughness on propagation of anti-plane short-length localized waves in a medium with surface coating. *International Journal of Engineering Science*. 2021;158: 103428.
- [15] Zhao X, Duddu R, Bordas S, Qu J. Effects of elastic strain energy and interfacial stress on the equilibrium morphology of misfit particles in heterogeneous solids. *Journal of the Mechanics and Physics of Solids*. 2013;61(6): 1433-1445.
- [16] Gurtin ME, Murdoch AI. A continuum theory of elastic material surfaces. *Archive for Rational Mechanics and Analysis*. 1975;57(4): 291-323.
- [17] Gurtin ME, Murdoch AI. Surface stress in solids. *International Journal of Solids and Structures*. 1978;14: 431-440.
- [18] Panat R, Hsiaa KJ. Evolution of surface waviness in thin films via volume and surface diffusion. *Journal of Applied Physics*. 2005;97: 013521.
- [19] Srolovitz DJ. On the stability of surfaces of stressed solids. *Acta Metallurgica*. 1989;37(2): 621-625.
- [20] Ryu JJ, Shrotriya P. Influence of roughness on surface instability of medical grade cobalt–chromium alloy (CoCrMo) during contact corrosion–fatigue. *Applied Surface Science*. 2013;273: 536-541.

- [21] Kostyrko SA, Altenbach H, Grekov MA. Stress concentration in ultra-thin coating with undulated surface profile. In: *Proceedings of the 7th International conference on coupled problems in science and engineering*. 2017. p.1183-1192.
- [22] Gao H, Nix WD. Surface roughening of heteroepitaxial thin films. *Annual Review of Material Science*. 1999;29: 173-209.
- [23] Asaro RJ, Tiller WA. Interface morphology development during stress-corrosion cracking: Part I. Via surface diffusion. *Metallurgical and Materials Transactions*. 1972;3: 1789-1796.
- [24] Freund LB, Suresh S. *Thin film materials: stress, defect formation and surface evolution*. New York: Cambridge University Press; 2004.
- [25] Novozhilov VV. *Theory of elasticity*. Oxford: Pergamon Press; 1961.
- [26] Ru CQ. Simple geometrical explanation of Gurtin – Murdoch model of surface elasticity with clarification of its related versions. *Science China: Physics, Mechanics and Astronomy*. 2010;53(3): 536-544.
- [27] Grekov MA, Vakaeva AB. The perturbation method in the problem on a nearly circular inclusion in an elastic body. In: *Proceedings of the 7th International Conference on Coupled Problems in Science and Engineering, COUPLED PROBLEMS 2017*. International Center for Numerical Methods in Engineering; 2017. p.963-971.
- [28] Vakaeva AB, Krasnitckii SA, Grekov MA, Gutkin MY. Stress field in ceramic material containing threefold symmetry inhomogeneity *Journal of Materials Science*. 2020;55(22): 9311-9321.
- [29] Miller RE, Shenoy VB. Size-dependent elastic properties of nanosized structural elements. *Nanotechnology*. 2000;11: 139-147.
- [30] Shenoy VB. Atomistic calculations of elastic properties of metallic fcc crystal Surfaces. *Physical Review B*. 2005;71: 094104.

## THE AUTHORS

### **Shuvalov G.M.**

e-mail: g.shuvalov@spbu.ru  
ORCID: 0000-0002-9039-4888

### **Kostyrko S.A.**

e-mail: s.kostyrko@spbu.ru  
ORCID: 0000-0003-3074-0969

## FAILURE ANALYSIS OF SEMI-ELLIPTICAL CRACK BEHAVIOR IN THE CEMENT MANTLE OF A TOTAL HIP PROSTHESIS

Samir Zahaf<sup>1✉</sup>, Mouloud Dahmane<sup>2</sup>, Azzeddine Belaziz<sup>3</sup>, Ismail Bouri<sup>4</sup>,  
Nasreddine Afane<sup>5</sup>

<sup>1</sup>Department of Technology, University of Djilali Bounaama-KhamisMeliana, AinDefla-Algeria

<sup>2</sup>Department of planning and hydraulic engineering, Higher National School of Hydraulics, Blida 9000, Algeria;  
LMA, USTO-MB, Oran 31000, Algeria

<sup>3</sup>Mechanical Research Center Constantine (CRM), University campus of châaberssas, Constantine, 25017,  
Algeria

<sup>4</sup>Department of Mechanical Engineering, Mostaganem University-Abdelhamid Ibn Badis, Algeria

<sup>5</sup>Department of Mechanical Engineering, National Polytechnic School of Oran -MA, BP 1523 ElMnaour, Oran,  
Algeria

✉ samir.zahaf@univ-dbk.m.dz

**Abstract.** Numerical modeling by finite element method offers valuable information and details on the mechanical behavior of the prosthesis in terms of stress and strain distribution, load transfer, stress intensity factors, etc. An explicit analysis conducted on the behavior of microcavity and cracking in PMMA surgical cement (polymethyl methacrylate) used for a total hip prosthesis (THP) is of great importance in collecting information about the nature of the loosening phenomenon of the cement application. The rupture of orthopedic cement is practically the main cause of this loosening. Understanding the different failure mechanisms provides a significant advance in the cemented total prostheses. To do this, a numerical analysis by 3D finite element method (FEM) model of the total hip prosthesis was carried out in order to evaluate the stress levels in the different components. We focused on the effect of the microcavity rotation and the semi-elliptical crack position on the stress distribution in THP elements and on the orthopedic cement, which represents the weakest link of the prosthesis. We concluded that the two mechanical defects (Microcavity, semi-elliptical crack) exhibit more intense stresses in the THP components and record a very intense stress level and stress intensity factor KI. These mechanical defects causing damage to the PMMA around the tip of the bone debris increase the loosening state of the total hip prosthesis.

**Keywords:** finite element method, mechanical, crack, microcavity, prosthesis, orthopedic cement, stress von Mises, strain, stress intensity factors

**Acknowledgements.** No external funding was received for this study.

**Citation:** Zahaf S, Dahmane M, Belaziz A, Bouri I, Afane N. Failure analysis of semi-elliptical crack behavior in the cement mantle of a total hip prosthesis. *Materials Physics and Mechanics*. 2022;48(2): 242-271. DOI: 10.18149/MPM.4822022\_9.

**Abbreviation:**

(THP): total hip prosthesis, (FEM): finite element method, (SIF): stress intensity factors, (THR): Total hip replacement, (THA): total hip arthroplasty, (PMMA): polymethyl-methacrylate, PEEK: Polyether Ether Ketone, (TKA): total knee artificial, (UHMWPE): Ultra High Molecular Weight Polyethylene, coxal-bone (pelvis).

**1. Introduction**

Total hip replacement is an intervention of a biological articulation with a prosthesis; her effectiveness depends on the quality of reconstruction, architecture, the mechanics of the hip, integrity, and equilibrium, for those used as medical implants for orthopaedic and dental surgery (80,000 hip replacements and 30,000 knee prostheses are implanted annually worldwide). According to the Swedish register of total hip replacement over a period of 19 years, 7.1% of patients who underwent cement less total hip arthroplasty will need a second surgery for replacing the first; this number is 13% for patients who underwent cement less (THA). The main reason for revisions (THA) is aseptic loosening in 71% of cases, followed by infection in 7.5% (Herberts and Malchau, 2000 [1]).

During a total hip arthroplasty, the surgeon replaces the two surfaces of the natural joint produced by the interlocking of the femoral head in the acetabulum of the hip iliac bone with two prosthetic components [1-5], Fig. 1:

- The cup is placed in the acetabulum after removal of the cartilage: this is the fixed part of the joint.
- The femoral implant is anchored in the medullary canal after resection (surgical removal) of the femoral neck and partial recess of the canal: this is the mobile part.

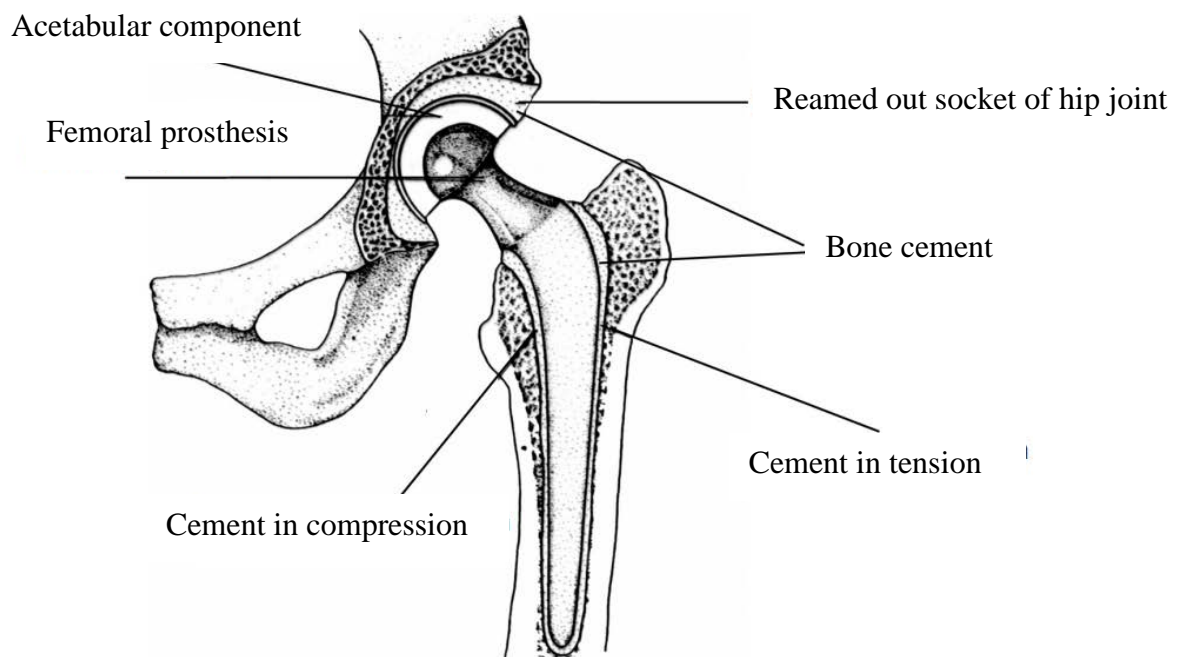


**Fig. 1.** Schematic diagram of prostheses and polymethyl-methacrylate (PMMA), bone cement in an acetabular socket and femur [6]

Operation of total hip replacement shows the increasing numbers and be successful. The cemented system is most widely used in total hip replacement. Reliability of the THR is important to the patient, orthopedics, and surgeons. Therefore, improved design, technology, and materials for inserting hip replacements are highly needed. This also includes whether the

design of the THR is cemented or uncemented. Bone cement is widely used to affix hip implants to the bone during total hip arthroplasty; therefore, many studies have been performed to investigate the reliability of cement mantle in a total hip replacement [7-8].

Sir John Charnley et al. used a cold-curing acrylic resin, surgical-grade polymethyl-methacrylate, for the fixation of prostheses in the supporting bone, that the long term stability of metal implants was achieved. PMMA is the only material currently used for anchoring prostheses in bone during cemented arthroplasties [9].

Fisher et al. observed the effect of the cement mantle thickness on strains on total hip replacement experimentally on stem components. The study was conducted on two stem components by varying the thickness of the cement mantle. Strain gauges were embedded in the cement mantle, and then the stem components were subjected to an axial load in walking and standing conditions.

The results showed that an increase in cement mantle thickness from 2.4 to 3.7 mm can decrease the strain on the cement mantle by about 40%-49%, so they concluded that by increasing cement mantle thickness the fatigue life of an implant may be increased [10].

Jamari et al. studied and analyzed an additional layer of cement mantle hip joints to reduce cracks [11]. A previous study showed that adding a metallic layer between the liner and the acetabulum could reduce the stress at the contact surface of the cement mantle. Several material properties of the layer were simulated using finite element analysis for maximum performance. Static contact analysis was used to simulate the stresses at the contact surface of the cement mantle. The results show that an additional layer of cobalt-chromium produced the best performance.

Ajay Kumar et al. studied and analyzed the effects of interfacial crack and implant material on mixed-mode stress intensity factor and prediction of interface failure of the cemented acetabular cup. A three-dimensional (3D) finite element (FE) model of implanted pelvic bone was developed based on the computed tomography (CT) scan data. Combinations of four materials were considered for implant material. The results show that the material properties of the implant play a vital role in interface failure. The values of KI and KII decrease as the implant material changes from UHMWPE-CoCrMo to the ceramic-ceramic material combination. This result suggested that the ceramic-ceramic material combination will perform better than other combinations [12].

Abdel-Wahab and Silberschmidt experimentally and numerically studied the dynamic behavior of a fracturing impact in the cortical bone tissue, using X-FEM [13]. Another study by Milena Babić et al. studied the fatigue life of a loosened total hip prosthesis femoral component cemented into bone and was investigated assuming loads specified by the standard ISO 7206-4. The total hip prosthesis CAD model was developed by implementing a 3D scanning procedure. Based on the created CAD model, the FE model was developed. A linear elastic analysis was carried out for the created FE model of the prosthesis. The analysis showed that high tensile stresses occur on the distal region of the femoral component shaft on the anterior lateral side, where fatigue cracks occur in real cases. This procedure can be implemented in other components where the geometry needs to be reconstructed by 3D scanning [14].

Ramos et al. experimentally observed that the position of an implant in the femur and assemblage with the femoral canal were two important issues in the formation mechanism of cracks between the two surfaces (bone-cement, cement-implant) [15].

Griza et al. analysed with FEM the stress distribution of the acetabular part in the (THP) using screw fixation. The analysis showed that it took a large amount of computational force to predict screw fracture in the case of the unbounded metal-backed and bone interface [16].

Latham Krista et al. Modelling of femur fracture using finite element procedures [17].

Najafi et al. simulated the cortical bone with the presence of micro-cracks. They showed that cracks propagation was strongly influenced by bone density, thus, suggesting that bone fracture toughness should be provided, at least in part, in such a manner that bone density could be quantified [18].

Milena Babić et al. studied and analyzed a fracture by the finite element of a loosened femoral component shaft of the total hip prosthesis damaged with a crack was performed assuming loading and boundary conditions given by the standard ISO 7206-4. In the femoral component shaft, a damaged crack was modelled, where several crack depths were considered. Mode I stress intensity factor KI values were calculated for nodes along the crack front for each of the considered crack depths. It was demonstrated that for the given loading conditions a critical crack size associated with fracture onset could be estimated [19]. Several experimental procedures have been carried out on the cement, showing the existence of cracks emanating from cavities within the body (McCormack and Prendergast, 1999). These cracks are mainly responsible for the loosening of the total hip prostheses [20].

EkoSaputra et al. investigated the effect of the layer variation between the liner and the cement mantle on the reduction of hip joint cracks in polymethyl-methacrylate material. Failure of cement mantle, and bond loosening between liner and cement mantle are important issues in total hip replacement. Two factors that are common because of cement mantle failure are initial crack and stress. A solution for reducing stress on the cement mantle consists to insert the material between the liner and cement mantle. Nevertheless, further study is needed to optimize the proposed solution. A potential option is to vary the insertion material thickness. If the polymethyl-methacrylate material thickness is constant, the insert thickness variation will be followed by the liner thickness variation. Consequently, the stress value in the liner will follow the liner thickness variation. Results revealed that stress magnitude and deflection decreased in the cement mantle and the liner with insert material thickness increased [21].

Lennert de Ruiter et al. studied and determined the quality of the implant-cement interface of a PEEK femoral TKA component and compare it to a CoCr implant. Implants were subjected to clinically relevant loading and motions for up to 10 million cycles (MC) in a knee simulator and a method was developed to assess the bonding between the implant and cement and the integrity of the cement mantle. It was hypothesized that, due to the difference in thermal conductivity and modulus of the implant materials, the bonding at the cement-implant interface and the cracking of the cement would differ between implant materials and that PEEK would show more debonding and cracks in the cement mantle than CoCr. This was a preliminary study to establish a method to evaluate the implant-cement interface and as such was carried out with small sample size. The results show poor initial bonding of the PEEK-cement interface; however, after 10 MC simulations, the bonding of the implant remained similar to that of the controls. For CoCr implants, good fixation was measured for the gait control samples, but, after 10 MC, substantial implant-cement interface debonding occurred. After 10 MC, there was no significant difference in implant-cement debonding for the femoral component materials investigated, nor were there significant differences in macroscopic damage of the cement mantle. Further investigations either using a more physiologically relevant simulation system or through either animal studies or a clinical trial may be necessary to confirm these findings [22].

Aleksandar Sedmak et al. studied and analysed fatigue crack growth in hip implants by the extended finite element method. Toward, the three-dimensional finite element model is created and used in ABAQUS and Morfeo/crack add-in for ABAQUS to simulate fatigue crack growth from initial value up to the critical point. Initial crack dimensions are assumed according to the experience with failures of hip implants, whereas the final, critical value was estimated using data for fracture toughness obtained by experimental testing of hip implants

made of Ti-6Al-4V alloy. Results for the equivalent stress intensity factor and number of cycles in each of 40 steps of fatigue crack growth are presented and analysed, indicating the point of unstable crack growth [23].

SaitKocak et al. investigated the strength effect of both implant-cement and cement-bone interfaces in a cemented implant. The effects of different implant materials, blasting sand particle size and cement mantle thickness on strength impact were investigated. The results show that surface roughness values of implant materials increased as larger blasting sand particles were applied. On the other hand, interfacial strength impact increase with surface roughness increase. The cement-bone interface strength was higher than the implant-cement interface. The optimum mantle thickness in terms of impact strength was found to be 2 mm under impact force, failure will occur at the implant-bone cement interface [24].

Cherfi et al. studied the effect of inclusion in some cement zones where loading conditions can lead to crack opening leading to their propagation and consequently aseptic THR loosening. The fracture behavior of bone cement includes a strange body (bone remains) from which crack onset is supposed. The loading conditions effect, geometry, presence of both crack and inclusion on stress distribution, and fracture behavior of the cement. The results obtained by the authors indicated that the highest stresses are located around the sharp tip of bony inclusion. Most critical cracks are located in the middle of the cement mantle when they are subjected to one leg standing state loading during walking [25].

Ali Benouis et al. studied the cracks behavior, initiated in the cement connecting the femoral stem with the bone, using FEM analysis. Their study is focused on stress intensity factor variation in modes I, II, and III. This rupture criterion is used according to crack nature, orientation, and location in the orthopedic cement. First, the von Mises stress level and distribution are analyzed, induced in the medial, proximal, and distal parts of the bone cement. Then, the behavior of different geometric forms of an elliptical crack is evaluated which are located and initiated within the body of these three parts [26].

Among the problems encountered by experts in cemented arthroplasty is the occurrence of defects in the cement. These defects can locally generate stress concentration zones producing potential cement rupture. In general, there are three defect types: porosities, inclusions, and cracks [26]. It is well known that cracks are the most dangerous defects due to high induced stress intensity. Three types of cracks can be identified in orthopedic cement [27]:

- Cracks initiated on voids (cavities during shrinkage).
- Cracks initiated during cement polymerization, when it has not yet hardened.
- Cracks initiated in the cement due to internal stresses.

Crack propagation can lead to abrupt rupture, and then prosthesis loosening. The concept of linear elastic fracture mechanics, such as stress intensity factors, the rate of energy release, etc., accurately describes crack behavior in brittle materials according to geometry and loading conditions.

The use of these concepts can be an effective tool to analyze orthopedic cement fracture behavior, which provides a predictive tool for an effective assessment of pre/post-cemented acetabular reconstruction operations. Despite numerous studies on cement fatigue [28] and developed finite element models of damage increase in the cement mantle [29], crack propagation has not yet been addressed using appropriate fracture mechanics techniques [30].

1-The aim of this study is to carry out a numerical study on the effect of femoral stem position on stress distribution in the orthopedic cement without defects. Next, we will present a detailed analysis of the microcavity position effect in the cement in order to locate stress concentration areas that represent potential sites of damage and microcracks initiation.

2- Crack behavior analysis in the reconstructed acetabular cement by stress intensity factor and J-integral assessment along the crack front. The finite element method is used to achieve this goal. The effects of both crack positions have been highlighted.

## 2. Three-dimensional numerical model

**Geometrical model and boundary conditions.** The three-dimensional geometrical model of the hip prosthesis is shown in Fig. 2 and Fig. 3. A polyethylene cup with an outside diameter of 54 mm had been sealed to an acetabulum of diameter 56 mm. The normal weight of a man with this acetabulum diameter is around 80 kg [29]. The cement layer thickness is 3 mm while the cup's internal diameter is 28 mm [30].

Figure 2 (a) and (b) show the reconstructed acetabulum geometrical model. This model has the advantage of getting closer to the real structure. The total hip prosthesis components are hip bone, cement, implant, and cup are clearly defined. The reliability of obtained results requires a very refined mesh, especially at the cement level considered as a determining prosthesis element.

The boundary conditions used in our case are:

1. A fixed embedment ( $U_x = U_y = U_z = R_x = R_y = R_z = 0$ ) on the pubis and on the iliac bone wing (see Fig. 4 (b)).
2. A concentrated load of 2400N was applied to the implant (see Fig. 4 (b)) [31].
3. We considered continuous rigid contact at the bone-cement and cup cement interfaces and a frictionless and non-interpenetrable interaction at the implant-cup interface (these conditions made by the code Ansys Workbench).

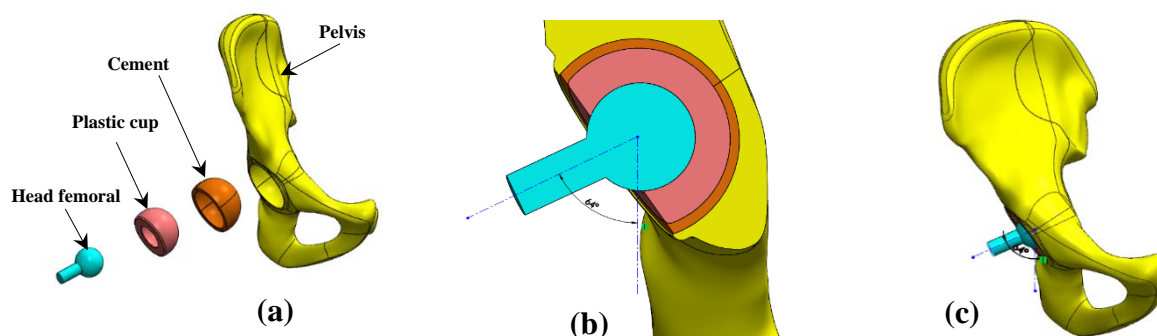


**Fig. 2.** 3D model of the total hip prosthesis by software SolidWorks, (a): exploded view of the THP, (b): cross-sectional view, (d): assembled view

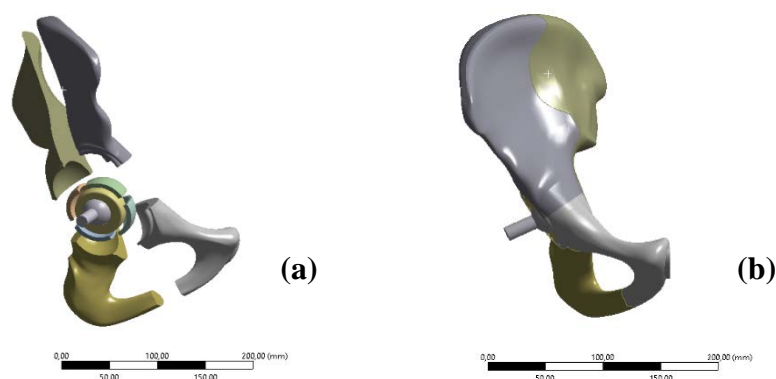


**Fig. 3.** Geometric model of the total hip prosthesis by the code AnsysWorkbench, (a): exploded view, (b): isometric view

This model permits the reproduction of all movement phases by just changing the applied force direction [32]. The loading cases analyzed in this study correspond to  $\alpha = 64^\circ$  (femoral head is in contact with one end of the cup). A large area of the cement's left part is under tension. It is generally known that cement does not well withstand tensile loading. The cement tensile, compressive, and shear strength are 25 MPa, 80 MPa, and 40 MPa respectively [33].

**Finite Element Model.** Numerical methods such as the finite element method are widely accepted in orthopedic biomechanics as an important tool used to design and analyze prosthesis mechanical behavior [34]. Several authors have used this method to analyze hip prosthesis mechanical behavior, Colombi [35-40].

The contribution in this area is based on crack behavior analysis in the cement layer which connects the acetabular cup to the adjacent bone, by evaluating the stress intensity factor along the crack front. This was done using the commercial finite element AnsysWorkbench [41-46]. A three-dimensional finite element model of the reconstructed acetabulum is studied, Fig. 4 (a). A 10-node tetrahedral element is used to mesh the hip bone and all other prosthesis components (Fig. 4 (a)). An appropriate refined mesh is performed in the cement, cup, and femoral stem to improve accurate results, Fig. 4 (a).

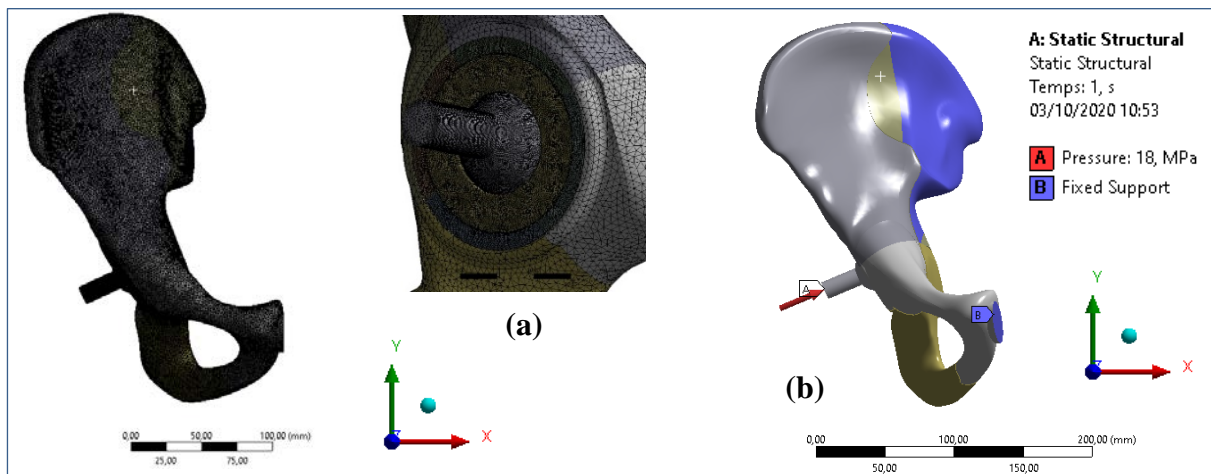


**Fig. 4.** (a): Total hip prosthesis mesh, (b): boundary conditions

### 3. Material Properties

Several types of materials were used for prosthesis components in this simulation. These materials are summarized in Table 1. All previous studies have assumed that the coxal-bone (pelvis) is divided into two components (cortical and cancellous) and each component takes on an elastic and isotropic behavior. Consequently, knowledge of the stress intensities and their distribution in the cement fixing the cup is of great importance for understanding the condition of the prosthesis in service and its loosening. On the other hand, for the boundary conditions, i.e. a fixed embedding at the level of the pelvis plus a force  $F$  is applied to the center of the femoral head, the interfaces between the cement, the pelvic bone, the plastic cup are perfectly glued (completely bonded). However, in this study, we propose that the coxal bone contains a single solid element called the cortical bone, which takes on an elastic and isotropic behavior. According to Anderson et al. [47], Fadela Allaoua et al. [48], and Ouinas et al. [49], the coxal bone has an elasticity modulus of 20000 MPa and Poisson's ratio of 0.25. Material for the cement mantle is adopted from Fadela Allaoua et al. [48], Ouinas et al. [49], and Azari Fahimeh et al. [50] with Young's modulus ranging from 2000 to 2300 MPa and Poisson's ratio of 0.3. Cement properties are: tensile strength 25 MPa, compressive strength 80 MPa (Rodriquez et al. [51]), shear strength 40 MPa (Merckx, [52]) and fatigue

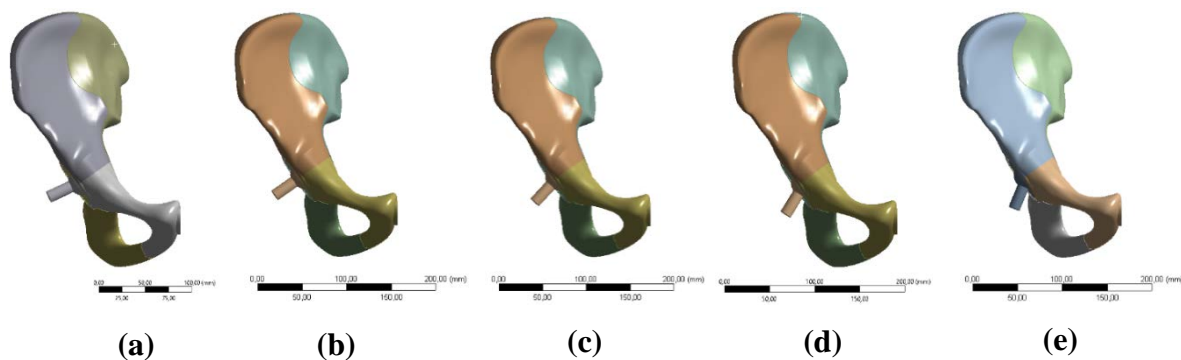
(108 cycles) 14 MPa (Pilliar et al. [53], Solt'esz. [54]). Ries et al. [55] found that the critical stress intensity factors KIC are between 0.96 MPa $\sqrt{m}$  to 1.76 MPa $\sqrt{m}$ . The plastic cup has an elasticity modulus of 750 MPa and Poisson's ratio of 0.25. The cement, plastic cup, and femoral head are considered linear isotropic elastic materials.

Table 1. Elastic properties of materials

Materials	Young's modulus E [MPa]	Poisson coefficient $\nu$
Plastic cup	750	0.25
Cement (PMMA)	2000	0.25
coxal bone	20000	0.25
femoral head	210000	0.3

**Effect of implant position.** The analysis of the stress distribution in the different cavities of the orthopedic cement of the acetabular part requires different types of loading, characterized by the position of the neck of the implant with respect to the cup axis (Fig. 5). We have opted for three defined orientations of 0°, 10°, 20°, 30°, and 40° respectively which reflect human body postures.

The distribution and the level of stress in the orthopedic cement of the THP, according to these orientations were carried out by the finite element method.



**Fig. 5.** Implant position with respect to the cup axis (a):  $\alpha = 0^\circ$ , (b):  $\alpha = 10^\circ$  (c):  $\alpha = 20^\circ$  and (d):  $\alpha = 30^\circ$ , (e):  $\alpha = 40^\circ$

#### 4. Results and Discussions

**Distribution of von Mises stress in the hip bone-prosthesis structure.** We analyzed distribution and stress level for the first implant position (alignment of the implant neck on the cup axis, characterized by an orientation angle  $\alpha = 0^\circ$ ) Fig. 5 (a).

The latter shows that von Mises equivalent stress distribution is not homogeneous throughout the coxal bone-THP junction. High stresses of 44.453 MPa value are located in the femoral stem (outline in red). This results from the application of the concentrated load on a small area of the femoral neck. This stress will be transmitted from the implant neck to other prosthesis components. In the pelvis, maximal stresses are in the pelvis bone (approximately 19.48 MPa) see Fig. 7(a).

The second implant position corresponds to a neck implant orientation of 10° with respect to the cup axis. Results showed the equivalent stress distribution in the entire coxal bone junction. THP reaches a von Mises stress of 44.06 MPa due to the contribution of THP system components. The third position of the implant corresponds to a 20° orientation of the implant neck relative to the axis of the cup. Such an orientation favors the increased stresses by the embedding Fig. 6 (c). We find that compared to an alignment of the implant on the axis

of the cup, the stress intensity can reach too high a level (around 121.12 MPa) greatly exceeding the actual values.

This results from the application of the concentrated load on a small area of the femoral neck. This stress will be transmitted from the neck of the implant to the other components of the prosthesis. At the level of the right hip bone, the greatest stresses are located in the hip joint (approximately 36.64 MPa). The four-position of the implant is characterized by a strong orientation ( $30^\circ$ ) of the implant relative to the cup. Under this effect, the implant abuts the upper part of the cup (Fig. 6 (d)). This area is highly stressed; such behavior leads to a degradation of the equivalent stress.

The greatest stress, on the order of (48.55 MPa), is exerted on the complete structure of the coxal bone-THP. The remaining part of the structure is subjected to relatively low equivalent stress (less than 18.187 MPa).

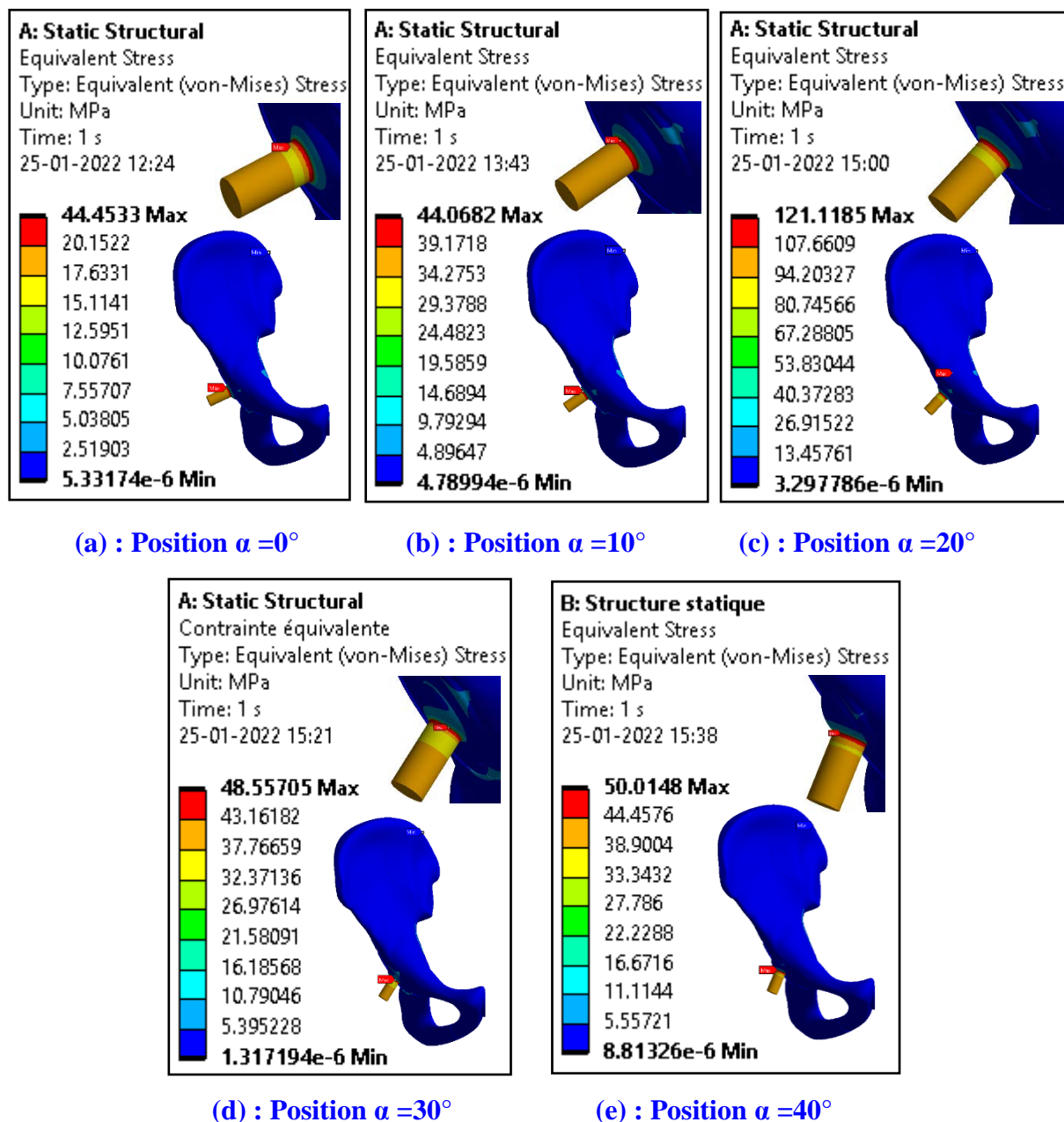


**Fig. 6.** Implant orientation effect on equivalent stress distribution in hip bone-prosthesis structure

The fifth position of the implant corresponds to an orientation of  $40^\circ$  of the neck of the implant with respect to the axis of the cup showing that the distribution of the von Mises equivalent stress throughout the coxal bone-THP junction is 50.01 MPa by the contribution of the other components of the THP system. This stress will be transmitted from the neck of the implant to the other components of the prosthesis. At the level of the pelvis, the strongest stresses are located in the coxal bone (approximately 12.44 MPa) see Fig. 7 (e).

**Distribution of von Mises stresses in the coxal bone (pelvis).**

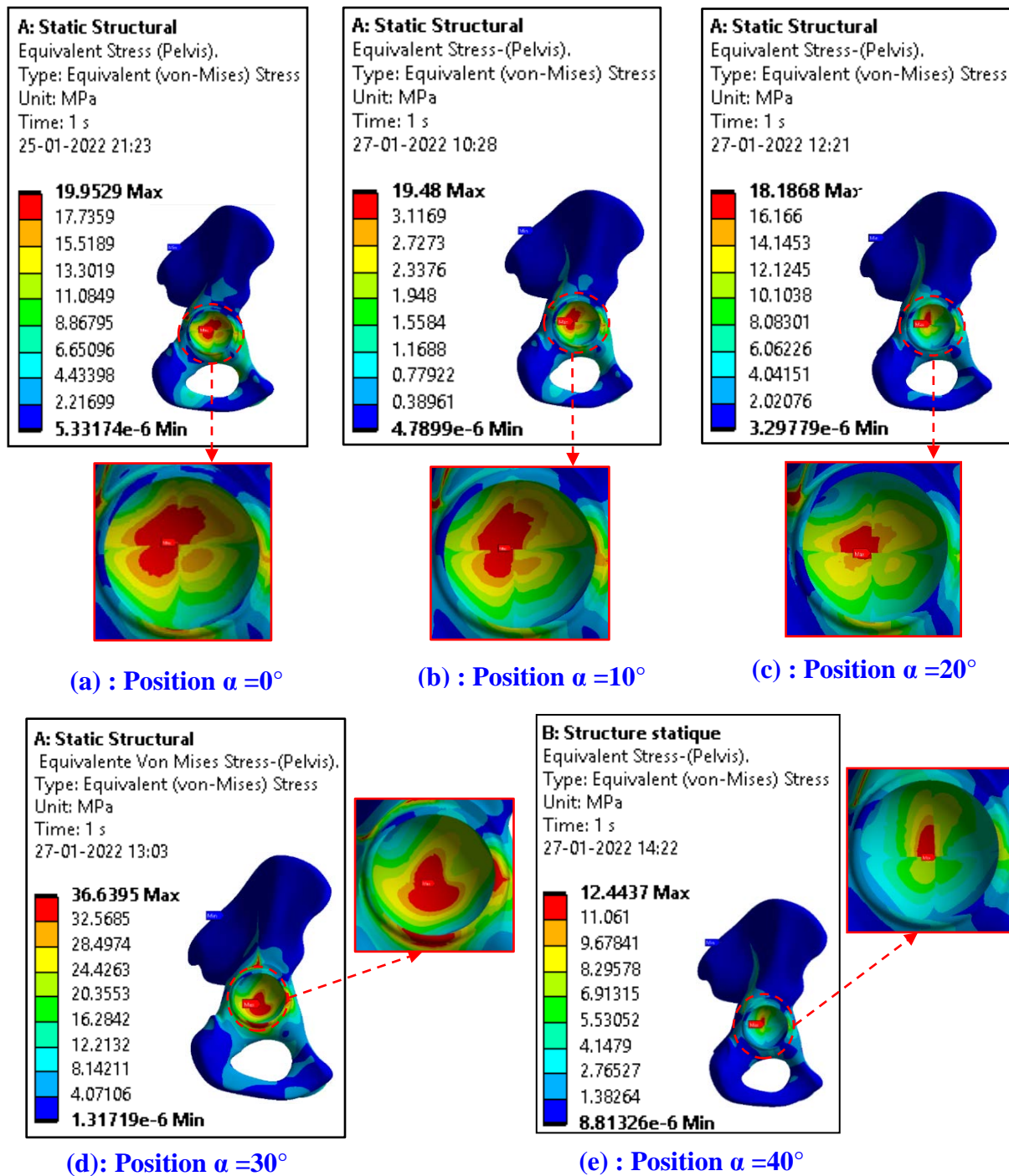


**Fig. 7.** Effect of implant orientation on the distribution of equivalent stress in the coxal bone (pelvis)

**Distribution of stress von Mises in cement (PMMA).** Cement is a very determining element of THP. Its analysis is of great importance for the life of the prosthesis. Therefore, we have studied the distribution and intensity of stresses in cement (Fig. 8). In the case of alignment of the implant on the axis of the cup, an area of the cement is under high stress; is in the direction of the load application. It is in this region that the stresses are greatest and are intensively localized at the cement-bone interface. In the rest of this structure, the stresses remain very low (Fig. 8 (a)). In 0° position, the stress is equal to 4.69 MPa.

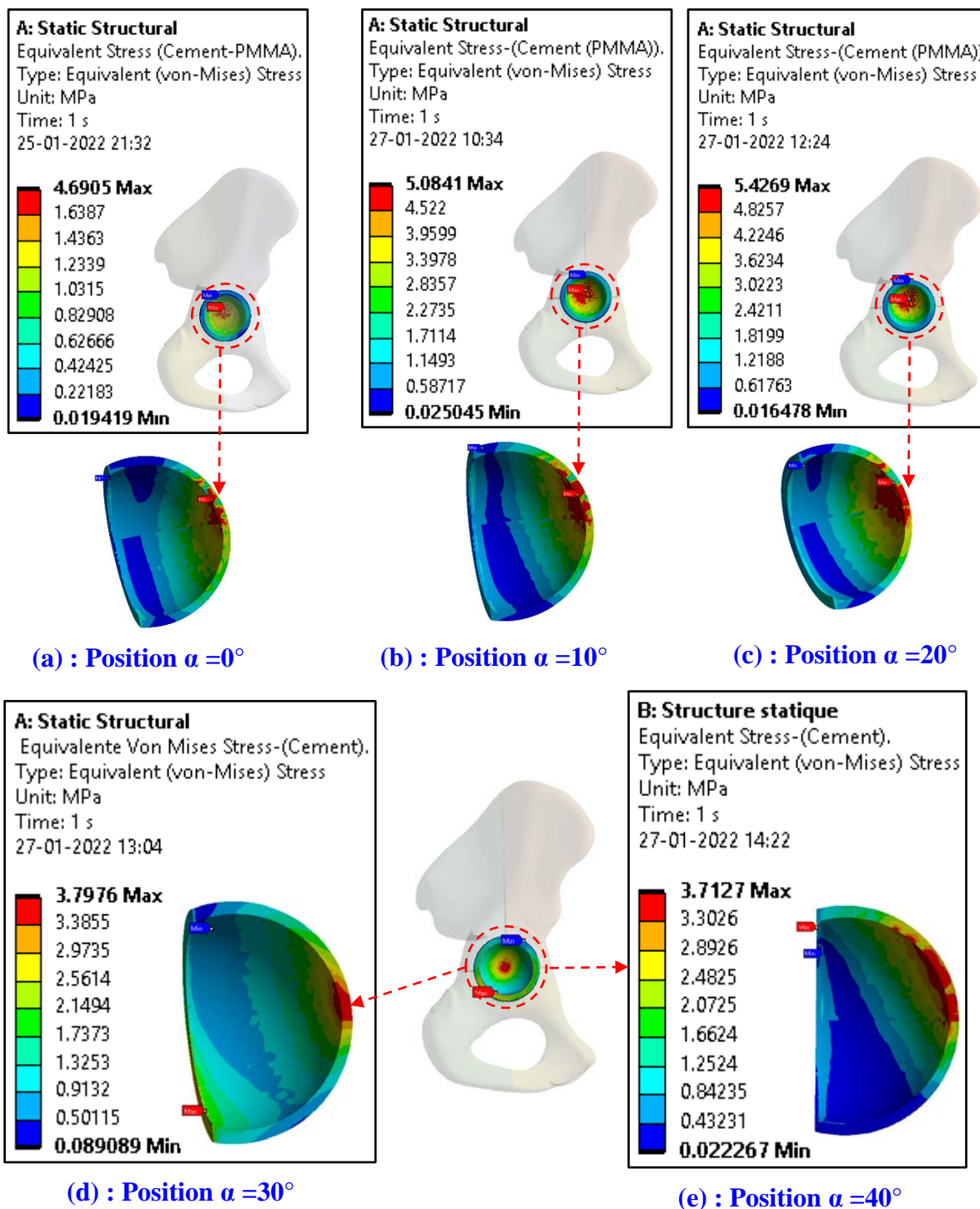


**Fig. 8.** Effect of implant orientation on the distribution of equivalent stress in the cement

An increase in the orientations of this implant ( $10^\circ$ ,  $20^\circ$ ) generates the most significant stress, located in the region subjected to mechanical loading with a greater amplitude than that resulting from the first stress and its effect is less extensive. The upper part of cement is the site of stress concentration, due to both the compressive stress field between the cup and the implant. It is in this part of the cement and near the interface with the coxal bone that the equivalent stress is strongly localized (Fig. 8 (b,c)). In this case, the stresses of von Mises are equal to (5.08MPa, 5.42MPa).

The equivalent stress is intensively localized in the convex part of the cement located in the direction of this inclination and more particularly at the cement-cup interface in its close vicinity (Fig. 8). At this level, a significant reduction in the von Mises stress compared to the first and second loading was noticed. This can be justified by the fact that the implant is almost along the axis consisting of the pubis and the iliac wing, eliminating the damping effect seen in the first case. The maximum stress is 3.79MPa, and 3.71MPa.

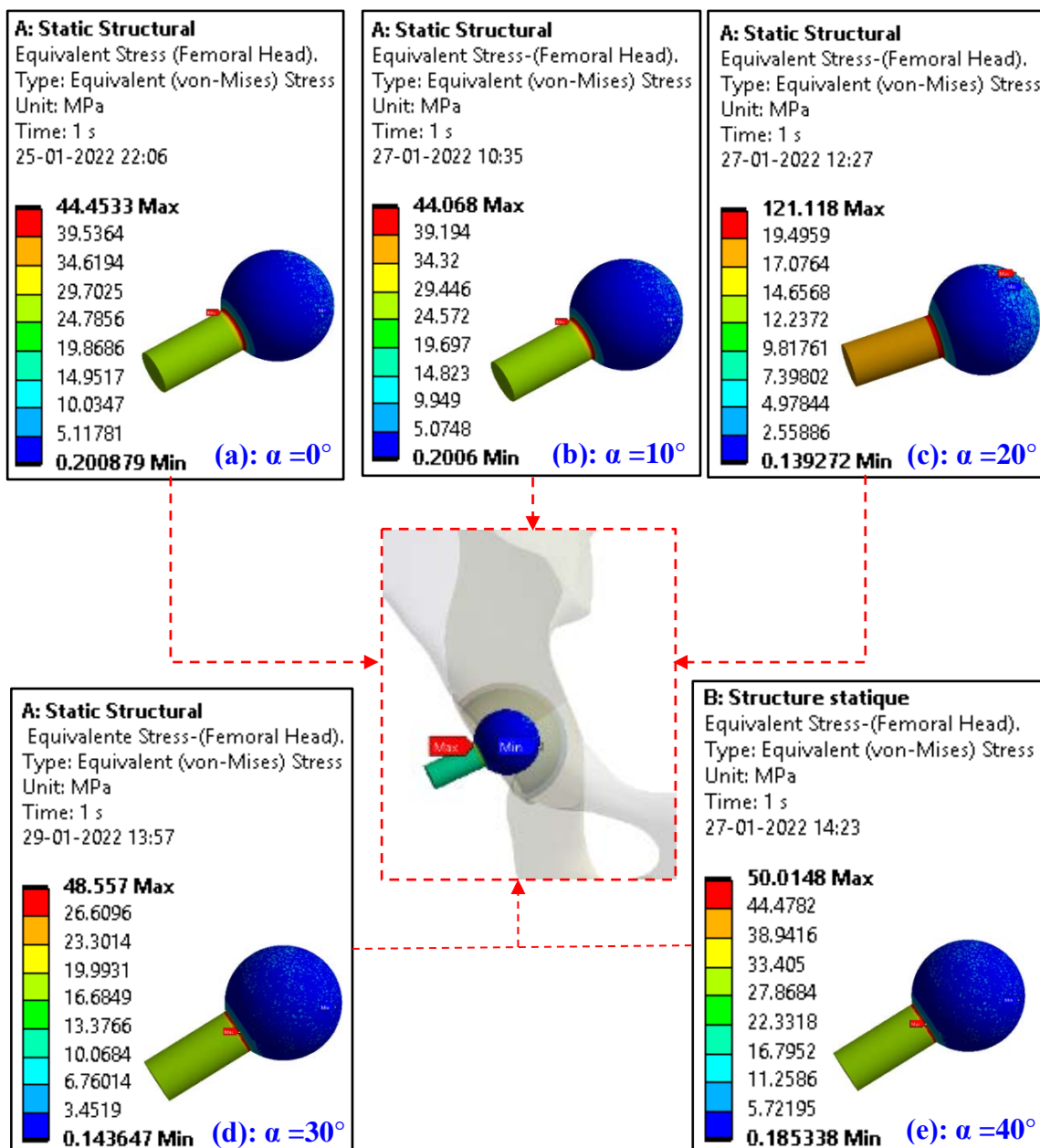
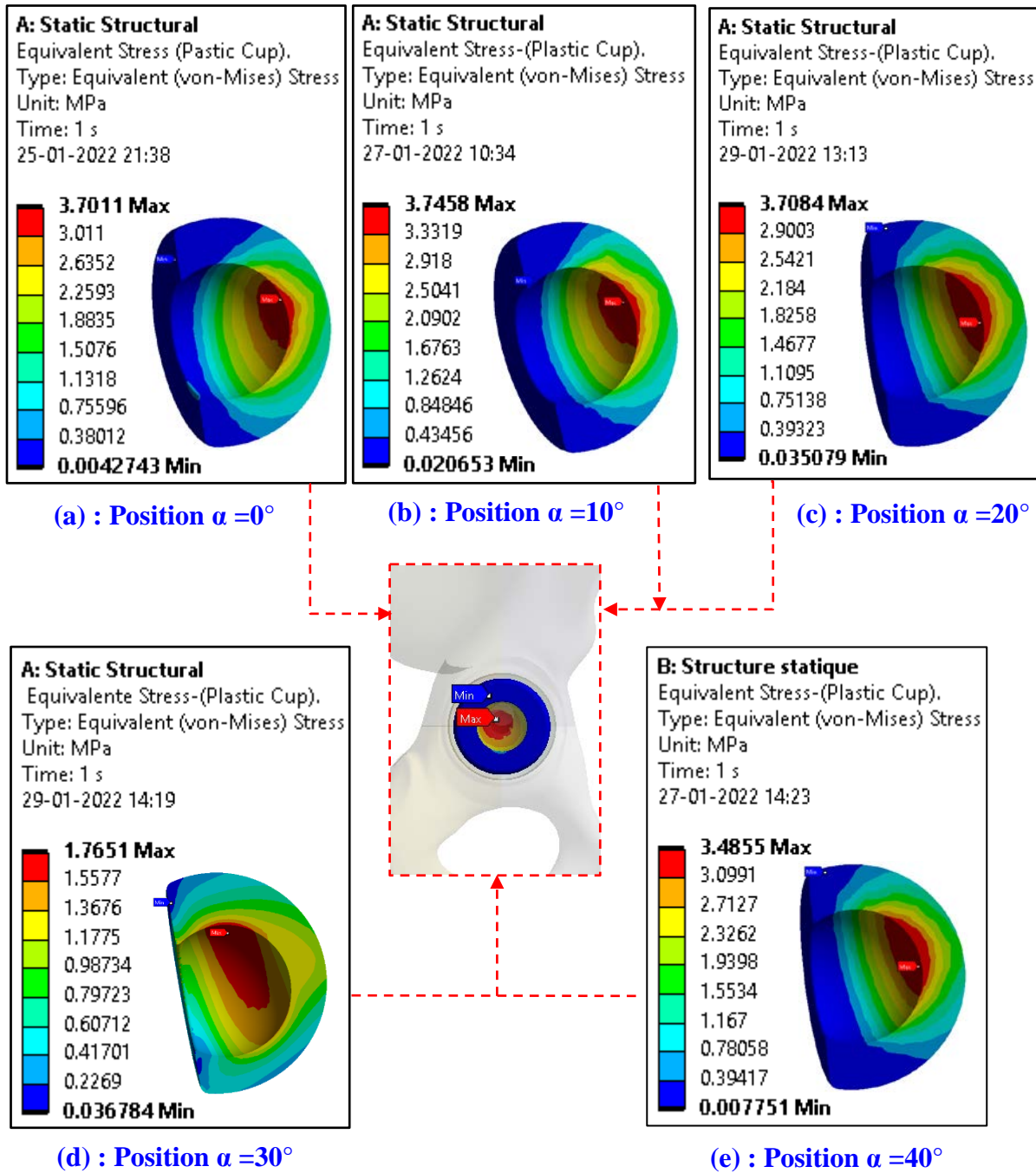


Fig. 9. Effect of implant orientation on the distribution of equivalent stress in the femoral stem

**Distribution of stress von Mises in femoral stem.** The results obtained for the analysis of the von Mises equivalent stress distribution in the implant are shown in Fig. 9. We find that the implant-cup axis alignment of (0°, 10°) results in a very small variation of the equivalent stress in the neck of the implant and in its extension in the femoral head (Fig. 9 (a,b)).

The stress is weakly concentrated on the sharp edges between the neck and the head of the implant. Orientation of the implant at 20° results in a very strong variation of the equivalent stress in the neck of the implant and in its extension in the femoral head which is equal to 121.12 MPa (Fig. 9 (c)).



**Fig. 10.** Distribution of the equivalent stress in the plastic cup

For the two orientations  $30^\circ$  and  $40^\circ$ , the von Mises stresses are stable and concentrated on the sharp edges between the neck and the head of the implant (see Fig. 9 (d,e)). Orientation of the implant at  $30^\circ$  and  $40^\circ$  (Fig. 5 (d,e)) does not cause any variation in this constraint regardless of the degree of inclination. This behavior is explained by the fact that the loading in this area has not changed.

**Distribution of the equivalent stress in the plastic cup.** In this section, an analysis of the stress distribution in the cup made of very high molecular weight polyethylene (UHMWPE: Ultra High Molecular Weight Polyethylene) as a function of the position of the implant with respect to the axis of the cup has been carried out. The results of this analysis show that the equivalent stress is more significant are located near the contact area with the femoral head (Fig. 10).

This behavior is due to the effects of the compressive stresses generated by the head of the implant on one side, and tensile stresses resulting from the fixation of the pubis on the other hand. Noting that the intensity of this stress remains low and does not constitute any danger for the patient.

The influence of the orientation of the implant on the distribution and the equivalent stress intensity in the cup was illustrated in Fig. 10. Compared to the first and the second mechanical solicitation (Fig. 10 (a)) and (Fig. 10 (b)), the third loading (Fig. 10 (c)) generates intensity and distribution stress constant (3.74MPa, 3.7MPa, 3.7MPa). However, the contact area with the implant head is subjected to compressive stresses. The high values recorded in this part are due to the contact effect.

The traction of the cup with the bone in the lower area of the cup is responsible for the increase in equivalent stress. In its upper part, the cup is more stressed. A strong orientation of the implant (Fig. 10 (d)) results in the intensification of the stresses which are located almost on the upper surface of the cup near the cup-head interface of the implant. It is of less intensity compared to those induced by the first and second orientation. The position of high-stress concentration is located in the area of application of the contact force of the cup with the head of the implant.

#### **Effect of micro-cavities.**

*Effect of cavity location on stress distribution.* Polymethyl-methacrylate (PMMA) is the only material currently used for fixing prostheses in bone during cementing arthroplasty; this connection is carried out via a mechanical coupling of cement overlay to bone surface defects (anchor). Roughness is a determining parameter for fastening the bone-cement-implant system; it can lead to a more secure cement attachment [56], but can also be a source of crack initiation due to the notch effect in cement, which can lead to loosening [57].

Cement is the weakest link of the chain transfer load implant-bone-cement, its damage is responsible for loosening the interface at the cement-implant where micro-cracks over time fatigue develop greater extent and take more significant sizes. These cracks lead to both cement destruction and implant mobility within the bone. Such behaviour results in a pelvic fracture in the patient [58] with intolerable pain.

Several types of research were dedicated to the analysis of cement damage, which is largely responsible for total hip prosthesis loosening.

Other numerical work [59-60] showed that the existence of microcavity promotes the initiation and propagation of cracks in the cup of cement. The stress intensity factor is strongly influenced by the nature of the bone-cement interface, cement-implant. Propagation mode is dependent on the priming site of the cracks initiated micro-cavities.

The study and analysis of the intensity and distribution of von Mises stresses are made according to the position of the microcavity in the cement. Our interest, in this case, relates to the von Mises stress in a spherical frame of coordinate  $(r, \theta, \varphi)$ , (Fig. 11).

In this part, we proposed five microcavity defects in different positions on the cement cut plane analyzed by the Ansys workbench code.

In order to demonstrate the effect of the presence of micro-cavities in orthopedic cement on the stress distribution, five different positions of 1mm diameter spherical cavities were tested (Fig. 11). These cavities were oriented at different angles  $\theta = \{30^\circ, 60^\circ, 90^\circ, 120^\circ, \text{ and } 160^\circ\}$  with respect to an axis OZ in a vertical plane contained in a zone under stress.

The effect of the previously discussed implant angle  $\varphi$  posture ( $\varphi = 0^\circ$ ) was also examined in combination with the different positions of the cavities.

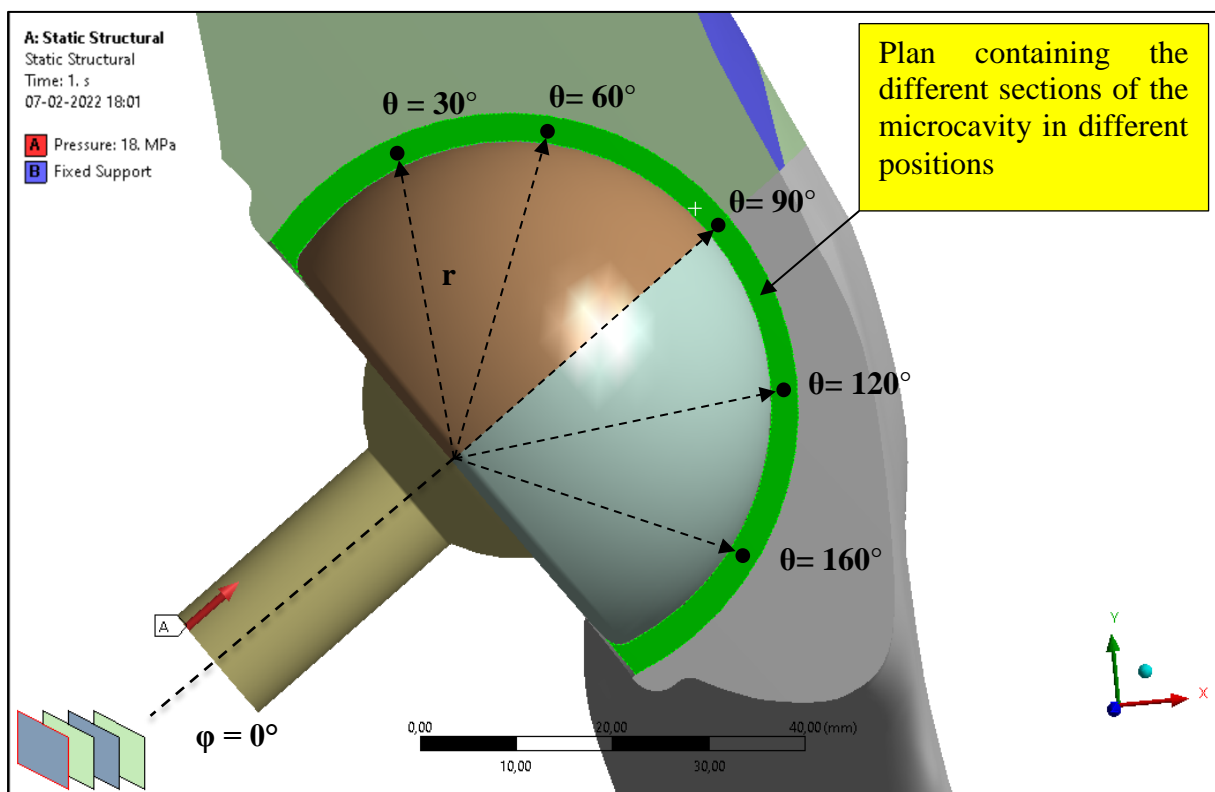


**Fig. 11.** Position of the microcavity in a spherical frame of reference ( $r, \theta, \varphi$ )

*Study of convergence of the mesh in the orthopedic cement.* Once the meshing method was chosen, the size controls of the mesh were analysed. The main parameters of size control were modified to obtain different meshes with different mesh densities. The mesh density is especially related to the number of nodes and number of elements, and it determines the validity of the results. The results obtained in Table 2 using a mesh with a low number of nodes could be right, but if a mesh with a high number of nodes is used, then the computation time to develop the analysis could be excessively high and the results are not correct. For this reason, a study of convergence of the results should be carried out, in order to ensure that the proper mesh density is chosen and to validate the results. To develop the study of convergence of the results, the analysis of the von Mises stress in the cement was carried out with different mesh densities.

The various analyzes were carried out by increasing the number of nodes, that is to say by increasing the density of nodes in the mesh. The results of Table 2 are transferred to Fig. 12 and Fig. 13 in order to analyze the convergence of the von Mises stress results in the orthopedic cement.

Table. 2. Convergence of von Mises stress results in bone cement for different element sizes

Element Size	Number of elements	Number of nodes	Stress von Mises (MPa)
2 mm	840046	1204720	1.98 MPa
1.75 mm	847494	1217278	2.03 MPa
1.5 mm	867355	1247675	2.04 MPa
1 mm	990809	1432502	2.1 MPa
0.75 mm	1220417	1766613	2.2 MPa
0.5 mm	2163511	3104955	2.78 MPa

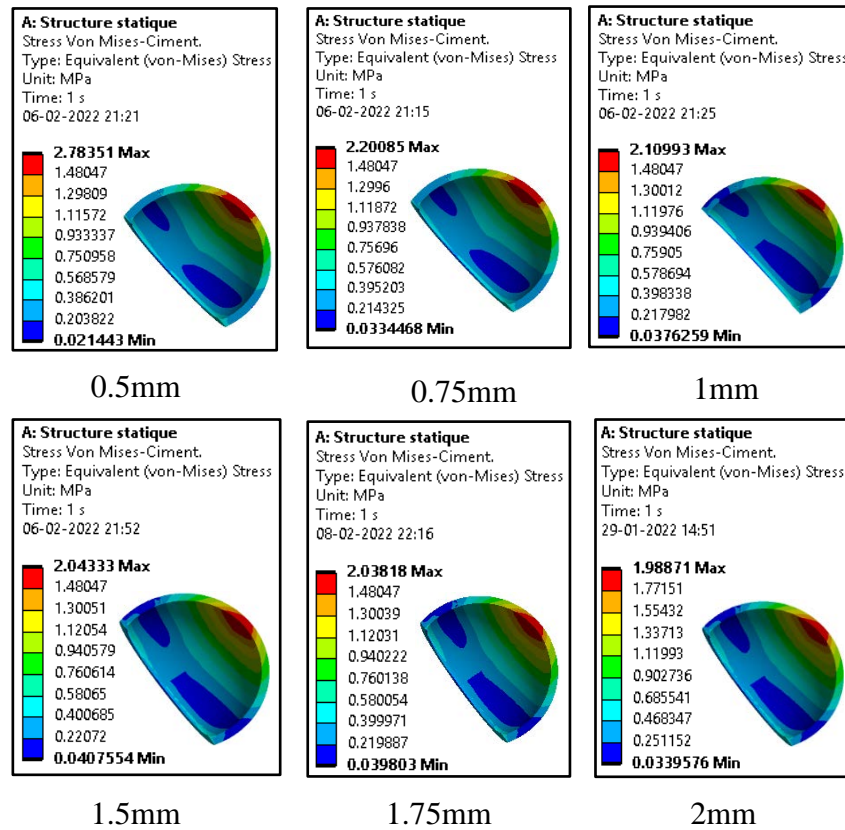


Fig. 12. Convergence of von Mises stress results in orthopedic cement

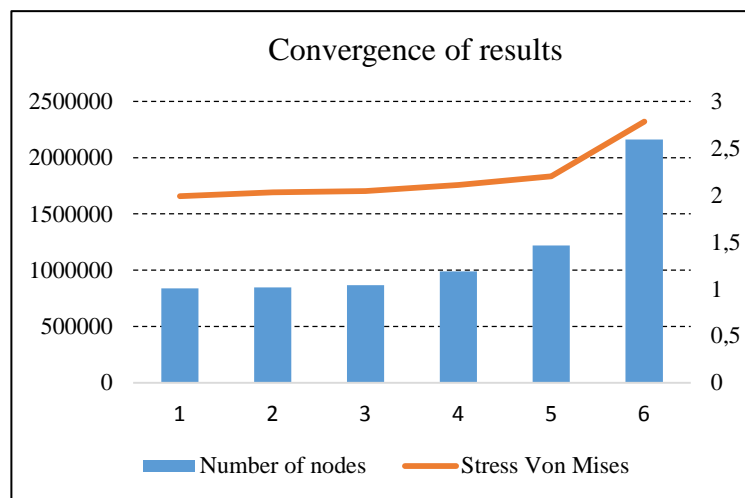
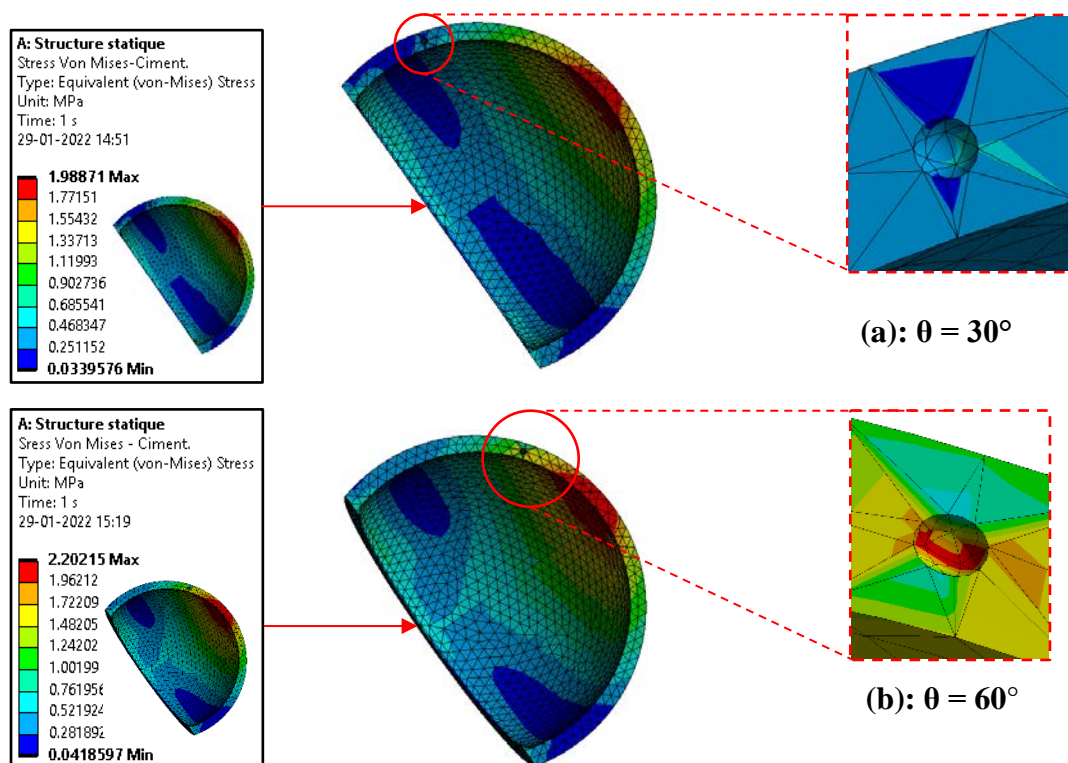


Fig. 13. Convergence of results

We note in Table 2, for the three element sizes (1.5 mm, 1.75 mm, 2 mm), the von Mises stresses in the orthopedic cement are (2.04 MPa, 2.03 MPa, 1.98 MPa) i.e. the von Mises stress convergence stabilizes in all three element sizes (see Fig. 12 and Fig. 13). On the other hand, we notice for a size of elements between 1 mm up to 0.5 mm, the von Mises stresses increase progressively (2.1 Mpa, 2.78 MPa).

It is noted that when an increases the number of nodes, the variation of the results obtained increases. In Fig. 13, we can observe that when the number of nodes is less than 870.000 nodes, a convergence in the results can be observed. On the contrary, when the number of nodes is greater than 870.000, there is a dispersion in the results obtained, i.e. the von Mises stress increases progressively (see Fig. 13).

Figure 14 presents the von Mises stress distribution for different positions of the cavity for an orientation of the implant  $\varphi = 0^\circ$ . We can notice that for the angles  $\theta = 30^\circ$ ,  $\theta = 60^\circ$  and  $\theta = 90^\circ$  belonging to the first quadrant, the intensity of the von Mises stresses in the cement increase considerably. For an angle of  $\theta = 30^\circ$ , the stresses of von Mises equal 1.98MPa,  $\theta = 60^\circ$ ,  $\theta = 90^\circ$ , the scale of the stresses of von Mises equal to (2.2MPa, 2.97MPa) by the contribution of the other components of THP system.



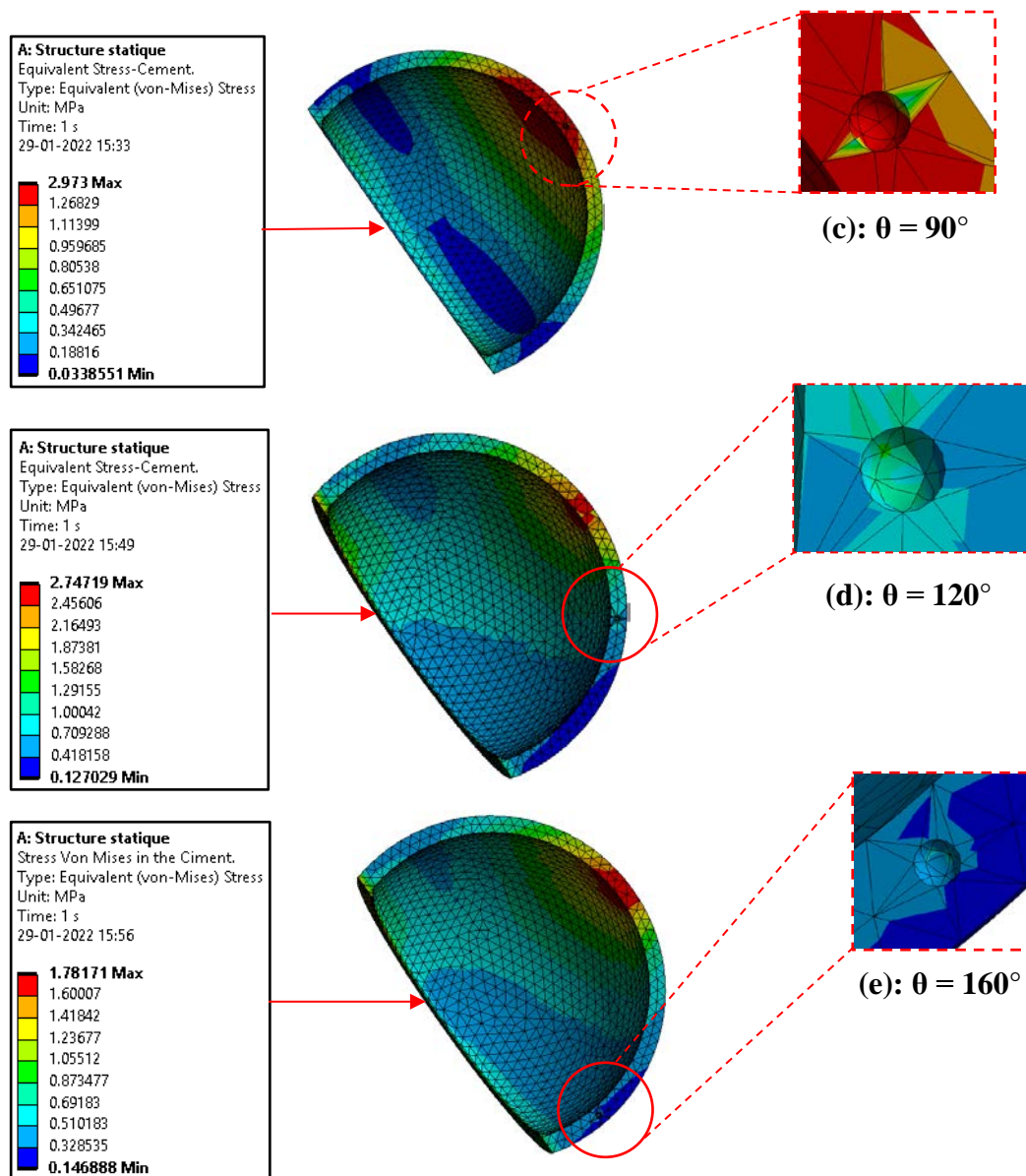
**Fig. 14.** Different meshes used for different positions of the cavities, (a):  $\theta = 30^\circ$ , (b):  $\theta = 60^\circ$

We can notice that for a microcavity angle  $\theta = 120^\circ$  belonging to the first quadrant, the equivalent stresses decrease considerably to a value equal to 2.74MPa (outline in red). Furthermore, for  $\theta = 160^\circ$ , the stress variations in the cement are very small (1.78MPa) and this is due to their position far from the point of application of the maximum load.

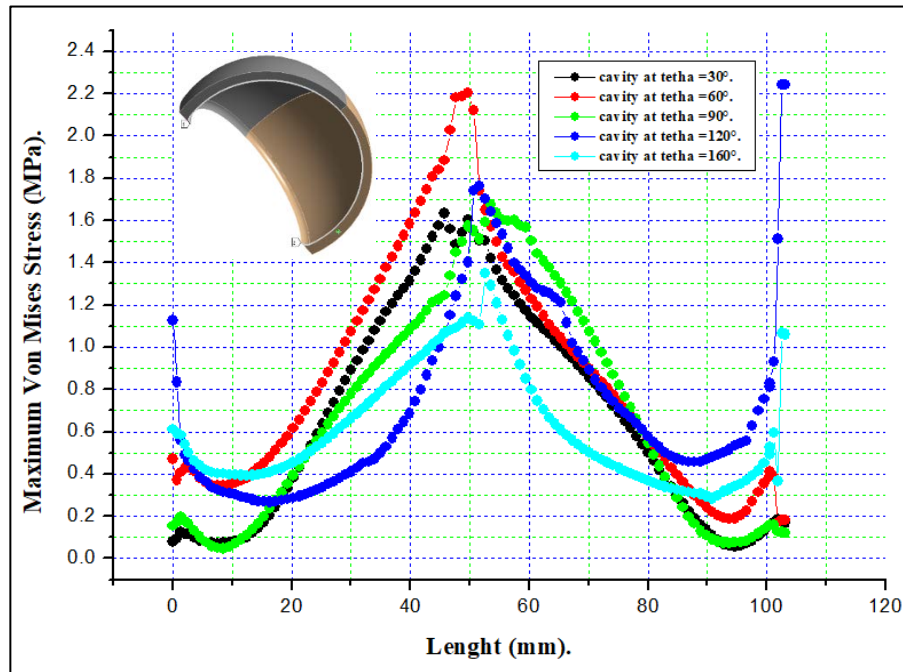
Noting that, all the von Mises stresses obtained for the different positions are tensile stresses varying from  $\sigma_{\min} = 0.041\text{MPa}$  to  $\sigma_{\max} = 2.2\text{MPa}$  which do not present any danger for the orthopedic cement in comparison with the breaking strength of the latter which is around 25 MPa. The value  $\sigma_{\max} = 2.2\text{MPa}$  clearly shows that the presence of micro-cavities within the cement contributes to a significant increase in the stresses in the latter since the maximum stress without cavity was approximately 5.0841MPa (See in Fig. 8).

Figure 14 represents the variations of the von Mises stress in the orthopedic cement for the positions of micro-cavities ( $\theta = 30^\circ$ ,  $\theta = 60^\circ$ ,  $\theta = 90^\circ$ ) depending on the angular position of the implant  $\varphi = 0^\circ$ . The results show that the important values of the von Mises stress in the cavities are equal to (1.98MPa, 2.2MPa, 2.97MPa). Noting that the maximum value is 2.97MPa (in the case where  $\theta = 90^\circ$ ), while the minimum value is 1.78MPa (in the case where  $\theta = 160^\circ$ ).

Figure 15 illustrates the distribution of the von Mises stresses placed along the contour of the cavity at ( $\theta = 30^\circ$ ,  $\theta = 60^\circ$ ,  $\theta = 90^\circ$ ,  $\theta = 120^\circ$ ,  $\theta = 160^\circ$ ) according to the angular position of the implant  $\varphi = 0^\circ$ . Note that the maximum value ( $\sigma_{\max} = 2.97\text{MPa}$ ) is obtained for an inclination angle of the cavity  $\theta = 90^\circ$ . It should also be noted that the cavity oriented at  $\theta = 120^\circ$  is subjected in the position of the implant  $\varphi = 0^\circ$  to von Mises stresses, which are relatively low (2.74MPa). In addition, we can observe that the two positions ( $\theta = 30^\circ$ ,  $\theta = 160^\circ$ ) generate the smallest variation in stress which is equal to (1.98 MPa, 1.78MPa).



**Fig. 15.** Different meshes used for different  $\theta$  positions of the cavities, (c):  $\theta = 90^\circ$ , (d):  $\theta = 120^\circ$ , (e):  $\theta = 160^\circ$



**Fig. 16.** Comparison of von Mises stresses along the contour for different cavity positions in the case of an implant orientation  $\Phi = 0^\circ$

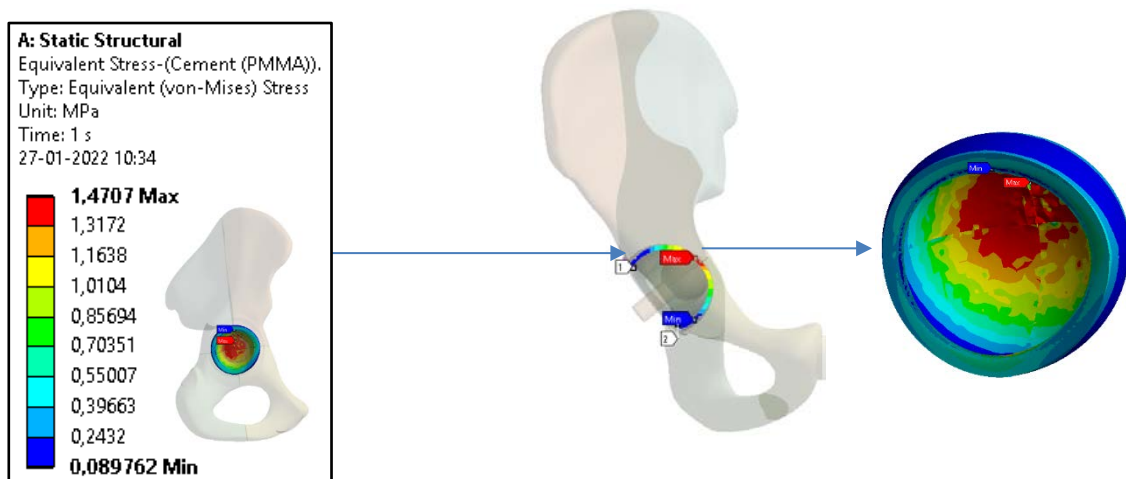


**Fig. 17.** Distribution of the equivalent stress in the cement,  $\varphi = 0^\circ$  and  $\theta = 0^\circ$

Noting that, all the stresses obtained for the different positions of the micro-cavities are tensile stresses, which are equal to (1.98MPa, 2.2MPa, 2.97MPa, 2.74MPa, 1.78MPa) which do not present any danger for the orthopedic cement in comparison with the breaking strength of the latter, which is of the order of 25 MPa. The value  $\sigma_{\max} = 2.97\text{MPa}$  clearly shows that the presence of micro-cavities within the cement contributes to a significant increase in the stresses in the latter given that the maximum stress without cavity was around 1.47MPa this mentioned in Fig. 16 and Fig. 17.

### Effect of semi-elliptical cracks

*Effect of the position of semi-elliptical cracks on the distribution of stresses.* It is considered that semi-elliptical cracks exist in four positions of the cement A, B, C, and D as

illustrated in Fig. 18. An elliptical crack of major  $2c = 4\text{mm}$  and minor axis  $2a = 1.2\text{mm}$  is assumed to be located on the left hand of the PMMA and perpendicular to x-axis (Fig. 19). The choice of this zone is due to high stress concentration.

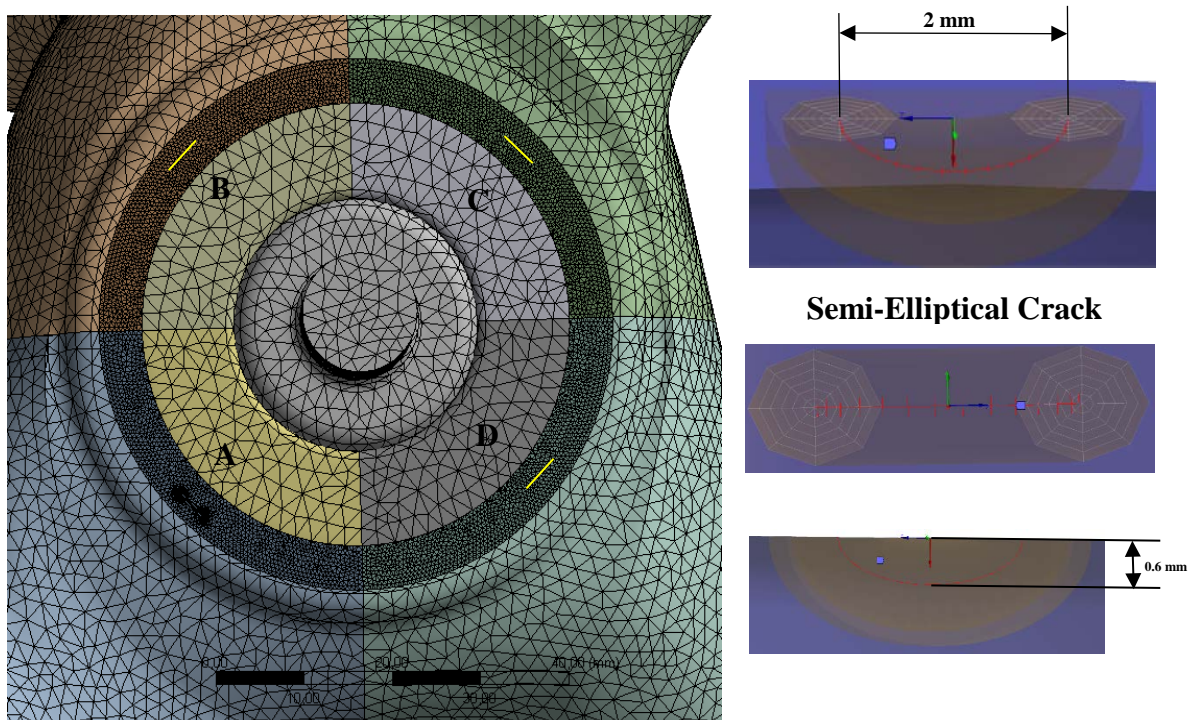


**Fig. 18.** Model of the mesh and position of semi-elliptical cracks

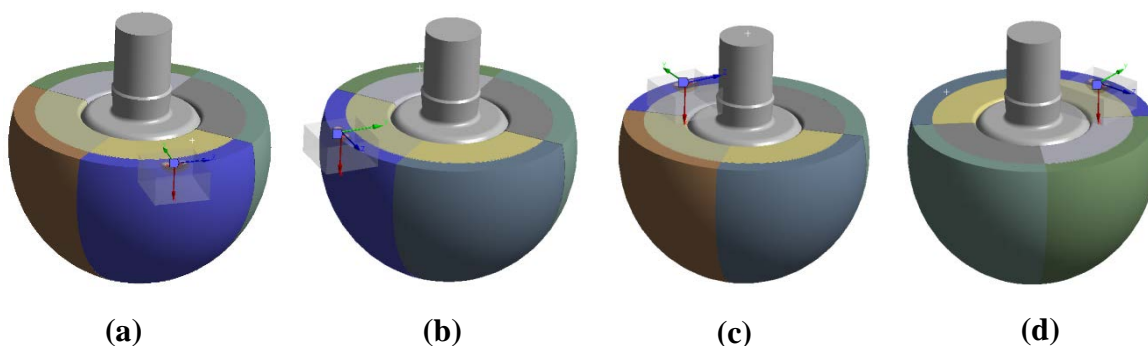


**Fig. 19.** Location of semi-elliptical cracks in orthopedic cement

*Determination of stress intensity factors of orthopedic cement.* Finite element analyzes of the cracked reconstruction were performed and stress intensity factor  $K_b$  was calculated for each crack point:

$$K_b = \frac{\sigma_{ij} \sqrt{\pi a}}{f_{ij}^b(b)}, \tag{1}$$

where  $b = 1$  corresponds to the mode I stress intensity factor (opening mode),  $b = 2$ , mode II stress intensity factor (sliding mode), and  $b = 3$ , the mode III stress intensity factor (tearing mode).

Toughness is part of the material property in the same way as its elasticity modulus or elastic limit.

$$K_b = \alpha \cdot \sigma_\infty \sqrt{\pi a_c}, \quad (2)$$

where  $a_c$  is the critical crack length for the stress applied. The objective of this study is to analyze the micro-crack effect on the cement part under high stresses.

Figure 20 presents the stress intensity factors  $K_I$  (in mode I) along the crack front for four crack positions (A, B, C, and D). It is clear that  $K_I$  is relatively higher for two crack positions. The crack position B, and C in the x-axis direction has a relatively higher  $K_I$  compared to positions A and D.

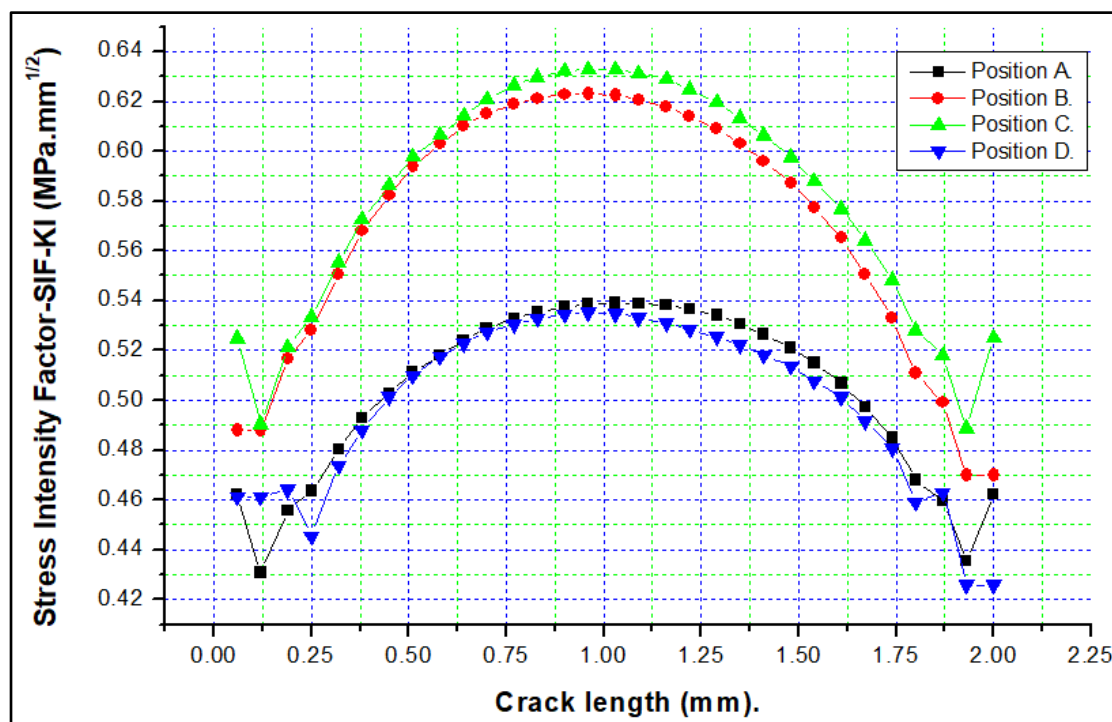


**Fig. 20.** Distribution of  $K_I$  along the crack front for different crack positions

We note in Fig. 20, that a change of semi-elliptical crack position on the orthopedic cement affects the variation of the  $K_I$  stress intensity factor and  $J$  integral. The crack positions (B, C) on the cement orthopedics indicate  $K_I$  and  $J$  maximum which values are equal to  $(0.62\text{MPa}\cdot\text{mm}^{0.5}, 0.0001836\text{mJ} / \text{mm}^2)$  and  $(0.63\text{MPa}\cdot\text{mm}^{0.5}, 0.0001880\text{mJ} / \text{mm}^2)$  with respect to other positions (A, D) (see Fig. 23 and 24).

It is noted that semi-elliptical crack size (length/depth ratio:  $c/a = 3.33 > 1$ ) considerably affects the distribution of  $K_I$  and  $J$  levels. For crack positions (A, B, C, D), we see in Fig. 20 and 25 that the highest values of  $K_I$  and  $J$  are located in the middle of the crack i.e. crack propagation will initiate from that middle.

Figure 21 shows the stress intensity factor  $K_{II}$  (in mode II) along the crack front for four crack positions (A, B, C, D). For a semi-elliptical crack of length 2mm and depth 0.6mm,  $K_{II}$  is practically negligible. The crack shear effect is therefore non-existent for these positions.

Figure 22 shows the stress intensity factor  $K_{III}$  (in mode III) along the crack front for four crack positions (A, B, C, D). The  $K_{III}$  value is very low; this is due to the fact that the distribution of the loading is essentially in the  $xy$  plane.

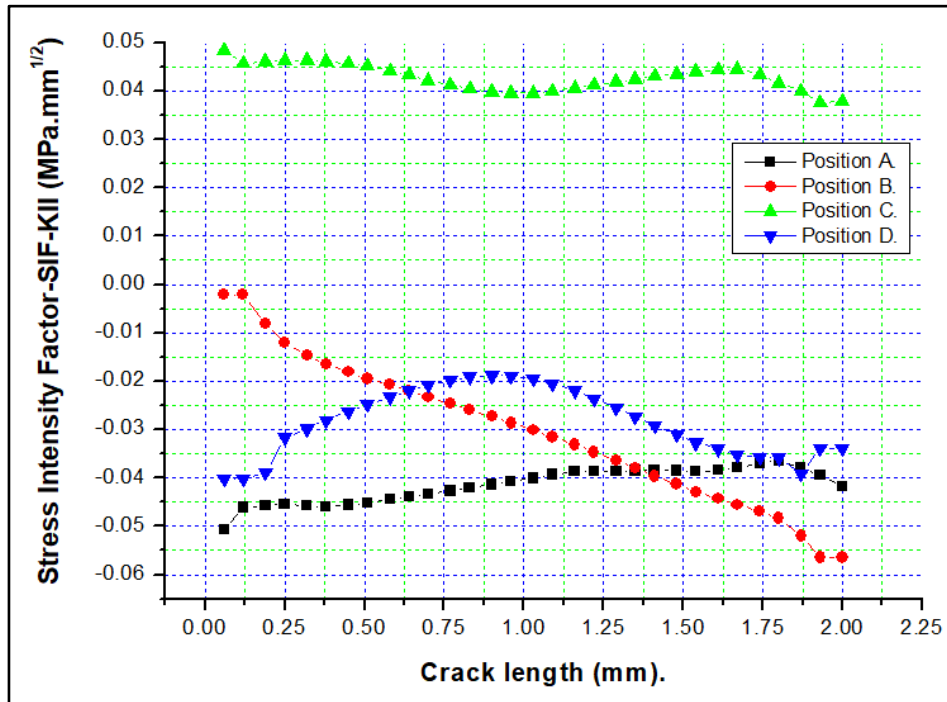


Fig. 21. Distribution of  $K_{II}$  along the crack front for different cracks positions

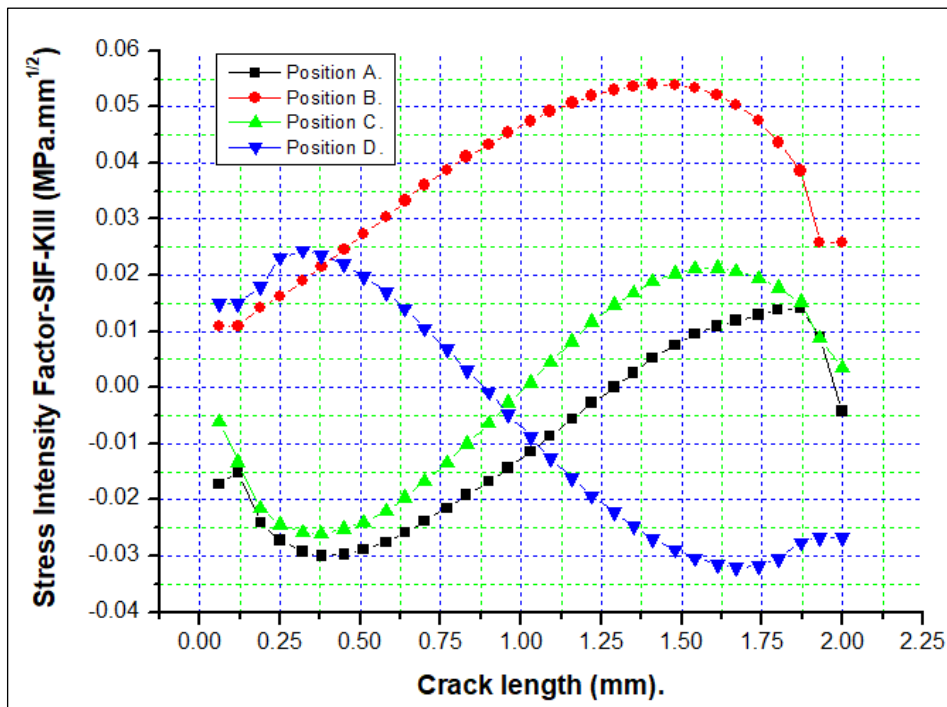
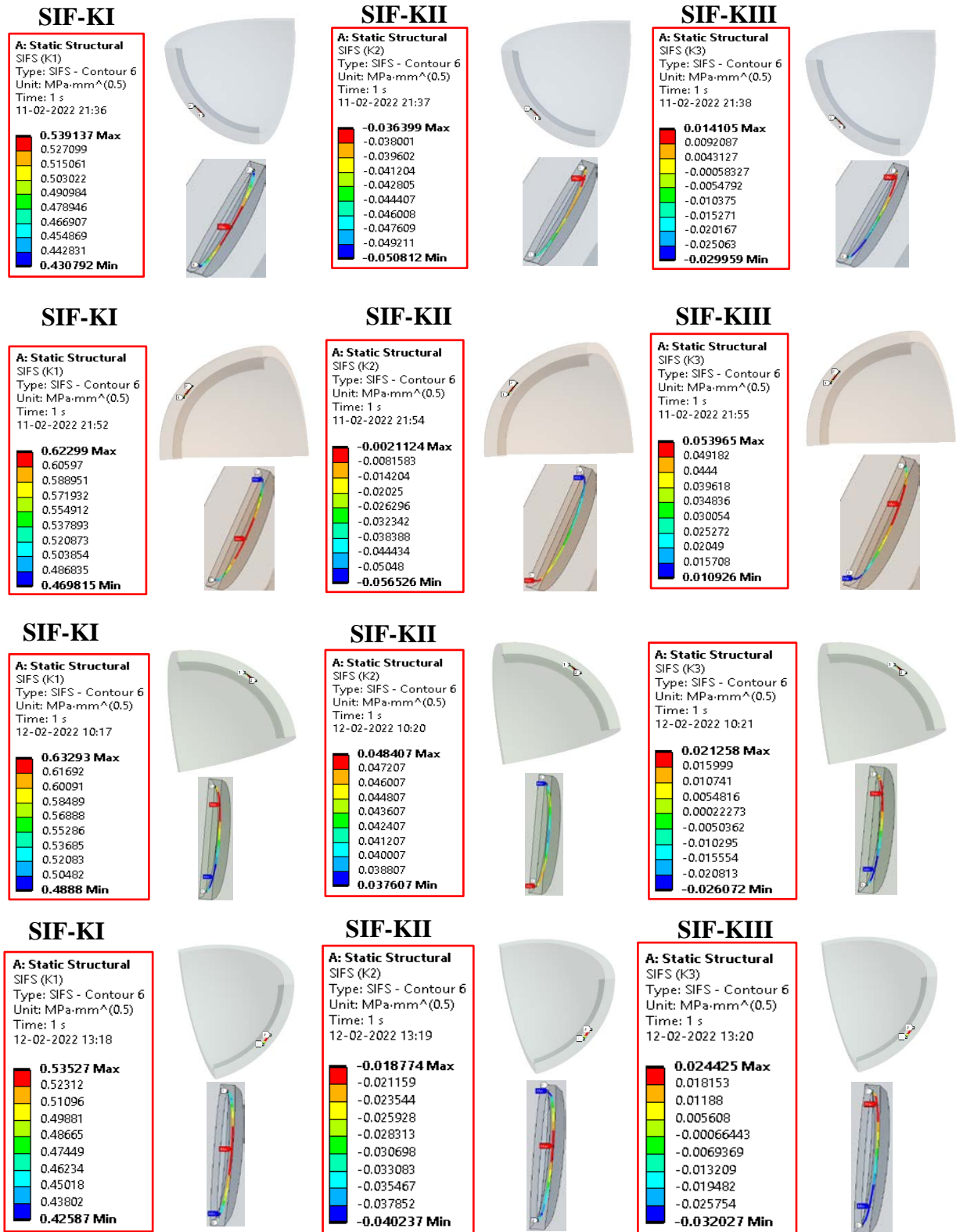


Fig. 22. Distribution of  $K_{III}$  along the crack front for different cracks positions

*SIF evolution for different cracks positions.*



**Fig. 23.** Distribution of stress intensity factors for different cracks positions

*Determination of J-integral (JINT).*

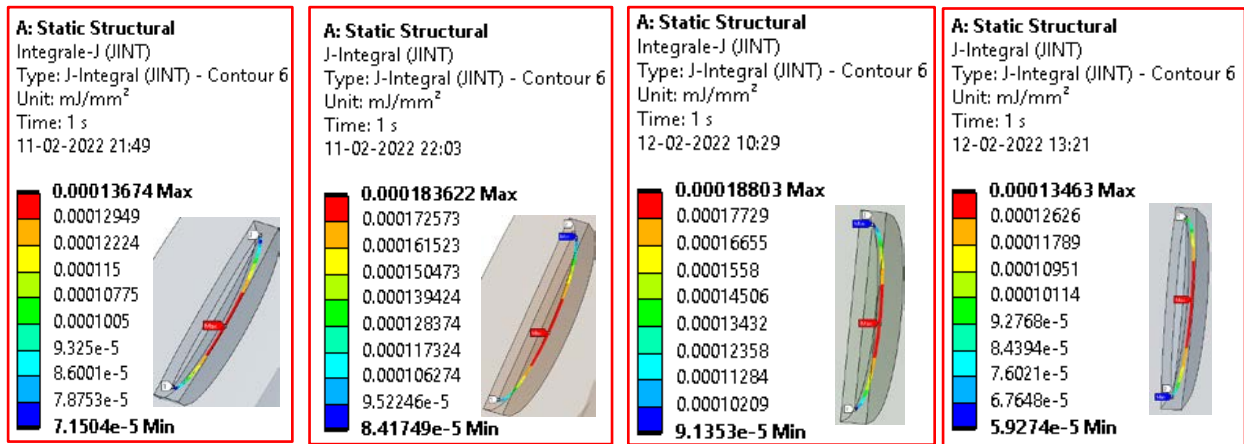


**Fig. 24.** Distribution of J-integral (JINT) along the crack front for different cracks positions

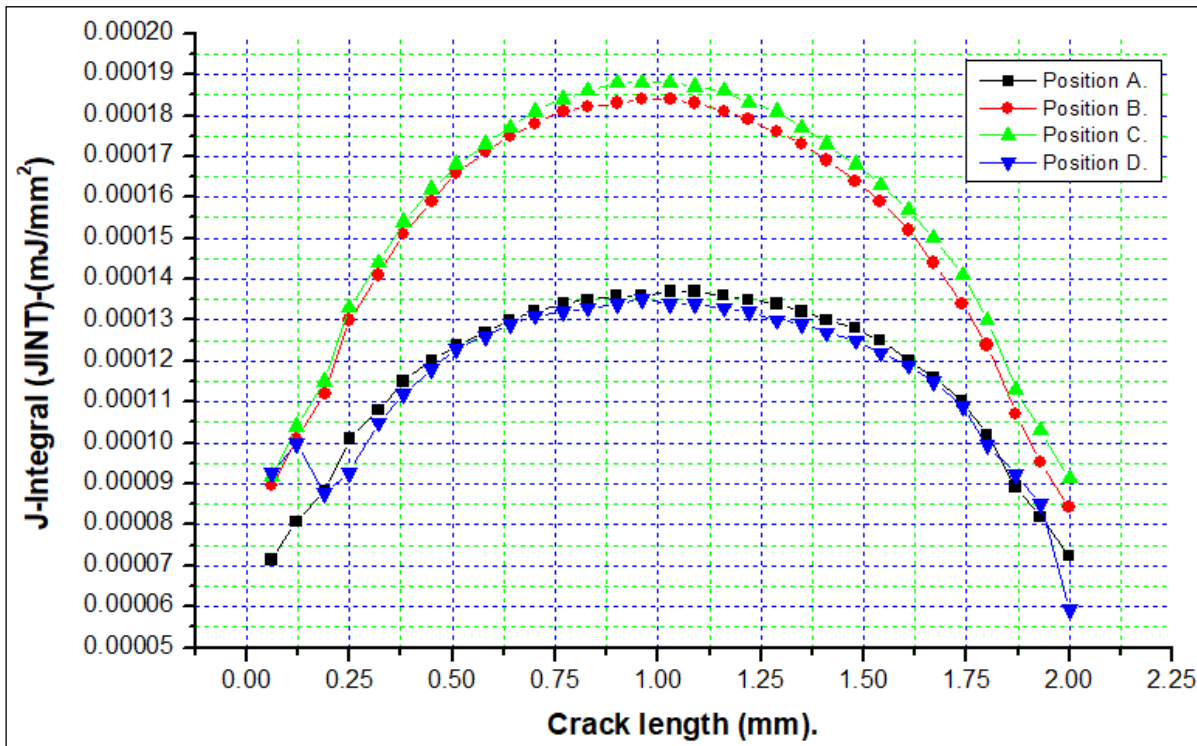


**Fig. 25.** Distribution of J-integral (JINT) along the crack front for different cracks positions

Figure 26 shows the distribution of von Mises stresses in the coxal-bone, cement, and plastic cup for different positions of the fissures. It can be noticed that the two positions of the semi-elliptical cracks (B, C) indicate maximum stresses at basin levels which are equal to (18.163MPa) respectively are greater than the two positions (A, D).

Figure 26 represents the legend of the von Mises stress in the orthopedic cement for different positions of semi-elliptical cracks. The results show that the important values of the von Mises stress in the cement are obtained for the two positions (B, C), while the lowest values are obtained for the two positions (A, D). In this case, we also noticed that the von Mises stress are symmetric between them.

On the other hand, the two positions of the crack (A, D) show maximum von Mises stresses with respect to the two positions (B, C). Noting that the maximum value is 4.24 MPa, while the minimum value is 3.86 MPa.

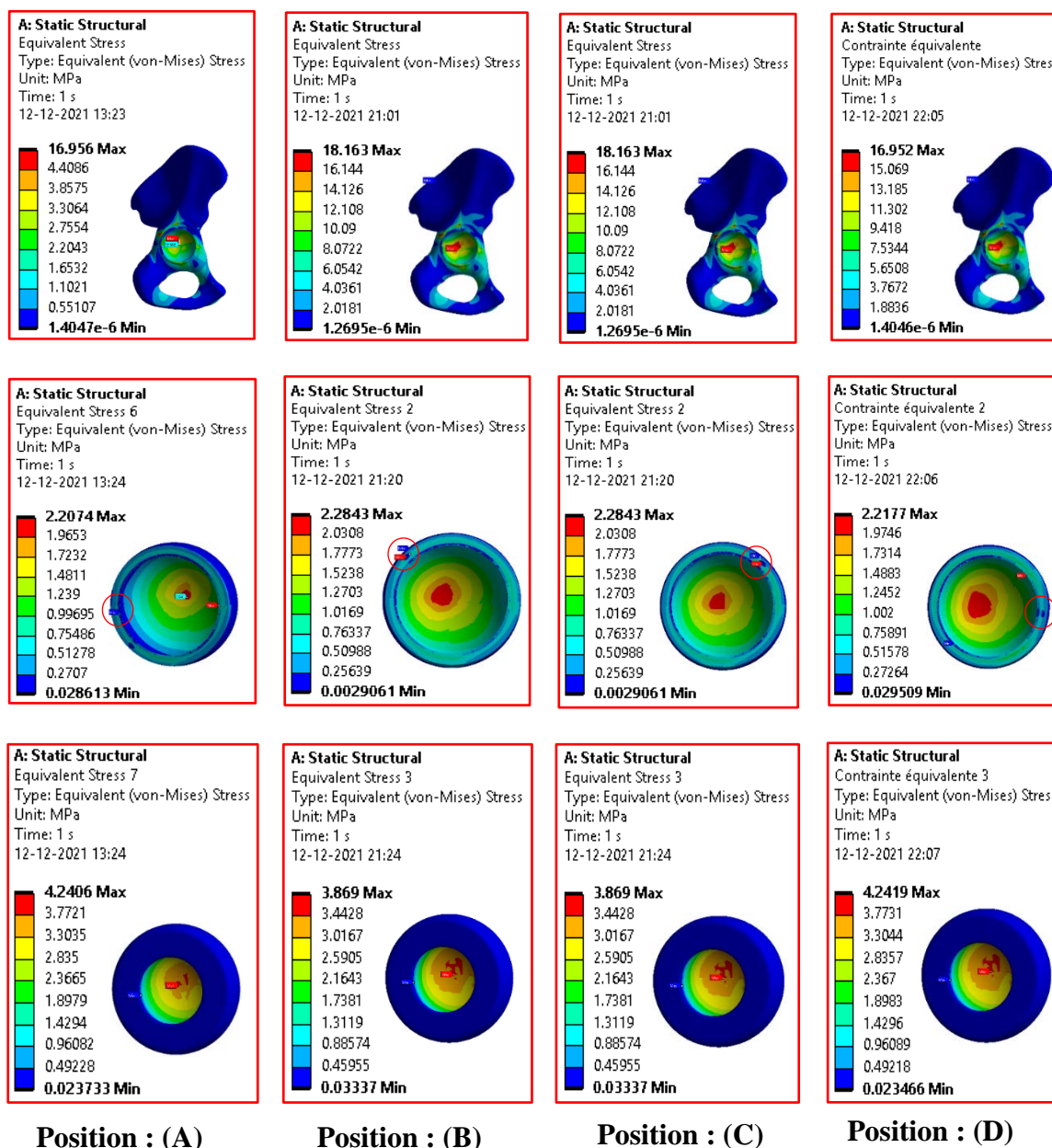


Fig. 26. Distribution of stress intensity factors for different crack positions

### 5. Conclusion

In orthopedic surgery and more particularly in total hip arthroplasty, the fixing of the implants is generally carried out by means of a surgical cement called (PMMA). This cement must ensure good adhesion between the constituents of the THP on the one hand and others to ensure a good transfer of the load, this element as if fragile, the stress gradient directly influences the functionality of the latter, which promotes the appearance of fractures. The first part of this work studied and analyzed the von Mises stress distribution in orthopedic cement around a spherical microcavity. The second part of this work studied the effect of four positions of the semi-elliptical cracks of length ( $c=1\text{mm}$ ) and depth ( $a=0.6$ ) located in the

cement of the reconstructed acetabulum by calculating the factors of stress intensity (KI, KII, KIII) and the J-integral along the crack front by the finite element method. We note in this work that the stress values were high when the implant is oriented with respect to the axis of the cup with orientation angles  $\alpha = 60^\circ$  and  $\alpha = 120^\circ$ . For the implant position  $\alpha = 0$ , the maximum stresses are recorded respectively for the cavities oriented at  $\theta = 60^\circ$  and  $\theta = 120^\circ$ , and the minimum stresses are recorded for  $\theta = 30^\circ$ ,  $\theta = 90^\circ$ , and  $\theta = 160^\circ$  corresponds to the position of the implant  $\alpha = 0$ . On the other hand, we notice in this study a considerable increase in the von Mises stresses of about 29.73% was observed under the effect of the presence of a cavity in the orthopedic cement. The risk is greater when the microcavity is located in orientation of  $\theta = 60^\circ$  and  $\theta = 120^\circ$  (high-stress field). For the loading conditions applied, the ends of the cement part are stressed to resist the tensile forces. This can pose a significant risk of crack initiation, as the cement does not resist traction well. It is clear that KI is relatively higher for the two crack positions (B and C) compared to the other positions (A and D). We concluded that the two mechanical defects (microcavity, semi-elliptical crack) show more intense stresses in the THP components and record a very intense level of stress and stress intensity factor KI. These mechanical defects cause damage to the PMMA around the tip of the bone debris, which favors the state of loosening of the total hip prosthesis.

## References

- [1] Herberts P, Malchau H. Long-term registration has improved the quality of hip replacement A review of the Swedish THR Register comparing 160,000 cases. *Acta Orthopaedica Scandinavica*. 2000;71(2): 111-121.
- [2] Foucat D. *Effects of the presence of a metallic grid within the cement for sealing the cupules of total hip prostheses: Mechanical and thermal study. Doctoral thesis*. Strasbourg: Louis Pasteur University; 2003.
- [3] Zahaf S, Kebdani S. Biomechanical Study between the Rigid and Dynamic Fixation Systems of the Spinal Column Analyzed by the Finite Element Method. *Nano Biomed. Eng*. 2017;9(2): 169-183.
- [4] Charnley J. *Low friction arthroplasty of the hip, Theory and practice*. Berlin: Springer; 1979.
- [5] Zahaf S, Mansouri B, Belarbi A, Azari Z. Obesity Effect on the Spine. *Advances in Bioscience and Biotechnology*. 2015;6(8): 556-571.
- [6] Bhambrik SK, Gilbertson LN. Micro mechanisms of fatigue crack initiation and propagation in bone cements. *Journal of Biomedical Materials Research*. 1995;29: 233-237.
- [7] Danny V, Wehmeyer M, Kebbach M, Heyer H, Bader R. Stress and strain distribution in femoral heads for hip resurfacing arthroplasty with different materials: A finite element analysis. *Journal of the Mechanical Behavior of Biomedical Materials*. 2021;113: 104115.
- [8] Lewis G. Properties of acrylic cement. State of the art review. *Journal of Biomedical Materials Research*. 1997; 38(2): 155-182.
- [9] Charnley J. Arthroplasty of the hip. A new operation. *The Lancet*. 1961;277(7187): 1129-1132.
- [10] Sanjay D, Mondal S, Bhutani R, Ghosh R. The effect of cement mantle thickness on strain energy density distribution and prediction of bone density changes around cemented acetabular component. Proceedings of the Institution of Mechanical Engineers, Part H: *Journal of Engineering in Medicine*. 2018;(232)9: 912-921.
- [11] Jamari J, Saputra E, Anwar IB, Van Der Heide E. Study of an additional layer of cement mantle hip joints for reducing cracks. *Journal of Functional Biomaterials*. 2019;10(3): 40.
- [12] Kumar A, Ghosh R, Kumar R. Effects of interfacial crack and implant material on mixed-mode stress intensity factor and prediction of interface failure of cemented acetabular

- cup. *Journal of Biomedical Materials Research Part B: Applied Biomaterials*. 2020;108(5): 1844-1856.
- [13] Abdel-Wahab AA, Silberschmidt VV. Numerical modeling of impact fracture of cortical bone tissue using X-FEM. *Journal of Theoretical and Applied Mechanics*. 2011;49(3): 599-619.
- [14] Babić M, Verić O, Božić Ž, Sušić A. Finite element modelling and fatigue life assessment of a cemented total hip prosthesis based on 3D scanning. *Engineering Failure Analysis*. 2020;113: 104536.
- [15] Ramos A, Relvas C, Completo A, Simoes JA. The formation of cracks at cement interfaces of different femoral stem designs. *European Orthopaedics and Traumatology*. 2013;4: 205-2156.
- [16] Griza S, Azevedo TF, dos Santos SV, Tentardini EK, Strohaecker TR. Metallurgical failure analysis of acetabular metal-backed screws. *Engineering Failure Analysis*. 2013;32: 178-187.
- [17] Latham KE, Miller JJ. DNA recovery and analysis from skeletal material in modern forensic contexts. *Forensic sciences research*. 2019;4(1): 51-59.
- [18] Najafi AR. Propagation of microcracks in bovine osteonal cortical bone. *Akademeia*. 2011;1: 1923-1504.
- [19] Babić M, Verić O, Božić Ž, Sušić A. Fracture analysis of a total hip prosthesis based on reverse engineering. *Engineering Fracture Mechanics*. 2019;215: 261-71.
- [20] McCormack BA, Prendergast PJ. Microdamage accumulation in the cement layer of hip replacements under flexural loading. *Journal of Biomechanics*. 1999;32(5): 467-75.
- [21] Saputra E, Jamari J, Lie HA, Anwar IB, Ismail R, Tauviqirrahman M, Van Der Heide E. The Effect of Layer Variation Between Liner and Cement Mantle on Reducing Cracks of PMMA Material Hip Joints. *E3S Web of Conferences*. 2018;73: 12013.
- [22] De Ruiter L, Cowie RM, Jennings LM, Briscoe A, Janssen D, Verdonschot N. The Effects of Cyclic Loading and Motion on the Implant–Cement Interface and Cement Mantle of PEEK and Cobalt–Chromium Femoral Total Knee Arthroplasty Implants: A Preliminary Study. *Materials*. 2020;13(15): 3323.
- [23] Sedmak A, Čolić K, Grbović A, Balać I, Burzić M. Numerical analysis of fatigue crack growth of hip implant. *Engineering Fracture Mechanics*. 2019;216: 106492.
- [24] Kocak S, Sekercioglu T. Impact strength of cemented implant interfaces. *Materials Testing*. 2020;62(3): 271-6.
- [25] Cherfi M, Abderahmane S, Benbarek S. Fracture behavior modeling of a 3D crack emanated from bony inclusion in the cement PMMA of total hip replacement. *Structural Engineering and Mechanics*. 2018;66(1): 37-43.
- [26] Pernod P, Hernigou P. Morphological aspect of cement porosity. *News in Biomaterials*. 1996;3: 235-240.
- [27] Zahaf S, Kebdani S. Study and Analysis of Mechanical Behavior between Rigid and Dynamic Fixation Systems Analyzed by the Finite Element Method. *Journal of Biomimetics, Biomaterials and Biomedical Engineering*. 2017;33: 12-31.
- [28] Krause W, Mathis RS. Fatigue properties of acrylic bone cement: Review of the literature. *J Biomed. Mater. Res: Applied Biomaterials*. 1988;22: 37-53.
- [29] Zahaf S, Mansouri B, Belarbi A, Azari Z. The Effects Induced by a Backpack Eccentric Load on the Spine of Children. *Biomedical Science and Engineering*. 2016;4: 6-22.
- [30] Stock J, Verdonschot N, Murphy PB, Prendergast PJ, Huikes R. Finite element simulation of anisotropic damage accumulation and creep in acrylic bone cement. *Eng.Fract.Mech*. 2004;71: 513-528.

- [31] Zahaf S, Kebdani S, Dahmane M, Azari Z. Biomechanical Comparison between Two Models of the Lumbar Intersomatic Fusion Cage Analyzed by the Finite Element Method. *Journal of Biomimetics, Biomaterials and Biomedical Engineering*. 2017;32: 40-58.
- [32] Tong J, Wong KY. Mixed mode fracture of reconstructed acetabulum. In: *Proceeding of the ICF 11 Torino*; 2005.
- [33] Bergmann G, Deuretzbacher G, Heller M, Graichen F, Rohlmann A, Strauss J, Duda GN. Hip contact forces and gait patterns from routine activities. *Journal of Biomechanics*. 2001;34: 859-871.
- [34] Schuller HM, Dalstra M, Huiskes R, Marti RK. Total hip reconstruction in acetabular dysplasia. A finite element study. *The Journal of Bone and Joint Surgery [Br]*. 1993;75-b: 468-474.
- [35] Dalstra M, Huiskes R. Load transfer across the pelvic bone. *Journal of Biomechanics*. 1995;28(6): 715-724.
- [36] Nocollela PN, Thacker BH, Katozian H, Davy DT. Probabilistic risk analysis of cemented hip implant. *Bioengineering Conference, BED*. 2001;50: 427-428.
- [37] Colombi P. Fatigue analysis of cemented hip prosthesis, Model definition and damage evolution algorithm. *Int. Journal of Fatigue*. 2002;24(8): 739-746.
- [38] Lennon AB, Pendegast PJ. Evaluation of cement stresses in finite element analysis of cemented orthopaedic implants. *J. Biomech Eng*. 2001;123(6): 623-628.
- [39] Harigan TP, Harris WH. A finite element study of the effect of diametral interface gaps on the contact area and pressure in uncemented cylindrical femoral total hip components. *J. Biomech*. 1991;24: 87-91.
- [40] Sim E, Freimuller W, Reiter TJ. Finite element analysis of the stress distribution in the proximal end of the femur after stabilization of pertrochantric model fracture: a comparison of two implants. *Injury*. 1999;26(7): 445-9.
- [41] Weinas H, HuiskesR, Van ribergen B, Summer DR, Turner TM, Galante JO. Adaptive bone remodelling around bonded noncemented total hip arthroplasty. A comparison between animal experiments and computer simulation. *J. of Orthopaedic Research*. 1993;11: 500-513.
- [42] Doblaré M, Garcia JM. Anisotropic bone remodelling model based on damage repair theory to the analysis of the proximal femur before and after total hip replacements. *J. of Biomechanics*. 2001;35(1): 17.
- [43] Delaunay C. Charnley total prosthesis: where is the "gold standard" of primary hip arthroplasty today. In: *Orthopedic Mastery*. 1999. p.83.
- [44] Fessy MH. Double mobilité-Historique. *Maitrise orthopédique*. 2006;152.
- [45] Bousnane T, Benbarek S, Sahli A, Serier B, Bachir Bouiadjra BA. Damage of the bone-cement interface in finite element analyses of cemented orthopaedic implants *Periodica Polytechnica Mechanical Engineering*. 2018;62(2): 173-178.
- [46] Beautiful JC. History of the treatment of femoral neck fractures. *Practical Rheumatology*. 2009: 33-36.
- [47] Sennou S. A Surgical treatment of femoral neck fractures by percutaneous screwing. *Medical thesis*. 2007;48.
- [48] Anderson AE, Peters CL, Tuttle BD, Weiss JA. Subject-specific finite element model of the pelvis: development, validation and sensitivity studies. *Journal of biomechanical engineering*. 2005;127(3): 364-73.
- [49] Allaoua F, Habib L, Abderrahmane B. Finite Element analysis of stress state in the cement of total hip prosthesis with elastomeric stress barrier. *Frattura ed Integrità Strutturale*. 2021;15(57): 281-290.
- [50] Ouinas D, Filiti A, Sahnoun M, Benbarek S, Taghezout N. Fracture behavior of the cement mantle of reconstructed acetabulum in the presence of a microcrack emanating from a microvoid. *International Journal of Materials Engineering*. 2012;2(6): 90-104.

- [51] Azari F, Sas A, Kutzner KP, Klockow A, Scheerlinck T, van Lenthe GH. Cemented short-stem total hip arthroplasty: Characteristics of line-to-line versus undersized cementing techniques using a validated CT-based finite element analysis. *Journal of Orthopaedic Research*. 2021;39(8): 1681-1690.
- [52] Rodriguez LC, Chari J, Aghyarian S, Gindri IM, Kosmopoulos V, Rodrigues DC. Preparation and characterization of injectable brushite filled-poly (methyl methacrylate) bone cement. *Materials*. 2014;7(9): 6779-95.
- [53] Merckx D. Orthopedic cements in the design of articular prostheses. Biomechanics and biomaterials. SOFCOT teaching notebooks. *French scientific expansion*. 1993;44: 67-76.
- [54] Pilliar RM, Vowles R, Williams DF. Note: fracture toughness testing of biomaterials using a mini-short rod specimen design. *Journal of biomedical materials research*. 1987;21(1): 145-54.
- [55] Soltész U. The influence of loading conditions on the life-times in fatigue testing of bone cements. *Journal of Materials Science: Materials in Medicine*. 1994;5(9-10): 654-6.
- [56] Ries MD, Young E, Al-Marashi L, Goldstein P, Hetherington A, Petrie T, Pruitt L. In vivo behavior of acrylic bone cement in total hip arthroplasty. *Biomaterials*. 2006;27(2): 256-61.
- [57] Speirs A, Slomczykowski M, Orr T, Siebenrock K, Nolte L-P. Three-dimensional measurement of cemented femoral stem stability: an in vitro cadaver study. *Clinical Biomechanics*. 2000;15: 248-255.
- [58] Bialoblocka-Juszczak E, Baleani M, Cristofolini L, Viceconti V. Fracture properties of an acrylic bone cement. *Acta of Bioengineering and Biomechanics*. 2008;10: 21.
- [59] Ouinas D, Flliti A, Sahnoun M, Benbarek S, Taghezout N. Fracture behavior of the cement mantle of reconstructed acetabulum in the presence of a microcrack emanating from a microvoid. *International Journal of Materials Engineering*. 2012;2(6): 90-104.
- [60] Lamvohee JMS, Ingle P, Cheah K, Dowell J, Mootanah R. Total hip replacement: Tensile stress in bone cement is influenced by cement mantle thickness, acetabular size, bone quality, and body mass index. *Journal of Computer Science and Systems Biology*. 2014;7(3): 72-78.
- [61] Zheng L, Chen X, Zheng Y, He X, Wu J, Lin Z. Cement augmentation of the proximal femoral nail antirotation for the treatment of two intertrochanteric fractures-a comparative finite element study. *BMC Musculoskeletal Disorders*. 2021;22(1): 1-13.

## THE AUTHORS

### **Zahaf S.**

e-mail: samir.zahaf@univ-dbk.m.dz

ORCID: 0000-0002-4138-1562

### **Dahmane M.**

e-mail: m.dahmane@ensh.dz

ORCID: 0000-0002-8510-353X

### **Belaziz A.**

e-mail: belaziz2013@gmail.com

ORCID: 0000-0002-4737-753X

**Bouri I.**

e-mail: bouri-ing@hotmail.fr

ORCID: 0000-0001-6464-8138

**Afane N.**

e-mail: afanenasreddine@gmail.com

ORCID: 0000-0001-6689-7314

## GLASS FORMATION AND SOME PHYSICAL PROPERTIES IN $\text{NaPO}_3\text{--LiF}$ AND $\text{NaPO}_3\text{--}(0.4\text{AlF}_3\text{--}0.6\text{CaF}_2)$ SYSTEMS

V.A. Klinkov<sup>✉</sup>, V.B. Archelkov

Peter the Great St. Petersburg Polytechnic University, St. Petersburg, Russia 195251

✉ klinkovvictor@yandex.ru

**Abstract.** The area of glass formation in  $\text{NaPO}_3\text{--LiF--}(0.4\text{AlF}_3\text{--}0.6\text{CaF}_2)$  system was determined. The glasses were synthesized using standard melt-quenching techniques. The concentration dependencies of the glass transition temperature, refractive index, density, molar volume, microhardness, and crystallization products were obtained. In  $(\text{NaPO}_3)_{100-x}\text{--}(\text{LiF})_x$  glass the linear decrease of noted parameters was observed. The LiF additives to the phosphate network caused the formation of a "friable" glass network. In  $(\text{NaPO}_3)_{100-x}\text{--}(0.4\text{AlF}_3\text{--}0.6\text{CaF}_2)_x$  system the concentration dependencies were more complex due to the formation of a mixed fluorophosphate network. It was assumed that the structural groups changed from metaphosphate  $(\text{PO}_3^-)_n$  in the initial composition to the combinations of  $\text{P}(\text{O},\text{F})_4\text{+[MeF}_6\text{]+[MeF}_4\text{]}$  in the final stage. The microhardness values ( $>360\text{ kg/mm}^2$ ) of  $\text{NaPO}_3\text{--}(0.4\text{AlF}_3\text{--}0.6\text{CaF}_2)$  glasses with high fluoride content were comparable to lead silicate glasses, which indicates the possibility of their practical application in optical instrumentation and devices.

**Keywords:**  $\text{NaPO}_3\text{--LiF}$ , fluorophosphate glass, calcium fluoroaluminate glass, refractive index, density, microhardness

**Acknowledgements.** *The research was supported by the Ministry of science and higher education of the Russian Federation (State Assignment for basic research 0784-2020-0022).*

**Citation:** Klinkov VA, Archelkov VB. Glass formation and some physical properties in  $\text{NaPO}_3\text{--LiF}$  and  $\text{NaPO}_3\text{--}(0.4\text{AlF}_3\text{--}0.6\text{CaF}_2)$  systems. *Materials Physics and Mechanics*. 2022;48(2): 272-281. DOI: 10.18149/MPM.4822022\_10.

### 1. Introduction

The development of advanced science and technology is closely related to the creation and study of new materials, including research in the field of optical materials. Alkaline fluorophosphate glasses have found application in laser technology, photonics, gradient optics, and dosimetry [1].

Phosphate and fluorophosphate glasses attract the attention of researchers, first of all, by their unusual optical constants and high light transmission in the ultraviolet region of the spectrum. Glasses containing phosphates and fluorides have extraordinary optical properties as applied to the creation of optical devices due to the anomalous behavior of the dispersion coefficient and deviation from the Abbe diagram. The fluoride-containing phosphate glasses are of special interest as a glass matrix for rare-earth ions, they combine the favorable optical properties of fluoride glasses and the high mechanical and thermal stability of phosphate glasses [2]. On the basis of systems  $\text{Al}(\text{PO}_3)_2\text{--BaF}_2$  [3], a group of "crowns" characterized by low dispersion and an increase in relative dispersion in the blue part of the spectrum was

obtained. Flint glasses have also been developed on a fluorophosphate basis [4]. The importance for the practical application of alkaline fluorophosphate glasses is a relatively low glass transition temperature, a large value of the linear expansion coefficient, and also high radiation resistance.

From the point of view of developing glasses with improved mechanical properties, phosphate glasses with high content of fluorides are also of great interest. The fracture strength and Young's modulus increase with increasing anisotropy. Earlier, it was shown that some compositions of alkaline and alkaline metaphosphate glasses, unlike most types of glasses, exhibit birefringence (significant anisotropy) after applying uniaxial tensile stress at temperatures above the glass transition temperature ( $T_g$ ) [5-7].

Glasses based on fluoride systems have a high tendency to crystallize; however, it is known that the addition of phosphates can significantly increase the glass-forming ability [8]. The glasses of the system (NaPO<sub>3</sub>)<sub>1-x</sub>-(AlF<sub>3</sub>)<sub>x</sub> (0<x<40) is a well-known model fluorophosphate glass [9]. However, other fluorine-containing metaphosphate alkaline glasses are very poorly covered in the literature. It is well known that calcium and aluminum fluorides have high glass formation ability. The ratio of AlF<sub>3</sub>/CaF<sub>2</sub>=0.4/0.6 was selected based on the phase diagram which is close to the eutectic and has a high glass-forming ability.

Thus, in this work, the objects of study were NaPO<sub>3</sub>-LiF and NaPO<sub>3</sub>-(0.4AlF<sub>3</sub> – 0.6CaF<sub>2</sub>) systems. The regions of glass formation, as well as the concentration dependences of the glass transition temperature, density, refractive index, molar volume, microhardness, and glass crystallization products, were studied.

## 2. Experimental techniques and objects of the study

The synthesis of glass samples was carried out in an electric furnace at a temperature of 900-1000°C for 30 minutes. The glass preparation was carried out in glassy-carbon crucibles in an argon atmosphere. The gas flow rate was controlled by an electronic flow meter. Reagents with a purity of at least 99.5% were used as raw materials for glass synthesis. Sodium metaphosphate was prepared by thermal decomposition of sodium dihydrogen phosphate at a temperature of about 240°C.

The estimation of the weight loss during glass synthesis did not exceed 5%. After synthesis, the samples were cut and polished.

The values of the glass transition temperature  $T_g$  were determined by differential thermal analysis method by "Termoscan-2" device (Analitpribor) with an accuracy of  $\pm 2^\circ\text{C}$ . Al<sub>2</sub>O<sub>3</sub> powders were used as standard.

The density  $\rho$  was determined by the hydrostatic method in toluene on polished glass samples. The error did not exceed 0.003 g/cm<sup>3</sup>.

The crystallization ability of glasses was determined visually by the polythermal method when they were kept in corundum boats in a gradient furnace for 30 minutes.

X-ray structural analysis was carried out on a D8-Advance diffractometer (Bruker).

The refractive index  $n_D$  was measured on an IRF-23 (LOMO) optical refractometer. The error did not exceed 0.0005.

The values of molar volume  $V$  were calculated by the following expression:

$$V = M / \rho, \quad (1)$$

where  $M$  is the average molar weight and  $\rho$  is the density of glass sample in g/cm<sup>3</sup>.

Microhardness by the method of indentation of a diamond pyramid (according to Vickers) was measured by PMT-3M device (LOMO). The instrument was calibrated against a sodium chloride crystal. The microhardness  $H$  was calculated according to the well-known formula:

$$H = \frac{1854 \cdot p}{< d >^2}, \quad (2)$$

where  $p$  is the normal load applied to the diamond tip,  $\langle d \rangle$  is the arithmetic mean of the length of the diagonal of the indentation in eyepiece divisions in mkm,  $d=0.31 \cdot T$ , where  $T$  is number of micrometer object divisions. As a load, a mass of 40 g was used at which there was no distortion of prints on the glass as a result of its destruction. The holding time was 30 sec. For each sample, the measurement was carried out at least 25 times, which made it possible to obtain the value of the hardware error of  $\pm 5 \text{ kg/mm}^2$ .

### 3. Results and discussion

**Glass formation and crystallization products.** Widely known optical materials, sodium metaphosphate, lithium, aluminum, and calcium fluoride, were chosen as the basis of the fluorophosphate system under study. Figure 1 shows the region of glass formation in the system  $\text{NaPO}_3\text{-LiF-(0.4AlF}_3\text{-0.6CaF}_2)$  built on the basis of experimental data.

In  $\text{NaPO}_3\text{-LiF}$  system the glasses were obtained up to 40 mol. % of LiF. At higher content of LiF, glass samples could not be obtained and partial crystallization was observed. We carried out controllable crystallization of glasses by keeping them at the crystallization temperature, which, according to the result of X-ray structural analysis, showed that the crystallization product at a LiF content from 0 to 30 mol. % was of crystalline  $\text{NaPO}_3$ , and at 30 – 40 mol. % was LiF (table 1).

As can be seen from the figure, in the  $\text{NaPO}_3\text{-(0.4AlF}_3\text{-0.6CaF}_2)$  pseudobinary system, the glass formation region was quite wide up to 80 mol. % of  $(0.4\text{AlF}_3\text{-0.6CaF}_2)$ . The obtained area of glass formation significantly exceeds the glass formation region in binary  $\text{NaPO}_3\text{-AlF}_3$  system (up to 40 mol. %) [10] and  $\text{NaPO}_3\text{-CaF}_2$  (up to 25 mol. %) [11]. The region of glass formation ends with the precipitation of a crystalline phase from the melt, whose composition is represented in Table 1.

Table 1. Glass crystallization products in system  $\text{NaPO}_3\text{-LiF-(0.4AlF}_3\text{-0.6CaF}_2)$

System	Composition area, mol. %	Crystallization products
$\text{NaPO}_3\text{-LiF}$	LiF 0 – 30	$(\text{NaPO}_3)_3$
	LiF 30 – 40	LiF
$\text{NaPO}_3\text{-(0.4AlF}_3\text{-0.6CaF}_2)$	$(0.4\text{AlF}_3\text{-0.6CaF}_2)$ 0 – 20	$(\text{NaPO}_3)_3$
	$(0.4\text{AlF}_3\text{-0.6CaF}_2)$ 20 – 50	$(\text{NaPO}_3)_3, \gamma\text{-Ca}_2\text{P}_2\text{O}_7$
	$(0.4\text{AlF}_3\text{-0.6CaF}_2)$ 50 – 70	$\text{CaF}_2, \gamma\text{-Ca}_2\text{P}_2\text{O}_7$
	$(0.4\text{AlF}_3\text{-0.6CaF}_2)$ 70 – 80	$\text{CaF}_2$
$\text{NaPO}_3\text{-LiF-(0.4AlF}_3\text{-0.6CaF}_2)$	$\text{NaPO}_3$ 50 – 70	$(\text{NaPO}_3)_3$
	$\text{NaPO}_3$ 70 – 100	$(\text{NaPO}_3)_3, \text{Ca}_3(\text{PO}_4)_2$

The analysis of the crystallization ability of  $\text{NaPO}_3\text{-LiF-(0.4AlF}_3\text{-0.6CaF}_2)$  glasses showed that the introduction of LiF (up to 30 mol. %) into  $\text{NaPO}_3$  increases the resistance of glasses to crystallization. Further, as LiF increases, the resistance to crystallization decreases. At first glance, this seems to contradict the available data that the introduction of alkali metal fluoride shortens long phosphate chains and thus creates favorable conditions for crystallization. However, if we consider the state diagram of systems of type  $\text{MePO}_3\text{-MeF}$ , and assume an analogy between them and  $\text{NaPO}_3\text{-LiF}$ , then the increase in resistance to crystallization is explained as the composition approaches the eutectic.

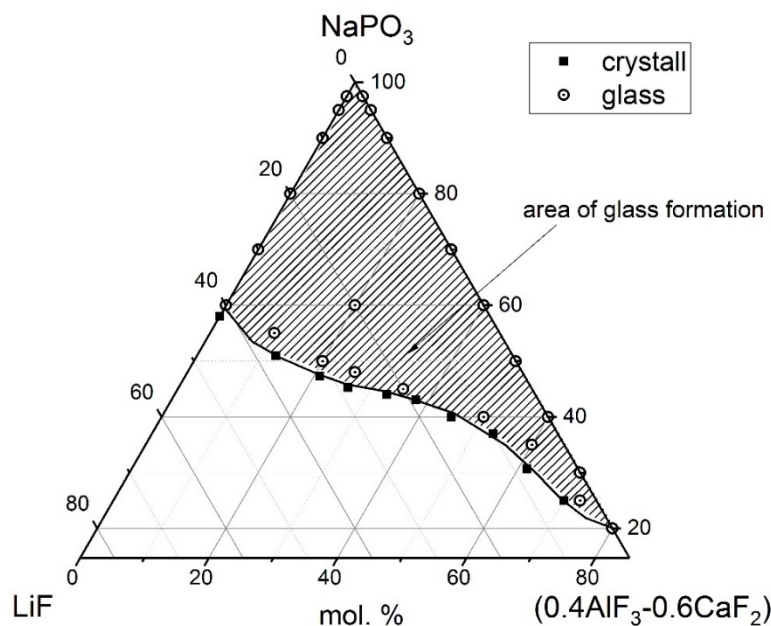


**Fig. 1.** The area of glass formation in  $\text{NaPO}_3\text{-LiF-(0.4AlF}_3 - 0.6\text{CaF}_2)$  system

In pseudobinary system  $\text{NaPO}_3\text{-(0.4AlF}_3 - 0.6\text{CaF}_2)$ , the introduction of  $0.4\text{AlF}_3 - 0.6\text{CaF}_2$  up to 20 mol. % increased the tendency to glass formation, then in the range from 20 to 50 mol. % the tendency to crystallization increased, and in the range of 50-70 mol. % tendency to glass formation increased again.

Figure 2, *a* and *b* shows the concentration dependences of  $T_g$  value in  $\text{NaPO}_3\text{-LiF}$  and  $\text{NaPO}_3\text{-(0.4AlF}_3 - 0.6\text{CaF}_2)$  glass systems, correspondingly.

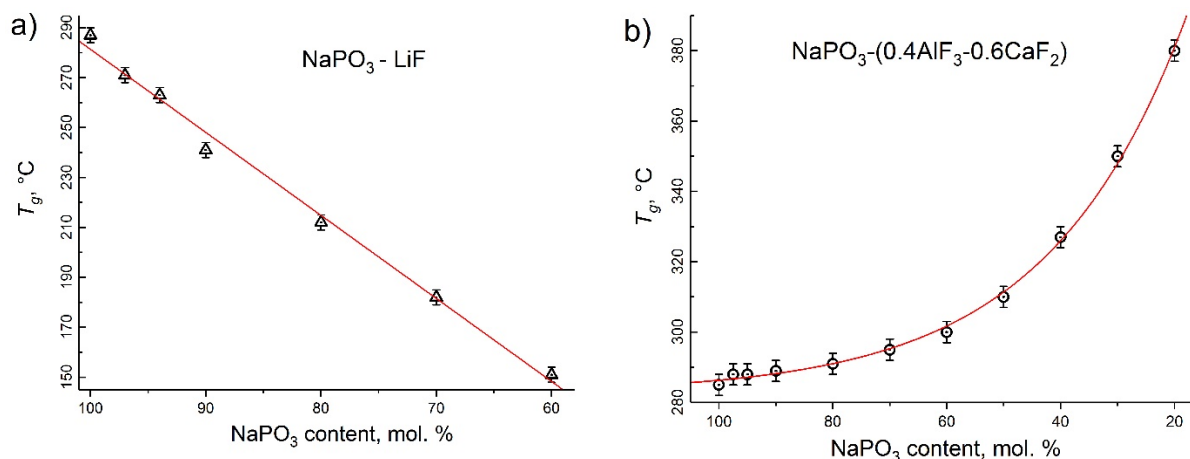


**Fig. 2.** Concentration dependences of glass transition temperature ( $T_g$ ) in  $\text{NaPO}_3\text{-LiF}$  (a) and  $\text{NaPO}_3\text{-(0.4AlF}_3 - 0.6\text{CaF}_2)$  (b) glass systems

Consider the experimental dependence for the lithium-containing system. It can be seen from Fig. 2, *a* that an increase in the fraction of fluorides significantly reduced the  $T_g$  value. A decrease in the  $T_g$  value can be explained by the following: the lithium fluoride introduction leads to the rupture of certain metaphosphate chains and the formation of chains with a shorter length; as a result, the bond strength weakens and causes an increase in the amplitude of thermal vibrations of weakly bound structural groups.

The dependence shown in Fig. 2, *b* has a completely different form – firstly, a significant increase in the glass transition temperature is observed with a decrease in the proportion of the phosphate component, and secondly, the dependence has an exponential form.

An increase in the  $T_g$  values indicates that less bound structural groups in the glass were replaced by more bound ones, which leads to an increase in the energy of the structural network of the glassy matrix. It should be noted that the formation of shorter meta- and pyrophosphate groups as a result of breaking long phosphate chains with fluorine atoms is also possible. The last one was confirmed by the presence of  $(\text{NaPO}_3)_3$ , and  $\gamma - \text{Ca}_2\text{P}_2\text{O}_7$  in crystallization products.

**Physical properties.** Figure 3 shows the dependencies of density and molar volume in both glass systems.

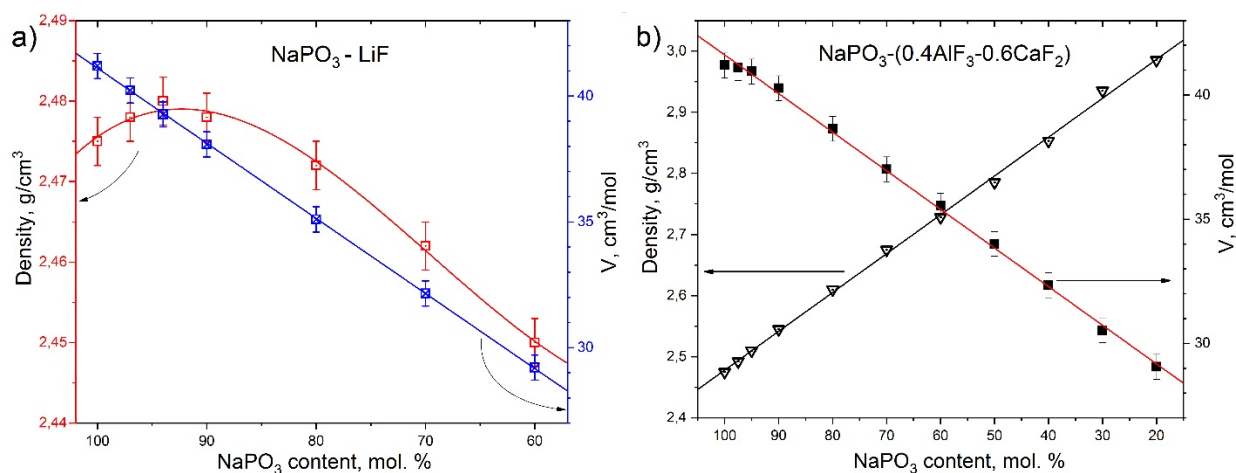


**Fig. 3.** Dependences of  $\rho$  and  $V$  versus  $\text{NaPO}_3$  content in studied glassy systems

The dependence of  $\rho$  shown in Fig. 3, *a* ( $\text{NaPO}_3$ -LiF) is more complex than for pseudo-binary system. The density of lithium fluorophosphate glasses initially slightly increased (up to 5 mol. % of LiF), and then a monotonic decrease was observed. The increase in density up to 5 mol. % can be explained by the incorporation of lithium fluoride into microvoids of  $\text{PO}_4$  tetrahedra of phosphate glass. This possibility is due to the small size of lithium ions, as well as its high mobility in glass. The transition from an increase in density to its decrease after 5 mol. % is associated with the exhaustion of noted microvoids and the beginning of the formation of fluoride structural fragments along with the existence of phosphate groups. The reason for the subsequent monotonic decrease of density is the replacing of the heavier component  $\text{NaPO}_3$  ( $M_{\text{NaPO}_3}=101.96$  g/mol) with a lighter one – LiF ( $M_{\text{LiF}}=25.94$  g/mol) and the formation of a "friable" glass structure due to the appearance of a mixed fluorophosphate matrix.

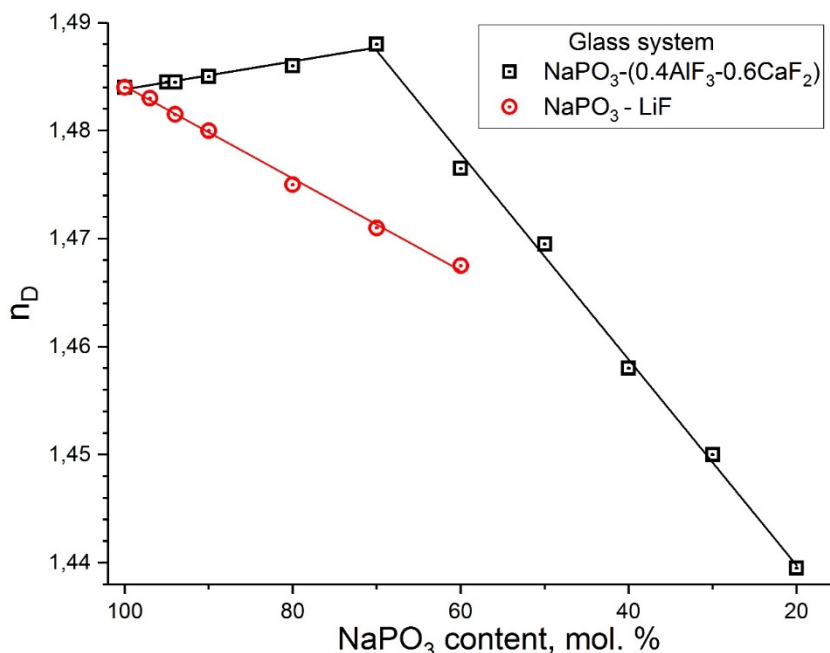
The molar volume characterizes the packing density of structural groups in glass. The LiF additives to the phosphate network reduced the molar volume and caused the shrinkage of the network. Li-ions at small content are a glass network modifier, which means the presence of it the glass network must form around these ions. Therefore, a decrease in both the density and the molar volume indicates an increase in the size of the interstitials in the phosphate network of the glass.

Figure 3, *b* shows the concentration dependencies in  $\text{NaPO}_3$ -(0.4AlF<sub>3</sub> – 0.6CaF<sub>2</sub>) system. It can be seen that dependencies of density and molar volume had an opposite linear character – with the introduction of fluorides, the density of glasses increases, and the molar

volume decreases. In contrast to the NaPO<sub>3</sub>–LiF system, the increase in the density value was observed with an increase in the proportion of the fluoride component.

The opposite dependences of  $\rho$  and  $V$ , indicate that despite the decrease in the average molar volume (through the addition of fluoride component with lower than NaPO<sub>3</sub>  $M_{\text{NaPO}_3}=101.96$  g/mol molar weight  $M_{\text{AlF}_3}=83.98$  g/mol,  $M_{\text{CaF}_2}=78.07$  g/mol), there is an increase in density. The increase in glass density is probably due to the fact that aluminum and calcium fluoride has a higher density than NaPO<sub>3</sub>.

From the point of view of glass formation, it is known that calcium and aluminum fluorides have a significantly greater tendency to form a glass network and fluorides have a higher electronegativity than oxides, so the distance between atoms is smaller. Therefore, the observed increase in the density of glasses is associated with a decrease in the average distance between the structural groups of glass – fluoride, and phosphate leading to the formation of a more tightly coupled glass network. The latter is confirmed by the results obtained for multicomponent fluorophosphate glasses, in which the formation of a mixed fluorophosphate glass framework was also found even at low content of phosphates [8].



**Fig. 4.** Concentration dependences of refractive index  $n_D$  in NaPO<sub>3</sub>-LiF and NaPO<sub>3</sub>-(0.4AlF<sub>3</sub>-0.6CaF<sub>2</sub>) glassy systems

Figure 4 shows the dependence of  $n_D$  in both series of studied glass samples. It is seen from the dependence of NaPO<sub>3</sub>-LiF system a linear decrease of glass refractive index with fluoride content growth. This corresponds to the well-known fact that the refractive index of fluoride materials, in general, is lower than that of oxide materials, for example,  $n_D(\text{LiF})=1.392$ ,  $n_D(\text{CaF}_2)=1.434$  [12], and  $n_D(\text{NaPO}_3)=1.484$ . The value of  $n_D$  changed in the studied area of compositions from 1.484 to 1.467. The  $n_D$  value for pure NaPO<sub>3</sub> coincides with that described in the literature [7], while the values for lithium fluorophosphate glasses are not found in the literature.

In a pseudo-binary system, the refractive index curve has an extremum in the region of 30 mol. % fluorides. A similar character of the  $n_D$  dependence was observed for other fluorophosphate glasses system, which was additionally studied by IR, Raman, and NMR spectroscopy [13,14]. However, in work [14], an extremum on the  $n_D$  dependence was observed at a fluoride content of about 36 mol. % in glass composition  $64\text{Ba}(\text{PO}_3)_2 \cdot 4\text{MgF}_2 \cdot 19\text{CaF}_2 \cdot 13\text{AlF}_3$ . The difference in the position of the maximum is

associated both with the difference in the chemical composition of the glasses and in the significantly larger step in fluoride concentration, which in [14] was 18 mol. %.

The probable cause of the observed maximum is the formation of glass consisting of fluoride and phosphate groups: in the inflection region (around 30 mol. % of fluorides), the prevailing but weak pyrophosphate chains collapsed and formed stronger fluoride chains. By analogy with the one proposed in work [14] and assuming a similar nature of the glass formation of phosphate and fluoride groups in studied compositions, it can be assumed that the structural groups forming the glass network changed from metaphosphate ( $\text{PO}_3^-$ )<sub>n</sub> in the initial composition to the combinations of  $\text{P}(\text{O},\text{F})_4 + [\text{MeF}_6] + [\text{MeF}_4]$  (where Me was Al or Ca) in the final stage.

**Glass microhardness.** The widespread use of miniature glass displays in modern mobile communications determines the relevance of considering the microhardness of glasses, and their resistance to abrasion. In addition, the dependences on microhardness make it possible to identify changes in the structure of glasses, which is certainly useful in the context of our study. The concentration dependences of the microhardness in both glass systems are shown in Fig. 5.

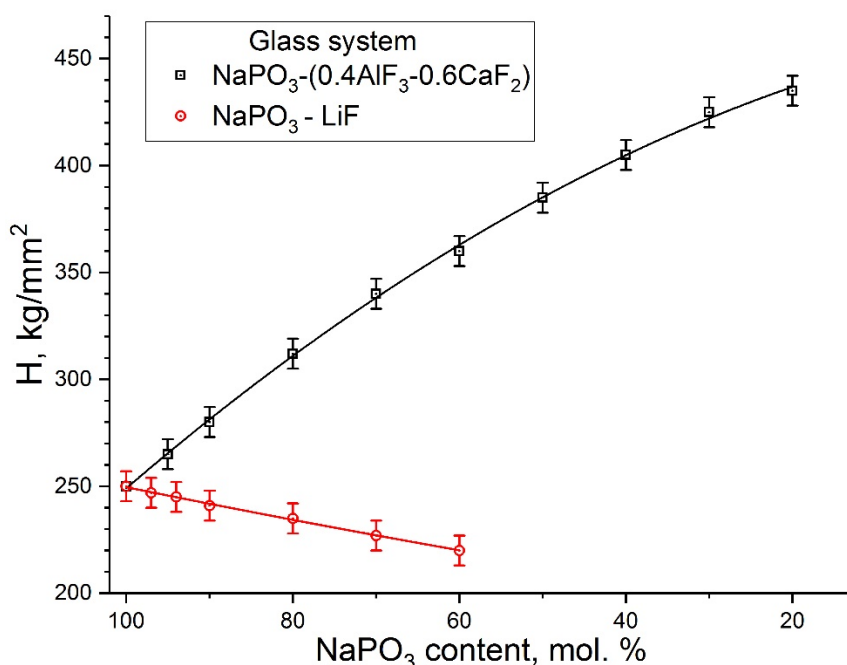


**Fig. 5.** Dependence of the microhardness in  $\text{NaPO}_3\text{-LiF}$  and  $\text{NaPO}_3\text{-(}0.4\text{AlF}_3\text{-}0.6\text{CaF}_2\text{)}$  glassy systems

For original phosphate glass, the value of the microhardness was  $250 \text{ kg/mm}^2$ . The introduction of lithium fluoride reduces the microhardness up to  $220 \text{ kg/mm}^2$ . This is apparently due to the destruction of strong bonds formed by phosphate groups in the glass and their replacement by short bonds of lithium fluoride.

The dependence on the pseudo-binary system had an increasing character. The introduction of a calcium fluoroaluminat eutectic into  $\text{NaPO}_3$  led to an increase in the microhardness value up to  $435 \text{ kg/mm}^2$ . Thus, with an increase in the fluoride content, the microhardness increases by 74% compared to phosphate glass. The latter is due to the greater hardness of glassy aluminum and calcium fluorides as such.

It should be noted that due to the low measurement accuracy ( $\pm 5 \text{ kg/mm}^2$ ), the exact course of the dependence and the function that describes it cannot be determined. However, it

can be said with certainty that the nature of the change is non-linear with an increase in the fluoride content.

The comparison of the microhardness values with other glass systems showed that microhardness of  $\text{NaPO}_3\text{-LiF}$  is 2.5 times lower than for lead silicate glass  $\approx 430\text{--}600\text{ kg/mm}^2$  [15] and is comparable to the value for alkali earth silicate  $280\text{ kg/mm}^2$  [16],  $\text{Sb}_2\text{O}_3\text{-ZnBr}_2 \approx 200\text{ kg/mm}^2$  [17] and ZBLAN  $\approx 200\text{ kg/mm}^2$  [18] glasses. For system  $\text{NaPO}_3\text{-(0.4AlF}_3\text{-0.6CaF}_2\text{)}$  the microhardness value is comparable to lead silicate glasses  $\approx 430\text{--}600\text{ kg/mm}^2$  [15], but still lower than for  $\text{Li}_2\text{O-ZnO-MgO-Al}_2\text{O}_3\text{-SiO}_2$  glasses  $\approx 700\text{ kg/mm}^2$  [19].

#### 4. Conclusions

The paper presents the results of a study of two glass systems based on  $\text{NaPO}_3\text{-LiF}$ , and  $\text{NaPO}_3\text{-(0.4AlF}_3\text{-0.6CaF}_2\text{)}$ . The glasses were synthesized using standard melt-quenching techniques. The area of glass formation in system  $\text{NaPO}_3\text{-LiF}$  was limited by 40 mol. % of lithium fluoride and in  $\text{NaPO}_3\text{-(0.4AlF}_3\text{-0.6CaF}_2\text{)}$  is limited by 80 mol. % of  $(0.4\text{AlF}_3\text{-0.6CaF}_2)$ .

The concentration dependences of the crystallization products, refractive index, glass transition temperature, microhardness, and density indicated on the formation of a mixed fluorophosphate glass network. The obtained concentration changes in the characteristics of glasses were due to a significant difference in the glass-forming ability, chemical and optical properties of phosphates and fluorides. The introduction of lithium fluoride into the  $\text{NaPO}_3\text{-LiF}$  led to the replacement of three-dimensional phosphate chains and the formation of short chains of LiF, which led to both a decrease in the bond strength between structural groups and an increase in the compactness of their arrangement.

The dependence of the density and molar volume on system  $\text{NaPO}_3\text{-(0.4AlF}_3\text{-0.6CaF}_2\text{)}$  had an antibatic character: with an increase in the fluoride content, the glass density increased, while the molar volume decreased. The greater electronegativity of fluorides and the shorter bond length than in sodium metaphosphate causes a decrease in the average distance between the structural groups of glass – fluoride, and phosphate and leadsto the formation of a more tightly coupled glass network.

In the system  $\text{NaPO}_3\text{-LiF}$ , the dependence of the refractive index had a linear decreasing form and is consistent with theoretical concepts. In a pseudo-binary system, the dependence of refractive index had extremum around 30 mol. % of fluorides, which is consistent with reported in the literature. The suggested reason for the noted character is that the network structural groups changed from metaphosphate  $(\text{PO}_3^-)_n$  in the initial composition to the combinations of  $\text{P(O,F)}_4+[\text{MeF}_6]+[\text{MeF}_4]$  (where Me was Al or Ca) in the final composition. However, to confirm this assumption, further studies of the glasses of this series by structurally sensitive methods, such as IR spectroscopy, are required.

The microhardness values for  $\text{NaPO}_3\text{-LiF}$  glasses lie in the region  $250\text{--}220\text{ kg/mm}^2$  which is comparable to fluorozirconate and alkaline earth glassy systems. The values of microhardness in the  $\text{NaPO}_3\text{-(0.4AlF}_3\text{-0.6CaF}_2\text{)}$  system are significantly higher than in lithium system, and it increases from 250 to  $435\text{ kg/mm}^2$  with increasing fluoride content and its maximum value is comparable to lead silicate glasses.

Thus, this study made it possible to clarify the areas of glass formation in fluorophosphate systems  $\text{NaPO}_3\text{-LiF}$  and  $\text{NaPO}_3\text{-(0.4AlF}_3\text{-0.6CaF}_2\text{)}$ , as well as to establish the regularities in the change of some physical properties of glasses with an increase in the content of fluoride components. For glasses in  $\text{NaPO}_3\text{-(0.4AlF}_3\text{-0.6CaF}_2\text{)}$  system the obtained relatively high microhardness values and the possibility of varying the refractive index values in a wide range indicates the possibility of their practical application in optical instrumentation and devices.

## References

- [1] Oueslati-Omrani R, Hamzaoui AH, Chtourou R, M'nif A. Structural, thermal and optical properties of phosphate glasses doped with SiO<sub>2</sub>. *Journal of Non-Crystalline Solids*. 2018;481: 10-16.
- [2] Velli LL, Varsamis CP, Kamitsos EI, Möncke D, Ehrt D. Structural investigation of metaphosphate glasses. *Physics and Chemistry of Glasses*. 2005;46(2): 178-181.
- [3] Margaryan A. *Ligands and Modifiers in Vitreous Materials: Spectroscopy of Condensed Systems*. World Scientific; 1999.
- [4] Jedamzik R, Yadwad H, Dietrich V. Results of a polishing study for SCHOTT XLD glasses. *International Society for Optics and Photonics*. 2015;9628: 96280T.
- [5] Braun M, Yue Y, Rüssel C, Jäger C. Two-dimensional nuclear magnetic resonance evidence for structural order in extruded phosphate glasses. *Journal of Non-Crystalline Solids*. 1998;241(2-3): 204-207.
- [6] Endo J, Inaba S, Homma O, Suzuki Y. Structural features of (Li, Na, K) PO<sub>3</sub> mixed alkali metaphosphate glass for significant anisotropy. *Journal of the American Ceramic Society*. 2022;105(1): 217-224.
- [7] Inaba S, Benino Y, Kohara S, Hosono H, Ito S. Anisotropic structure of alkali metaphosphate glasses. *Journal of the American Ceramic Society*. 2020;103(6): 3631-3641.
- [8] Sirotkin SA, Sysoev DS, Bocharova TV, Ziatdinov AM, Klinkov VA, Loboda VV, Tagil'tseva NO. Spectroscopic properties of the glass of fluoroaluminate systems with small additives of barium metaphosphate activated with the ions of rare-earth elements. *Glass Physics and Chemistry*. 2015; 41(3): 265-271.
- [9] Bradtmüller H, Zhang L, de Araujo CC, Eckert H, Möncke D, Ehrt D. Structural studies of NaPO<sub>3</sub>-AlF<sub>3</sub> glasses by high-resolution double-resonance nuclear magnetic resonance spectroscopy. *The Journal of Physical Chemistry C*. 2018; 122(37): 21579-21588.
- [10] Möncke D, da Cruz Barbosa Neto M, Bradtmüller H, de Souza GB, Rodrigues AM, Elkholy HS, Othman HA, Moulton BJ, Kamitsos EI, Rodrigues AC, Ehrt D. NaPO<sub>3</sub>-AlF<sub>3</sub> glasses: fluorine evaporation during melting and the resulting variations in structure and properties. *Journal of Chemical Technology & Metallurgy*. 2018;53(6): 1047-1060.
- [11] Ojha N, Dmitrieva I, Blanc W, Petit L. Tailoring the glass composition to increase the thermal stability without impacting the crystallization behavior of oxyfluorophosphate glass. *Ceramics*. 2021;4(2): 148-159.
- [12] Li HH. Refractive index of alkali halides and its wavelength and temperature derivatives. *Journal of physical and chemical reference data*. 1976;5(2): 329-528.
- [13] Galleani G, Bradtmüller H, Fares H, Santagneli SH, Nalin M, Eckert H. BiF<sub>3</sub> Incorporation in Na/Ba Mixed Network Modifier Fluoride-Phosphate Glasses: Structural Studies by Solid-State NMR and Raman Spectroscopies. *The Journal of Physical Chemistry C*. 2020;124(46): 25578-25587.
- [14] Karmakar B, Kundu P, Dwivedi RN. IR spectra and their application for evaluating physical properties of fluorophosphate glasses. *Journal of Non-Crystalline Solids*. 2001;289(1-3): 155-162.
- [15] Shrikhande VK, Mirza T, Sawant BB, Sinha AK, Kothiyal GP. Micro hardness measurements on lead silicate glass. *Bulletin of Materials Science*. 1998;21(6): 493-497.
- [16] Goswami M, Kumar R, Patil AS, Sahu AK, Kothiyal GP. Effect of Cr<sub>2</sub>O<sub>3</sub> on solubility and thermo-physical properties of BaO-CaO-Al<sub>2</sub>O<sub>3</sub>-B<sub>2</sub>O<sub>3</sub>-SiO<sub>2</sub>. *AIP Conference Proceedings*. 2012;1447(1): 609-610.
- [17] Legouera M, Kostka P, Poulain M. Glass formation in the Sb<sub>2</sub>O<sub>3</sub>-ZnBr<sub>2</sub> binary system. *Journal of Physics and Chemistry of Solids*. 2004;65(5): 901-906.
- [18] Delben AA, Messaddeq Y, Caridade MD, Aegerter MA, Eiras JA. Mechanical properties of ZBLAN glasses. *Journal of Non-Crystalline Solids*. 1993;161: 165-168.

[19] Al-Harbi OA. Effect of different nucleation catalysts on the crystallization of Li<sub>2</sub>O–ZnO–MgO–Al<sub>2</sub>O<sub>3</sub>–SiO<sub>2</sub> glasses. *Ceramics International*. 2009;35(3): 1121-1128.

## THE AUTHORS

**Klinkov V.A.**

e-mail: klinkovvictor@yandex.ru

ORCID: 0000-0002-5527-7256

**Archelkov V.B.**

e-mail: seva.archelkov@gmail.com

ORCID: 0000-0003-3935-9873

# MECHANICAL PROPERTIES OF MARBLE DUST REINFORCED ALUMINUM MATRIX STRUCTURAL COMPOSITES FABRICATED BY STIR CASTING PROCESS

Sandeep Kashyap<sup>1</sup>, Hariom Tripathi<sup>2</sup>✉, Naveen Kumar<sup>2</sup>

<sup>1</sup>Mechanical Engineering Department, Motilal Nehru National Institute of Technology Allahabad, Prayagraj-211004, India

<sup>2</sup>Applied Mechanics Department, Motilal Nehru National Institute of Technology Allahabad, Prayagraj-211004, India

✉ hariom.tripathi7@gmail.com

**Abstract.** The use of aluminium and its alloys in aerospace, transportation, automobile, and power transmission is growing these days because it has good corrosion resistance, is lightweight, and has high specific strength. But aluminium and its alloys have some drawbacks, such as low absolute strength at higher temperatures, low impact resistance, low hardness, etc. In this research, the aluminium metal matrix composite has been manufactured with the help of the stir casting technique to improve the aluminium alloy's mechanical properties. Where, Al6063 has been taken as the matrix material and the graphite (Gr) (2 wt.%), glass fibre (2 wt.%), boron carbide (B<sub>4</sub>C) (4 wt.%), and marble dust (2 wt.%, 4 wt.%, and 6 wt.%) in powder form have been taken as the reinforcement materials. The present research work has been undertaken to explore marble dust as a reinforcing material as a low-cost option for improving mechanical properties.

**Keywords:** aluminum metal matrix structural composite, stir casting technique, graphite, glass fibre, boron carbide, marble dust

**Acknowledgements.** No external funding was received for this study.

**Citation:** Kashyap S, Tripathi H, Kumar N. Mechanical properties of marble dust reinforced aluminum matrix structural composites fabricated by stir casting process. *Materials Physics and Mechanics*. 2022;48(2): 282-288. DOI: 10.18149/MPM.4822022\_11.

## 1. Introduction

Composite materials are the unique system of two or more materials popularly known as matrix and reinforcement [1-3]. Matrixes are the basic part of the composite system whose properties can be altered by adding the secondary phases (reinforcement materials). The main functions of matrix materials are to transfer the stresses generated due to the application of the load to the reinforcement particles or fibres to protect matrix materials [4-7]. Reinforcement phases are generally particles or fibre dispersed in a controlled amount within the matrix for getting the desired properties. The reinforcement particles generally improve the mechanical properties like hardness, wear resistance, ultimate strength and stiffness, etc. [8-12].

Based on the chemical nature of the matrix materials, composites are divided into three groups polymer matrix (PMC), metal matrix (MMC), and ceramic matrix composites (CMC).

Nowadays, MMCs are quite popular among researchers due to their capability to change the physical properties (thermal expansion, density and thermal diffusivity, etc.) and mechanical behaviour (ultimate strength, fatigue strength, creep strength, corrosion and wear resistance, etc.) of matrix materials by changing the different reinforcement phase [13,14]. Also, the increase in the demand for aerospace, structural components, and lightweight automotive applications like brake disks and engine pistons led to rapid growth in the field of MMCs [15]. Aluminium MCs are more prevalent in MMCs due to their lightweight, corrosion resistance, good electrical conductivity, and high specific strength.

In general, composites of aluminium can be fabricated by semisolid processing (Friction stir processing), liquid state processing (squeeze casting, stir casting, etc.), and powder metallurgy method [16-18]. Generally, hard particles like ceramics (boron carbide, alumina, graphite, silicon carbides, etc.) are used as reinforcements in the case of AMCs.

On the externally applied load to the AMCs, aluminium matrix transfers load to disperse reinforcement particles, and the applied external load is shared by both reinforcement and matrix; this is the leading cause for the strengthening of the matrix material. A strong interface between the matrix and the dispersed reinforcement particles is required to obtain higher mechanical properties of composites. The mutual dissolution creates the interface bonds throughout the casting, so superior wetting is required for the reinforcement particles [19,20].

The objective of this work is to fabricate of an advanced series of Al6063 based MMCs reinforced with and without marble dust particles and observe the effect of reinforcement particles on the mechanical properties

## 2. Experimental Procedure

**Selection of Matrix and Reinforced Materials.** In this present research work, Al6063 alloy having a density 2.7gm/cc and melting point 655°C was used as the matrix material, and glass fibre (2%) (0.005 - 0.01mm dia.), graphite (2%), B<sub>4</sub>C (4%) and varying % of marble dust powder (0, 2, 4, 6%) were added as the reinforcement particles for the preparation of hybrid composite. Marble dust having a density of 2.8gm/cc is an industrial waste utilized in this research work; it contains approximate 28.35% SiO<sub>2</sub>, MgO 16.25%, CaO 40.45%, and Fe<sub>2</sub>O<sub>3</sub> 9.7%. Graphite powders of size 25-35µm, boron carbide particles of size 20-30µm, and marble dust of size 30-50µm were used for this research work. During casting, 1-1.1wt% of magnesium was also added to the molten metal to enhance the wettability of reinforcement particles with the molten matrix metal (aluminium 6063). The chemical compositions of al 6063 used as the composite matrix are shown in Table 1.

Table1. Chemical composition of Al6063

Elements	Al	Mg	Si	Fe	Others
Wt.%	Max 97.5	0.45-0.90	0.2-0.6	Max 0.35	0.65

**Preparation of AMCs.** Marble dust reinforced hybrid AMCs were produced by stir casting technique in the electrical resistance furnace, as shown in Fig. 1. Matrix material (Al6063) was placed inside the graphite crucible. It was melted inside the electric furnace in the inert atmosphere. When the temperature of liquid metal reached 770-790°C, magnesium powder was added to enhance the bonding between the aluminium and reinforcement particles.

By adding magnesium particles to the melted aluminium, the viscosity and surface tension of the molten matrix metal decreases. After that, preheated reinforced particles (glass fibre (2%), graphite (2%), B<sub>4</sub>C (4%), and varying % of marble dust powder (0, 2, 4 and 6%

weight)) were added through a funnel, and the mixture of melted metal and reinforcement particles were stirred at 450-550 rpm for 15-20 minutes. After that, the liquid mixture was poured into the sand mould (as shown in Fig. 2), and the melted composites were allowed to cool, and by this way, four different grades (0, 2, 4, and 6 weight % of marble dust) of AMC's were prepared. The details of prepared different aluminium matrix composites composition are presented in Table 2.



**Fig. 1.** Stir casting setup



**Fig. 2.** Sand mould with casted product

Table 2. Designation of samples

Designation	Composition (wt %)
A0	Al 6063+ Glass Fiber (2%) + Gr (2%) + B <sub>4</sub> C (4%)
A1	Al 6063+Glass Fiber (2%) + Gr (2%) +B <sub>4</sub> C (4%) + Marble Dust (2%)
A2	Al 6063+ Glass Fiber (2%) + Graphite (2%) + B <sub>4</sub> C (4%) + Marble Dust (4%)
A3	Al 6063+Glass Fiber (2%) + Gr (2%) + B <sub>4</sub> C (4%) + Marble Dust (6%)

**Mechanical Testing.** Test specimens were cut using wire-cut EDM to find out the change in the microhardness, tensile strength, and flexural strength of different AMCs. Samples for hardness were finished using emery papers and cloth polishing. Micro-hardness of different composites was determined with the help of a Vickers microhardness tester as per the guidelines of ASTM E384. Mirror polished samples of the composite were placed on Bakelite so that the hardness sample could not slide on the load application. In the hardness test, a load of 5 kg was applied with the help of a diamond indenter for 15-20 seconds, and for getting an accurate hardness value, five readings were taken for each sample.

Instron UTM was used for testing the tensile behaviour of different composites. The test was conducted at room temperature at a strain rate of  $1.5\text{min}^{-1}$ . Samples for tensile testing were prepared with the help of wire EDM as per the standard (ASTM E8).

Tinius Olsen UTM was used for the flexural (bending) strength test, as shown in Fig. 3. For the flexural test, samples were prepared according to standard (ASTM-E290-14), and flexural tests were performed at 1.5 mm/min.



**Fig. 3.** Flexural strength testing machine

### 3. Results and discussion

**Micro-hardness.** The hardness of a metal matrix composite is defined as the resistance to scratch and indentation. It is a surface property of the material. The microhardness of all the four composites is shown in Fig. 4. The strength of bonding (interfacial strength) between the aluminium matrix and the different reinforcement particles present in the composite tell us about the microhardness. Fig. 4 shows that adding varying % of marble dust in Al-based composite improves the hardness of composite (76 Hv to 88 Hv). The maximum hardness (88 Hv) was observed for the 6 wt. % marble dust reinforced composite, and minimum hardness (76 Hv) was observed for unreinforced marble dust composite. This shows that the hardness of AMC can be improved by using varying % of marble dust because well interfacial bonded hard particle resists the motion of dislocations.

**Tensile strength.** The behaviours of tensile strength with varying wt. % of the marble dust have shown in Fig. 5. It is observed from the data of the tensile test that the strength (tensile) of the marble reinforced composites has higher tensile strength as the % of marble dust particles increases from 0 to 4% (180 MPa to 249 MPa); this is because the load is transferred to the reinforcement particles which are strongly bonded with the matrix of aluminium and due to pinning effect.

It was observed that the tensile strength of the AMC sample reinforced with 6% marble dust was around 242MPa. So, on further increase in marble dust content beyond 4%, tensile strength decreased because of the aggregation of marble dust particles in the AMC sample reinforced with 6% marble dust.

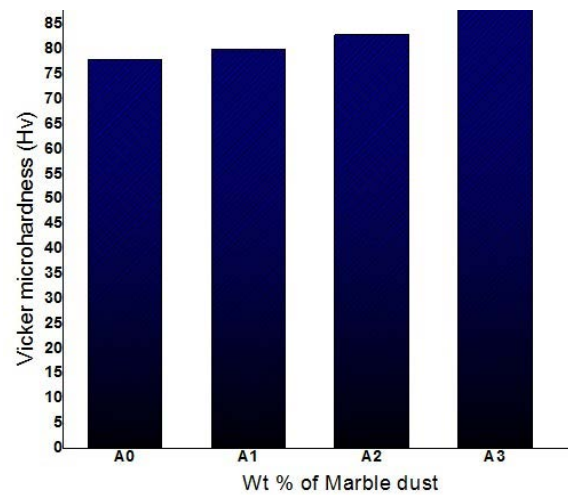


Fig. 4. Vickers micro-hardness results

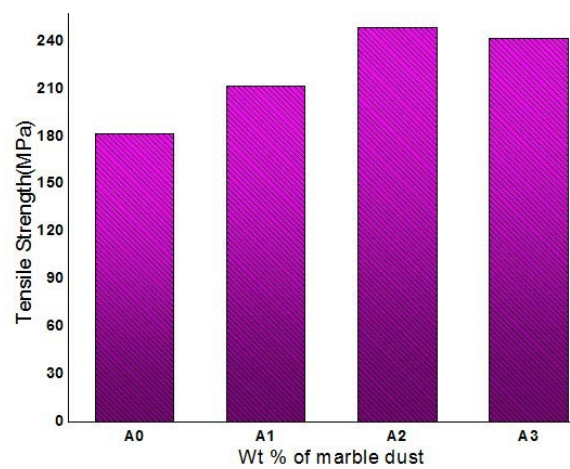


Fig. 5. Tensile behaviour of Al composites

**Flexural strength.** With the help of the 3-point-bend test, flexural strength has been obtained. The behaviour of the bend test for different % of marble dust has shown in Fig. 6. Marble dust reinforced composites show higher flexural strength than unreinforced marble dust composites. The maximum value of flexural strength (262 MPa) is for 4% reinforced marble dust and the minimum value of flexural strength (210 MPa) for unreinforced marble dust composite.

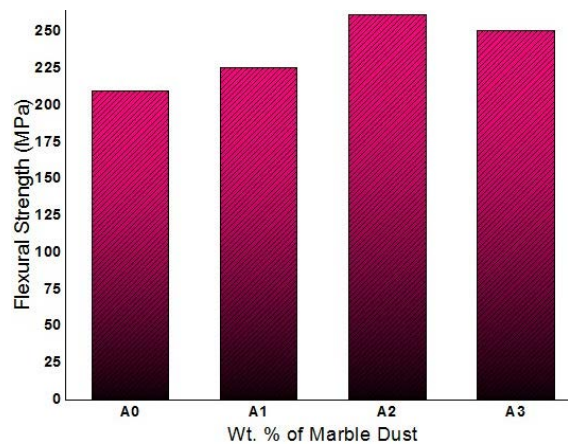


Fig. 6. Flexural behaviour of Al composites

This increase in flexural property occurs due to the good interface bonding between the hard particles and the matrix material. But it is observed that in the case of 6% reinforced marble particles; the flexural strength is equal to 251 MPa; this is less than 4% marble reinforced system because for 6% reinforced system, agglomeration of marble dust particles took place.

#### 4. Conclusion

In this research, it is concluded that after the addition of marble reinforcement:

- The addition of varying % of marble dust in Al-based composite improves the hardness of composite (76 Hv to 88 Hv), and the maximum hardness (88 Hv) was observed for the 6 wt % and minimum for unreinforced.
- The tensile strength of the marble reinforced composites has higher tensile, and flexure strength as the % of marble dust particles increases from 0 to 4% (180 MPa to 249 MPa for tensile and 210MPa to 262 MPa for flexure).
- It is observed that for the case of 6% reinforced marble particles, the tensile and flexural strength comes to be equal to 242 MPa and 251 MPa, respectively, these values are less as compared to 4% marble reinforced system this is because agglomeration of marble dust particle takes place for 6% reinforced system.

#### References

- [1] Mathews FL, Rawlings RD. *Composite Materials; Engineering and Science*. Woodhead Publishing; 1999.
- [2] Tripathi H, Bharti A, Vishal A, Kumar N. Effect of Tool Rotation on Microstructure and Hardness of AZ31 Mg Alloy Processed by FSP. In: *Advances in Mechanical Engineering*. 2020. p.677-684.
- [3] Kumar N, Bharti A, Saxena KK. Effect of Ti Reinforcement on the Physical and Mechanical Properties of AZ91/Ti Composites. *Indian Journal of Engineering and Materials Sciences*. 2021;28(6): 602-607.
- [4] Kumar N, Bharti A, Dixit M. Powder Compaction Dies and Compressibility of Various Materials. *Powder Metallurgy and Metal Ceramics*. 2021;60(7-8): 403-409.
- [5] Kumar N, Bharti A. Review on Powder Metallurgy: A Novel Technique for Recycling and Foaming of Aluminium-Based Materials. *Powder Metallurgy and Metal Ceramics*. 2021;60(1-2): 52-59.
- [6] Bharti A, Tripathi H. Enhancement of Fatigue Life of TIG-Welded Joint by Friction Stir Processing. In: *Renewable Energy and its Innovative Technologies*. Springer; 2018. p.51-59.
- [7] Xavier LF, Suresh P. Wear Behavior of Aluminium Metal Matrix Composite Prepared from Industrial Waste. *The Scientific World Journal*. 2016;2016: 6538345.
- [8] ASTM Standard E384, 2011e1. *Standard Test Method for Knoop and Vickers Hardness of Materials*. ASTM International; 2011.
- [9] ASTM Standard E8/E8M-16a. *Standard Test Methods for Tension Testing of Metallic Materials*. ASTM International.
- [10] Kumar N, Bharti A, Chauhan AK. Effect of Ti Reinforcement on the Wear Behaviour of AZ91/Ti Composites Fabricated by Powder Metallurgy. *Materials Physics and Mechanics*. 2021;47(4): 600-607.
- [11] Melgarejo HZ, Suarez OM, Kumar S. Microstructure and Properties of Functionally Graded Al-Mg-B Composites Fabricated by Centrifugal Casting. *Composites Part A: Applied Science and Manufacturing*. 2008;39(7): 1150-1158.
- [12] Kumar GBV, Rao CSP, Selvaraj N, Bhagyashekhar. Studies on Al6061-SiC and Al7075-Al<sub>2</sub>O<sub>3</sub> Metal Matrix Composites. *Journal of Minerals & Materials Characterization & Engineering*. 2010;9(1): 43-55.

- [13] Kennedy AR. The Microstructure and Mechanical Properties of Al-Si-B<sub>4</sub>C Metal Matrix Composites. *Journal of Materials Science*. 2002;37: 317-323.
- [14] Sharifi EM, Karimzadeh F, Enayati MH. Fabrication and Evaluation of Mechanical and Tribological Properties of Boron Carbide Reinforced Aluminum Matrix Nanocomposites. *Materials & Design*. 2011;32(6): 3263-3271.
- [15] Mishra SK, Satapathy A. Ceramic Particulate Filled ZA-27 Metal Matrix Composites: Comparative Analysis. *Materials Science and Technology*. 2014;30(12): 1495-1499.
- [16] Kumar D, Bharti A, Azam SM, Kumar N, Tripathi H. Investigations of Mechanical Properties of Copper Matrix Hybrid Composite. In: *Advances in Mechanical Engineering*. Singapore. Springer; 2020. p.671-676.
- [17] Kumar N, Bharti A, Tripathi H. Investigation of Microstructural and Mechanical Properties of Magnesium Matrix Hybrid Composite. In: *Advances in Mechanical Engineering*. 2020. p.661-669.
- [18] Bandyopadhyay NR, Ghosh S, Basumallick A. New Generation Metal Matrix Composites. *Materials and manufacturing processes*. 2007;22(6): 679-682.
- [19] Rohatgi PK. Metal Matrix Composites. *Defence Science Journal*. 2003; 323-349. Available from: DOI:10.14429/dsj.43.4336.
- [20] Behera R, Das S, Chatterjee D, Sutradhar G. Forgeability and Machinability of Stir Cast Aluminum Alloy Metal Matrix Composites. *Journal of Minerals and Materials Characterization and Engineering*. 2011;10(10): 923-927.

## THE AUTHORS

### **Kashyap S.**

e-mail: sandeepkashyap38@gmail.com

ORCID: 0000-0002-6969-2207

### **Tripathi H.**

e-mail: hariom.tripathi7@gmail.com

ORCID: 0000-0002-5752-8848

### **Kumar N.**

e-mail: chaudhary56naveen@gmail.com

ORCID: 0000-0002-6918-4384

## STUDY OF POLYLACTIDE 3D-PRINTED SAMPLES WITH DOUBLE-LAYER WEAVE

A.V. Pogrebnoi<sup>✉</sup>

JSC "Central Research Institute for Machine Building", 4 Pionerskaya St., Korolev, Moscow Region, 141070,  
Russia

✉ a.v.pogrebnoi@yandex.ru

**Abstract.** Fused Deposition Modeling method (FDM) is widely used in various fields of science for prototyping and manufacturing of final functional parts. The actual problem of the FDM method is the low bond strength between the layers of printed parts. Proposed 3D-printing method is based on the formation of double-layer weave between polymer threads. An unfilled polylactide (PLA) was used for fabrication of samples to demonstrate the proposed method. PLA samples with double-layer weave obtained by fused deposition modeling method are studied. Characteristics of samples obtained by static tension test are compared. Their structure and fracture mode are investigated. It is found that double-layer weave affects bond strength between layers of 3D-printed samples. The obtained results show that the proposed method in combination with other methods can be implemented for other polymer materials and composites for local reinforcement of printed parts.

**Keywords:** adhesion, mechanical properties, tensile strength, reinforcement, double-layer weave, fused deposition modeling, polylactide

**Acknowledgements.** No external funding was received for this study.

**Citation:** Pogrebnoi AV. Study of polylactide 3D-printed samples with double-layer weave. *Materials Physics and Mechanics*. 2022;48(2): 289-299. DOI: 10.18149/MPM.4822022\_12.

### 1. Introduction

Currently, Fused Deposition Modeling (FDM) invented by S. Crump in 1989 is one of the most widespread technologies of additive manufacturing in the world. Thanks to low equipment cost and availability of consumables, FDM finds wide application in various fields of science and technology for the purpose of prototyping and manufacturing final functional parts [1].

The method consists in slicing a 3D computer model of the part into separate layers, each of which is successively printed on a build platform using a print head. The print head moves on a programmed trajectory represented in the form of the set of commands in the *G-code* language. 3D printing uses a thread-like polymer material (filament) as the main build consumable, which is extruded into the print head, heated to the melting temperature, and pressed through a nozzle of set diameter [2].

The FDM method can be applied in aircraft engineering to design aircraft, bulk elements, and other small-batch parts [3-5]. The costs of molding equipment production for the FDM fabrication of wing covering parts can be reduced by 6–7 times [4], while the time of the equipment production can be reduced by 2–4 times [4,5].

In rocket and space structures, the FDM method can be employed to fabricate parts from engineering thermoplastics capable of long-term operation in high load and temperature conditions [6]. Polyetherimide (PEI), polyether ether ketone (PEEK) [9], and their composites are an example of such materials. Despite the need for further tuning of the technology, certain publications note that the FDM method can be used to produce parts during a space flight to solve the task of on-site repair of malfunctioning devices [10,11-12].

Low bond strength between the layers of the printed parts remains one of the most critical shortcomings of the FDM method [13-14,15]. This issue causes delamination of the fabricated parts in the process of cooling and loss of resistance to various gasses and liquids, including organic solvents [16]. Weak adhesion between the layers of the material requires making the part design stronger and more complex, which increases its weight and fabrication time [17].

The performed analysis of the literature showed that the solutions to this issue can be conditionally divided into three groups.

The first group relates to the optimization of the main technological parameters of 3D printing and includes methods aimed at increasing the bond between the layers of FDM products, mainly by reducing the interval between the threads [18-20], shifting the layers relative to the direction of laying the melt threads [21-22], reducing the layer height [23], and increasing the extrusion temperature during 3D printing [21,24].

The second group refers to the provision of external thermal effects on the product during 3D printing and includes methods based on the use of laser, infrared or ultrasonic sources. Thus, in the process of 3D printing, the required area of the part is locally heated to increase the bond between the layers [25].

The third group of methods is based on improving the properties by adding binders and polymer additives, as well as discrete reinforcing fibers to the composition of the building material [26].

An analysis of publications [13-26] showed that none of the known methods is able to significantly increase the strength of the bond between the layers of printed products.

One of the possible reasons could be the use of standard slicing algorithms that cut the digital model of the part into separate flat (2D) layers.

In this regard, it seems interesting to study the case in which 3D printing is carried out not in a plane, but in space, that is alternately in several layers, with the polymer threads interweaving. The simplest example would be a double-layer weave formed between two adjacent layers of the material.

The aim of this work was to study the effect of double-layer weaving on the strength of the bond between the layers of samples obtained by 3D printing.

## 2. Experimental Part

Samples were obtained from unfilled white polylactide (PLA) with a density of  $1.25 \text{ g/cm}^3$  and a filament diameter of 1.75 mm manufactured by REC, Russian Federation. The choice of PLA for the study was because it is the most widely used material for FDM 3D printing [15,25], and a desktop FDM 3D printer can be used to make samples from PLA [15,17,23].

For the purpose of this work, it was extremely important to comply with the specified geometric dimensions of the samples. The equipment had to have a rigid metal body and kinematics that ensured the movement of the print head in the horizontal plane and the vertical movement of the heated build platform.

Therefore, a widely available desktop 3D printer "Flying Bear Ghost 5" (Jinhua Flyingbear Intelligent Technology Co., Ltd, People's Republic of China) with a print area of 255x210x200 mm (length, width, and height) was used to obtain the samples. 3D printing was carried out in the Cartesian coordinate system.

It is common knowledge that the current mechanical test standards of the GOST, ISO or ASTM series were developed for samples obtained by casting, pressing, or machining [17,23]. Due to the lack of a single standard suitable for testing samples with a complex structure obtained by 3D printing, in this research, all samples were made in the form of a rectangular strip 121 mm long, 20.7 mm wide, and 2.8 mm thick. Each sample consisted of 14 layers of material 0.2 mm thick and was printed at a printing speed of 11.7 mm/s on a substrate that ensured reliable contact with the build platform. The same PLA material was used to print the samples and the substrate. The substrate had a thickness of 0.05 mm and was printed at a speed of 33.3 mm/s. Test samples were printed in the amount of 5 pcs in each series and then marked (series *A* without thread weave, series *B* with double-layer thread weave). In both cases, the polymer filaments were oriented perpendicular to the tensile load axis (i.e. at an angle of  $90^\circ$  to the OX axis). For better contact between the surface of the samples and the grips of the testing equipment, in the first and last layers of the samples of both series, the polymer filaments were also oriented at an angle of  $90^\circ$ .

The method for obtaining the double-layer weave in the designed samples of the *B* series consisted of the alternate laying of polymer filaments in two adjacent layers with the formation of a gap necessary for laying polymer filaments during the reverse movement of the print head (Fig. 1). The dotted lines show the movement of the print head along the corresponding axes of the Cartesian coordinate system. Commands 1.10 and 2.10 are responsible for shifting the print head before repeating path sections 1.1–1.9 and 2.1–2.9.

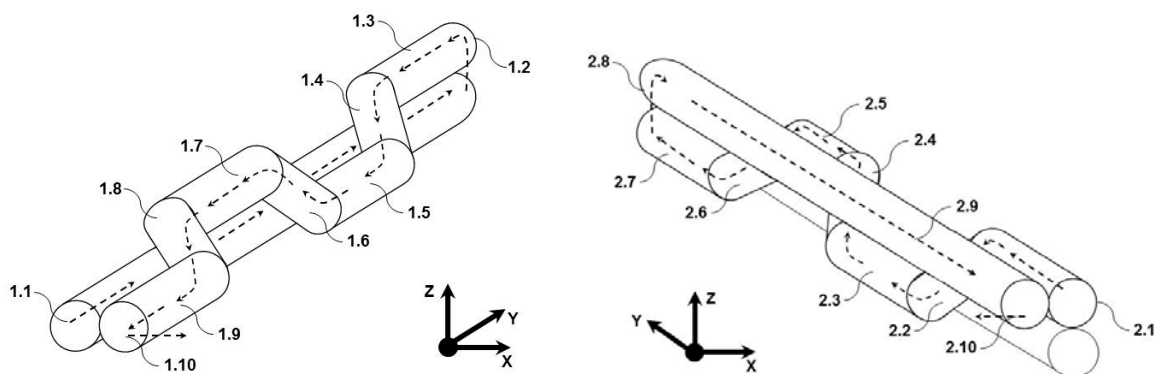


**Fig. 1.** Method of alternate laying of polymer threads from left to right (a) and right to left (b)

The symbols in the Figure show typical sequential commands in the *G-Code* language, which controlled the movement of the print head along a three-dimensional trajectory. The pseudocode of the algorithm for creating a double-layer weave is shown in Table 1 and contains the specified *G-Code* commands for 3D printing a sample from left to right and right to left. Symbols 1.1–1.10 and 2.1–2.10 in the Table mark the corresponding sections of the trajectory of the print head.

After executing a series of commands 1.1–1.10 in the amount necessary to make a sample from left to right, the print head moved to the height of the second layer. Then the next series of commands 2.1–2.10 was performed to print the sample in the right-to-left direction so that the polymer threads were laid in the resulting gaps. After that, the print head moved to the height of the next layer, and the above process was repeated until the pattern was printed in-depth. The result of the formation of a double-layer weave is shown in Fig. 2.

Table 1. Pseudocode of the 3D printing algorithm for double-layer weave

No.	G-Code commands for 3D printing from left to right	No.	G-Code commands for 3D printing from right to right left
1.1	G1 X0 Y+Y <sub>11</sub> EE <sub>11</sub> FF <sub>11</sub>	2.1	G1 X0 Y+Y <sub>21</sub> EE <sub>21</sub> FF <sub>21</sub>
1.2	G0 Z+ΔZ	2.2	G1 X-X <sub>22</sub> Y+Y <sub>22</sub> Z-ΔZ EE <sub>22</sub> FF <sub>22</sub>
1.3	G1 X0 Y-Y <sub>13</sub> EE <sub>13</sub> FF <sub>13</sub>	2.3	G1 X0 Y+Y <sub>23</sub> EE <sub>23</sub> FF <sub>23</sub>
1.4	G1 X+X <sub>14</sub> Y-Y <sub>14</sub> Z-ΔZ EE <sub>14</sub> FF <sub>14</sub>	2.4	G1 X+X <sub>24</sub> Y+Y <sub>24</sub> Z+ΔZ EE <sub>24</sub> FF <sub>24</sub>
1.5	G1 X0 Y-Y <sub>15</sub> EE <sub>15</sub> FF <sub>15</sub>	2.5	G1 X0 Y+Y <sub>25</sub> EE <sub>25</sub> FF <sub>25</sub>
1.6	G1 X-X <sub>16</sub> Y-Y <sub>16</sub> Z+ΔZ EE <sub>16</sub> FF <sub>16</sub>	2.6	G1 X-X <sub>26</sub> Y+X <sub>26</sub> Z-ΔZ EE <sub>26</sub> FF <sub>26</sub>
1.7	G1 X0 Y-Y <sub>17</sub> EE <sub>17</sub> FF <sub>17</sub>	2.7	G1 X0 Y+Y <sub>27</sub> EE <sub>27</sub> FF <sub>27</sub>
1.8	G1 X+X <sub>18</sub> Y-Y <sub>18</sub> Z-ΔZ EE <sub>18</sub> FF <sub>18</sub>	2.8	G1 Z+ΔZ EE <sub>28</sub> FF <sub>28</sub>
1.9	G1 X0 Y-Y <sub>19</sub> EE <sub>19</sub> FF <sub>19</sub>	2.9	G1 X0 Y-Y <sub>29</sub> EE <sub>29</sub> FF <sub>29</sub>
1.10	G1 X+ΔX	2.10	G1 X-ΔX



**Fig. 2.** Example of the two-layer weave of polymer threads in the right-to-left direction

The main technological parameters of 3D printing of PLA samples are shown in Table 2. The extrusion temperature during printing was chosen close to the melting temperature of PLA plastic. This mode was chosen in order to ensure faster cooling of the material before applying the next layer, as well as to reduce the effect of high melting temperature on the strength properties of the resulting samples.

Table 2. Main technological parameters of FDM 3D printing of PLA plastic samples

No.	Parameter name	Value
1	Print head nozzle diameter	0.4 mm
2	Layer height	0.2 mm
3	Extrusion temperature	185°C
4	Heated platform temperature	60°C
5	Infill	100%
6	Orientation of polymer filaments on the build platform	90° (along OY axis)
7	Orientation of the sample on the platform	0° (along OX axis)

### 3. Research Methods

In order to confirm the feasibility of 3D printing with alternate laying of a polymer thread in two adjacent layers, the internal structure of the obtained samples was studied. Visual analysis was carried out on Dino-Lite Premier AM7013MZT digital microscope (AnMo Electronics Corporation, Taiwan) with a resolution of 5 MP at 30x magnification.

To assess the effect of the internal structure on the strength of the interlayer bond of the material, the method of static tensile tests was used on Instron 3369 electromechanical tensile testing machine, UK. The essence of the method was to apply a tensile load to the sample until its destruction at a constant temperature and a constant speed of movement of the active grip of the testing equipment equal to 2 mm per minute. Strength tests were carried out at a temperature of 20°C.

The geometrical parameters (width and thickness) of the test samples were measured using an electronic caliper of the ShTsTs-I-125-GOST 166-89 type (ZAO PO Chelyabinsk Instrumental Plant, Russian Federation).

### 4. Results of the study of strength properties and structure of samples and their discussion

We tested the samples with and without interweaving for tension in the direction across the threads. According to the results of static tests (Table 3), the minimum tensile strength for samples of series A turned out to be 32.64 MPa (with an average value of 37.71 MPa).

The digital microscope photograph (Fig. 3) shows that the destruction of the series A samples occurred strictly along the line of contact between the melt threads. This type of destruction has already been noted in [13, 23] and is due to the weak bond between the polymer threads.

Table 3. Comparison of static tensile test characteristics for samples with and without weaving

Sample Ref. No.	Sample width $b_i$ , mm	Sample thickness $h_i$ , mm	Maximum load before failure $F_{imax}$ , N	Ultimate tensile strength $\sigma_{bi} = \frac{F_{imax}}{b_i \cdot h_i} 10^{-3}$ , MPa	Average tensile strength $\bar{\sigma}_b$ , MPa	Standard deviation, $S$
A1	20.72	2.85	2029.98	34.38	37.71	3.95
A2	20.69	2.85	2336.60	39.63		
A3	20.68	2.87	1937.53	32.64		
A4	20.73	2.86	2464.86	41.57		
A5	20.77	2.89	2422.29	40.35		
B1	20.86	2.85	2465.03	41.46	40.63	0.81
B2	20.79	2.87	2386.50	39.99		
B3	20.90	2.85	2356.21	39.56		
B4	20.89	2.85	2447.88	41.12		
B5	20.89	2.85	2442.62	41.03		

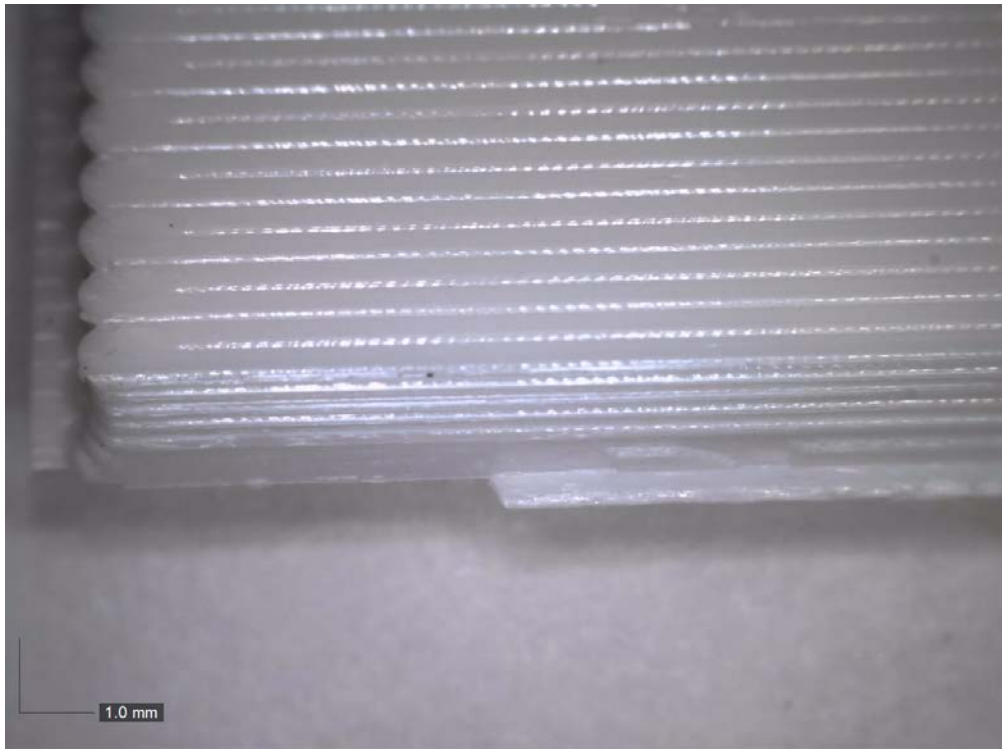


**Fig. 3.** Fracture surface of A3 sample made of PLA without weave (side view)

The minimum tensile strength for series *B* samples was 39.56 MPa (with an average value of 40.63 MPa). Weave samples have a characteristic transverse fracture pattern (Fig. 4–7).

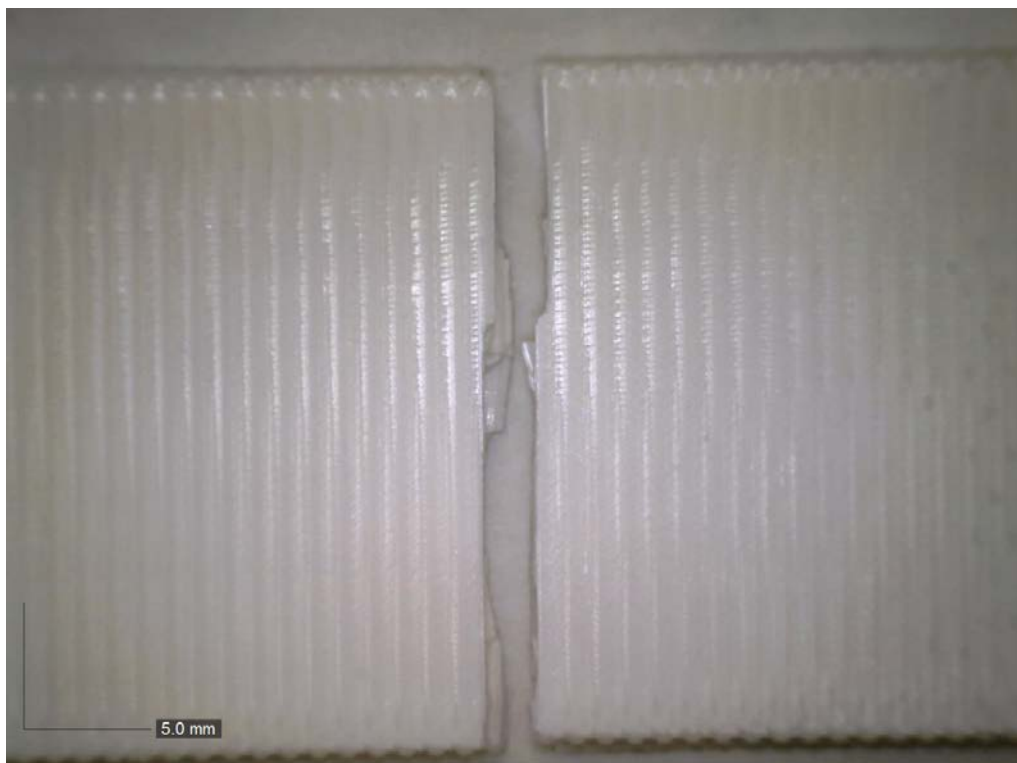


**Fig. 4.** Fracture surface of B1 sample made of PLA with double-weave (top view)

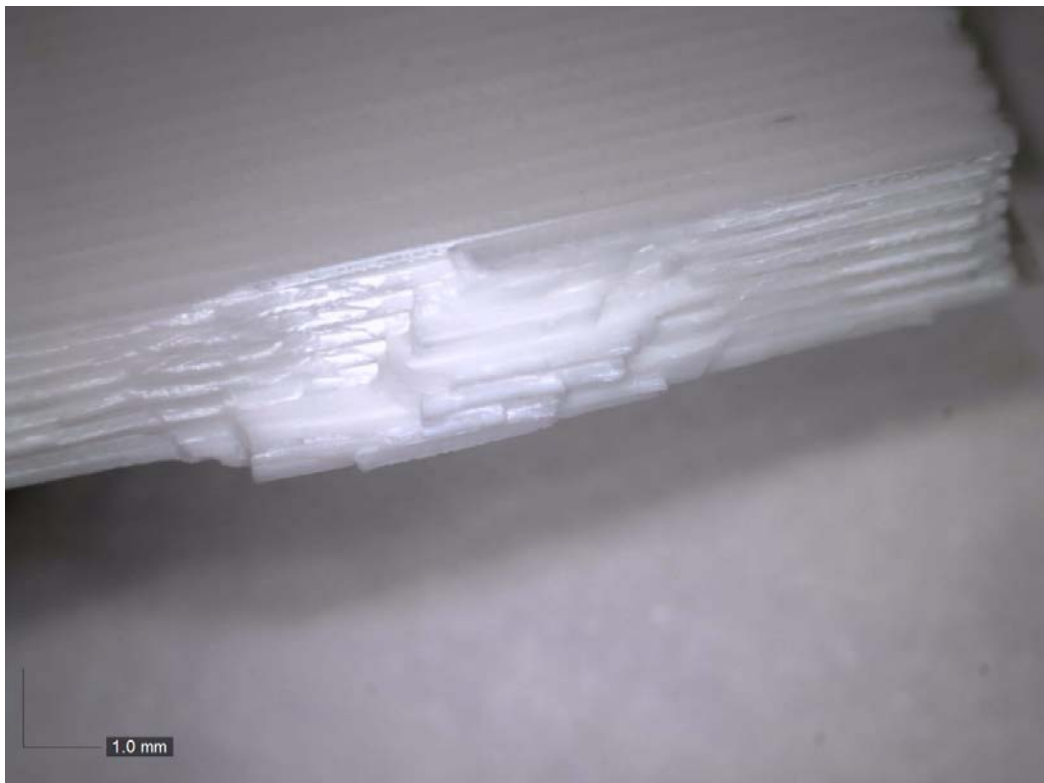


**Fig. 5.** Fracture surface of B1 sample made of PLA with double-weave (side view)



**Fig. 6.** Fracture surface of B5 sample made of PLA with double-weave (top view)

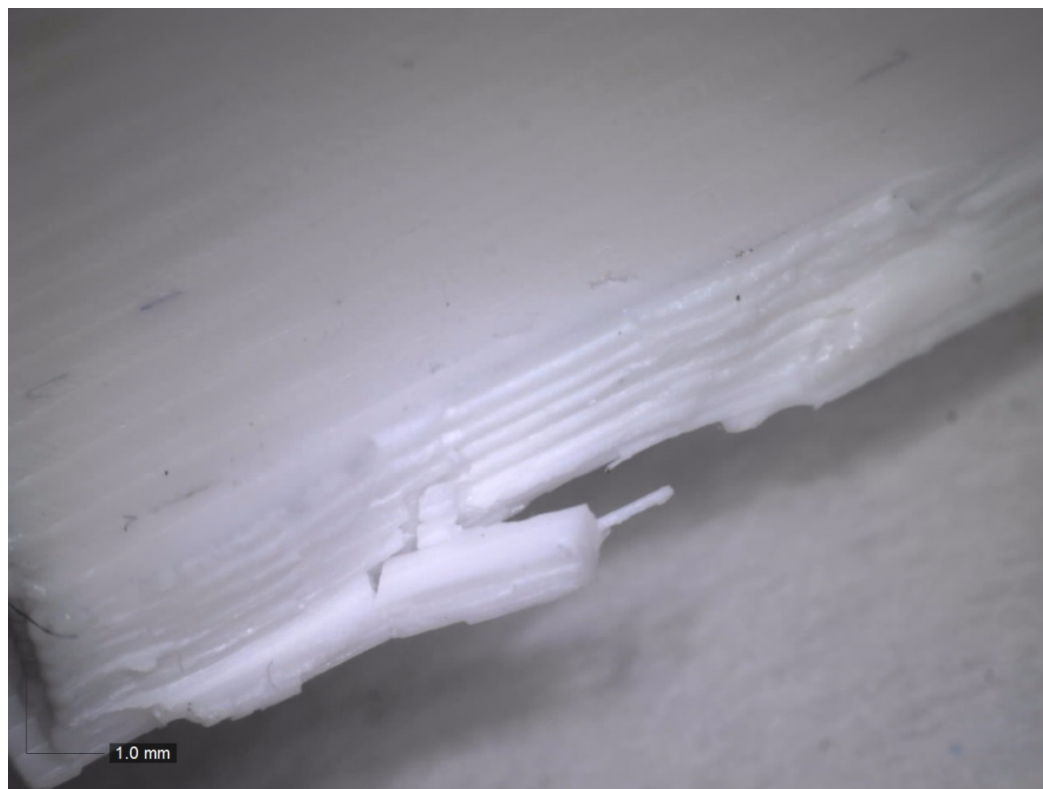


**Fig. 7.** Fracture surface of B5 sample made of PLA with double-weave (side view)

The results presented above can be supplemented with diagrams of the nominal stress dependence on the strain for samples with and without weaving (Fig. 8). The nominal stress values were calculated as the ratio of the acting load to the cross-sectional area of the samples.

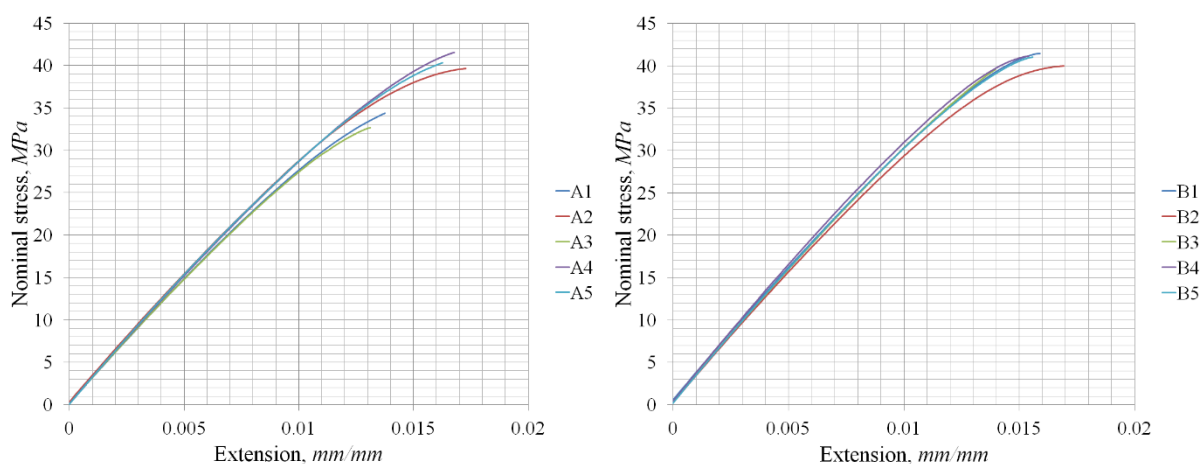


**Fig. 8.** Diagrams of nominal stress versus strain (extension) for samples with and without weaving

Presented in Table 3 and Fig. 8, the characteristics obtained during static tension of the samples and the typical transverse fracture pattern allow us to draw the following conclusions.

First, the double-layer weave affects the bond strength between the layers of printed PLA samples. Compared to series *A* samples, series *B* samples show an increase in strength from 8% (when comparing average tensile strength values) to 21% (when comparing minimum tensile strength values). The proposed mechanism of influence may be that the double-layer weave prevents a crack from forming along any one line at the polymer

filaments interface. As a result, the direction of propagation of a crack formed in one of the layers of the sample changes when it interacts with the melt threads of the adjacent layer.

Secondly, with a relatively small difference in strength, the value of the standard deviation for samples with the weave turned out to be significantly less than for samples without it. A double-layer weave allows for a smaller variation in tensile strength values relative to the average and, therefore, provides better repeatability and predictability of strength properties.

Thirdly, the double-layer weaving of polymer threads makes it possible to achieve an increase in strength comparable to other methods. A similar result was obtained using the layer height control method. For comparison, when the layer height is halved (from 0.2 to 0.1 mm at a constant nozzle diameter of 0.4 mm), the ultimate strength of the samples increases by 18% [23]. Therefore, the use of double-layer weaves turns out to be the preferred method, as it does not entail an increase in the number of layers and 3D printing time.

Fourthly, the results obtained made it possible to confirm the possibility of 3D printing of samples with a more complex internal structure than in samples with an orientation of 0°, 45°/45°, 90°, and other directions for laying threads. In a similar way, various variants of multilayer weaves can be implemented.

In addition, we should note an increase in shear resistance of the *B* series samples. When twisted around the longitudinal axis, the two-layered samples of the *A* series broke at angles up to 30°, while the double-layer weave samples could be twisted at an angle exceeding 90°. The degree of influence of the features of the internal structure on the strength properties of FDM products under various types of loading and complexity of weaving is to be determined in subsequent works.

## 5. Conclusions

The implemented scheme of double-layer weaving of polymer threads influenced the strength of the bond between the layers and the nature of the fracture of the samples obtained by the FDM method.

It is shown that the tensile strength of PLA samples obtained by the FDM method increases from 8% to 21% with a double-layer weave of threads due to strengthening of the bond between the layers of the polymer material. With a relatively small difference in strength values, samples with interweaving have better repeatability of strength properties compared to samples without it. This effect is important in predicting the properties of materials obtained by 3D printing, as well as in designing parts with specified strength properties.

The results obtained indicate that the proposed method, in combination with other methods, can be implemented for polymeric materials and composites based on them and used for local hardening of printed parts, allowing for the requirements of minimum weight, cost, and resistance to environmental factors.

## References

- [1] Vyavahare S, Teraiya S, Panghal D, Kumar S. Fused deposition modelling: a review. *Rapid Prototyping Journal*. 2020;26(1): 176-201.
- [2] Gibson I, Rosen D, Stucker B. *Additive Manufacturing Technologies: Rapid Prototyping to Direct Digital Manufacturing*. NY: Springer; 2015.
- [3] Azarov AV, Antonov FK, Golubev MV, Khaziev AR, Ushanov SA. Composite 3D printing for the small size unmanned aerial vehicle structure. *Composites Part B*. 2019;169: 157-163.
- [4] Petrova GN, Larionov SA, Platonov MM, Perfilova DN. Thermoplastic materials for new generation for aviation. *Aviation Materials and Technologies*. 2017;S: 420-436.

- [5] Lopatin AN, Zverkov ID. Shaping molding tools production for composite parts by means of additive technologies. *Aviation Materials and Technologies*. 2019;2(55): 53-59.
- [6] Azarov AV, Latysheva TA, Khaziev AR. Optimal design of advanced 3D printed composite parts of rocket and space structures. *IOP Conference Series: Materials Science and Engineering*. 2020;934: 012062.
- [7] Gebisa AW, Lemu HG. Influence of 3D Printing FDM Process Parameters on Tensile Property of ULTEM 9085. *Procedia Manufacturing*. 2019;30: 331-338.
- [8] Padovano E, Galfione M, Concialdi P, Lucco G, Badini C. Mechanical and Thermal Behavior of Ultem® 9085 Fabricated by Fused-Deposition Modeling. *Applied Sciences*. 2020;10(9): 3170.
- [9] Zanjanijam AR, Major I, Lyons JG, Lafont U, Devine DM. Fused Filament Fabrication of PEEK: A Review of Process-Structure-Property Relationships. *Polymers*. 2020;12(8): 1665.
- [10] Cowley A, Perrin J, Meurisse A, Micallef A, Fateri M, Rinaldo L, Bamsey N, Sperl M. Effects of variable gravity conditions on additive manufacture by fused filament fabrication using polylactic acid thermoplastic filament. *Additive Manufacturing*. 2019;28: 814-820.
- [11] Prater T, Bean Q, Werkheiser N, Grguel R, Beshears R, Rolin T, Huff T, Ryan R, Ledbetter F, Ordonez E. Analysis of specimens from phase I of the 3D printing in Zero G technology demonstration mission. *Rapid Prototyping Journal*. 2017;23(6): 1212-1225.
- [12] Prater T, Werkheiser N, Ledbetter F, Timucin D, Wheeler K, Snyder M. 3D Printing in Zero G Technology Demonstration Mission: complete experimental results and summary of related material modeling efforts. *The International Journal of Advanced Manufacturing Technology*. 2019;101, 391-417.
- [13] Ahn SH, Montero M, Odell D, Roundy S, Wright PK. Anisotropic material properties of fused deposition modeling ABS. *Rapid Prototyping Journal*. 2002;8(4): 248-257.
- [14] Ziemian C, Sharma M, Ziemian S. Anisotropic Mechanical Properties of ABS Parts Fabricated by Fused Deposition Modelling. In: Gokcek M. (ed.) *Mechanical Engineering*. London: IntechOpen; 2012. p.159-180.
- [15] Dey A, Yodo N. A Systematic Survey of FDM Process Parameter Optimization and Their Influence on Part Characteristics. *Journal of Manufacturing and Materials Processing*. 2019;3(3): 64.
- [16] Erokhin KS, Gordeev EG, Ananikov VP. Revealing interactions of layered polymeric materials at solid-liquid interface for building solvent compatibility charts for 3D printing applications. *Scientific Reports*. 2019;9: 20177.
- [17] Kuznetsov VE, Tavitov AG, Urzhumtsev OD, Mikhailin MV, Solonin AN. Design and Fabrication of Strong Parts from Poly (Lactic Acid) with a Desktop 3D Printer: A Case with Interrupted Shell. *Polymers*. 2019;11(5): 760.
- [18] Sun Q, Rizvi GM, Bellehumeur CT, Gu P. Effect of processing conditions on the bonding quality of FDM polymer filaments. *Rapid Prototyping Journal*. 2008;14(2): 72-80.
- [19] Bellehumeur C, Li L, Sun Q, Gu P. Modeling of Bond Formation Between Polymer Filaments in the Fused Deposition Modeling Process. *Journal of Manufacturing Processes*. 2004;6(2): 170-178.
- [20] Onwubolu GC, Rayegani F. Characterization and Optimization of Mechanical Properties of ABS Parts Manufactured by the Fused Deposition Modelling Process. *International Journal of Manufacturing Engineering*. 2014;2014: 598531.
- [21] Spoerk M, Arbeiter F, Cajner H, Sapkota J, Holzer C. Parametric optimization of intra- and inter-layer strengths in parts produced by extrusion-based additive manufacturing of poly(lactic acid). *Journal of Applied Polymer Science*. 2017;134(41): 45401.
- [22] Slonov AL, Khashirov AA, Zhansitov AA, Rzhetskaya EV, Khashirova SY. The influence of the 3D-printing technology on the physical and mechanical properties of polyphenylene sulfone. *Rapid Prototyping Journal*. 2018;24(7): 1124-1130.

- [23] Kuznetsov VE, Solonin AN, Urzhumtsev OD, Schilling R, Tavitov AG. Strength of PLA Components Fabricated with Fused Deposition Technology Using a Desktop 3D Printer as a Function of Geometrical Parameters of the Process. *Polymers*. 2018;10(3): 313.
- [24] Aliheidari N, Christ J, Tripuraneni R, Nadimpalli S, Ameli A. Interlayer adhesion and fracture resistance of polymers printed through melt extrusion additive manufacturing process. *Materials & Design*. 2018;156: 351-361.
- [25] Liu Z, Wang Y, Wu B, Cui C, Guo Y, Yan C. A critical review of fused deposition modeling 3D printing technology in manufacturing polylactic acid parts. *The International Journal of Advanced Manufacturing Technology*. 2019;102: 2877-2889.
- [26] Polyakov IV, Vaganov GV, Yudin VE, Smirnova NV, Ivan'kova EM, Popova EN. Study of Polyetherimide and Its Nanocomposite 3D Printed Samples for Biomedical Application. *Polymer Science, Ser. A*. 2020;62: 337-342.

#### THE AUTHOR

**Pogrebnoi A.V.**

e-mail: a.v.pogrebnoy@yandex.ru

ORCID: 0000-0001-7296-5387

### **Submission of papers:**

Manuscript should be submitted (**both MS Word and PDF**) by e-mail to: **mpmjournal@spbstu.ru**

After a confirmation of the paper acceptance, the authors should send the signed hard copy of the "Transfer of Copyright Agreement" form (available at <http://www.mpm.spbstu.ru> section "Authors") by regular post to "Materials Physics and Mechanics" editorial office:

*Periodicals Editorial Office, Institute of Advanced Manufacturing Technologies, Peter the Great St.Petersburg Polytechnic University, Polytechnicheskaya, 29, St.Petersburg 195251, Russia.*

The scanned copy of the signed "Transfer of Copyright Agreement" should be send by e-mail to: **mpmjournal@spbstu.ru**.

### **Filetype:**

Authors are invited to send their manuscripts **as MS Word file with PDF format copy**.

MS Word file should be prepared according to the general instructions bellow; we are kindly asking the authors to look through the detail instruction at: <http://www.mpm.spbstu.ru>.

### **Length:**

Papers should be limited to 30 typewritten pages (including Tables and Figures placed in the proper positions in the text).

### **Structure of the manuscript:**

**PAPER TITLE: CENTERED,**

**TIMES NEW ROMAN 14 BOLD, CAPITAL LETTERS**

**A.B. Firstauthor<sup>1</sup>, C.D. Secondauthor<sup>2\*</sup>** -Times New Roman 12, bold, centered

<sup>1</sup>Affiliation, address, country - Times New Roman 10, centered

\*e-mail: e-mail of the corresponding author - Times New Roman 10, centered

**Abstract.** Times New Roman 12 font, single line spacing. Abstract should not exceed 12 lines.

**Keywords:** please, specify paper keywords right after the abstract.

**Paper organization.** Use Times New Roman 12 font with single line spacing. Use *Italic* font in order to stress something; if possible, please, use **bold** for headlines only.

**Page numbering.** Please, do not use page numbering.

**Tables, Figures, Equations.** Please, see the sample file at <http://www.mpm.spbstu.ru> for more details.

### **References**

References should be subsequently numbered by Arabic numerals in square brackets, e.g. [1,3,5-9], following the sample style below:

[1] Koch CC, Ovid'ko IA, Seal S, Veprek S. *Structural Nanocrystalline Materials: Fundamentals and Applications*. Cambridge: Cambridge University Press; 2007.

[2] Hull D, Bacon DJ. *Introduction to Dislocations*. 5nd ed. Amsterdam: Butterworth-Heinemann; 2011 Available from: <https://www.sciencedirect.com/science/book/9780080966724?via%3Dihub> [Accessed 19th June 2018].

[3] Romanov AE, Vladimirov VI. Disclinations in crystalline solids. In: Nabarro FRN (ed.) *Dislocations in Solids*. Amsterdam: North Holland; 1992;9. p.191-402.

[4] Mukherjee AK. An examination of the constitutive equation for elevated temperature plasticity. *Materials Science and Engineering: A*. 2002;322(1-2): 1-22.

- [5] Soer WA, De Hosson JTM, Minor AM, Morris JW, Stach EA. Effects of solute Mg on grain boundary and dislocation dynamics during nanoindentation of Al–Mg thin films. *Acta Materialia*. 2004;52(20): 5783-5790.
- [6] Matzen ME, Bischoff M. A weighted point-based formulation for isogeometric contact. *Computer Methods in Applied Mechanics and Engineering*. 2016;308: 73-95. Available from: [doi.org/10.1016/j.cma.2016.04.010](https://doi.org/10.1016/j.cma.2016.04.010).
- [7] Joseph S, Lindley TC, Dye D. Dislocation interactions and crack nucleation in a fatigued near-alpha titanium alloy. To be published in *International Journal of Plasticity*. *Arxiv*. [Preprint] 2018. Available from: <https://arxiv.org/abs/1806.06367> [Accessed 19th June 2018].
- [8] Pollak W, Blecha M, Specht G. *Process for the production of molded bodies from silicon-infiltrated, reaction-bonded silicon carbide*. US4572848A (Patent) 1983.
- [9] Brogan C. *Experts build pulsed air rig to test 3D printed parts for low carbon engines*. Available from: <http://www.imperial.ac.uk/news/186572/experts-build-pulsed-test-3d-printed/> [Accessed 19th June 2018].

### **Правила подготовки статей:**

Рукопись (**английский язык, MS Word и копия PDF**) должна быть направлена в редакцию журнала по электронной почте: **mpmjournal@spbstu.ru**.

После подтверждения принятия статьи в печать, авторы должны отправить подписанные:

1. Соглашение о передаче авторских прав (<http://www.mpm.spbstu.ru>, раздел «Авторам»);
2. Экспертные заключения о том, что материалы статьи не содержат сведений, составляющих государственную тайну, и информацию, подлежащую экспортному контролю; по адресу:

*Россия, 195251, Санкт-Петербург, Политехническая, д. 29, Санкт-Петербургский политехнический университет Петра Великого, Институт передовых производственных технологий, Редакция периодических изданий.*

Скан-копии подписанных документов просим направить по электронной почте: **mpmjournal@spbstu.ru**

### **Тип файла:**

Редакция принимает **файлы MS Word с копией в формате PDF**. Статья должна быть подготовлена в соответствии с настоящей инструкцией, мы просим авторов также следовать более подробным инструкциям на сайте журнала <http://www.mpm.spbstu.ru> в разделе «Авторам».

### **Длина статьи:**

Статья не должна превышать 30 страниц формата А4, включая Таблицы и Рисунки, размещенные непосредственно в соответствующих местах.

### **Общие правила оформления статьи:**

**НАЗВАНИЕ СТАТЬИ: ВЫРОВНЯТЬ ПО ЦЕНТРУ,**

**ШРИФТ, TIMES NEW ROMAN 14 BOLD, ЗАГЛАВНЫЕ БУКВЫ**

Автор(ы): **А.Б. Первыйавтор<sup>1</sup>, В.Г. Автор<sup>2\*</sup>** - шрифт Times New Roman 12, bold, по центру

<sup>1</sup>Наименование организации, адрес, страна - шрифт Times New Roman 10, по центру

\* e-mail автора, представившего статью - шрифт Times New Roman 10, по центру

**Аннотация.** Аннотация статьи составляет не более 12 строк. Используйте шрифт Times New Roman 12, одинарный межстрочный интервал.

**Ключевые слова:** укажите ключевые слова после аннотации.

**Как организовать текст статьи.** Используйте шрифт Times New Roman 12, одинарный межстрочный интервал. При необходимости выделить какую-либо информацию используйте *курсив*. Используйте **полужирный** шрифт только для заголовков и подзаголовков.

**Номера страниц.** Пожалуйста, не используйте нумерацию страниц

**Таблицы, Рисунки, Уравнения.** Подробные правила оформления данных элементов статьи приведены в инструкции на сайте журнала <http://www.mpm.spbstu.ru>

### **Литература**

Ссылки приводятся в тексте в квадратных скобках [1,3,5-9]. Стиль оформления ссылок:

[1] Koch CC, Ovid'ko IA, Seal S, Veprek S. *Structural Nanocrystalline Materials: Fundamentals and Applications*. Cambridge: Cambridge University Press; 2007.

[2] Hull D, Bacon DJ. *Introduction to Dislocations*. 5nd ed. Amsterdam: Butterworth-Heinemann; 2011 Available from: <https://www.sciencedirect.com/science/book/9780080966724?via%3Dihub> [Accessed 19th June 2018].

[3] Romanov AE, Vladimirov VI. Disclinations in crystalline solids. In: Nabarro FRN (ed.) *Dislocations in Solids*. Amsterdam: North Holland; 1992;9. p.191-402.

[4] Mukherjee AK. An examination of the constitutive equation for elevated temperature plasticity. *Materials Science and Engineering: A*. 2002;322(1-2): 1-22.

- [5] Soer WA, De Hosson JTM, Minor AM, Morris JW, Stach EA. Effects of solute Mg on grain boundary and dislocation dynamics during nanoindentation of Al–Mg thin films. *Acta Materialia*. 2004;52(20): 5783-5790.
- [6] Matzen ME, Bischoff M. A weighted point-based formulation for isogeometric contact. *Computer Methods in Applied Mechanics and Engineering*. 2016;308: 73-95. Available from: [doi.org/10.1016/j.cma.2016.04.010](https://doi.org/10.1016/j.cma.2016.04.010).
- [7] Joseph S, Lindley TC, Dye D. Dislocation interactions and crack nucleation in a fatigued near-alpha titanium alloy. To be published in *International Journal of Plasticity*. *Arxiv*. [Preprint] 2018. Available from: <https://arxiv.org/abs/1806.06367> [Accessed 19th June 2018].
- [8] Pollak W, Blecha M, Specht G. *Process for the production of molded bodies from silicon-infiltrated, reaction-bonded silicon carbide*. US4572848A (Patent) 1983.
- [9] Brogan C. *Experts build pulsed air rig to test 3D printed parts for low carbon engines*. Available from: <http://www.imperial.ac.uk/news/186572/experts-build-pulsed-test-3d-printed/> [Accessed 19th June 2018].

# МЕХАНИКА И ФИЗИКА МАТЕРИАЛОВ

48 (2) 2022

Учредители: Санкт-Петербургский политехнический университет Петра Великого,

Институт проблем Машиноведения Российской академии наук

Издание зарегистрировано федеральной службой по надзору в сфере связи,  
информационных технологий и массовых коммуникаций (РОСКОМНАДЗОР),

свидетельство ПИ №ФС77-69287 от 06.04.2017 г.

## Редакция журнала

Профессор, д.т.н., академик РАН, А.И. Рудской – главный редактор

Профессор, д.ф.-м.н., член-корр. РАН, Д.А. Индейцев – главный редактор

Профессор, д.ф.-м.н. И.А. Овидько (1961 - 2017) – основатель и почетный редактор

Профессор, д.ф.-м.н. А.Л. Колесникова – ответственный редактор

Доцент, к.т.н. А.С. Немов – ответственный редактор

А.Ю. Ромашкина, к.т.н. – выпускающий редактор

Л.И. Гузилова – редактор, корректор

## Телефон редакции

+7(812)552 77 78, доб. 224

E-mail: [mpmjournal@spbstu.ru](mailto:mpmjournal@spbstu.ru)

Компьютерная верстка А.Ю. Ромашкина

---

Подписано в печать 30.05.2022 г. Формат 60x84/8. Печать цифровая  
Усл. печ. л. 10,0. Тираж 100. Заказ \_\_\_\_.

---

Отпечатано с готового оригинал-макета, предоставленного автором  
в Издательско-полиграфическом центре Политехнического университета Петра  
Великого. 195251, Санкт-Петербург, Политехническая ул., 29.  
Тел.: +7(812)552 77 78, доб. 224.



- Effects of different factors on the heat conduction properties of carbon nanotubes.....147-160**  
Junjie Chen
- Study of the influence of structural heritage and operating conditions on the durability of safety valve springs from steel 50KHFA .....161-174**  
M. Tupitsin, I. Trishkina, S. Sycheva, E. Storozheva, R. Novikov
- Changes in rock permeability near-wellbore due to operational loads .....175-183**  
V.V. Poplygin, E.P. Riabokon, M.S. Turbakov, E.V. Kozhevnikov, M.A. Guzev, H. Jing
- Analysis of CuCrZr/316L(N) bimetallic joint with and without nickel interlayer for plasma-facing components .....184-198**  
P. Piskarev, A. Gervash, S. Bobrov, V. Ruzanov, A. Ogurski, I. Mazul, R. Giniyatulin, B. Ermakov, O. Sevryukov
- Experimental study of ductile and fragile pipe cracked in High-Density Polyethylene (HDPE) .....199-207**  
Azzeddine Belaziz, Mohamed Mazari, Mohammed Bouamama, Samir Zahaf, Dahmane Mouloud
- Unstable plastic flow in structural materials: time series for analysis of experimental data .....208-216**  
Vladislav K. Kazankov, Anna G. Shmeleva, Ekaterina V. Zaitseva
- Experimental investigation of the mechanical behavior of honeycomb sandwich composite under three-point bending fatigue.....217-231**  
Hocine Mzad
- Stability analysis of nanoscale surface patterns in ultrathin film coating .....232-241**  
G.M. Shuvalov, S.A. Kostyrko
- Failure analysis of semi-elliptical crack behavior in the cement mantle of a total hip prosthesis.....242-271**  
Samir Zahaf, Mouloud Dahmane, Azzeddine Belaziz, Ismail Bouri, Nasreddine Afane
- Glass formation and some physical properties in NaPO<sub>3</sub>– LiF and NaPO<sub>3</sub>– (0.4 AlF<sub>3</sub> – 0.6 CaF<sub>2</sub>) systems .....272-281**  
V.A. Klinkov, V.B. Archelkov
- Mechanical properties of marble dust reinforced aluminum matrix structural composites fabricated by stir casting process.....282-288**  
Sandeep Kashyap, Hariom Tripathi, Naveen Kumar
- Study of polylactide 3D-printed samples with double-layer weave.....289-299**  
A.V. Pogrebnoi